

AN ABSTRACT OF THE THESIS OF

Kevin J. Greek for the degree of Master of Science
in Nuclear Engineering presented on December 2, 1986.

Title: OPTIMUM TEMPORAL AND CONTRAST CONSIDERATIONS IN
EXTREMELY HIGH SPEED NEUTRON RADIOGRAPHY

Abstract Approved: Redacted for privacy
A. H. Robinson

A facility developed using the OSU TRIGA pulsing capability and high speed motion photography has been used successfully for more than a decade to produce dynamic neutron radiographs of solid propellant combustion, two phase flow, and liquid streamflow. The existing imaging components have undergone little modification since the experiment's inception and include a LIF-ZnS neutron imaging scintillator, an image intensifier, and a high speed framing camera. Previous research has shown motion of large objects traveling at 100ft/s may be resolved at a framing rate of 10,000frame/s sampling each 40 microseconds. Few experiments, however have challenged system response beyond half this framing rate. Upon demand to record increasingly shorter events with greater time resolution

during the TRIGA 8ms pulse width, the camera was improved to allow exposure times as short as 2 microseconds. The existing system, however, demonstrates a minimum practical exposure time of 3 microseconds under the best flux and processing conditions for ordinance radiography.

The OSU high speed neutron radiography facility exhibits temporal and spacial resolution limitations as well as contrast restrictions when attempting to record extremely high speed events. An attempt was made to define present limitations in order to recognize areas of improvement. Transfer and modulation efficiency of each component (i.e. the reactor, collimator, object, neutron scintillator, intensifier, camera optics, and film) was analyzed and image blur due to object motion accounted. Treated analytically, system modulation, exposure, and noise contribution to the film image showed adequate agreement to existing measurements. This analysis demonstrated the most serious exposure loss is due to camera optics itself, static resolution is limited predominantly by the scintillator, and phosphor persistence at exposure times below 50 microseconds seems the most significant cause of motion blur. Quantum noise should deteriorate image quality if neutron exposure falls below 10^6 n/cm^2 but observation is exposure limited at this level. To improve exposure requires replacement of the rotating prism camera for more efficient optical

transfer; however, use of a faster film would increase system response on the short term. Scintillator resolution improvement would appear more practical once other components of the system have improved efficiency. Finally, increased flux levels and scintillator-photocathode efficiency would improve gain and especially noise conditions but is difficult to accomplish without compromise in resolution.

Optimum Temporal and Contrast Considerations
in Extremely High Speed Motion Neutron Radiography

by

Kevin J. Greek

A THESIS

submitted to

Oregon State University

in partial fulfillment of
the requirements for the
degree of

Master of Science

Completed December 2, 1986

Commencement June 1987

APPROVED:

Redacted for privacy

~~Professor of Nuclear Engineering in charge of major~~

Redacted for privacy

~~Head of Department of Nuclear Engineering~~

Redacted for privacy

~~Dean of Graduate School~~

Date thesis is presented December 2, 1986

Typed by Kevin J. Greek for Kevin J. Greek

TABLE OF CONTENTS

I.	INTRODUCTION TO NEUTRON RADIOGRAPHY	1
1.1	Objective of radiography	1
1.2	Historic background of neutron radiography	5
1.3	Neutron radiography methods	7
1.4	Neutron sources for radiography	12
1.5	Neutron moderation	17
1.6	Neutron collimation	18
1.7	Neutron foil detectors	22
1.8	Light emitting image detectors	25
1.9	Image recording devices	31
1.10	Motion neutron radiography	38
II.	HIGH SPEED MOTION NEUTRON RADIOGRAPHY COMPONENTS AT OSU	40
2.1	Research background of the OSU radiography facilities	40
2.2	High speed motion neutron radiography beam port configuration	42
2.3	TRIGA pulse behavior	46
2.4	Collimation	76
2.5	Scintillators	79
2.6	Image intensifier	80
2.7	High speed camera	83
2.8	Film and processing	85
2.9	Event synchronization	86
2.10	Event	93
2.11	System effectiveness	95
III.	INFORMATION RETRIEVAL ASPECTS	96
3.1	Information interpretation	96
3.2	System analysis	102
IV.	SYSTEM TRANSFER FUNCTION	118
4.1	Electrographic analysis	118
4.2	Flux magnitude available for imaging	119
4.3	Subject transfer, g_2	122
4.4	Scintillator absolute efficiency	124
4.5	Scintillator-intensifier coupling	154
4.6	Intensifier gain, g_4	156
4.7	Optical attenuation, g_5	158
4.8	Film transfer function	160
4.9	System image transfer	167
V.	IMAGE RESOLUTION	185
5.1	Introduction	185
5.2	MTF measurement	188
5.3	Static resolution	190
5.4	Dynamic image resolution	207
5.5	Object modulation	219
5.6	Noise	221

VI.	PROPOSED SYSTEM ENHANCEMENTS	235
6.1	Summary of present limitations	235
6.2	Possible improvements	237
6.3	Recommendations	251
VII.	REFERENCES	253
IX.	APPENDICES	
A.	Spectral matching factors	262
B.	LiF-ZnS scintillator efficiency program	272
C.	Computer simulation of OSTR pulses	284
D.	Neutron attenuation program	292

LIST OF FIGURES

Figure	Page
1.1 Mass absorption coefficients of the elements	9
1.2 Static neutron radiograph of a pressurized spray can	11
1.3 Unsharpness effects of finite aperture (a) Parallel beam (b) Point source (c) Finite source size	19
2.1 TRIGA mark II beam port configuration	43
2.2 Diagram of beam port #3 blockhouse and equipment	44
2.3 OSTR core loading diagram	48
2.4 Prompt negative temperature coefficient of reactivity for full FLIP core	51
2.5 TRIGA pulse power and peak fuel temperature relative behavior	67
2.6 Comparison of measured and computed TRIGA power traces	68
2.7 Pulse height variation with reactivity	69
2.8 Pulse duration at FWHM variation with reactivity	70
2.9 Maximum fuel temperature following a pulse as a function of reactivity	71
2.10 Scatter diagram of TRIGA pulse height	72
2.11 Beam port #3 collimation and details	77
2.12 Timing diagram of high speed synchronization	87
2.13 Block diagram of event synchronization	88
2.14 Temporal density characteristic of four high speed neutron radiography films	91

2.15	Averaged temporal density variation of four high speed neutron radiography films	92
3.1	Hierarchy of motion radiography information	99
3.2	Magnitude variation of an image element	107
3.3	Modulation transfer and the modulation transfer function (MTF)	112
	(a) Object bar chart	
	(b) System image response	
	(c) Graphical representation of modulation	
	(d) System MTF	
3.4	Arrangement of imaging components	117
4.1	LiF-ZnS scintillator quanta transmission and conversion	126
4.2	Monte Carlo scintillator model	131
	(a) Unit cell	
	(b) 2D cell	
	(c) Slab dimensioned to average chord length	
	(d) Half slab	
4.3	Scintillation transmission model about differential area	136
4.4	Scintillator efficiency prediction by approximate and Monte Carlo models	141
4.5	Computed and measured radiant emission of polyethylene binder LiF-ZnS scintillators	146
4.6	Comparison of scaled polyethylene scintillator absolute efficiency predictions to measurements	148
4.7	Correlation of measured relative and calculated absolute efficiency of OSU scintillators	152
4.8	Characteristic curves for 2484 and 2475 films for P11 source	161
4.9	System derived and reference P11 characteristic curves for 2484 film (8min)	171
4.10	System derived and reference P11 characteristic curves for 2484 film (4min)	172
4.11	System derived and reference P11 characteristic curves for 2475 film	173

4.12	System derived intensifier radiant gain behavior from 2484 films (8min)	176
4.13	System derived intensifier radiant gain behavior from 2484 films (4min)	177
4.14	System derived intensifier radiant gain behavior from 2475 films	178
4.15	Effect of object attenuation on reconstructing film performance	183
	(a) Exposure with attenuation	
	(b) Exposure without attenuation	
5.1	Measurement of unsharpness from the image spread signal	186
5.2	Geometric unsharpness in collimation	191
5.3	Geometry for point spread function calculation from subject	193
5.4	Behavior of β with thickness of four materials	197
5.5	Measured and correlated data for the OSU #51 scintillator	199
5.6	Static MTF for common ordinance application	205
	(a) Component	
	(b) System	
5.7	Component motion MTF	214
5.8	Limiting MTF for 100ft/s Cd bar	216
	(a) Component motion MTF	
	(b) System MTF	
5.9	Neutron flux modulation of a subject element	220
5.10	Signal-to-noise characteristic of common ordinance application	232
6.1	Modulation characteristics of several scintillators	240
B.1	Polyethylene binder scintillator program	278
B.2	Waterglass binder scintillator program	280
C.1	TRIGA pulse simulation program PULSE	289

LIST OF TABLES

Table	page
1.1 Beam characteristics of neutron radiography facilities	16
2.1 OSTR thermal and kinetic characteristics	62
4.1 Beam port #3 flux values at 35kW	120
4.2 Range and energy values for alpha and triton particles	129
4.3 Measured absolute efficiencies for various composition LiF-ZnS scintillators	144
4.4 Absolute efficiency of OSU scintillators	153
4.5 P11 CRT exposure index for five high speed films	163
4.6 System transfer function and components	168
4.7 Background on radiographs analyzed	174
4.8 Contributions to error in Figs. 4.12 to 4.14	180
5.1 Object point spread function parameters	195
5.2 Modulation parameters of three Kodak RAR films	202
5.3 Neutron radiography system and component modulation transfer functions	204
5.4 Image quality and the S/N ratio	233
6.1 Absolute efficiency of optimum forms of LiF-ZnS, glass, and Gd_2O_2S scintillators	242
A.1 Spectral matching factors	265
B.1 SCNT symbols	275
B.2 Sample output listing of CH_2 binder scintillator program	282
B.3 Sample output listing of waterglass binder scintillator program	283

C.1	PULSE symbols	287
C.2	Sample output listing of PULSE	290
D.1	MNTE symbols	295
D.2	Sample output listing of MNTE	297

OPTIMUM TEMPORAL AND CONTRAST CONSIDERATIONS IN EXTREMELY HIGH SPEED MOTION NEUTRON RADIOGRAPHY

I. INTRODUCTION TO NEUTRON RADIOGRAPHY

1.1 OBJECTIVE OF RADIOGRAPHY

Non-destructive testing has become an indispensable tool of scientific research and industrial production as growing emphasis is placed on the integrity and safety of devices, on advanced sophistication in design, and conservation of materials. Modern methods of non-destructive testing and materials evaluation are the outcome of a large investment in scientific research and development which allow visual examination of the intrinsic constituents of a device without regard to its optical transmission properties. Although the information desired from a subject may be simple, the challenge of non-destructive testing is the means whereby this information may be extracted without disruption of the subject's enclosure or the process for which it was designed. This complication resembles the proverbial black box which cannot be opened but may be rattled or thumped until the object characteristics inside may be

identified by sound or feel. The indirect means required to visualize the interior of a device in this field has prompted the development of instrumentation which will detect its characteristic transmission properties to radiation or electromagnetic waves.

One aspect of non-destructive testing employs penetrating radiation to produce a recorded image modulated by its transmission properties. Radiography, as it is called, must be comprised of three fundamental elements: a directed source, the object under evaluation, and an imaging system. The radiographic source is required to provide a directed beam of radiation which can penetrate the subject. Beam intensity becomes attenuated as the radiation travels into the object and undergoes scattering or absorption interactions. Radiation escaping from the opposite side of the sample has a spacial intensity distribution once it encounters the image plane of the imaging system. The imaging system, in turn, must convert as much of the remaining radiation as possible to light or charged particles available to record the image with film or a television system. In essence, the procedure records an image outline representing radiation interaction within the subject according to distribution of isotopic quantities. Beam energy and the nature of radiation influence the manner of interactions within the object and some degree

of choice is possible to exploit this behavior and produce radiographs which respond to different subject constituents.

The ideal requirements for radiography can be conveniently expressed in terms of the ideal radiographic image. This ideal radiographic image will be a true representation of the object in regard to high resolution and sharpness, freedom from distortion, and high degree of contrast between areas for which the transmitted intensity differs. Since human visual interpretation is exceedingly difficult to treat in a quantitative manner, the extent that radiographic quality approaches perfection is hard to define. Instead it is necessary to consider its quality from the best objective viewpoint obtained. The finite integrity of the imaging system is a further restriction of image definition, and, provided this can be interpreted objectively, may be the subject of considerable research in pursuit of an optimum system.

Unlike the health sciences objective of radiology, radiography encompasses the highly varied applications of industrial evaluation and development. Radiography originated with the discovery of X-rays, has developed during eighty years of X-ray practice, and X-ray imaging continues as its mainstay. However, an urgent requirement for more quantitative interpretation in

radiography has resulted in development of areas utilizing three forms of penetrating radiation--X-rays, gamma rays, and neutrons.

1.2 HISTORIC BACKGROUND OF NEUTRON RADIOGRAPHY

Compared to X-radiography, neutron radiography has not had significant application until as recently as the 1960's when adequate neutron sources became widely available. Although neutron radiography was first demonstrated from the experimental work of Kallman and Kuhn in 1935 using a small accelerator, strong development did not proceed until nuclear reactors were licensed for public possession and thereafter could serve as a prolific neutron source (1). Thewlis initiated reactor neutron radiography from his work in 1956. Ten years later further development was pursued by Berger at Argonne National Laboratory and by independent research at Harwell and Dounreay reactor sites. The early research work on neutron radiography concentrated on developing useful techniques and outlining applications while laboring under the disadvantage of very low output neutron sources. Once the nuclear reactor was available as a neutron source, the detection techniques were very rapidly optimized so that by 1968 the basic parameters of neutron detection and collimation were well understood (2).

Routine inspection using neutron radiography was first used extensively by the Apollo space program. In the late sixties industrial neutron radiography was

considered only for inspection of space system components and other high reliability systems. Later, as the space program slowed, applications reduced to inspection of components for military aircraft and missiles (3). Since that time, neutron radiography has expanded into an important interrogating probe in industry and research serving in conjunction where conventional radiography methods, such as X-radiography, fail.

In order to facilitate wide application of the technique independent of a reactor, optimum detection methods are now being combined with a return to smaller, low output and cost neutron sources. This trend has made on-site neutron radiography possible and promises vast acceptance of the method.

Nearly a hundred neutron radiography facilities now operate worldwide and are involved in highly diverse applications ranging from spent nuclear fuel evaluation to dentistry (2,4). Professional societies such as the American Society for Testing and Materials and the American Society for Nondestructive Testing recognize the importance of the method and provide for certification and standards services in an attempt to unify the approach of measurement of radiographic quality.

1.3 NEUTRON RADIOGRAPHY METHODS

The concentration of radiation attenuated in its passage through a radiography subject is characterized by the material's mass absorption coefficient for that particular radiation, which represents the probability a particle or photon will be absorbed within. The mass absorption coefficient has units of cm^2/g and is given by

$$\mu_a/\rho = \text{mass absorption coefficient (photons)}$$

$$\Sigma_a/\rho = \text{mass absorption coefficient (neutrons)}$$

where the variables specified for the material in question are:

$$\mu_a = \text{gamma or X-ray macroscopic absorption cross section (cm}^{-1}\text{)}$$

$$\Sigma_a = \text{neutron macroscopic absorption cross section (cm}^{-1}\text{)}$$

$$\rho = \text{density of material (g/cm}^2\text{)}$$

Physically, the macroscopic absorption cross section represents the reciprocal of the average distance the photon or neutron will travel in the material before absorption and often is defined as the probability per unit path length for an absorption to occur. This coefficient itself is determined by the concentration of the material and the energy as well as form of radiation.

Ionizing electromagnetic radiation such as X-rays

and gamma rays interact with the electron cloud of atoms and therefore as the atomic number of the element increases, the probability of radiation interaction with an electron increases also, providing element concentration and beam energy remain constant. This trend is shown for X-ray interactions as a steadily increasing mass absorption coefficient with atomic number (Fig. 1.1). Where the attenuation of X-rays in materials increases with increasing atomic number of the absorbing material, the mass absorption coefficients for neutrons at thermal energies, if arranged in order of increasing atomic number of the absorber, appear almost completely random. Unlike ionizing radiation, neutron absorption is independent of the electron structure of the atom and interacts only with the atomic nuclei. In comparison with X-ray attenuation, thermal neutrons (so called because they are in thermal equilibrium with their surroundings at or near room temperature) have high absorption characteristics for some light elements such as hydrogen, lithium, and boron as well as certain rare earth metals such as dysprosium and gadolinium whereas a few heavy metals such as lead and iron have low absorption. Neutron absorption coefficients also vary between different isotopes of the same element.

The distinction in absorption coefficients for X-ray and neutron interactions indicate potential advantages of

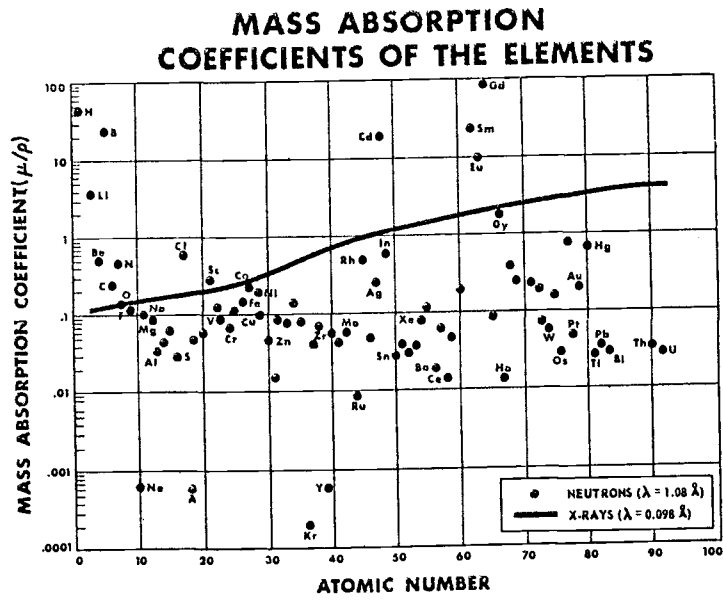


Fig. 1.1: Mass absorption coefficients of the elements.

radiography with thermal neutrons. The most important case is that of hydrogen which is characterized by such a high scattering of thermal neutrons that there is a strong possibility of imaging hydrogenous components such as water, oil, or plastic within metal. Figure 1.2 is a neutron radiograph which demonstrates this advantage. Pictured is a pressurized spray can half full of mineral oil complete with a plastic cap and two nozzle extension tubes, actual size. Because the hydrogenous nature of the oil and plastic have a thermal neutron absorption coefficient much greater than the steel can, its contents and the extension tubes behind the can are clearly visible. A comparable X-ray of this subject would only reveal the steel can. Note this positive photographic image represents dark areas as those which attenuate the neutron beam.

Since the neutron mass absorption coefficient fails to produce an orderly relationship with atomic number as does the X-ray mass absorption coefficient, the neutron interaction probability is as well depicted by the neutron macroscopic cross section, or simply cross section, for any material, and often is since it is a very familiar parameter in nuclear theory.



Fig. 1.2: Static neutron radiograph of a pressurized spray can.

1.4 NEUTRON SOURCES FOR RADIOGRAPHY

Neutrons utilized in radiography span an energy range that can be designated in four groups:

1. Fast neutrons--energies exceeding 0.1MeV
2. Epjthermal neutrons--energies between 0.3 - 10^4 eV
3. Thermal neutrons--energies between 0.01 - 0.3eV
4. Cold neutrons--energies between 0 - 0.01eV

Neutron energy alters the behavior of the mass absorption coefficient or cross section and in certain radiography applications sources of neutrons above or below thermal energies are desirable. With fast neutrons the cross sections of different elements tend to decrease and become less separated resulting in poor material discrimination, thus fast neutron radiography is at a disadvantage compared to other radiographic methods. A mass absorption coefficient decrease and stabilization for all elements is characteristic of ~~the~~ increasing energy X-ray interactions as well. The decrease in cross section implies, however, that large thicknesses of materials may be penetrated (2). Cold neutron radiography appears advantageous since penetration of some thick materials is possible due to reduced cross sections below the Bragg cutoff. This trend reverses below 0.001eV as neutron absorption increases providing capabilities to image extremely dilute concentrations of hydrogenous materials within a very thin layer sample

(5). Epithermal neutrons offer some possibilities which do not yet seem to have been explored, however several large changes in cross section which exist for materials in this energy region offer alternatives in material discrimination.

Several potential sources of intense neutron beams exist, nearly all of which require an energy reduction or moderation from fast to thermal energy levels. These sources, in decreasing order of source intensity, complexity, and cost, are:

1. Nuclear reactors
2. Positive ion accelerators
3. High energy X-ray machines using a (X,n) conversion e.g. linacs
4. Radioactive sources using (α ,n) or (γ ,n) reactions
5. Radioisotope direct neutron emitters

Due to the superior thermal neutron beam intensity obtained from reactors, the majority of neutron radiography has been performed using reactors as sources. Any reactor equipped with beam ports and capable of operating at a power greater than 1kW may be useful for radiography however higher reactor powers produce better radiographs in shorter exposure time. The most widely used reactors are those built for research purposes and range in power from 5kW to 50kW producing core fluxes of 2.5×10^{11} to 5×10^{14} n/cm²-s (6). Reactor pulsing operation whereby power may be boosted several magnitudes above thermal power for a short duration often presents no

difficulties for some reactors due to their inherent shut-down capability. Pulsed reactors may not only considerably shorten radiographic exposure time but radiograph moving objects or transient events.

Positive ion accelerators produce thermal neutrons indirectly using deuteron bombardment of beryllium or tritium targets then thermalizing the fast neutrons produced with a moderator. Accelerators based on the $T(d,n)$ reaction produce fast neutrons above 14MeV in energy and may be used to induce fast fission in uranium to enhance neutron yield. Sealed tube $T(d,n)$ neutron generators have output yields of up to $10^{13}n/cm^2-s$ but have a limited lifetime of a few hundred hours. The accelerator sources are unique in that their radiation may be turned "on" and "off" at will leaving negligible radioactivity. One development in accelerator structure that promises an important contribution as a practical and superior source of fast neutrons for neutron radiography is the radio frequency quadrupole (RFQ). The RFQ linac is attractive because of its reliability, high current, simplicity of operation, and capability of being rendered mobile (7,8). Linacs provide the advantage of conversion between X-ray and neutron generation in addition to high neutron yield, though at greater expense.

Radioisotope sources are portable, require little

skill to operate, but produce the least intense radiographic neutron beam and therefore subjects require long exposure times. Four radioisotopes have known to be used in neutron radiography and include $^{124}\text{Sb-Be}$, $^{241}\text{Am-Be}$, $^{242}\text{Cm-Be}$, and ^{252}Cf . Californium 252 is a transuranic element made artificially which produces neutrons by spontaneous fission. A one milligram source of ^{252}Cf produces a high neutron yield of $2.3 \times 10^9 \text{ n/cm}^2\text{-s}$ and therefore is the preferred radioisotope source.

Table 1.1 summarizes the neutron flux generator capabilities of various different neutron generating facilities. It has been estimated that $10^5 \text{ n/cm}^2\text{-s}$ is required to impinge on a detector to produce a reasonable image, and $10^9 \text{ n/cm}^2\text{-s}$ for a high quality image so that Table 1.1 demonstrates clearly the excellent choice of the nuclear reactor source (9).

Table 1.1: Beam characteristics of neutron radiography facilities (10).

Source	Fast neutron flux (n/s)	Thermal beam	
		L/D	Flux @ film site (no object) (n/cm ² -s)
Large research reactor	10^{14}	250	10^8
Small reactor	10^{12}	250	10^6
1mg Cf-252	2×10^9	12	10^4
5.5Mev linac; Be(X,n)	4×10^8	18	8×10^4
Neutron tube T(d,n)	10^8	18	2×10^4
3Mev van de Graaff	3×10^9	33	2×10^5
15Mev linac; Pb(X,n)	3×10^{11}	8	10^5
Sb-Be, 270Ci	1.5×10^9	10.5	2×10^4

1.5 NEUTRON MODERATION

All neutron sources produce a large concentration of fast neutrons and, except for the thermal neutron beam extracted from an appropriate part of a reactor, require the beam to be thermalized using a moderator such as water or high density polyethylene. As fast neutrons slow to thermal energies by energy loss in multiple collisions within the moderator, thermal neutrons scatter randomly within the moderator volume. An outlet for thermal neutrons is provided by extending a moderator free tube into the volume through protective shielding surrounding the source and moderator. This tube does not necessarily have to point directly at the source of fast neutrons; its direction and distance into the moderator for optimum outlet flux must be determined by experiment or calculation (10).

1.6 NEUTRON COLLIMATION

An important characteristic of a neutron source beam is its divergence. The images produced in neutron as well as general radiography are simple shadow images and therefore are influenced by source aperture. If the radiographic image is to be undistorted this would require that the incident radiation takes the form of a broad parallel beam. In most cases this cannot be achieved and certainly cannot with neutrons since their uncharged aspect prohibits focusing to the degree required by utilizing the magnetic moment of the neutron. A possible alternative is to use a neutron point source, preferably at a fairly large distance from the subject. When the distance is very large, the incident radiation is nearly a parallel beam however reduced in intensity due to the inverse square law. A point source configuration is easily obtained in X-radiography but is seldom practical for neutron radiography. Figure 1.3 attempts to illustrate the effect of finite source size upon image sharpness. In Fig 1.3b a point source illuminates an object of width AB without region of partial shadow whereas in Fig 1.3c a source of finite size on object AB casts a shadow which consists of an umbra on region of total shadow A'B' surrounded by a penumbral region of partial shadow as shown at A'A'' and

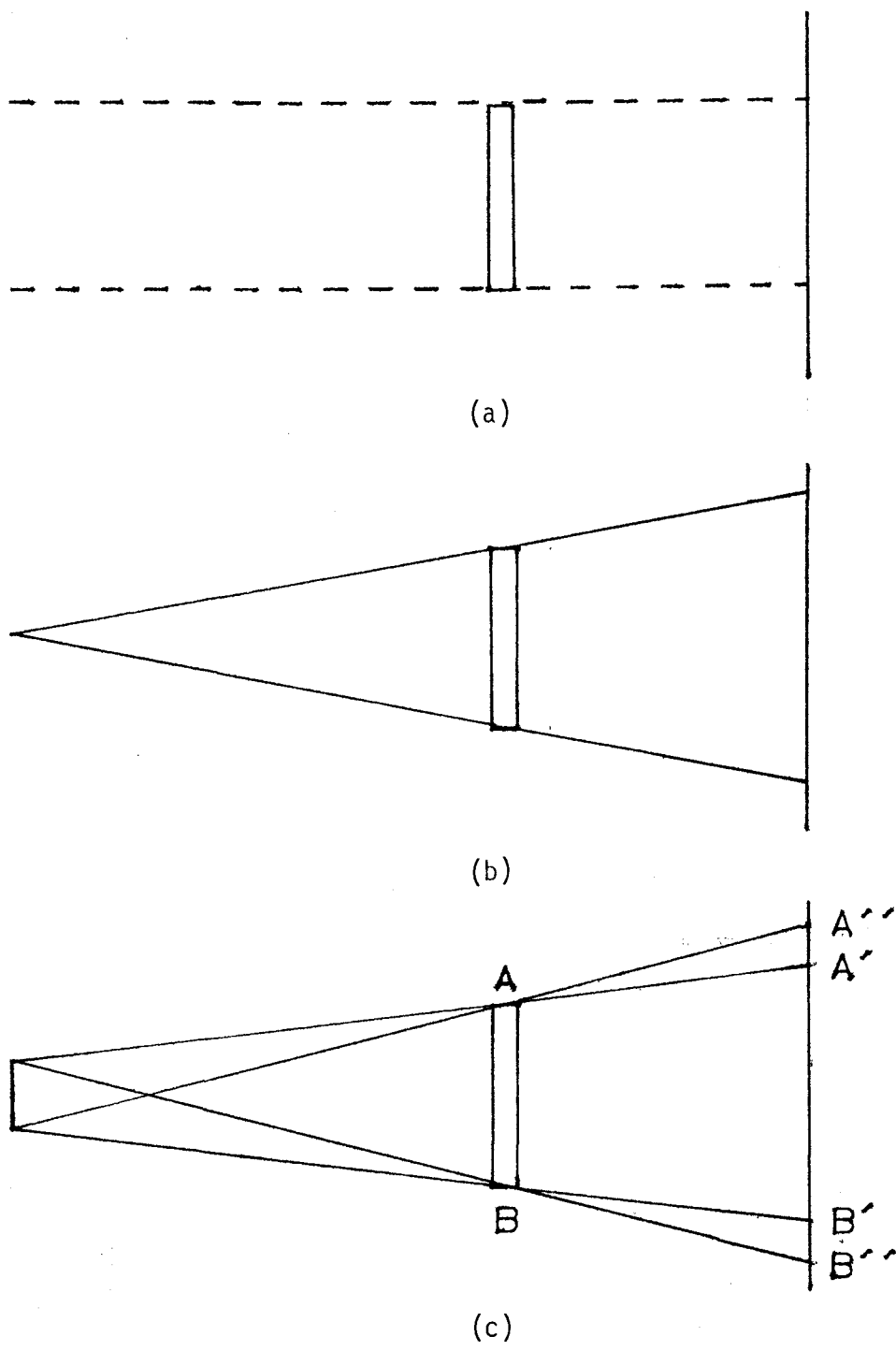


Fig. 1.3: Unsharpness effects of finite source aperture
(a) Parallel beam. (b) Point source. (c) Finite source size.

B'B''. This penumbra represents a degree of image unsharpness and will, therefore, reduce image clarity and resolution. The diagram shows an exaggerated case of unsharpness and such extreme changes in apparent shape are rare. Distortion can be minimized by not only increasing distance from the source or reducing aperture but maintaining as close a contact between the subject and image plane as possible.

A collinear neutron beam may be simulated using a long neutron absorber lined tube extended from a large area of the moderator volume. This collimating device selects neutrons traveling essentially in a parallel direction by removing those which stray into high thermal neutron absorption materials such as boron or cadmium. Due to high energy gamma emission following absorption in ^{113}Cd , however, materials based on boron compounds have become the preferred absorber.

Collimator tube configuration is not necessarily a simple parallel design, divergent and convergent-divergent forms have been devised, of which the divergent configuration is now favored despite a larger gamma concentration in the beam (11-15). Neither is the effect of collimator tube configuration and position simple, since both determine thermal neutron intensity, gamma to neutron ratio, and neutron energy spectrum of the beam. The primary defining factor of beam definition following

collimation is characterized by only the length and diameter of the smallest collimator opening and is expressed as a ratio (L/D). For both collimation types, image unsharpness varies inversely with this ratio and the neutron flux reaching the object is a function of the inverse square of L/D. The highest quality beams from nuclear reactors typically have L/D ratios of 150, but, for conservation of flux in lower output accelerator and radioisotope based systems, use of L/D ratios from 30 to 18 are adequate if some loss in image quality can be tolerated.

Moderation and collimation reduce available intensity several orders of magnitude. Typically the thermal beam produced is 10^{-5} to 10^{-6} of the initial source intensity, depending on the amount of collimation chosen (10). These severely attenuated beam intensities place restrictions on subject penetration width and exposure and thereby direct considerations for efficient imaging components necessary to compensate for beam loss.

1.7 NEUTRON FOIL DETECTORS

The uncharged property of the neutron which makes it valuable and unique also makes it difficult to detect. Following irradiation of the radiography subject, a means to convert the modulated neutron image into a form that may be recorded is necessary. Although photographic film alone is sensitive to neutrons through the $^{107}\text{Ag}(n,q)$ and $^{109}\text{Ag}(n,q)$ reactions, there is insufficient silver present in X-ray or thick "nuclear" emulsions for it to be used directly. Therefore conversion to forms of radiation films are most sensitive to, such as ultraviolet light, will shorten exposure time. A neutron can be detected using the energy released from a charged recoiling atom or particle produced by scattering or absorption interactions within a conversion screen. Two requirements are imposed upon efficient neutron conversion; the converter must both possess a high neutron absorption to gather the neutron image and an efficient emission of secondary radiation. For thermal neutron radiography, the most effective absorbers in general use are dysprosium, boron, gadolinium, indium and lithium. Neutron absorption reactions with these materials produce energetic charged particles which can excite a phosphor or expose X-ray film. Converters may be based on either light emitting scintillator screens or

particle emitting metal foils of indium, gadolinium, and dysprosium. Other conversion methods are available but uncommon in routine radiography.

Foil conversion screens, sometimes known as intensifying screens, expose X-ray film by beta emission upon direct interaction with X-rays or neutrons. Due to the short range of beta particles emitted by the foil under irradiation, an intimate contact between the foil and X-ray film is required to maximize exposure and image sharpness. A light tight film cassette is used to clamp the film and foil together either under vacuum or force in both neutron and X-radiography.

The gadolinium foil is preferred for neutron radiography due to its extremely high thermal neutron absorption. Gadolinium foils are very thin ranging in thickness of 10 - 25 micrometers yet can absorb about 75% of a thermal neutron beam releasing internal conversion electrons of about 70keV (16). Thin highly absorbing foils and close film contact reduce the scattering distance of an electron prior absorption in the photographic emulsion and therefore high resolution radiographic images may be recorded using gadolinium screens.

Unfortunately, the direct exposure method above may be plagued by detection of interfering radiation, such as gamma radiation within the neutron beam or by prompt

emission from neutron reactions with the inspection object or with other objects in the beam path (17). An indirect means of exposure may also be more suitable in some situations to prevent thermal damage to the film. A method whereby the foil itself is activated by the modulated neutron beam then later allowed to expose the X-ray film during decay circumvents these problems. The transfer exposure technique requires a screen material of high neutron absorption with an isotope production of convenient half life, the latter being long enough to provide good emulsion recording within time needed for next use. The short duration of electron emission following activation of gadolinium has made this metal unsuitable for transfer radiography. Instead indium and dysprosium beta emitting foils are in regular use for transfer neutron radiography. Each has their own merits; indium provides slightly better resolution at a given thickness and has a significant response to epithermal neutrons whereas dysprosium is a more durable foil, has a larger cross section and longer half life which allows radiography using weaker beams (18). Neutron detection using transfer screens is not useful at neutron fluxes below about $5 \times 10^4 \text{ n/cm}^2\text{-s}$ due to insufficient activity even following saturation to produce a high photographic density (19). This problem is only significant during activation from low flux sources such as radioisotopes.

1.8 LIGHT EMITTING IMAGE DETECTORS

The long exposure and processing times characteristic of conversion foil neutron radiography are often inconvenient. Neutron radiographic recording of dynamic subjects or real-time imaging requires an alternate conversion screen known as a scintillator which can display the modulated neutron beam as a luminous image for film or electronic recording. Scintillators are produced as a combination of two components; a neutron absorber that releases a charged particle upon interaction with a neutron and a phosphor which emits light upon excitation. Emission of the image as light allows standard photographic or X-ray film detection by its most sensitive means possible and therefore is capable of a substantial decrease in exposure. Three classifications of scintillators exist:

1. Crystalline
2. Heavy metal (Gadolinium)
3. Glass

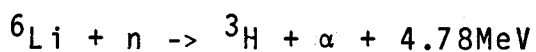
1.8.1 Crystalline Scintillators

Alpha emitting neutron absorbers such as ^{10}B and ^6Li are most important for scintillator use due to the high energy release and short range of their particles. These high thermal neutron absorbers have been extensively

studied for use in scintillation neutron counters and were among the first scintillators to be applied. Combined with a phosphor such as silver-activated zinc sulphide, these absorbers make the most sensitive light-emitting detectors and will produce good images when struck by only a few hundred neutrons/cm² (20). Scintillator construction is performed with naturally occurring chemical forms of these isotopes such as the powders LiF or boric acid (H₃BO₃) and may be enriched with ⁶Li or ¹⁰B to enhance neutron absorption. These absorbers as well as the phosphor ZnS are white opaque powders which must be held together in mixture by a transparent binding material of polyethylene, lucite, epoxy, sodium silicate or other appropriate materials and is often affixed to an aluminum substrate. The concentration of these scintillation materials must be carefully chosen since altogether they have a synergistic effect upon optimum scintillator performance. Scintillator thickness is an additional consideration. The scintillator's conversion efficiency increases with increasing thickness of any scintillation screen for small values of thickness. However, increased thickness decreases resolution and at large values of thickness it also decreases the amount of light reaching the film by light scatter within the phosphor.

The LiF-ZnS screens are among the most widely used

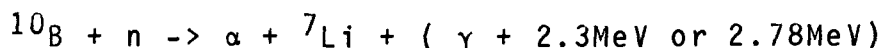
scintillators for radiography due to high yield, durability, and simplicity of construction. Their optimum response has been studied in detail by Spowart and others who determined a 1:4:1 mixture by weight of ${}^6\text{LiF}$, ZnS(Ag) , and polyethylene provides best detection by photosensitive film; other researchers specify a ratio of 1:2 for LiF to ZnS(Ag) as optimum regardless of binder concentration (21-23). The nuclear reaction involved



is highly exothermic such that both the alpha particle and triton have considerable kinetic energy. The particles are released at an angle of 180° apart with a sum equal to the 4.78MeV Q value of the reaction (the alpha particle carries 2.05MeV and the triton has an energy of 2.73MeV). Both highly ionized particles travel through the scintillator losing their energy by excitation and ionization, although the alpha particle has a range much shorter due to its greater mass and charge. Provided at least one strikes a ZnS crystal many photons of light are produced which the clear binding material conducts to the surface. Zinc sulphide emission peaks in the blue region of the light spectrum (450nm) and acts as a good spectral match to detectors using a photocathode or orthochromatic photographic emulsion.

Scintillators constructed with boron absorbers are characterized by absorption cross sections nearly five

times that of the LiF-ZnS scintillator however yield less energetic alpha particles following the neutron interaction:



An alpha particle released with 1.47MeV in kinetic energy is available to excite the phosphor following 93% of each interaction. This lower energy alpha particle may be expected to have a shorter range within the phosphor and therefore the overall image resolution of scintillators using boron compounds should be better than the LiF-ZnS scintillator but at reduced image intensity. Comparisons between these scintillators have produced mixed results (22, 24-28).

1.8.2 Gadolinium Scintillators

The high thermal neutron absorption of gadolinium compared to that of lithium has made it a likely candidate for scintillator use although its heavy atom content presents increased sensitivity to gamma rays. Poor image intensity due to the low energy emission of internal conversion electrons (70keV) and a characteristic peak spectral emission of blue-green color (540nm) require increased exposure time by common blue light detectors. Image resolution is excellent, however, comparable to that obtained using metal foil screens.

Gadolinium oxybromide (GdOBr:Er) and gadolinium oxysulphide screens ($\text{Gd}_2\text{O}_2\text{S:Tb}$) are now available commercially for X-radiography. Research indicates optimum scintillator thickness for neutron detection is about 100 micrometers (29).

1.8.3 Glass Scintillators

The heterogeneous nature and opacity of crystalline scintillators produce grainy radiographs. A completely homogeneous structure characteristic of glass scintillators eliminates radiographic mottle as a direct consequence of granular screens. Glass scintillators are based on combinations of lithium or boron neutron absorbers with cerium-activated scintillating glass which is transparent to its own scintillations thereby allowing light produced deep within the scintillator to be recorded. Although this inorganic scintillator was developed over 25 years ago for neutron counting applications, suitable scintillators for neutron imaging applications were not available until thin slices of the glass could be manufactured. Since boron-loaded scintillation glasses have reduced light output as well as difficulties in production of more than a few grams, the lithium-loaded glasses are only of current interest in neutron radiography (30). Glass scintillators using

large amounts of Li_2O enriched to 95% ^6Li are available and typical samples are highly neutron absorbing; an NE905 glass sheet 1mm thick will absorb about 80% of a thermal neutron beam (31). Despite this, the lithium-loaded glass is less sensitive than LiF-ZnS scintillators and although increased thickness will enhance emission, resolution may decrease due to light scattering too deep within the glass (32). These scintillators emit blue light like the LiF-ZnS screens.

1.9 IMAGE RECORDING DEVICES

Four methods are available to record and integrate a fixed radiographic image:

1. Track-etch detectors
2. Thermoluminescent detectors
3. Photographic film
4. Electronic means

The first two means listed provide for both neutron detection and image recording whereas film and electronic cameras register a radiographic image following detection. Photographic film image recording has been used predominantly throughout the history of radiography and has had an extensive background in research and application. Comparatively recently, electronic photosensitive devices have been combined with high density analog and digital recording media to produce video radiography systems which may serve in conjunction with traditional photographic emulsions.

1.9.1 Track-Etch Detectors

Track-etch is a method used in neutron radiography to detect and record a neutron image as radiation damage tracks in a dielectric material made visible by the selective use of chemical etching agents. Radiation tracks left by massive charged particles are made visible

by etching with hot sodium hydroxide solution. The number of tracks etched is a linear function of neutron exposure over the range $10^3 - 10^{20}$ n/cm² (33). An alpha emitting converter screen such as ⁶LiF with several alpha sensitive cellulose nitrate plastics is utilized to record tracks upon neutron interaction in most viable track etch systems. Exposure is comparable to dysprosium transfer radiography by these screens (34,35). Attempts in contrast enhancement to extend the range of information extracted have been reported using polarized light, colored cellulose layers, and impregnation with fluorescent dye (33,36).

Track-etch radiography is independent of gamma irradiation like the transfer technique. Many more attractions are provided by track-etch radiography namely:

1. Detector insensitivity to light thereby eliminating need for a light tight enclosure or darkroom.
2. High spacial resolution
3. Exposure which can continue indefinitely.

1.9.2 Thermoluminescent Detectors

A background of LiF use with dosimetry applications has encouraged development of thermoluminescent materials for neutron imaging. Here a thin sheet of ⁶Li-loaded LiF is exposed to a modulated thermal neutron beam. Once

neutron exposure to the absorber is complete, the radiographic image is released as light by heating the LiF at 210° , hence the term thermoluminescent detector.

The luminescent image is recorded by photographic film. Unfortunately, the aspect of thermal damage to the emulsion when in contact with the hot image plate has prevented widespread use of this technique due to complex methods required against film damage. A camera may be used to photograph the phosphor during heating but this leads to an unfortunate loss of light from the characteristically narrow angle light collection of optics systems. High numerical aperture fiber optics could reduce loss. One method of circumventing this problem releases the stored energy in the LiF by means of ultrasonic excitation while the film is immersed in water to prevent overheating (37).

As with the track-etch method thermoluminescent detection requires a high exposure on the order of 10^9 n/cm^2 to produce an image. The major advantage of the system lies in its freedom from reciprocity failure at low exposure levels and its capability to accumulate thermal neutron images over extended periods.

1.9.3 Photographic Film

There are two types of photographic film in common use for neutron radiography. First, X-ray films are the most appropriate choice for use with electron emitting screens. Although both double sided and single sided emulsion X-ray films are used, double emulsion films are inappropriate for gadolinium screens due to negligible electron penetration to the second emulsion and the undesired gamma exposure it absorbs (16,38). For use with light emitting screens, on the other hand, orthochromatic or panchromatic graphic arts films are best suited for recording the blue light emitted from zinc sulphide phosphors.

The photosensitive properties of the silver halide emulsion is common to both X-ray and graphic arts films. It consists of a suspension of silver halide in a thin layer of gelatin. When radiation is absorbed by the emulsion extremely small particles in the silver halide crystals are converted to metallic silver. These traces of silver are so minute that the emulsion is, to all appearances, unchanged, but a number of particles are formed proportional to the amount of incident radiation such that a latent image exists in the emulsion. When the film is developed, the developer attacks exposed grains differentially, those grains which have received a

high exposure are reduced to a black metallic silver quickly while those which received slight exposure are converted slowly, therefore the latent image becomes visible as a stable black silver deposit. Once initiated the development could proceed until all the silver halide is reduced to metallic silver but in practice development continues for a limited time only and the undeveloped halide is removed by means of a fixing agent. The amount of silver deposited then bears a definite relationship to exposure or the quantity of radiation incident on the film.

Photographic films are available with a range of sensitivities or exposure "speeds". An exposure of 10^8 n/cm^2 is required to produce a reasonable photographic density for an average speed film. Due to the poor collimated beam strength of most non-reactor thermal neutron sources the fastest X-ray films appear to be the best choice in terms of available exposure. Extended development time in high energy developers for either films will enhance film speed further. High film speed, however, is usually achieved at the expense of granularity of the negative. High speed films are produced with a high halide grain mass and size to increase quantum absorption probability and thus are subject to inherent granularity. A compromise must then be made between image density and resolution when using

low flux neutron sources.

1.9.4 Electronic Image Recording

Photographic film is the cheapest material a high density neutron image may be recorded upon with reasonable efficiency. Silver halide films, however, also have several inherent limitations that are difficult to overcome, namely 1) the requirement of "wet" processing, 2) the delay associated with processing, and 3) the materials are non-reusable once exposed. If the radiographic image can be detected by electronic means the image may be displayed on a monitor, stored in analog form on magnetic disc or tape, or in digital memory following analog to digital conversion. Once the image is represented in an electronic form, image processing instrumentation can enhance, restore, measure, or perform pattern recognition upon the radiographic image as it is acquired. Delay time reduction from exposure to radiographic examination as well as the capability to reinstate storage media is a powerful advantage of electronic "real-time" radiographic instrumentation.

The equipment necessary to complete a real-time radiography system is now commonplace. Most such systems convert the image into an electronic form by coupling a thermal neutron scintillator to a sensitive intensified

vidicon scanning at standard TV frame rates (41,42). Research with experimental image detection cameras using the electron sensitive properties of CCD arrays, directly software configurable vidicons or CCDs, highly sensitive slow scan cooled target vidicons, or multiwire proportional chambers (MWPC) has shown promising success for application in real-time radiography (43-45). Perhaps the greatest shortfall with current real-time radiography systems is the slow sampling rate required for comparable resolution images achieved by photographic emulsions. Object size must be restricted within the small input diameter determined by physical or commercial manufacturing limits for high resolution optical imaging devices such as vidicons, CCDs, or intensifiers, although the MWPC imaging plane can be constructed of size comparable to X-ray films (47). Real-time radiography is rapidly expanding in non-destructive applications where reduced speed and resolution are tolerable, however, and instrumentation and software development continue to optimize the method.

1.10 MOTION NEUTRON RADIOGRAPHY

Motion neutron radiography is a variation of the neutron nondestructive evaluation method whereby sequential time resolved images may be recorded of events which undergo changes in physical constitution. The first fundamental difference of motion radiography resides in use of a framing image recorder such as a motion picture camera which will record a number of image frames within a short controlled length of time. Secondly, as opposed to conventional or static radiography a great demand is placed on the imaging system requiring the fastest possible in both exposure time and response. Separate considerations for temporal image integrity require image blur to be minimized. Often, however, attempts to minimize both exposure and blur at once produce contradictory results and imaging aids must be used such as image enhancement or intensification to extend framing rate. Framing rates above 1000 fps may be classified as high speed radiography; here high gain instrumentation becomes the rule.

A number of sources in literature refer to the characteristic exposure required to produce a visual image using a converter-film combination or simply its image transfer efficiency as its "speed" (e.g. a

"slow"). Because of the confusion between distinguishing converter speed and response time due to image motion, particularly in motion neutron radiography where response time becomes important, a distinction has been made here to use the term "exposure" to represent converter efficiency and "speed" to denote response time.

II. HIGH SPEED MOTION NEUTRON RADIOGRAPHY COMPONENTS AT OSU

2.1 RESEARCH BACKGROUND OF THE OSU RADIOGRAPHY FACILITIES

The Oregon State University Radiation Center utilizes a TRIGA Mark II research reactor on site in training and research. Static and motion neutron radiography facilities were developed from the TRIGA beam ports during the early 1970's by A. H. Robinson and his associates. These facilities have enabled considerable research and scholarship by OSU graduate students regarding evaluation of two phase flow, propellant burning patterns in ordinance work, neutron radiography feasibility with reactor assemblies, and response of liquid streams (49-53). Besides research on neutron radiography applications, studies have been performed on measured limitations and optimization of the radiography facilities themselves by A. H. Robinson, J. P. Barton, R. H. Bossi, and their associates (54,55). Research has been performed under the sponsorship of the US DOD in the past. Presently, studies for improvement of the original high speed motion neutron radiography facility are being made as well as attempts on implementation of real-time imaging evaluation and

neutron holography.

2.2 HIGH SPEED MOTION NEUTRON RADIOGRAPHY BEAM PORT CONFIGURATION

Irradiation facilities of the TRIGA include one thermal column, four horizontal beam ports, one pneumatic system, and a rotary specimen rack. Although the TRIGA has four beam ports only two are presently accessed, both for neutron radiography; one radial beam port (#1) and the tangential beam port (#3). Beam port 1 has been configured for a static neutron radiography facility since its beam tube has collimators available which can provide L/D ratios between 100:1 to 400:1 as necessary for high resolution X-ray films. High speed motion neutron radiography is performed in beam port 3 at a much lower collimation ratio (30:1) so as not to compromise flux intensity required for high frame rate imaging with scintillators. A unique feature of beam tube 3 is its tangential orientation with the core which allows for minimization at the beam port opening of gamma radiation. Figure 2.1 represents a horizontal view of the TRIGA reactor which shows this tangential arrangement.

The equipment for high speed motion neutron radiography is contained within a heavily shielded concrete blockhouse alongside the reactor wall. Within the existing facility, a steel equipment bench, image

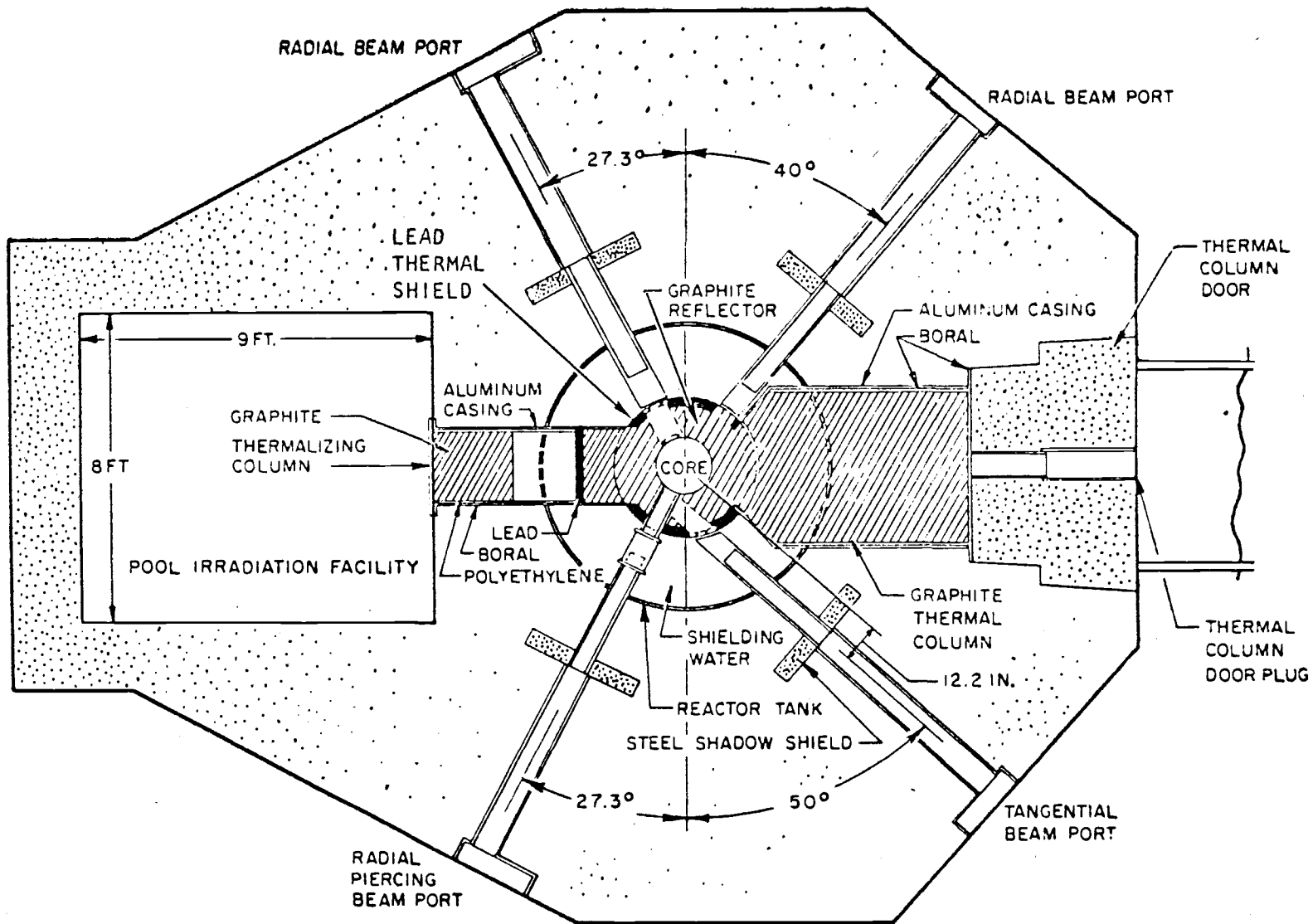


Fig. 2.1: TRIGA mark II beam port configuration.

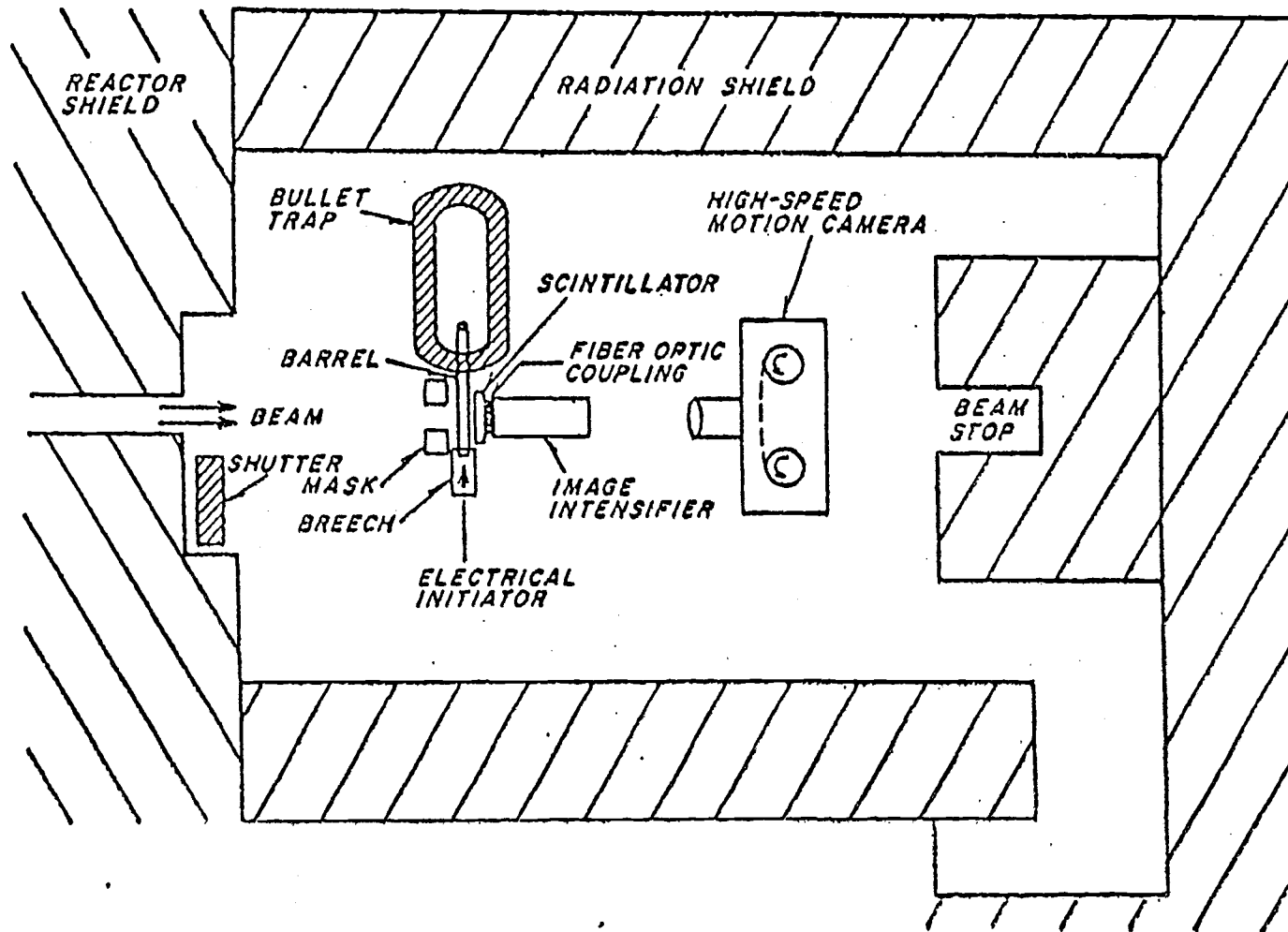


Fig. 2.2: Diagram of beam port #3 blockhouse and equipment.

intensifier, and high speed framing camera are centered about the beam opening (approx. 4x5") as shown in Fig. 2.2. Prior to performing radiography, the subject is positioned as close as possible to a LiF-ZnS(Ag) scintillator mounted on the input end of the intensifier. The camera records the intensified image on high speed film during a reactor pulse and initiates remote electronic synchronization of the reactor pulse and event. Afterwards, the film is developed by an automatic processor in a high energy developer. The result is some few feet of exposed 16mm film. Most of the above equipment and methods present a significant contribution in determining how information of the event is recorded. Individual performance of the existing camera, intensifier, scintillator, film, and pulse behavior determine the intensity and resolution of the final image.

2.3 TRIGA PULSE BEHAVIOR

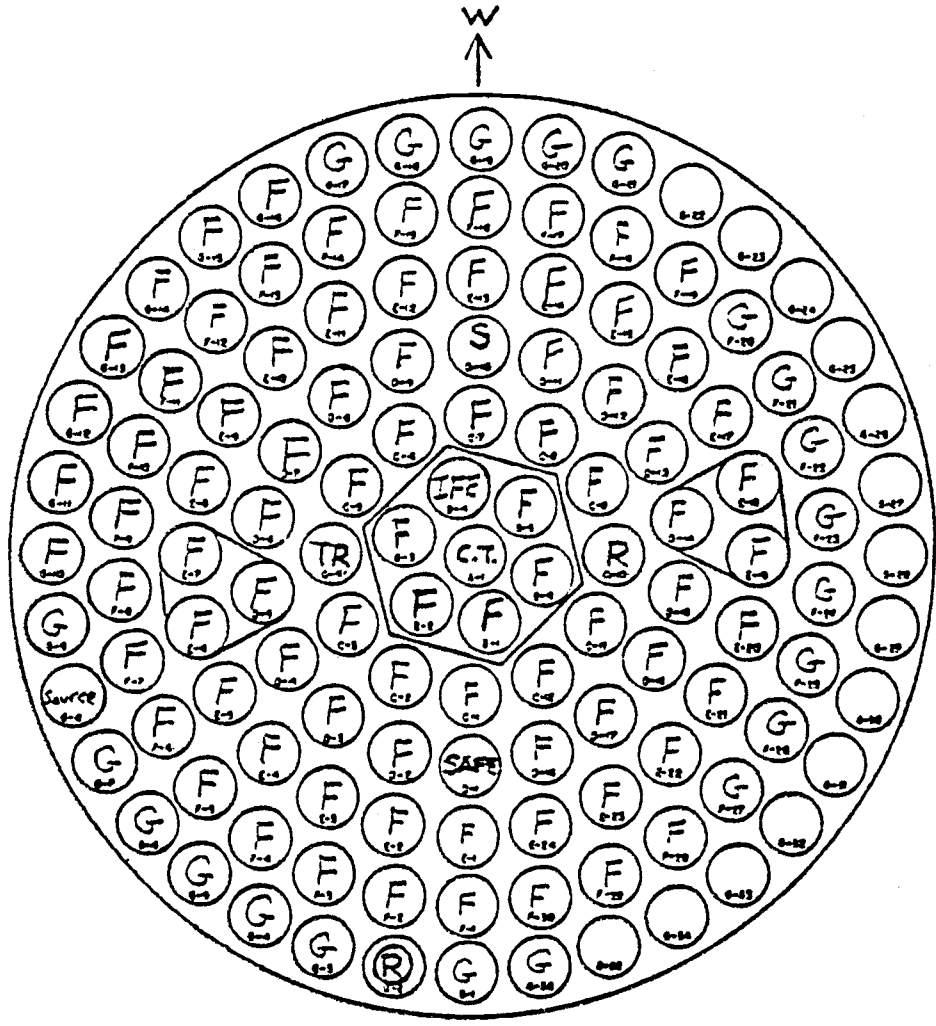
2.3.1 OSTR Pulsing Capabilities

The Oregon State TRIGA Reactor (OSTR) is a training and research nuclear reactor of the swimming pool type, moderated and cooled by light water. The OSTR is licensed to operate at a maximum steady state thermal power of one megawatt or pulse with a maximum reactivity insertion of \$2.55. It is the TRIGA pulsing behavior that serves as the high intensity neutron source for high speed neutron radiography. When pulsed, the OSTR is capable of a peak thermal power thousands of times larger than its maximum steady state power and therefore provides the extremely large neutron flux necessary for high contrast short exposure radiographic images. If the OSTR is pulsed with a \$2.55 reactivity insertion, a peak thermal power of 3100MW may be obtained within a pulse width of 8ms and produce a thermal flux available for high speed neutron radiography applications of about 4×10^{11} n/cm²-sec.

The OSTR full-FLIP (Fuel Lifetime Improvement Program) fueled core is arranged in a concentric ring circular grid pattern submerged in an aluminum tank under about 16 feet of water. Although the OSTR is a Mark II TRIGA, it uses a Mark III core for added

versatility in operation. A core map representing the position of the 85 fuel elements, 21 graphite elements, the control rods, as well as the central aluminum thimble is shown in Fig. 2.3. An additional fuel element located near the core center in the B-ring has three thermocouples embedded in the fuel enabling measurement of maximum fuel rod temperature within the core. This instrumented fuel rod temperature is displayed at the reactor console, and, following each pulse, recorded by the reactor operator. Core thermal power is measured by an ion chamber inserted into the core whereby the peak power is recorded following a pulse.

The FLIP fuel elements in use in the OSTR consist of a homogeneous mixture of an alloy composed of 1.6 weight percent natural erbium as burnable poison, zirconium hydride (ZrH) moderator, and 8.5 weight percent uranium enriched to 70% ^{235}U . The FLIP fuel loading replaces a low enrichment (20% ^{235}U) standard fuel core to extend useful core lifetime. Both TRIGA standard and FLIP fuels were designed for inherently safe operation with a large prompt negative temperature coefficient of reactivity for the uranium-zirconium hydride fuel-moderator material which reduces fuel fission rate at elevated temperatures. This reactivity feedback mechanism has demonstrated routine and safe



- | | | | |
|-------|---------------------------|--------|-----------------|
| (G) | GRAPHITE ELEMENT | (CT) | CENTRAL THIMBLE |
| (L) | FUEL ELEMENT | (TR) | TRANSIENT ROD |
| (IFE) | INSTRUMENTED FUEL ELEMENT | (S) | SHIM ROD |
| () | EMPTY | (R) | REGULATING ROD |
| | | (SAFE) | SAFETY ROD |
| | | (R) | RABBIT FACILITY |

Fig. 2.3: OSTR core loading diagram.

prompt shutdown operation during tens of thousands of pulses performed on TRIGA reactors (56).

The prompt negative temperature coefficient (α) characteristic is the result of basic physical processes that occur when the fuel-moderator elements are heated. Although fuel rod heating produces a reactivity feedback mechanism available for both standard and FLIP fuels, the means necessary to produce feedback as well as the coefficient's behavior are different for each fuel due to rod enrichment and erbium content. The necessary feedback mechanism for both fuels, however, resides in the thermally altered neutron absorption within the fuel-moderator rod material.

FLIP fueled cores have a core spectrum hardening characteristic similar to standard cores. Unlike the standard core, FLIP fuel is 70% enriched and therefore due to a reduced neutron mean free path, the neutron escape probability in the fuel is not significantly influenced by temperature. Instead, the fuel element materials are intimately mixed with a small concentration of a low energy resonance material which parasitically absorbs thermal neutrons. Erbium (Er^{167}), which has two large absorption peaks at 0.5eV, is used in the FLIP fuel not only to enhance the prompt negative coefficient as thermally excited neutrons encounter its resonance but doubles as a burnable poison to control

core reactivity over core lifetime. Compared to the rather constant temperature value of the prompt negative temperature coefficient for standard fuel (about $9.5 \times 10^{-5} \text{ }^\circ\text{C}^{-1}$), FLIP fuel has a linear temperature dependent coefficient as shown in Fig. 2.4. This temperature dependence character of the FLIP coefficient provides an advantage in reactor operation since little reactivity loss is encountered at low or normal operation but allows increased shutdown reactivity at abnormally high fuel temperatures.

To prepare a pulse for radiography, the reactor is first brought critical to a low power level (100W) by partial removal of the safety, regulating, and shim control rods from the core with the transient rod still completely inserted. The transient control rod, unlike the remaining control rods, is pneumatically operated to rapidly expel the required fraction of the rod element from the core. At the reactor console the operator adjusts the transient rod's limit of travel by positioning the transient rod carrier/shock absorber for the equivalent reactivity insertion desired. When the reactor operator receives notice or when externally triggered by the radiography system, the transient control rod is ejected by a blast of compressed air and the selected amount of positive reactivity is inserted. Soon the reactor becomes supercritical and its power

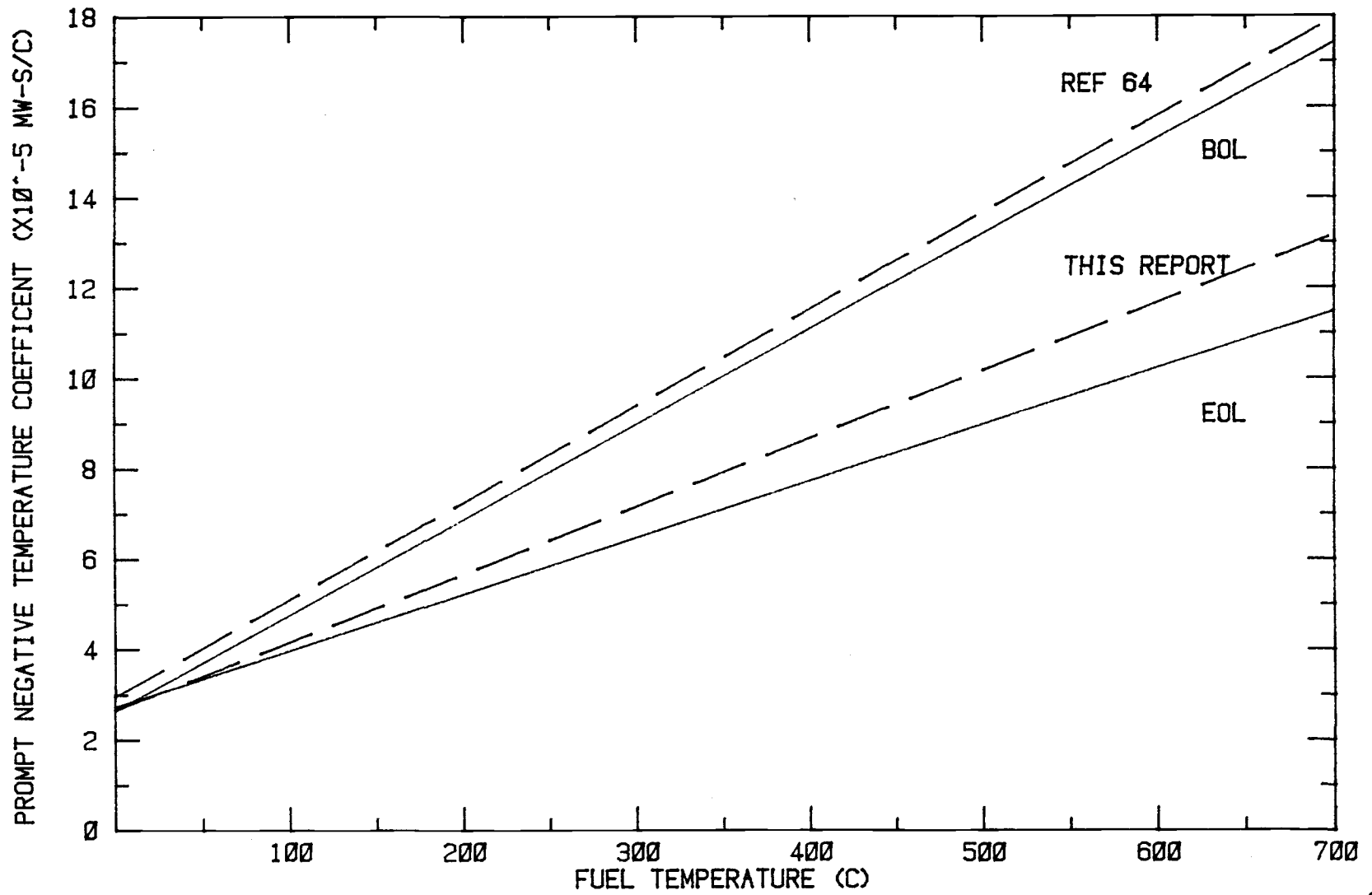


Fig. 2.4: Prompt negative temperature coefficient of reactivity for full FLIP core.

increases exponentially until increasing fuel temperature reduces power climb due to the fuel's inherent reactivity mechanism. Once the fuel temperature reaches its maximum ascent, the power reaches a peak and the reactor becomes subcritical. Following the pulse the operator manually scrams the reactor and the transient rod drops back into the core within four seconds as air pressure from its pneumatic cylinder is released. Moments after the pulse, the fuel temperature reaches its maximum value then will decrease to its initial equilibrium value (approx. 24°C) in five minutes.

2.3.2 Pulse Predictions

When a reactor pulse provides the neutron source in neutron radiography applications and the high speed camera framing rate changes insignificantly during the pulse, the recorded background radiographic film density is never constant along the film length exposed. This presents a difficulty between distinguishing modulation produced by physical changes of the radiography event and density produced by available source intensity, particularly if the dynamic processes of the event are recorded during a large portion of the pulse. If, in order to extract more radiographic information over an

extended length of film, scanning densitometry and computerized image analysis is employed, a distinction of image and source intensity modulation must be included. One example of this dilemma has been neutron radiography of burning propellant at OSU; the observed distribution of burning propellant and its gases cloud several frames during pulse peak and decay. Without accounting for pulse power decay of these films a precise densitometric analysis of propellant behavior would not be possible.

If negligible source intensity change occurred over the entire recorded film length no concern of pulse power temporal behavior would be necessary. Reactor operation at a steady state but low power (35kW) is possible for the high speed neutron radiography facility, however framing rate would require a reduction an order of magnitude or more to produce a visible image. Wider pulse widths may be produced with less reactivity insertion but at the sacrifice of power magnitude. Instead, measurement or prediction of pulse waveshape with the intention to correct image modulation following exposure is viable without reduction of camera frame rate.

2.3.3 Pulse Measurement

A recording of reactor pulse power as a function of time is known as a power trace. A power trace may be recorded by monitoring core flux from a fission probe inserted into the core central thimble and displaying its output using a strip chart recorder or oscilloscope. Both methods record a symmetrical exponential ascent and descent about the power peak in a form that suggests a Gaussian function and clearly identify the position of peak and the pulse duration at Full Width Half Maximum (FWHM, the time required for the pulse to climb and decay from one-half the peak power). Additional pulse information, the peak power, pulse energy released, and fuel temperature, is recorded at the reactor console during the pulse. Peak power, peak fuel temperature, and reactivity insertion is recorded as archival data for each pulse by the reactor operations staff and is available for reference.

2.3.4 Prediction by Fuch-Nordheim Model

Although power trace measurement is a simple reliable method of recording the TRIGA pulse waveshape, it is seldom performed routinely. An alternative to the power trace well suited for computer image analysis is

an algorithm based on the Fuch-Nordheim equations and suitable measured core characteristics to determine pulse power and fuel temperature as a function of time. The Fuch-Nordheim model is applied assuming the reactivity insertion is of such magnitude that the only relevant thermal and kinetic effects are prompt, and therefore assumes no significant heat transfer during the short period of the transient or contribution by delayed neutrons. This model has been used elsewhere assuming heat loss during the transient occurs, however (57). The Fuch-Nordheim model defined by a pair of coupled first order nonlinear differential equations with the variable prompt negative temperature coefficient of reactivity and heat capacity common for FLIP fuel is given below:

$$\dot{P} = \frac{(\rho - \alpha(T)(T - T_{ss}))P}{l} \quad 2.1$$

$$\dot{T} = \frac{P - P_0}{C_0 + \gamma(T - T_{ss})} \quad 2.2$$

$$\alpha(T) = a_1 T + a_0 \quad 2.3$$

where

- $\alpha(T)$ = prompt negative temperature coefficient
- l = prompt neutron lifetime (s)
- ρ = prompt reactivity insertion
- T = average fuel temperature ($^{\circ}\text{C}$)
- T_{ss} = initial steady state fuel temperature ($^{\circ}\text{C}$)

- C_0 = heat capacity of fuel at T_{ss} (MW-s/C)
 γ = rate of change of fuel heat capacity
(MW-s/C²)
 a_1 = rate of change of prompt negative
temperature coefficient (°C⁻²)
 a_0 = prompt negative temperature coefficient at
 T_{ss} (°C⁻¹)
 P_0 = initial steady state reactor power (MW).

Unfortunately, due to the complicated nonlinear coupling between these equations, an exact analytic solution is not possible. These equations may be solved using a fourth order Runge-Kutta numerical technique to determine power and temperature as a function of time into the transient.

A good approximation of peak power and fuel temperature may be obtained by analytic simplification. Introducing the definitions of

$$\alpha_0 = a_1 T_{ss} + a_0 \quad 2.4$$

$$T_{\Delta} = T - T_{ss} \quad 2.5$$

into the Fuch-Nordheim equations we have

$$\dot{P} = \frac{(\rho - (a_1 T_{\Delta} + \alpha_0) T_{\Delta}) P}{\lambda} \quad 2.6$$

$$\dot{T}_{\Delta} = \frac{P - P_0}{C_0 + \gamma T_{\Delta}} \quad 2.7$$

Since the time derivative of power at the pulse peak is zero, the average fuel temperature above steady state at peak power, $T_{\Delta m}$, is given by

$$a_1 T_{\Delta m}^2 + \alpha_0 T_{\Delta m} - \rho = 0 \quad 2.8$$

$$T_{\Delta m} = \frac{-\alpha_0 + \sqrt{\alpha_0^2 + 4a_1\rho}}{2a_1} \quad 2.9$$

where the negative root has been rejected. Next, the Fuch-Nordheim equations may be combined in a time dimensionless form by division

$$\frac{dP/dt}{dT_{\Delta}/dt} = \frac{dP}{dT_{\Delta}} = \frac{(\rho - (a_1 T_{\Delta} + \alpha_0) T_{\Delta})(C_0 + \gamma T_{\Delta})P}{1(P - P_0)} \quad 2.10$$

If the power near the peak is likely to be much larger than the initial power P_0 (i.e. $P \gg P_0$) then

$$\frac{dP}{dT_{\Delta}} = \frac{(\rho - (a_1 T_{\Delta} + \alpha_0) T_{\Delta})(C_0 + \gamma T_{\Delta})}{1} \quad 2.11$$

This first order linear differential equation may be

solved at peak power

$$\begin{aligned}
 \int_{P_0}^{P_m} dP &= \int_0^{T_{\Delta m}} (\rho - (a_1 T_{\Delta} + \alpha_0) T_{\Delta}) (C_0 + \gamma T_{\Delta}) dT_{\Delta} \\
 &= \frac{-a_1 \gamma}{4} T_{\Delta}^4 - \frac{(\gamma \alpha_0 + a_1 C_0)}{3} T_{\Delta}^3 + \frac{(\gamma \rho - \alpha_0 C_0)}{2} T_{\Delta}^2 \\
 &\quad + \rho C_0 T_{\Delta} \Big|_0^{T_{\Delta m}} \\
 (P_m - P_0) &= \frac{-a_1 \gamma}{4} T_{\Delta m}^4 - \frac{(\gamma \alpha_0 + a_1 C_0)}{3} T_{\Delta m}^3 + \frac{(\gamma \rho - \alpha_0 C_0)}{2} T_{\Delta m}^2 \\
 &\quad + \rho C_0 T_{\Delta m} \tag{2.12}
 \end{aligned}$$

Since $\rho = a_1 T_{\Delta m}^2 + \alpha_0 T_{\Delta m}$ (Eq. 2.8) then

$$\begin{aligned}
 T_{\Delta m}^2 \rho &= a_1 T_{\Delta m}^4 + \alpha_0 T_{\Delta m}^3 \\
 \frac{T_{\Delta m}^2 \rho \gamma}{4} + \frac{T_{\Delta m}^3 \alpha_0 \gamma}{12} &= \frac{a_1 T_{\Delta m}^4 \gamma}{4} + \frac{\alpha_0 \gamma T_{\Delta m}^3}{3}
 \end{aligned}$$

Substituting this above and using once again the

assumption that $P_m \gg P_0$

$$P_{\max} = \frac{-(\alpha_0 \gamma + 4a_1 C_0) T_{\Delta m}^3}{12} + \frac{(\gamma \rho - 2\alpha_0 C_0) T_{\Delta m}^2}{4} + \rho C_0 T_{\Delta m} \quad 2.13$$

The same trick may be applied again using Eq. 2.8 so that

$$\frac{T_{\Delta m} \rho C_0}{3} + \frac{\alpha_0 C_0 T_{\Delta m}^2}{6} = \frac{4a_1 C_0 T_{\Delta m}^3}{12} + \frac{2\alpha_0 C_0 T_{\Delta m}^2}{4}$$

Now making this substitution

$$P_{\max} = \frac{-\alpha_0 \gamma T_{\Delta m}^3 + (3\gamma \rho - 2\alpha_0 C_0) T_{\Delta m}^2 + 8\rho C_0 T_{\Delta m}}{12} \quad 2.14$$

Next, if $P = P_0$ at the pulse tail then

$$-3a_1 \gamma T_{\Delta}^3 - 4(\gamma \alpha_0 + a_1 C_0) T_{\Delta}^2 + 6(\gamma \rho - \alpha_0 C_0) T_{\Delta} + 12\rho C_0 = 0 \quad 2.15$$

By Descartes' rule of signs there is only one positive real root, $T_{\Delta f}$, for a solution. This may be found simply by using a numerical root finding routine for Eq. 2.15 so that

$$T_f = T_{\Delta f} + T_{ss} \quad 2.16$$

2.3.5 OSTR Pulse Prediction Program

An OSTR pulse prediction program has been developed (Appendix C) which solves Eq. 2.15 by a half-interval root finding method and prints as a heading "analytic" solutions for peak fuel temperature following the pulse and the pulse height using Eq. 2.9 and 2.14. Pulse power and peak fuel temperature is solved directly from the Fuch-Nordheim equations using a fourth order Runge-Kutta solution and output as a data table. Given a suitably small timestep interval, the Runge-Kutta solution can calculate a peak pulse power and final peak fuel temperature within 0.05% error of the analytic solutions above, provided peak power is greater than 100 times the initial critical power level (i.e. prompt reactivity insertions are greater than \$0.005).

Standard radiography pulses (\$1.52 prompt insertion from $P_0=100W$) produce average pulse heights of 3000MW,

final fuel temperatures of 400°C, and pulse widths of 8ms. For the program to produce results compatible to average measured pulse values, the listed TRIGA specifications for prompt neutron lifetime, fuel heat capacity, and prompt negative temperature coefficient were adjusted within reasonable limits of their measurements. Since this data is seldom measured on a routine basis, most data appears based on research by General Atomic upon safety considerations of a prototype reactor, and calculations assume the reactor produces an ideal transient, some adjustment of thermal and kinetic data in order to simulate measured pulse behavior appears justified.

2.3.6 Parameter Determination for use in Fuch-Nordheim Model

Measured TRIGA thermal and kinetic parameters have been listed by several researchers, however listings are poorly documented regarding their derivation with the exception of the General Atomic data (58-64). The information has been gathered in a table from a number of sources where the distinction whether the data was measured by the researcher or simply recorded could not be made. Table 2.1 attempts to summarize all listings as well as include parameters produced from this data

Table 2.1: OSTR thermal and kinetic characteristics.

Reference	Prompt neutron Lifetime, λ (microseconds)	Heat capacity, $C_0 + \gamma T_\Delta$ (10^{-6} MW-s/ $^{\circ}$ C-fuel ele)	Prompt neg. temp. coeff., $a_0 + a_1 T$ (10^{-5} MW-s/ $^{\circ}$ C)
Full FLIP			
63	16 BOL 20 EOL	$785 + 1.61 T_\Delta$	$2.65 + .0211 T$ BOL $2.73 + .0125 T$ EOL
62	19	$720 + 1.48 T$	$2.97 + .0214 T$
This report	29.5	$785 + 1.65 T_\Delta$	$2.67 + .015 T$
Standard			
58	43	$1120 + 1.69 T_\Delta$ 68 fuel ele ^A	1.26
23,53	43	838	1.2
59	43	$1088 + 2.04 T_\Delta$	1.34

Table 2.1: Cont.

Standard radiography pulse constants

Pulse reactivity insertion (ρ)	\$1.52 + .01
Initial critical power (P_0)	100W
Initial fuel temperature (T_{ss})	24°C
Number of fuel elements	85
Peak to average fuel temperature ratio	1.17
Total delayed neutron fraction	.00071

Due to a calculation error, the value of C_0 is incorrectly given as 825×10^{-4} MW-s/°C on page 3-52 of the Torrey Pines' SAR but the correct value later appeared on page 8-12 (63). Bossi and Simnad have listed this incorrect value and Bossi has misplaced the decimal point on γ as well (23,56).

adjusted to approximate several measured power traces by a computer using the Fuch-Nordheim model. In most cases, data for the prompt negative temperature coefficient (α) was presented in graphical form and it was necessary to prepare a correlation for this table. Also, although it has been some time since the OSTR last operated with standard TRIGA fuel, its parameters are listed for reference.

Besides the obvious difference in parameters between standard and FLIP fuel, core configuration and operation influence the prompt negative temperature coefficient of reactivity and prompt neutron lifetime. Fuel consumption reduces the prompt negative temperature coefficient of FLIP fuel as shown in Fig. 2.4. The prompt neutron lifetime depends upon core thermal neutron absorption and is defined by

$$l = P_{n1} / (v \Sigma_a)$$

where

P_{n1} = nonleakage probability--the ratio of the number of neutrons absorbed to those that are either absorbed or leak.

v = neutron velocity (cm/s)

Σ_a = total macroscopic absorption cross section of core (cm^{-1}).

Neutron absorption within the core depends upon changes in the fuel erbium concentration and xenon poisoning as well as the reactor operating conditions that produce the xenon. Except for the total number of fuel elements

in use, core heat capacity ($C_0 + \gamma T$) appears independent of reactor status and therefore unlike prompt neutron lifetime would not be expected to alter between core loadings.

After first operating the program with the parameters of Table 2.1 a comparison with typical radiography pulse peak power and width measurements showed discrepancies. Some investigation with parameter variation and response of calculated time at FWHM (t_f) and pulse height (P_{max}) indicated the following relationships:

$$P_{max} \propto \frac{\rho C(\gamma, C_0)}{l\alpha(a_1, a_0)}$$

$$t_f \propto 1/\rho$$

where C and a varies directly with the heat capacity and prompt negative temperature coefficients, respectfully. Note also from Eq. 2.15 the final temperature is independent of prompt neutron lifetime. These conclusions follow the results of a simpler constant heat capacity and prompt negative temperature coefficient presented by Hetrick (65). Since the analysis was performed with a constant reactivity, the pulse duration appeared to be only dependent on prompt neutron lifetime. Several measured FWHM intervals from

either the strip chart or scope indicated an adjustment of prompt neutron lifetime to 30 microseconds would produce the 8ms duration. Once the prompt neutron lifetime had been determined, the fuel specific heat and prompt negative temperature coefficient were adjusted to reproduce the average peak power of 3000MW and its waveshape. A graph demonstrating this correlation is shown in Fig. 2.6.

Since the Fuch-Nordheim equations use a core average fuel temperature in its solution, it was necessary to use a peak-to-average power correction factor to obtain peak fuel temperatures corresponding to those measured by the instrumented fuel rod. A factor of 1.4 peak B-ring/average power density ratio has been estimated at the core midplane; this investigation suggests a comparable peak to average power ratio of 1.2 is needed to produce a typical peak final fuel temperature of 400^oC (65).

2.3.7 Pulse Height Variation

The pulse prediction program has been quite successful in duplicating average measured pulse power performance as a function of time and reactivity, pulse duration variation with reactivity, and final peak fuel temperature according to reactivity insertion (Figs. 2.5

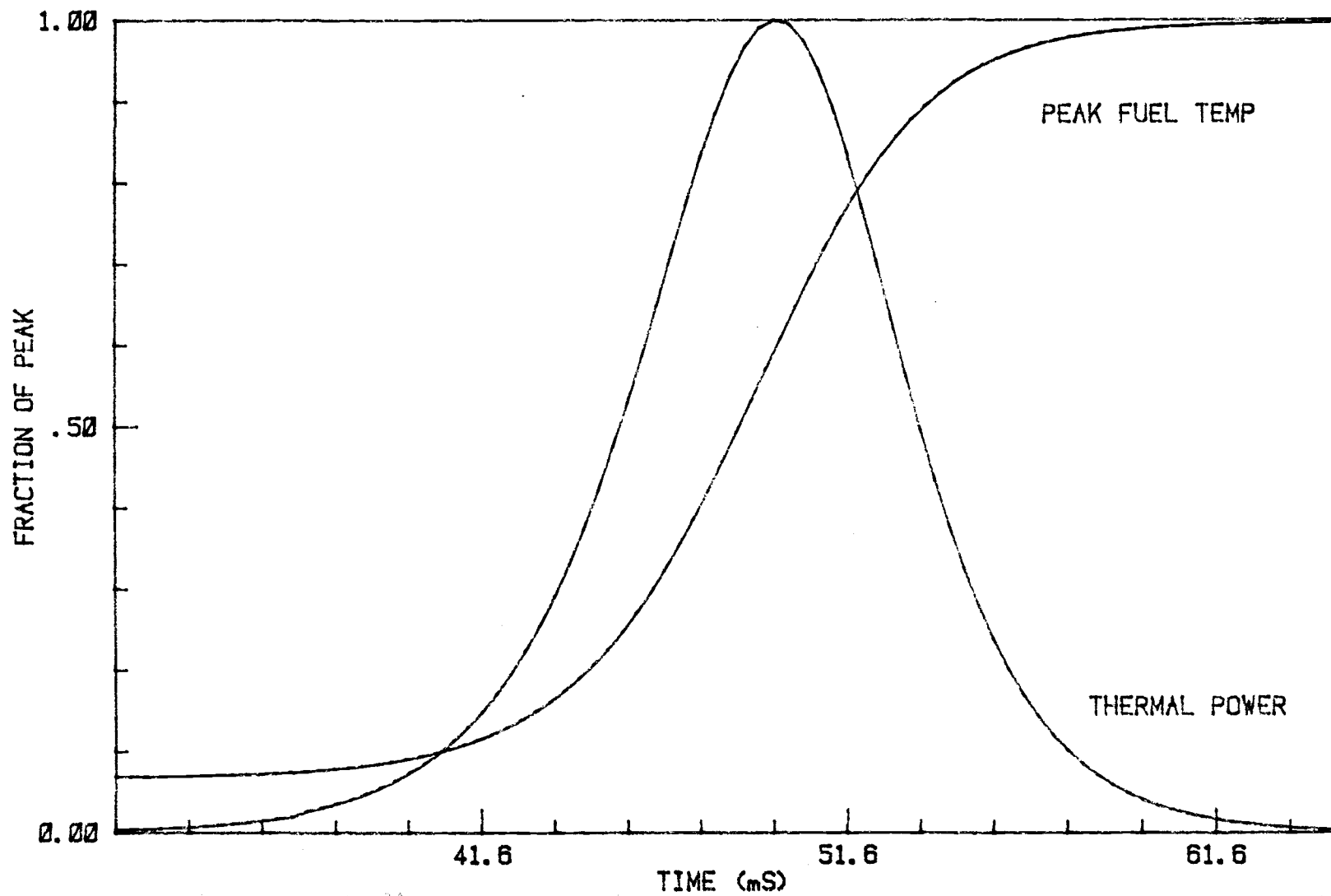


Fig. 2.5: TRIGA pulse power and peak fuel temperature relative behavior

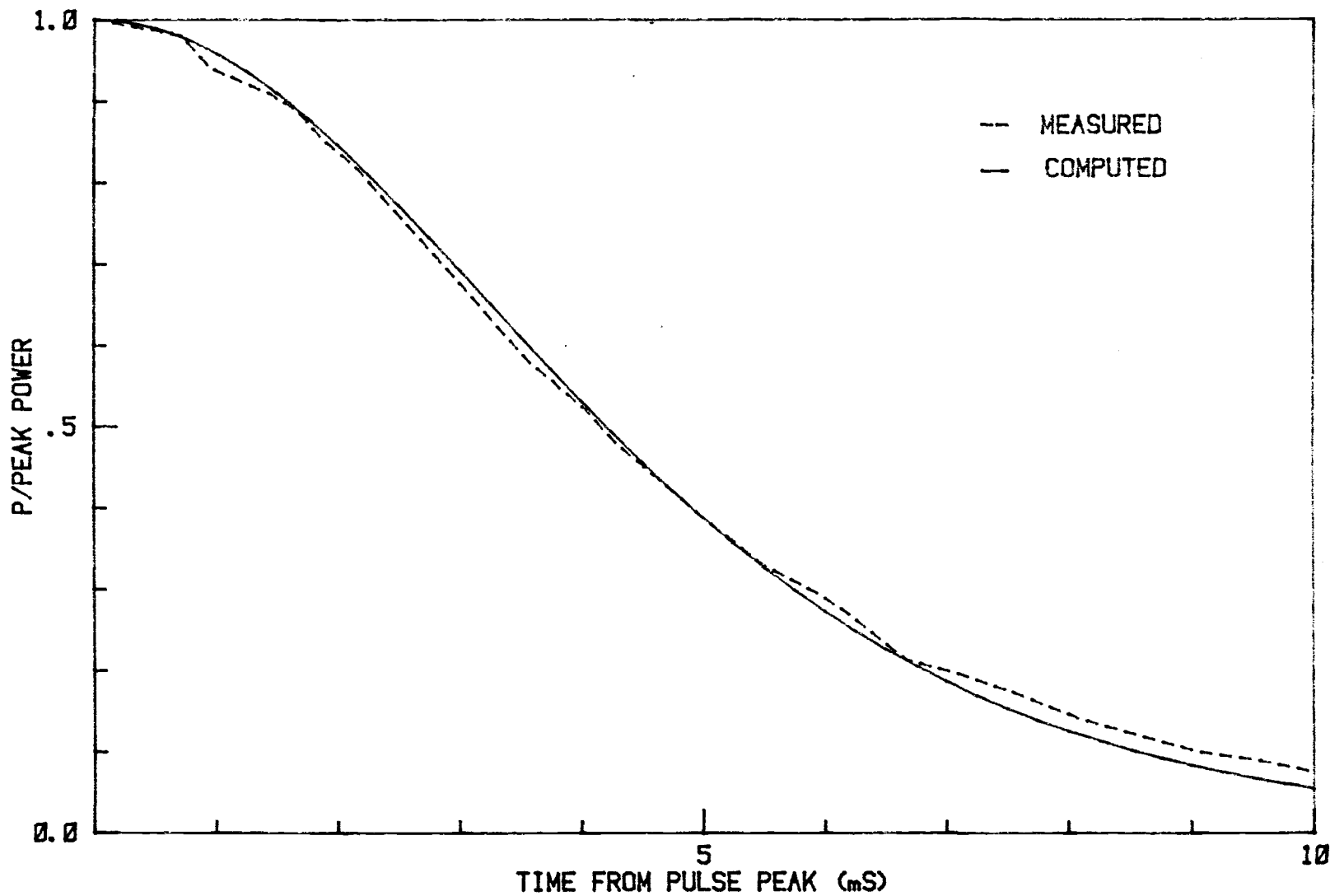


Fig. 2.6: Comparison of measured and computed TRIGA power traces.

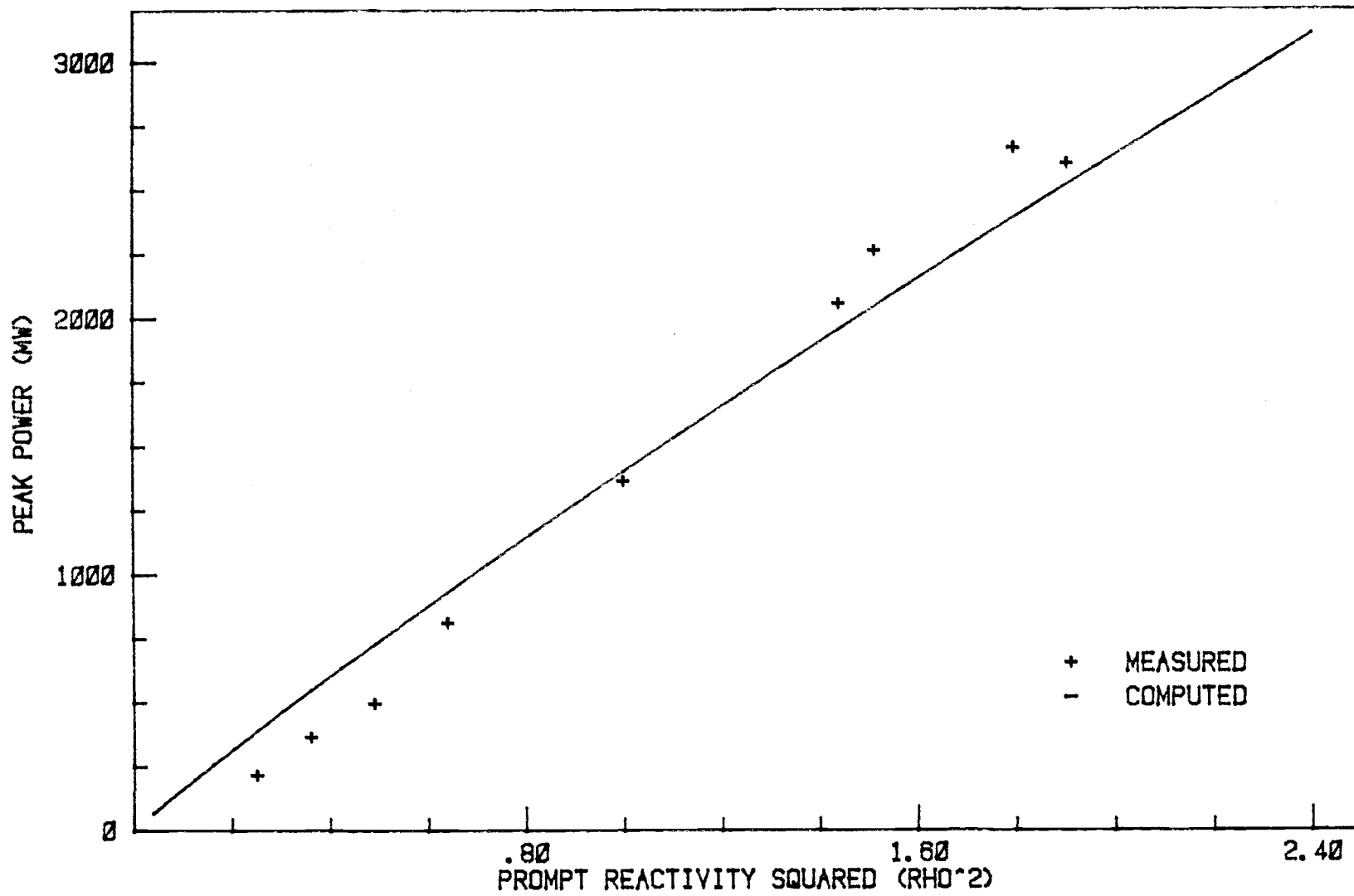


Fig. 2.7: Pulse height variation with reactivity.

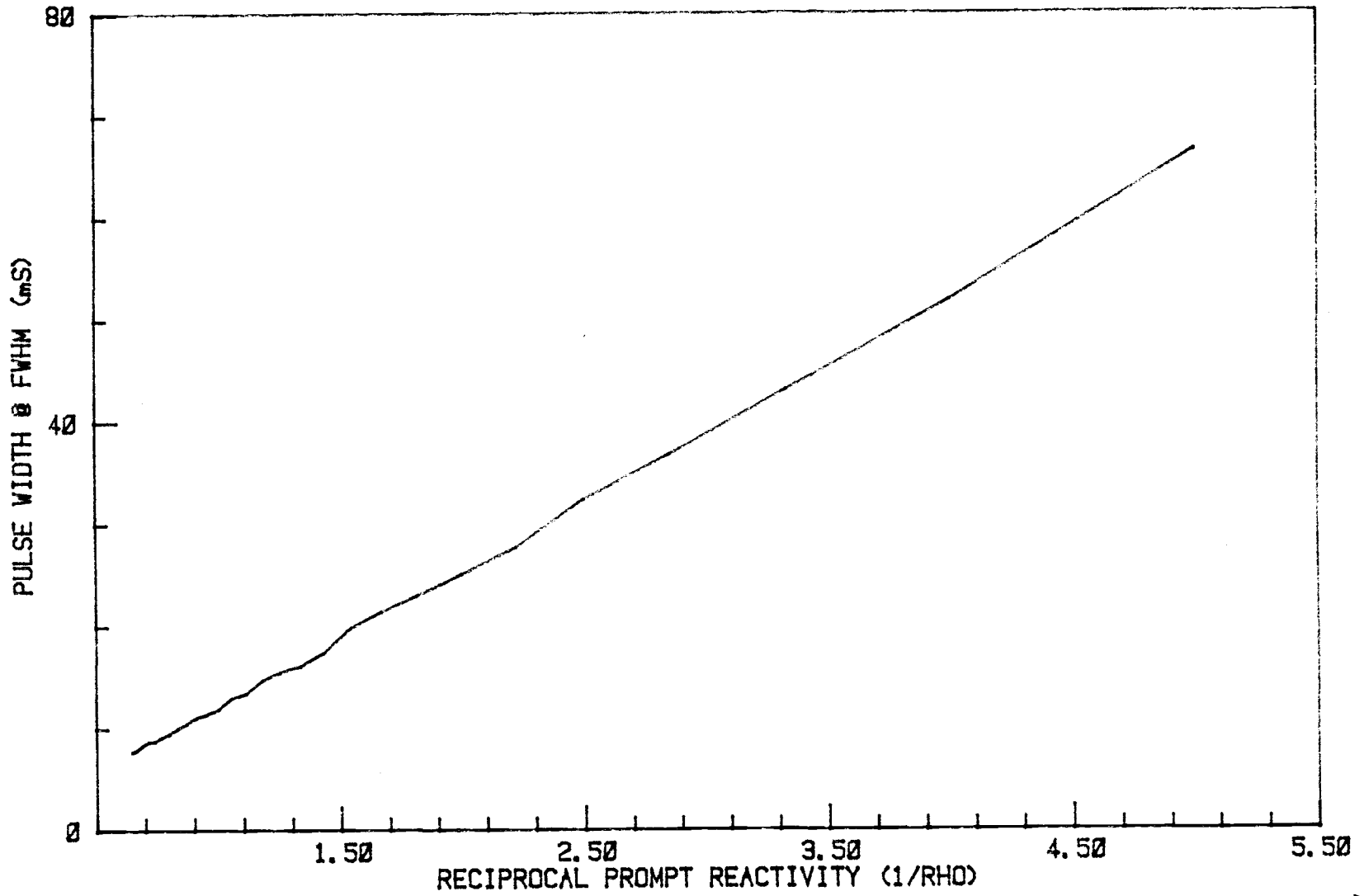


Fig. 2.8: Pulse duration at FWHM variation with reactivity.

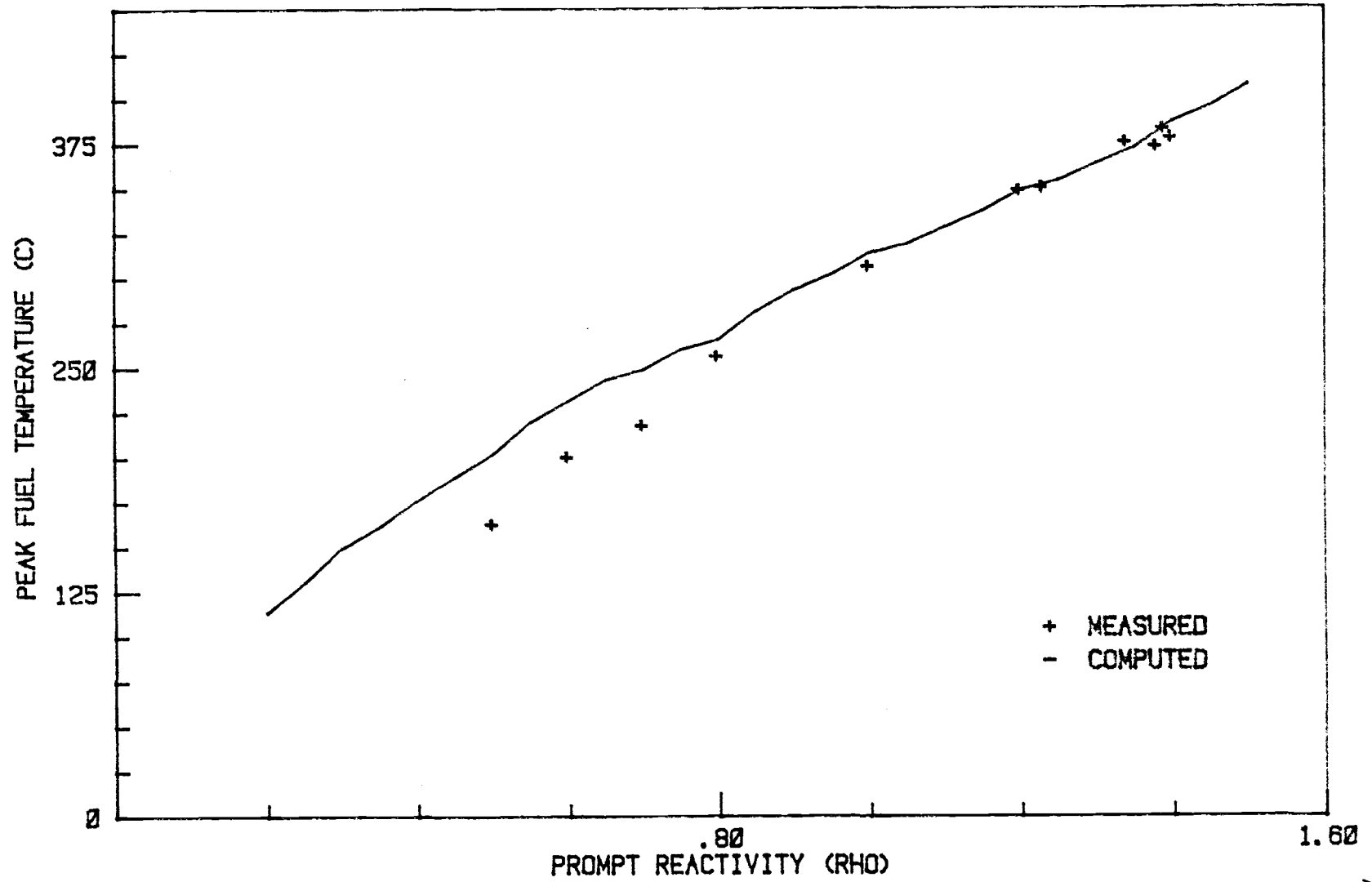


Fig. 2.9: Maximum fuel temperature following pulse as a function of reactivity.

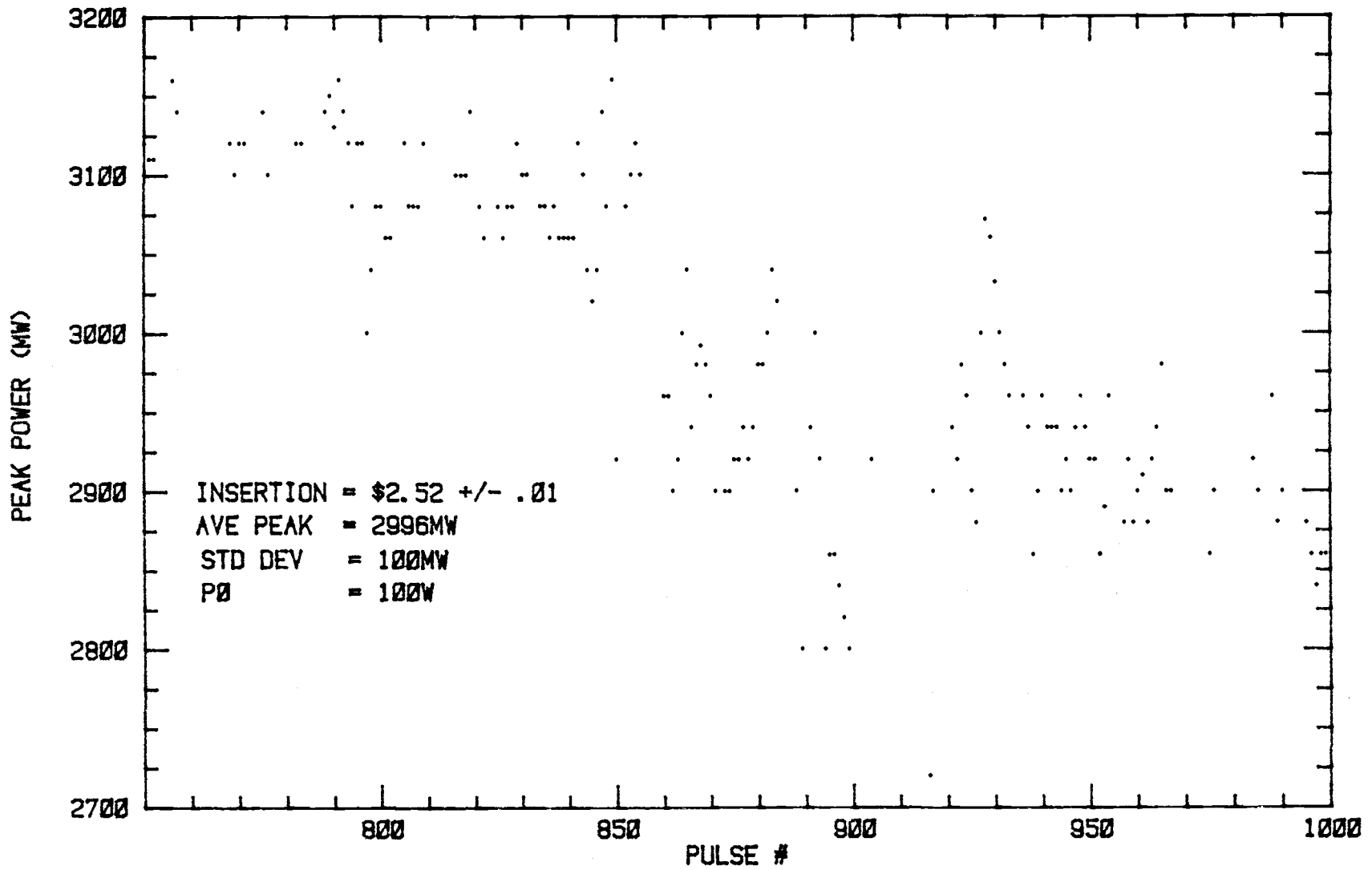


Fig. 2.10: Scatter diagram of TRIGA pulse height.

to 2.9). Insufficient data exists to demonstrate its capability to predict temporal behavior of fuel temperature. Due to unaccountable erratic influences of the TRIGA pulsing system, however, the computer model cannot simulate individual pulses. Figure 2.10 is a history of 160 standard radiography pulse peak magnitudes over a period of two years. This figure identifies the random nature of OSTR pulse magnitudes which appear to cluster about two means in this diagram; 3100MW for pulse numbers 750 to 850 and 2900MW from 850 to 1000. Compared to pulse height variation, peak final fuel temperature and pulse width appear to vary as equally about the typical prompt reactivity insertion of \$1.52. Attempts for several explanations of reactor phenomena which contribute to the variable behavior of each pulse have been made.

2.3.7.1 Transient rod acceleration

If the pneumatic system pressure required to expel the transient rod drifts from its setting between pulses, the transient rod acceleration would be expected to change. The computer model does not account for the transient rod motion nor assumes any physical delay associated with its withdrawal. Neglect of this rod delay has a significant effect upon both height and

width of the pulse. An attempt to account for this delay was included into the program by assuming the reactivity insertion was a simple linear function of time from pulse initiation until the full measure of reactivity was inserted. A study performed with the TRIGA reactor indicated transient rod withdrawal duration is less than 100ms (67). If a full 100ms is required to insert the reactivity, a pulse height reduction and pulse width increase of both 5% would be expected and is equivalent to those results obtained by either decreasing reactivity inserted or increasing prompt neutron lifetime in the model without rod delay. A more accurate representation of rod insertion delay should account for the rod worth curve, rod acceleration, as well as the measured duration of the rod expulsion.

2.3.7.2 Rod calibration

The amount of transient rod removal from the core is determined by the setting of its electromechanical drive as operated at the reactor console. To prepare for a pulse, the reactor operator adjusts this setting using a reactivity versus rod position chart to introduce the reactivity desired. Transient rod reactivity, however, is not a direct function of its

position since the behavior of the rod calibration curve drifts under reactor operating conditions and history. Rod calibration is performed routinely but infrequently following a long reactor shutdown duration so that the curve represents the greatest rod reactivity available. After a few hours of reactor operation the reactivity associated with its position may have changed and therefore only an approximate value of the reactivity inserted is known (68).

Pulse measurement instrumentation error is another consideration. For example, the bimodal behavior of Fig. 2.10 seems caused by a systematic error introduced after the position of a power detector was slightly shifted within the core. This effect was not uncovered until this figure was completed (68).

2.3.7.3 Core composition changes

Poison concentration, fuel burn-up, replacement, addition, or removal can change the prompt negative temperature coefficient, heat capacity, and prompt neutron lifetime of the core. If fuel is added to the core its heat capacity increases and its prompt neutron lifetime and peak to average power ratio decreases (68). Fuel consumption, however, is a long term effect over reactor lifetime. Xenon, produced in the core during

operation, competes against the fission chain reaction in neutron absorption but should be of no concern due to compensation by control rod position. Instead, the additional fuel brought into the core by withdrawal of the fuel-follower control rods may tend to increase the pulse peak.

Daily changes in OSTR workload with respect to scheduled pulse operation alter a large number of core operation variables in an unpredictable but bounded manner so that variation in pulse behavior may be considered as a normal probability distribution. The standard deviation of the 160 pulse magnitudes shown in Fig. 2.10 is 100MW, identical to the deviation proposed by a separate researcher (70). Therefore, a statement may be made about pulse reproducibility: 68% of pulse peaks recorded in Fig. 2.10 are within 100MW of the mean power peak (2996MW).

2.4 COLLIMATION

The collimation for the high speed motion neutron radiography facility is located within the OSTR tangential beam tube (#3). This beam tube has been designed such that its opening coincides with a moderating graphite collar inserted into a radial port (beam port #4). The graphite contains a lead plug for experiments in the radial beam port and acts as a source block for the tangential beam tube. This configuration allows reduced gamma concentration within the radiography source beam.

The collimator construction and configuration is shown schematically in Fig. 2.11. Within the collimator are four evenly spaced lead, masonite, and cadmium rings which act to absorb stray neutrons and gamma reaction products as the neutrons stream down the tube. The smallest rectangular aperture of the collimator measures 11.4 by 8.9cm provided the variable aperture device comprised of two cadmium faced lead bricks is hinged fully open. Although the variable aperture bricks may be used to provide control over the intensity and divergence of the beam, in practice they are always fully open for high speed motion neutron radiography applications.

The collimator opening to the facility has a cross

BEAM PORT #3 COLLIMATOR

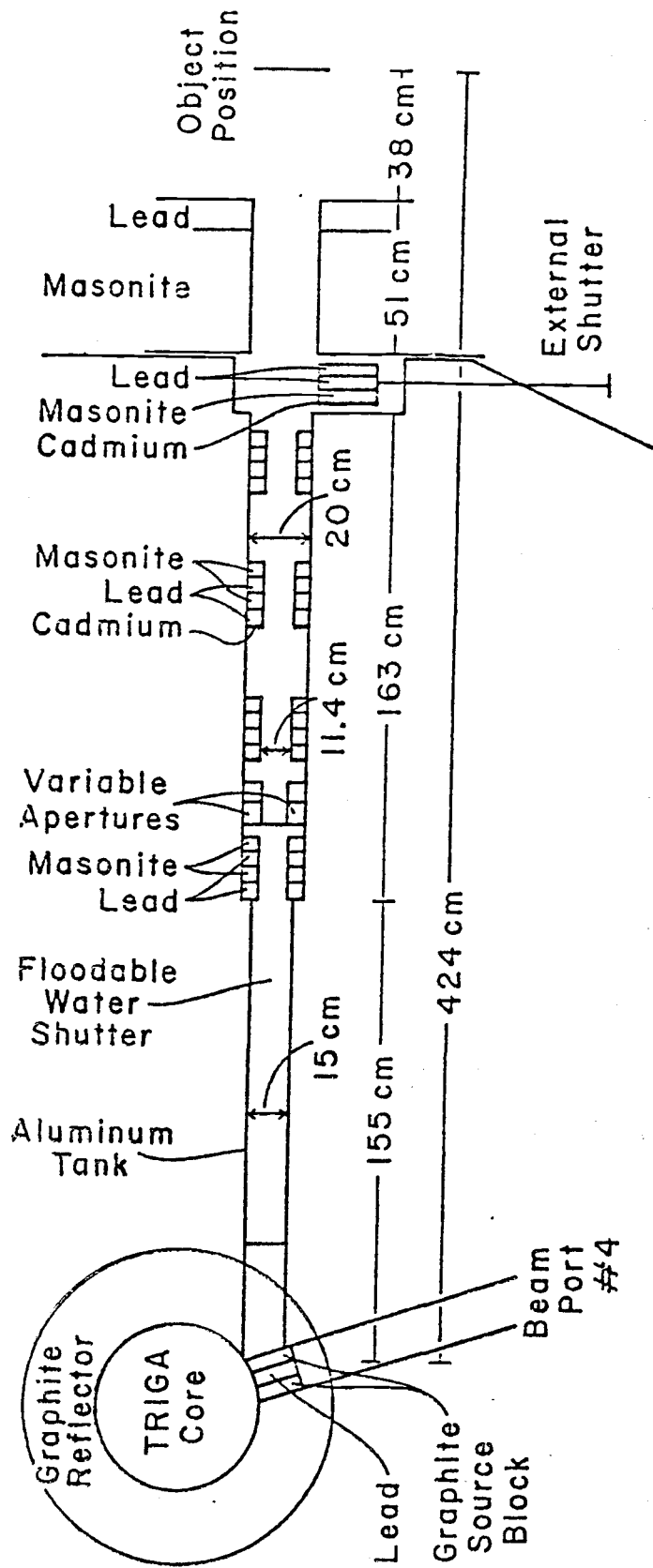


Fig. 2.11: Beam port #3 collimation and details.

section of 20 by 10cm and is spaced approximately 38cm from the subject. Often only a small aspect of the subject needs to be radiographed within this field. To reduce neutron scatter from the object or surrounding material which can cause imaging and contrast problems about an aspect, a cadmium mask with an opening of close proportions to the aspect is mounted in front of the subject. The mask serves in conjunction with the collimator to reduce geometric unsharpness of the image.

2.5 SCINTILLATORS

The LiF-ZnS(Ag) neutron image scintillators in present use for neutron radiography have been constructed at OSU. These scintillators are composed of a 2:1 mixture of 10 micron particle ZnS to enriched ^6Li LiF in sodium silicate (waterglass) binder attached to an aluminum plate. Details on scintillator construction at OSU have been reported by Bossi (71).

2.6 IMAGE INTENSIFIER

Due to the insufficient light output from the scintillator, the neutron image cannot be photographed directly without an unsuitable exposure time.

Considerably shortened exposure times are required for high frame rate applications and are likely if the radiant image intensity is increased. At OSU a first generation two stage image intensifier makes this possible.

The intensifier's input faceplate is composed of a high density fiber optics bundle capable of transmitting the neutron image presented by the scintillator mounted outside to a photocathode. As light quanta strike the photocathode, photoelectrons are released and accelerated through an electrostatic potential of about 25kV before striking an anode phosphor material. An electro-optics system minimizes electronic image distortion during this excursion and consists of annular metal electrodes positioned in such a manner as to focus the electrons on the phosphor. The phosphor converts the electron momentum into light producing a radiant image. This photoemission-acceleration-display process constitutes a single stage of intensification with a typical gain of 100 for incandescent light. Additional intensification stages may be cascaded by fiber optic coupling thereby

offering enhanced gain. If the photocathode is sensitive over a narrow region of the light source's spectral emission, the effective stage gain is reduced compared to a broad color spectrum source, which encompasses the photocathode sensitivity spectrum. For this reason, effective stage gain for a phosphor is less than that of an incandescent illumination.

Electrostatically focused image intensifiers have a characteristic pincushion distortion caused by greater image magnification near the tube edges than at the center. Although curvature of the photocathode and phosphor surfaces aids in reducing such distortion, image distortion becomes appreciable near periphery of the imaging area, especially for multistage tubes. The compound distortion as well as noise problems of these tubes, however, make any number of stages greater than three impractical.

A two stage image intensifier is required at OSU for high speed photographic recording. The intensifier now in use is a 40mm diameter ITT image intensifier (No. F4751) with a radiant power gain of 332 and unity magnification. An S20 photocathode and a P11 phosphor screen is incorporated in both stages as is typical with most intensifiers of its type. This phosphor is considered highly appropriate for use with panchromatic and orthochromatic films due to high spectral matching

characteristics. The intensifier is equipped with an internal high voltage DC to DC converter utilizing automatic brightness control (ABC) to step up a 6.75V external supply to the required accelerating potential. Use of an external regulated low voltage supply offers simple and consistent intensifier gain. According to the manufacturer, the ABC feature eliminates phosphor saturation and image burn-in during pulsed input operation and therefore minimizes image retention during a reactor pulse. In use, the scintillator is clamped over the input face-plate, the subject is positioned as close as possible to the combination, and the camera lens is focused on the intensifier output.

2.7 HIGH SPEED CAMERA

A Hycam model 41-0004 (formerly K20S4E) rotating prism camera is used as the high speed recording device. Unlike the intermittent film movement operation of conventional motion picture cameras, in rotating prism cameras the film moves continuously from one spool to another, and a rotating prism moves the image at the film speed. On certain positions of the prism and rotating slotted shutter the light does not reach the film, and thus effectively spaces out the frames on the film.

This camera can operate at frame rates of up to 11,000 frames/second (fps) if 400ft 16mm film spools are loaded. Routine use of shorter 125 foot rolls allow the camera to accelerate to a maximum frame rate of 8000fps before the supply roll is exhausted, however. At speeds above 5000fps, camera speed is unregulated and an exponential function of time. Interchangeable shutters or optical heads are available for the Hycam allowing shorter frame exposures or increased frame speeds at fractional width.

Additional instrumentation and modifications are necessary to make the Hycam a viable research device. Since the Hycam spools film onto a take up reel from an initial standstill, one or two seconds are required for the camera to reach maximum acceleration. A signal

actuator switch installed in the camera is made available to trigger external events based on the film remaining in the supply reel. This switch is set by experiment or calculation to the position where the camera accelerates past some declared frame rate. To later enable determination of film speed, a time dot generator using a neon lamp internal to the Hycam photographically marks the film margin at periodic intervals as the event is recorded. An additional circuit produces a synchronization mark on the opposite margin to indicate when the pulse peak occurs.

Some modifications were not viable. The natural aperture of the Hycam's rotating prism optics restricts its maximum aperture to $f/3.3$ regardless of the objective lens. Previous researchers believed a high aperture lens (55mm, $f/1.2$) would provide greater light collecting capacity than the original (25mm, $f/1.9$) when mounted on the Hycam, however this improvement was not justified. The increased focal length lens also requires longer extensions to provide proper close up magnification thereby risking lens stability.

The Hycam is shock mounted on a solid concrete pedestal at the beam port rear. This physical isolation from the steel equipment bench coupled with firm weighting upon the camera base ensures recorded image quality against vibration from the event or camera.

2.8 FILM AND PROCESSING

Fine grain rapid arts recording (RAR) films exhibit high photographic detail and contrast and are most appropriate for high speed image recording. The Kodak 16mm films most often used in high speed neutron radiography include RAR 2496, 2498, 2484, and 2475, in order of decreasing use and increasing sensitivity and graininess. The films are developed as a negative using automated processing which provides good control of time and chemical distribution. High quality processing of these panchromatic films has produced low fog and few artifacts in the final image compared to manual processing. Increased development time and temperature increase film contrast needed for light starved high speed recording, but increases graininess as well. A standard procedure in negative processing has shown from experience that an eight minute developing time in D-19 at 68⁰F provides the best results.

2.9 EVENT SYNCRONIZATION

For information of a dynamic subject to be successfully recorded on film, camera speed and reactor flux must coincide at useful, predictable values before data collection. Therefore, system synchronization is necessary to be certain the events surrounding the subject occur as desired.

Although some success was made by timing event initiation from the reactor trigger signal during earlier research with the facility, variance in operating conditions made the synchronization circuit independable. The existing synchronization circuit chains camera, reactor, and subject triggering by the devices themselves and has proven extremely reliable, given experienced personnel. A timing diagram of this circuit's control sequence and system response is shown in Fig. 2.12 and a block diagram of the trigger chain is represented by Fig. 2.13.

Once the radiography facility has been evacuated, the reactor has steadied at a low critical power, and operations personnel acknowledges preparation to continue procedure with a pulse, the synchronization sequence begins. The reactor operator first starts the Hycam remotely from the control room and the camera accelerates. Once its film supply spool is emptied

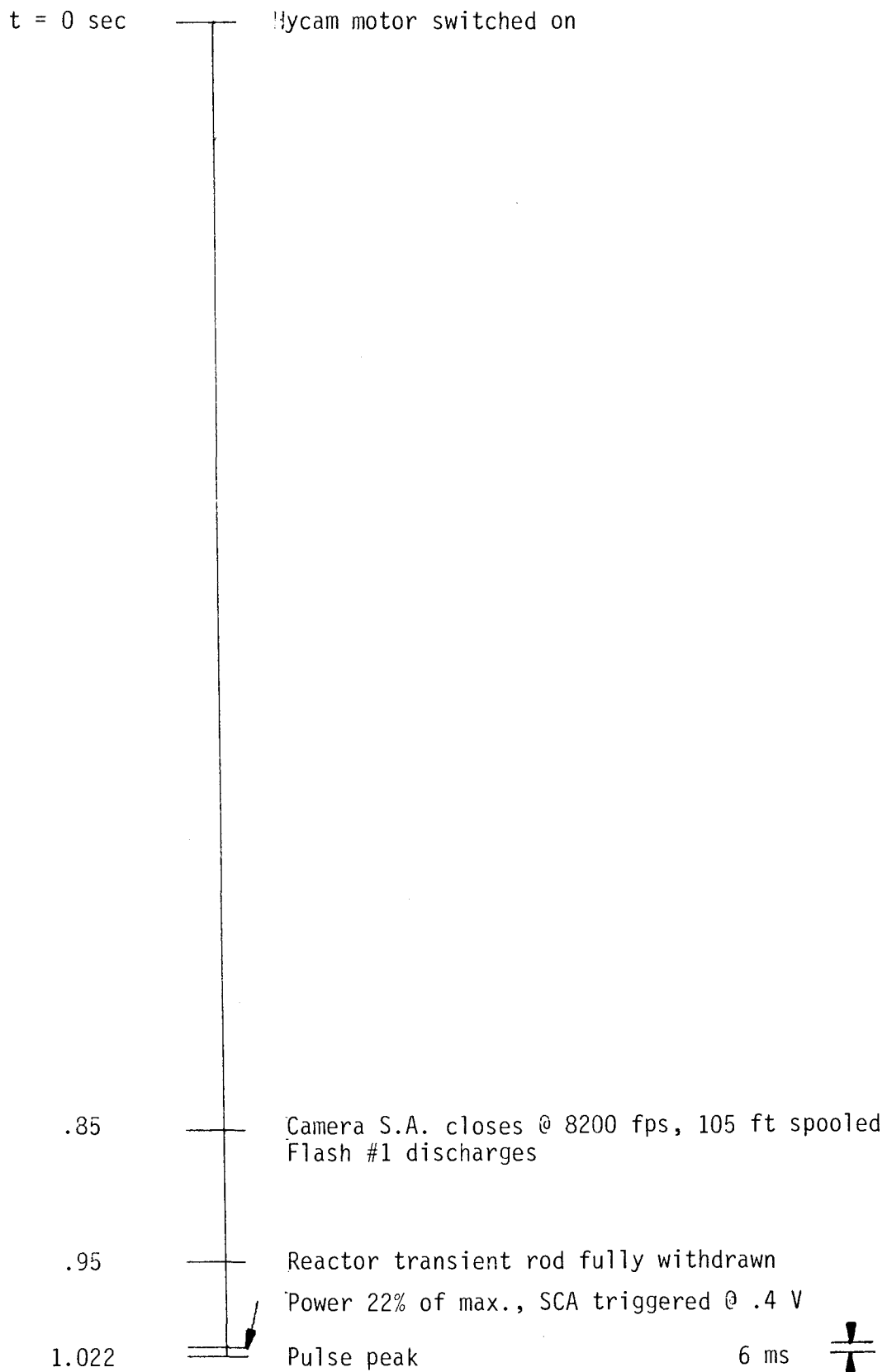


Fig. 2.12: Timing diagram of high speed synchronization.

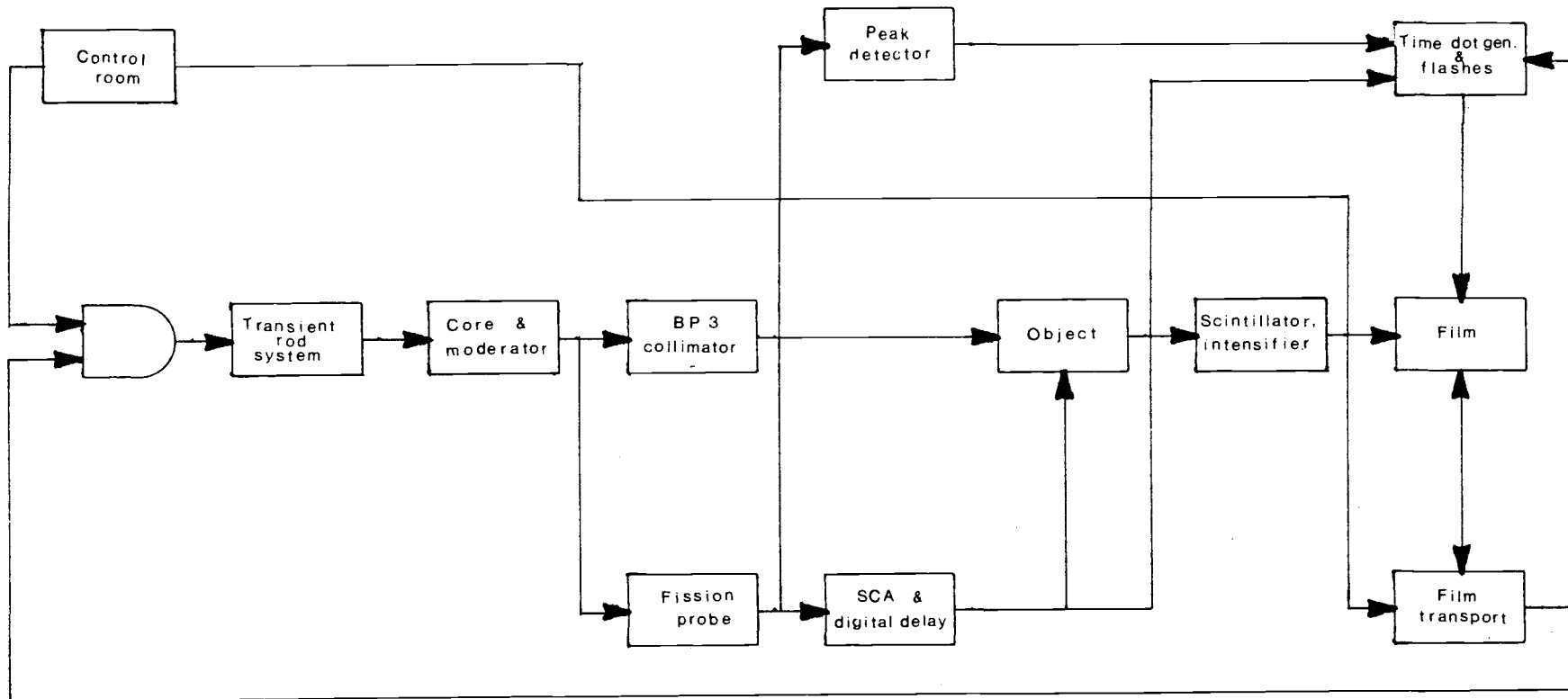


Fig. 2.13: Block diagram of event synchronization.

beyond a declared length the signal actuator switch closes and initiates the reactor transient rod pneumatic drive should this option be selected in the control room.

If an event is always repetitive or its action persists long enough to start before and continue during a pulse, then an event trigger signal would never be needed. The majority of dynamic radiography applications have been in ordinance evaluation characterized with event durations shorter than the pulse itself. In this case an event trigger signal must be generated once the reactor power approaches its peak. A fission probe inserted in the central core thimble produces a voltage across a load resistor proportional to core neutron generation. A single channel analyzer (SCA) senses this voltage and when reactor power reaches approximately 22% of peak a digital timer is triggered. About this time the reactor flux in beam port 3 reaches a magnitude enabling an image to be recorded on film. Once the timer delay has completed (normal settings range from 2-8ms) the event is initiated. The objective of the timer is to delay the event until the high image density pulse peak and although adjusting the SCA threshold may achieve the same means, such an adjustment produces obscure results due to nonlinearity of power level and trigger margin setting. The fission probe provides another function;

its output when applied to a peak detector circuit can produce a timing mark on the film margin to indicate when the pulse peak occurred.

A subtle difference, however, exists between when the peak flux occurs at the subject position and when it is measured within the core. Due to the most probable velocity for thermal neutrons (2200m/s) and the distance from the core center where the fission probe is positioned to the subject location (424cm) a finite flight time is required. The moment the peak pulse mark is recorded on film therefore precedes the actual peak subject density point. Some attempt was made to verify this flux lag. Figure 2.14 shows the temporal density characteristic of four pulses as recorded on film in reference to the peak core flux time. Each of these curves were obtained by painstaking manual density measurements upon a high density and seemingly undisturbed reference region of the recorded image once every two frames. Obviously by each curve's appearance grain noise, densitometer positioning, or some other influence has superimposed noise upon the signal. It should be noticed the curves are generally symmetrical and Gaussian shaped. In Figure 2.15 these curves have been combined and averaged. The time delay measured from the core pulse peak appears to match well within 5% of the theoretical delay as shown.

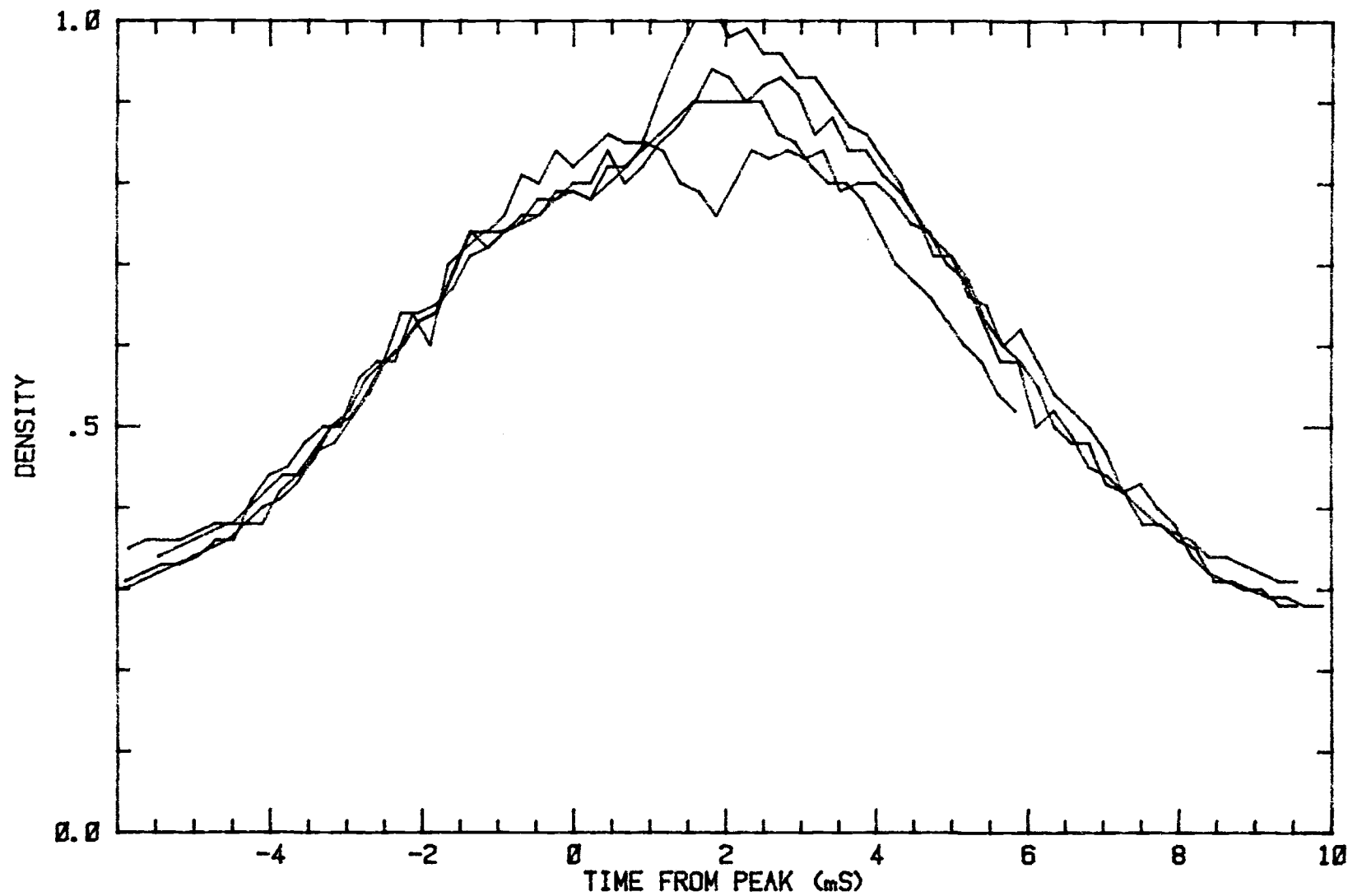


Fig. 2.14: Temporal density characteristic of four high speed neutron radiography films.

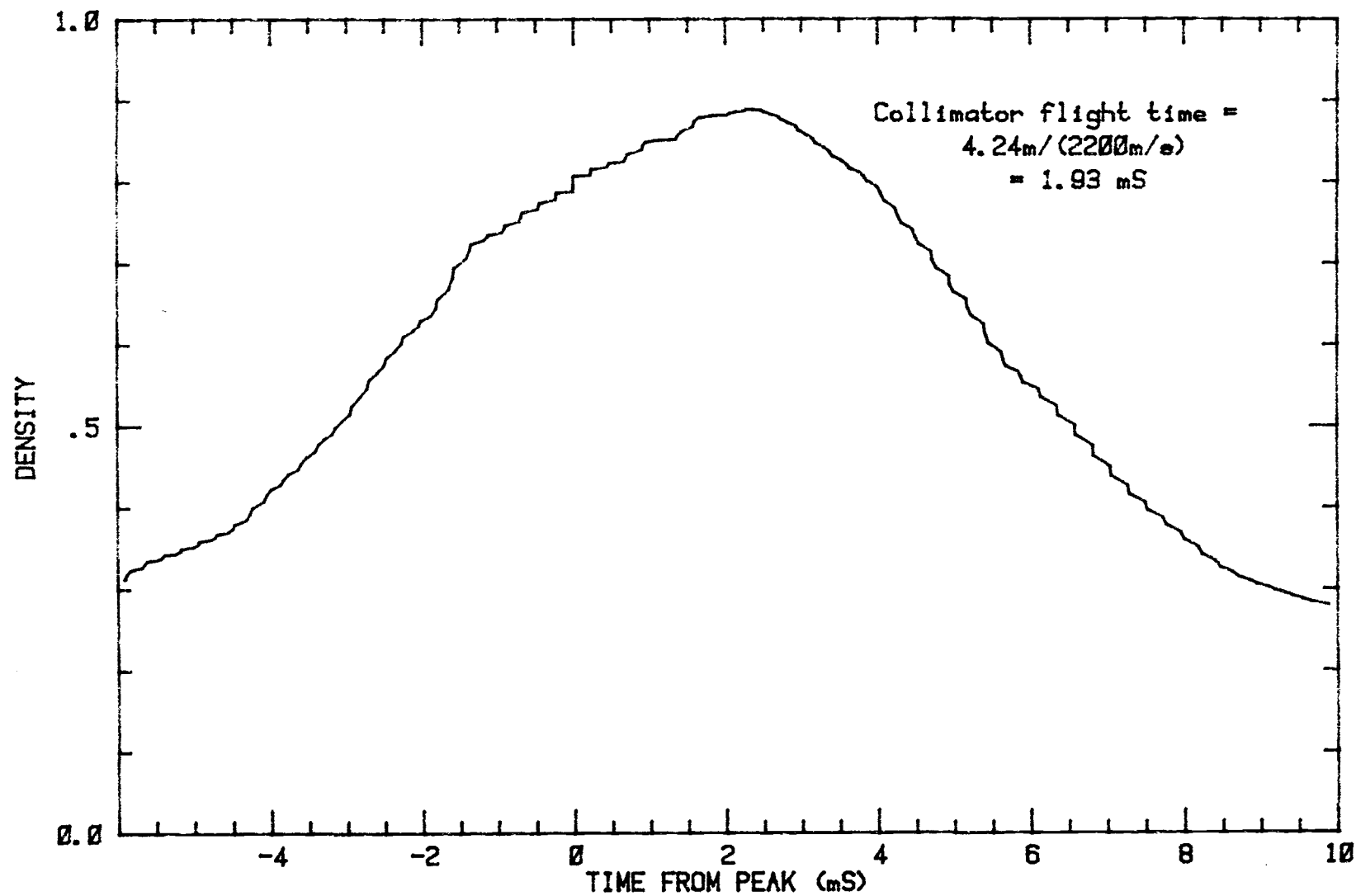


Fig. 2.15: Averaged temporal density variation of four high speed neutron radiography films.

2.10 EVENT

The most natural limitation upon choice of the dynamic radiography subject or event is its cross sectional area. Since the beam width is defined by the smallest opening (11.4x8.9cm) of the collimator, the area of the subject to be radiographed must be within this field. A more serious restriction is the input diameter of the existing image intensifier which allows a height of only 40mm. However, the useful subject size must be further reduced and centered to the intensifier's fiber optic faceplate if pincushion distortion of the image is to be avoided. If one half the total intensifier input diameter is useful for a low distortion image, the total practical imaging area is 4cm^2 .

If the event is not repetitive, a means to initiate it electrically or electromechanically must be available not only as necessary for remote operation from the beam port, but for timing purposes since initiation must wait until both camera and reactor operation are prepared and stable.

A more subtle radiography restriction is the thickness or radiographic contrast of the subject's constituents. If the subject is a thick high attenuation material, the exposure to produce a useful radiograph will need to be increased. Discrimination of the

subject's constituents may be poor if similar neutron attenuating materials comprise the subject. In this case enhanced contrast may be obtained by doping the constituents differentially with a high thermal neutron absorber, e.g. cadmium or gadolinium.

Displacement and duration of event information during recording is a final consideration; information may be lost if the event occurs within a few camera frames or during frame interstitial period.

2.11 SYSTEM EFFECTIVENESS

A number of subjects have been studied using the high speed neutron radiography facility each providing a number of problems to solved. In this regard high speed neutron radiography at OSU has never become routine, especially since some radiographs have challenged interpretation within the few feet of film they develop. In particular, recognition is difficult since the image resolution obtained is several times less than neutron radiography with foil screens. Times have also occurred when the event under evaluation changed its physical characteristics too fast to record. If a significant improvement could be achieved in both resolution and density of the overall image the magnitude of information obtained could be increased and the user's task considerably simplified.

III. INFORMATION RETRIEVAL ASPECTS

3.1 INFORMATION INTERPRETATION

The essential requirement of motion neutron radiography is to record a subject's internal features the best way and find in real time that information considered important. Since film is used as the recording media, all image information must inevitably be extracted from microscopic blackened silver halide grains developed from an exposed radiograph and should convey relevant temporal position and modulation by grain density, grouping, and size. Although image extraction can be improved by magnification, microdensitometry, computer image enhancement, and color enhancement of density gradations, no information can be recovered from a radiograph if it is not from a blackened film grain.

If one examines in finer and finer detail an image definition on film (i.e. an image element with one transition from high to low signal intensity), the dark silver grains settled on acetate will become visible. Regions which appear darkest unmagnified contain the highest density of darkened grains whereas a low grain density appears light. The image modulation of this region of interest is the ratio of its peak to average

density and is necessarily a function of the exposure intensity above background. As the size of a definition becomes progressively small and grain size becomes comparably large, fewer silver halide grains become exposed. Due to finite grain size, film modulation and recorded resolution tend to decrease as the demand for spacial resolution continues to increase. Also if significant image motion occurs, a distribution of film grains expose as image details move and the resulting blur decreases resolution. Thus, overall data quality relies upon successful interpretation of the film image evolved from these darkened grains and the circumstances that produce them.

Since the demand upon system imaging capabilities varies with subject complexity, it is natural to attempt extension of system information capacity to anticipate more challenging subjects or obtain further data from existing subjects. Like many engineering systems, several independent constraints control the performance of the radiography system and some may outlie the component's best operation range. In the search for the optimum system, then, one must recognize that from the outset the whole of the system is not necessarily the product of its parts because of possible interactions. An intricate interrelationship does exist between resolution, modulation, and temporal optimization of a

recorded image. Figure 3.1 is one representation for the hierarchy of information derived from the motion neutron radiography components and is divided into two categories--modulation and temporal resolution. As shown, film density may be improved by exposure increases in either exposure time, neutron beam magnitude, optical transmission, scintillation, or intensification. An increase in film processing time will improve density as well. Static spacial resolution, as opposed to image definition limited by motion blur, could be improved if fine grain phosphor devices or films are used and geometric unsharpness is minimized. Finally, temporal resolution is enhanced when increased frame rates, decreased image-film motion, and low persistence phosphors are emphasized. Attempts to increase modulation, resolution, and temporal information combined often meet opposition; although improved density is obtained by increased processing, its background fog and granularity reduce film resolution; increased frame rates allow high temporal resolution but reduce exposure; and films of reduced grain size characteristically require greater exposure. These examples do not exhaust all self-restricting variations, and, in general, methods attempting to improve density tend to decrease spacial resolution and reduced exposure time needed to enhance temporal resolution decreases density. Only static

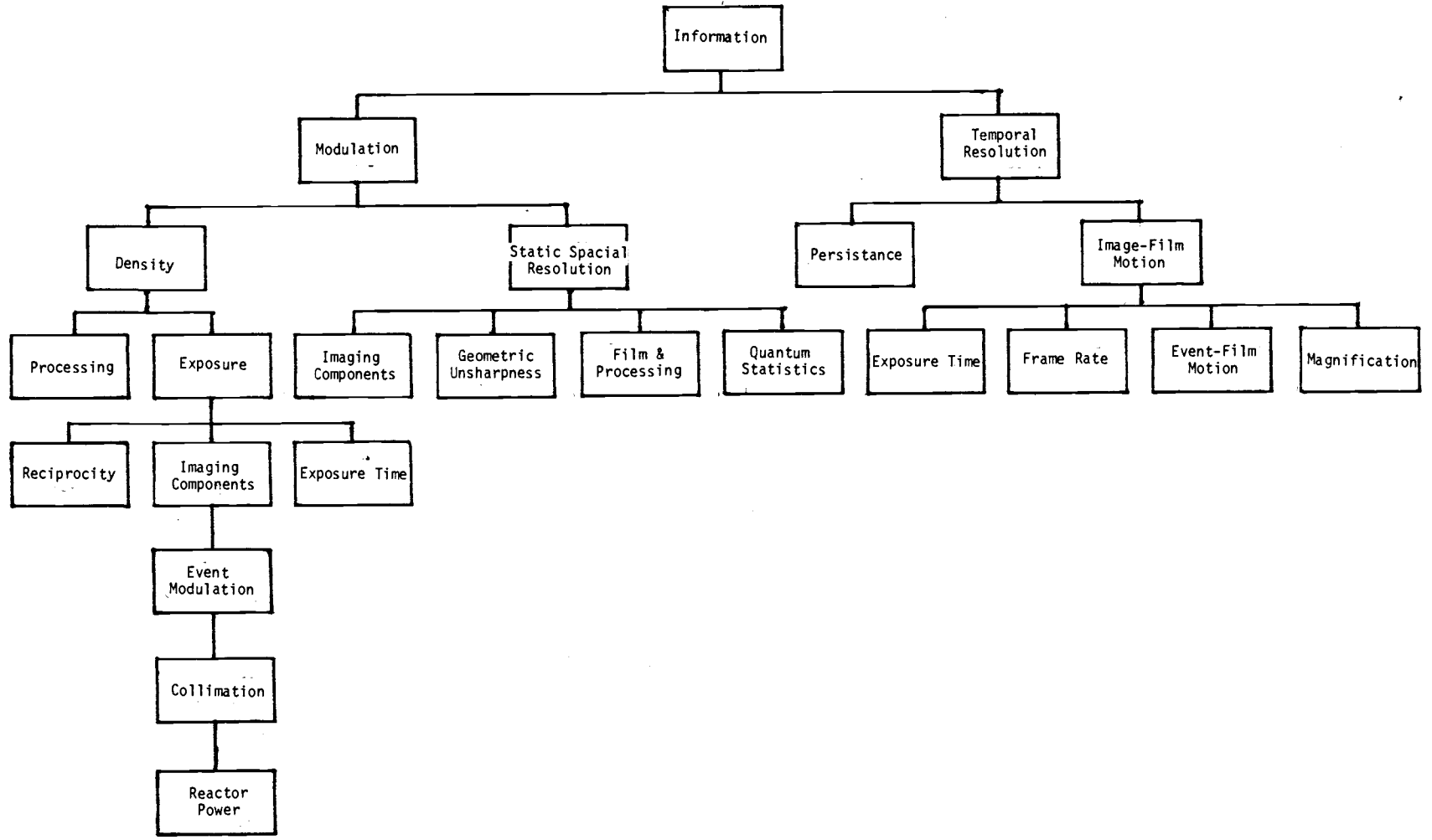


Fig. 3.1: Hierarchy of motion radiography information.

spacial resolution is independent of temporal resolution. Therefore, subject to the many physical restraints imposed upon the system, one would very often be willing to forgive information loss in one category in order to increase the quality of another. Tradeoffs on information desired would depend upon priorities established for the subject.

Perhaps the most challenging understanding required for successful interpretation is not to what ability radiographic instrumentation may operate, but what is desired to make a decision from the results. Vision is usually the final information link between the object and the observer's brain and often the most misrepresented factor in design when electro-optical systems are combined from components evaluated by poorly suited specifications. An ability exists to produce instruments which will meet any reasonable prescribed specification, but agreement upon which of two devices (e.g. scintillators, intensifiers, etc.) is more capable as measured by human perception and laboratory instrumentation is more difficult. One photo-optical researcher has stated in this way the dilemma of system performance evaluation between visual interpretation and use of engineering specifications which poorly represent physiological and psychological aspects of vision:

The process begins in this manner: We receive requirements that are well meant, but vague. From these requirements, we draft a set of specifications which are at best unclear. Then, acceptance trials, which are completely irrelevant, are conducted and the equipment is put into operation with inevitable shortcomings and complaints registered (73).

Without careful training or practice for the interpreter, subject details may be overlooked or mistaken.

Radiographs of even simple phenomena may not be possible to explain by a trained observer if such phenomena is unknown and no alternative exists to perceive more than its shadow image. If conclusions are to be useful of unusual radiographs, confidence of image integrity must be maintained. An understanding is therefore important that radiographic instrumentation operates normally in an expected behavior closely described by factors which govern the user's ability to extract information.

Given the several restraints of an engineering nature, one may ask what variables are at the disposal of the user to control the system's ability to present information to be visually interpreted with a minimum of distortion and noise. This discussion will attempt to prepare a unified model for modulation magnitude and spacial resolution to evaluate the high speed neutron radiography system, then determine its current limitations and suggest improvements.

3.2 SYSTEM ANALYSIS

Due to the majority of optical components in use for the high speed motion neutron radiography facility, a system analysis should not proceed using the traditional evaluation methods of foil-film cassette radiography. The following discussion instead is appropriate for electrographic systems (i.e. low light level photography using an image intensifier) (74).

Evaluation of electrographic systems, in general, begins with a desire to predict how the system operates on the input image upon each component level. Although each component may operate on an input or "object" subject and produce an output "image" in different forms (e.g. light, nuclear radiation, or electric signal representations), in general the manner in which the resulting image can be characterized by intensity and dimension to its object image can be studied in the same way. Predictions upon the response of the system to produce a final image can therefore proceed knowing the characteristics and interactions for each component.

There is some question which subject--object or image--an analysis should ultimately predict when an object is imaged; although need exists to interpret object information prior system transmission noise and point spread, and a possibility exists to remove these by

image restoration, it is the recorded image which is usually first rendered. From the standpoint of the relative uncertainty of the subject due to distortion or noise, there is no difference in the final calculation whether an analysis chooses the object or image as the reference plane. This analysis procedure will choose the object plane for reference but is equally appropriate when the image plane is reference if magnification and gain terms are inverted in the following equations.

An image may be synthesized by a large number of individual points of various intensities, such as the familiar half tone printing employed in newspaper photography, or grouping of equal intensity points, such as darkened film grains in an emulsion. In a sense, these "points" provide the basic building blocks of any image. Each imaging component in an electrographic system alters an image point in magnification and signal intensity, whether desired or not. Ideally, the imaging system could change as desired the point intensity within an infinite range of values and is capable of grouping an infinite number of independent image values into any finite image element. Actual image devices limit the range of intensity values which may be distinguished reliably by superimposing noise upon the image signal and influence the signals of surrounding points by any single image point due to image spread. There are thus four

characteristics of an imaging process that must be accounted in an electrographic system--magnification, image transfer characteristic, image spread, and noise.

3.2.1 Magnification

Magnification of an image device scales the spacial dimension of an object to that of its image. If magnification varies over object space, this is known as distortion. System magnification is given by

$$M = \prod_{i=1}^n m_i \quad 3.1$$

where

M = system magnification for a system of n devices

m = device magnification

$$= \frac{\text{output image scale}}{\text{input image scale}}$$

3.2.2 Transfer characteristic

A device transfer function represents the image intensity conveyed from object to image signal values by either equation or graph and when expressed as a nondimensional ratio is known as the gain. Transfer characteristics have been measured for a number of electro-optical instruments and are available for

reference. However, since the performance of any detector of electromagnetic radiation is more sensitive to some portions of the spectrum than others, transfer characteristics measured for a particular source are useless when the device is applied to a source with a different spectral distribution. For example, it would not be expected that either the film or intensifier would respond equivalently to equal magnitudes of phosphor excitation or the tungsten calibration source most often used by manufacturers to provide gain characteristics. Transfer function calculations normally account for the fraction of the emission spectrum detected by including the degree of spectral fit between the source and detector as a separate factor in transfer calculations with a gain factor valid at peak detector sensitivity (see Appendix A). The correct gain of a device can then be accounted provided a reference gain measurement and an appropriate factor. A system transfer characteristic is then

$$G = \prod_{i=1}^n \alpha(i-1,i)g_i' \quad 3.2$$

where

G = system gain for all n components

g_i' = component reference gain

$$= \frac{\text{output signal magnitude}}{\text{input signal magnitude}} = s_o/s_i$$

$a(i-1,i)$ = spectral matching factor for source
distribution $i-1$ and detector i

g_i = component gain corrected for source
distribution

$$= \alpha(i-1,i)g_i'$$

Once the system gain is determined, its usefulness resides in the ability to determine the output signal magnitude from the product of system gain and any input magnitude. When gain varies as a function of source intensity, the device is said to be nonlinear in gain. Most electrographic devices have nonlinear transfer properties but may be considered linear over an appropriate range. Of particular concern are those nonlinear devices whose transfer properties cannot be expressed as a gain ratio since this excludes their use in equation 3.2 to determine system gain in a closed form.

System modulation is closely related to the transfer abilities of a system and represents the relative change of signal magnitude by an an image element as opposed to the signal magnitude of a single image point. Modulation is defined as the peak image signal magnitude divided by the average signal level, and is compatible with the definition employed in communications for amplitude modulation (Fig. 3.2). By this definition, a very large change of relative signal magnitude would possess a modulation approaching unity whereas zero modulation

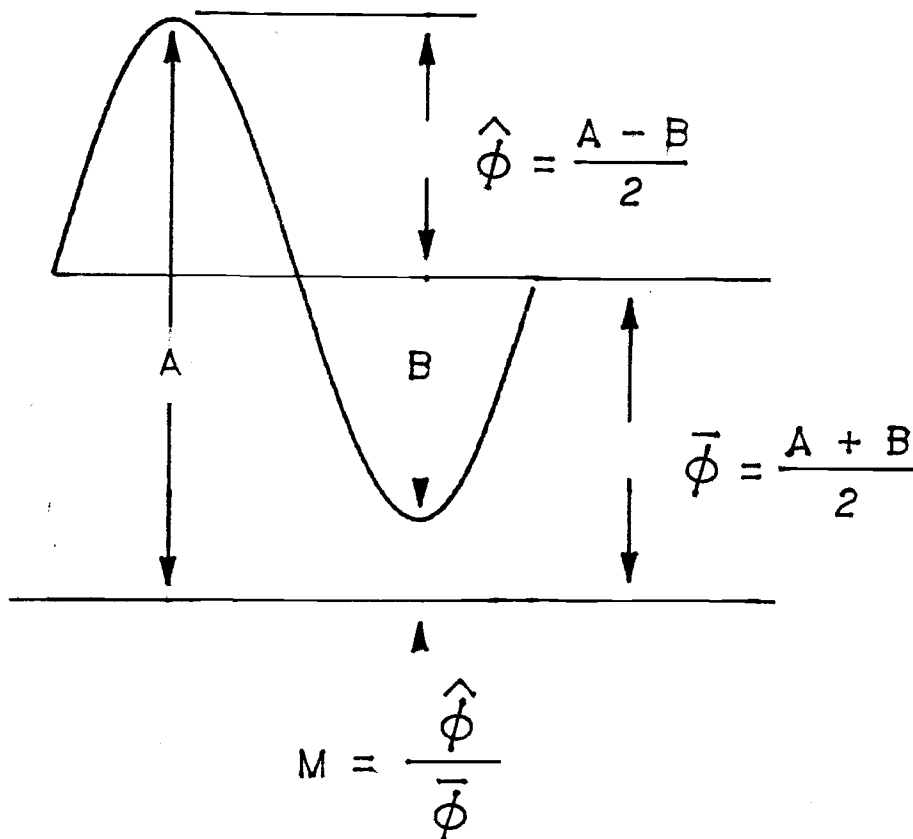


Fig. 3.2: Magnitude variation of an image element.

would correspond to no relative change of magnitude. In the visual sense, a unity modulation is of highest visibility or contrast. However, the term "modulation" is preferred to use of "contrast" which has suffered from ambiguity in the literature, being defined by various authors as $A - B$, $(A - B)/A$, $(A - B)/B$, A/B , $(A - B)/(A + B)$, etc.

The concept of gain, the ratio of output to input signals a system operates on, is a useful concept in linear systems, however when the gain varies with the signal in nonlinear systems, differential gain becomes important. The differential gain is defined as the ratio of output change to input signal change, as the latter approaches zero, and is:

$$g_{\text{nonlinear}} = \lim_{\Delta s \rightarrow 0} (\Delta s_o / \Delta s_i) = \frac{ds_o}{ds_i}$$

Relative differential gain, or gamma, is a dimensionless quantity defined as the differential gain evaluated relative to the gain proper:

$$\gamma = \frac{g_{\text{nonlinear}}}{g_{\text{linear}}} = \frac{s_i ds_o}{s_o ds_i} \approx \frac{\Delta s_o / s_o}{\Delta s_i / s_i}$$

When the transfer characteristic of a nonlinear system is plotted on log-log coordinates, the linear slope of this plot defines the system gamma at the point at which the slope is determined. This slope is also the system gamma since

$$\gamma = \frac{d(\log(s_o))}{d(\log(s_i))} = \frac{ds_o/s_o}{ds_i/s_i} \approx \frac{\Delta s_o/s_o}{\Delta s_i/s_i}$$

Thus, for small values of modulation, the output modulation is obtained from the input modulation by multiplication with the differential gain:

$$M_o = \gamma M_i \quad 3.3$$

Although the gamma characteristic of a nonlinear system is most often identified with that of film, the concept of relative differential gain permits application of linear analysis methods to all nonlinear components, and, just like the transfer function, becomes simply another modulation gain factor.

3.2.3 Spread function

In any imaging system some blurring of a point image occurs producing an intensity spreading in the image plane. The point spread function is simply the two dimensional mapping of this intensity spreading by position normalized such that the integral over the function is unity. Similarly, if a narrow line is imaged the blurred response may be described by a line spread function in a single dimension. It has become common practice to characterize the response of an imaging

component by its point and line spread functions. Use of the spread function can be compared with the concept of impulse response in an electronic system or the Green's function; in either case the response of a device to any object, the image function, can be determined by the convolution of the spread function with the object function. The need for performing convolution can be avoided by working with the Fourier transforms of object, image, and spread functions (known as object and image spectra and transfer function, respectively) so that the image spectrum is obtained as the product of object spectrum and transfer function.

Just as modulation defines the relative change in signal magnitude and the transfer function describes signal magnitude transfer, the spread function has its complement with regard to quality of spacial information transfer; the modulation transfer function, which describes the relative change of modulation in image space. The magnitude of the Fourier transform for a device's line spread function is defined as the modulation transfer function (MTF) for that device and is given by

$$T(v_i) = \int_{-\infty}^{\infty} L(x) e^{i2\pi v_i \cdot x} dx \quad 3.4$$

where

v_i = image spacial frequency (mm^{-1})

$L(x)$ = characteristic line spread function

x = perpendicular distance from object line (mm)

i = complex operator.

The spacial frequency v and distance x denote vectors in one, two, or three (if variations in time are to be considered) dimensional image space and have units chosen to correspond to those in conventional use in photographic and optical analysis. The MTF, in its simplest form, represents the relative modulation expected for an electro-optical device according to the Fourier frequency components that comprise an image signal variation. It is directly analogous spacially to the measure of frequency (in time) response characteristics of electronic systems (i.e. the Bode plot) as the ratio of output (image) modulation to input (object) modulation. Figure 3.3 provides an example MTF response for an object image of progressively narrowing bars (Fig. 3.3a & b) and the corresponding reduction in modulation (Fig. 3.3c & d). Notice that as the bars get closer together their highlights dim until only a gray area is recorded. Conventional resolving power measurements constitute one point only on such a curve. For further background, a good introductory article on MTF may be found in the references (76).

For a system of n cascaded components, the total MTF

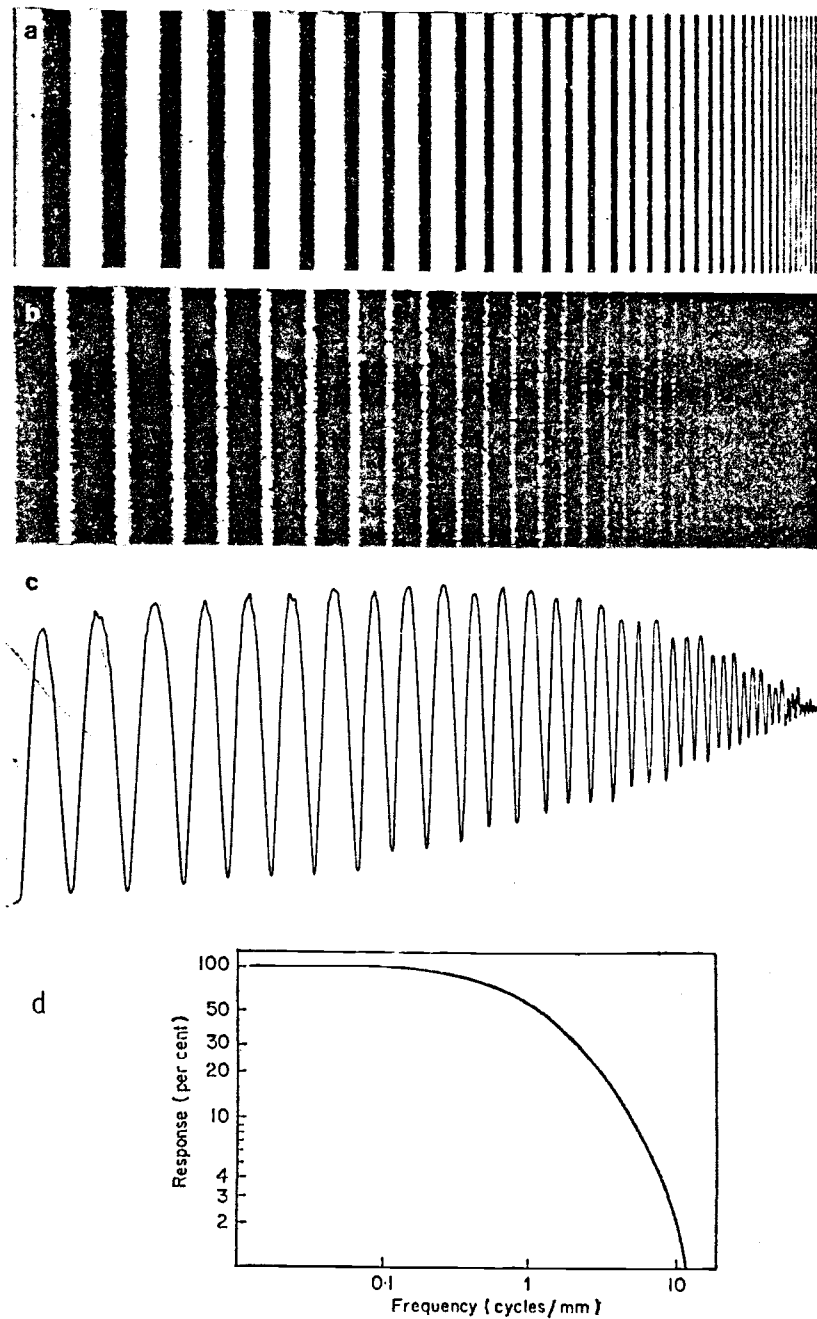


Fig. 3.3: Modulation transfer and the modulation transfer function (MTF). (a) Object bar chart. (b) System image response. (c) Graphical representation of modulation. (d) System MTF.(75)

is obtained as the product of each component transfer function. The MTF of a system of n components is then

$$T = \prod_{i=1}^n T_i(\mathbf{v}_i)$$

Since intermediate stage magnification changes detail size, image spacial frequency of component i , n_i , depends upon cumulative magnification of all prior components and not necessarily the object or system image dimensions. If the arguments (spacial frequencies) of all transfer functions are mapped into a common reference region (namely the object plane), a more universal expression for the system modulation transfer function is possible. Introducing the cumulative magnification, M_i ,

$$M_i = \prod_{j=1}^i m_j \quad 3.5$$

we have

$$T(\mathbf{v}) = \prod_{i=1}^n T_i(\mathbf{v}/M_i) \quad 3.6$$

where \mathbf{v} is the spacial frequency in the object plane.

Some attempt has been made to return to a single value definition of component limiting resolution under the explicit conditions of MTF measurement. The equivalent pass band N_e is one such figure and is defined as an equivalent number of cycles (e.g. the number of black and white lines) having unity modulation from zero up to N_e and having zero modulation at all spacial

frequencies above N_e which encloses an area equal to the area of the measured MTF squared. One half the equivalent pass band is defined as the noise equivalent bandwidth

$$NBW = \int_0^{\infty} T^2(\nu) d\nu$$

and the equivalent pass band is then

$$N_e = 2NBW$$

3.2.4 Noise

The presence of noise upon the signal path of any imaging system disguises information desired to be recorded of an object. Methods exist, in principle, that enable image reconstruction from any deviation of the ideal image if the system characteristics are known, however the effect of noise cannot fully be removed due to its random nature. Therefore noise is an essential cause of information loss in any system.

The smallest detail discernible in an image is limited ultimately by the number of particles recorded. A natural statistical fluctuation occurs in the arrival rate of these quanta, much like raindrops upon a given area of ground. With regard to information transmission, the probability distribution which occurs when the information arrives in packets or quanta is Poisson.

Although other noise distributions have, in general, been observed, the Poisson distribution is a valuable first approximation for the random arrival or development in time of the following occurrences:

1. Neutrons upon a target.
2. Electrons in an electronic transmission system.
3. Photons in optical imaging.
4. Grains in a photographic emulsion.

If the information channel is of such quantum nature, the variance (s^2) is equivalent to the mean number of particles occurring (\bar{n}). If the average number of occurrences may be taken as the signal magnitude and the standard deviation may be taken as the rms noise amplitude, the signal-to-noise ratio, R , may then be written as

$$R = \bar{n}/s$$

$$R = (\bar{n})^{1/2}$$

Paradoxically, for a Poisson distribution both noise and signal-to-noise ratio increase with the standard deviation. The inverse square of the signal-to-noise ratio, known as the specific noise, is often more convenient to work with since the sum of the specific noise contributions equals the system specific noise.

Noise may enter the signal path of an imaging system from any component and be amplified together with the object signal. For a Poisson noise source entering a $j =$

1 component stage and continuing with the signal to the i th stage, the specific noise is

$$R_i^{-2} = 1/G_i n_0 \quad 3.7$$

where n_0 is the number of quanta at the system input and the cumulative gain, G_i , is defined as

$$G_i(\nu) = \prod_{j=1}^i g_j T_j(\nu/M_j) \quad 3.8$$

The cumulative gain is similar to the system gain G for the first i components only now the MTF must be taken into account, but is equivalent to the system gain at the object spacial frequency $\nu=0$. If a number of individual noise sources enter the system at different stages, the combined specific noise is, in general by means of the central limit theorem,

$$R^{-2} = \sum_{i=1}^n R_i^{-2} \quad 3.9$$

3.2.5 Technical description

Figure 3.4 provides technical dimensions and information regarding the beam port electrographic system to be analyzed. Aside from the reactor and synchronization electronics, each radiography component is represented by this figure and identified by number.

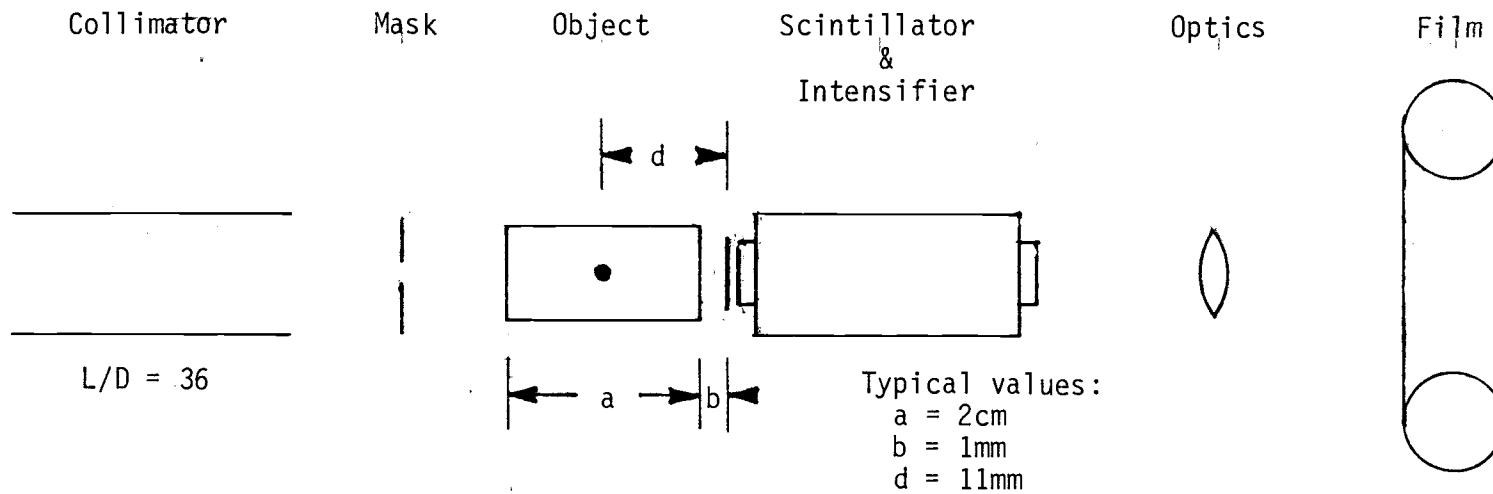


Fig. 3.4: Arrangement of imaging components.

IV. SYSTEM TRANSFER FUNCTION

4.1 ELECTROGRAPHIC ANALYSIS

For a single frame of exposed film the exposure time is constant over the frame so that the density of the recorded image is a direct function of the intensity of the image irradiating the focal plane. Over a single frame a minute image detail of uniform density is therefore determined by the radiant intensity of the detail. This image element is subject to the transfer properties of the optical system, intensifier, scintillator, and object itself. Finally, reactor power during the moment the frame was recorded determines its photographic density. Although the object itself may produce a complicated modulation, an intensity transfer analysis may be performed independent of position given such a small region. Since the neutron beam is well uniform over the imaging area such that a flux of equal intensity exposes the object, a general form for the system gain may be obtained.

4.2 FLUX MAGNITUDE AVAILABLE FOR IMAGING, I₁

The neutron flux magnitude available at the beam port #3 collimator opening has been measured using gold foil irradiation at a moderate power level of 35kW. To obtain beam port flux values at peak power levels required for high speed motion neutron radiography (about 3000MW), the tabulated thermal flux values given in Table 4.1 are extrapolated to the peak power levels measured at the reactor console. Explicitly, the reactor thermal power (P) in terms of the average core neutron flux (ϕ) is

$$P = k \int \phi \Sigma_f dv$$

where the integral is evaluated over core volume, Σ_f is the average thermal fission macroscopic cross section in cm^{-1} , and k is the energy yield due to fission ($3.2 \times 10^{-11} \text{W-s/fission}$). Since the macroscopic fission cross section varies as the number of fissile nuclei in the core, it would therefore be a matter of some concern if core burnup and loading were altered since beam port flux would change from its reference value. Beam port #3 flux has been measured as late as 1983, however, without showing significant change in flux values. Some flux prediction error may also be introduced from reactor

Table 4.1: Beam port #3 flux values at 35kW (77).

Date	Total	Flux (10^6 n/cm ² -s)		Cd Ratio
		Epi-cadmium	Thermal	
1983	8.48	3.39	5.09	2.44
1976	8.86	3.96	4.90	2.24

pulse power measurements using the percent power chamber. Errors may be encountered if the chamber inserted into the core behaves nonlinearly at power levels above one megawatt where chamber operation cannot be verified easily.

By proportion, the thermal neutron flux available at the object site at any power level is

$$\begin{aligned} I_1 &= (I_0/P_0)P \\ &= 145 \times 10^6 P \text{ nv/MW} \end{aligned} \quad 4.1$$

where P is the reactor power, P_0 and I_0 are the reference power (35kW) and neutron flux ($5.09 \times 10^6 \text{ nv}$) respectively (the term nv is an abbreviated form of units for neutron flux).

4.3 SUBJECT TRANSFER, g_2

Image magnitude is determined by the subject's neutron transmission properties and tends to decrease exponentially with its thickness. Given a subject of single or homogeneous material, the fraction of neutron intensity transmitted without interaction to incident intensity (I_2/I_1) is

$$\begin{aligned}g_2 &= I_2/I_1 \\ &= e^{-\Sigma_t x}\end{aligned}$$

where Σ_t is the material total macroscopic absorption cross section (cm^{-1}) and x is the subject thickness (cm). Transmission for subjects composed of layered materials may be modeled as the product of the transmission for each individual layer. Subjects of any interest for neutron radiography are seldom single materials, however, just as not all neutrons escaping the subject arrive without scattering once. More complicated methods may be applied to predict neutron transmission (e.g. Monte Carlo) if the type, concentration, and position of each constituent is known. In practice, this is seldom done but for simple test subjects since image details are best obtained by performing the radiograph itself. However the simple model above may serve to approximate minimum subject transmission for appropriate selection of film exposure time and latitude even when applied to

complicated heterogeneous objects with highly dissimilar neutron cross sections.

A Monte Carlo program presented in Appendix D has been used for this research since a simple exponential law has been found inadequate to model attenuation in a common subject material for neutron radiography--iron. A scattering interaction is five times more likely to occur than an absorption in iron and therefore this alternate method was necessary. This program models neutron interactions within a slab upon a probabilistic basis and therefore requires much operating time to accumulate a statistically significant answer. The long run time necessary to predict g_2 especially for very thick slabs is the greatest disadvantage of this method.

4.4 SCINTILLATOR ABSOLUTE EFFICIENCY

Once the thermal neutron image has been transmitted by the subject the LiF-ZnS scintillator converts a portion of the neutron beam to light so the remainder of the radiography system may amplify and record the image. Without understanding the value of radiant power released from the scintillator due to the magnitude of incident flux, no exposure calculation can be made. Measurement of absolute scintillator efficiency is considerably more complicated than relative efficiency comparisons between various scintillators, and, unfortunately, although a plethora of research has been conducted upon relative scintillator efficiency meant for particle detection in other nuclear disciplines, very few absolute efficiency details for the LiF-ZnS scintillator exist. Scintillator construction influences the efficiency obtained so existing absolute efficiency data may not apply to scintillators created of different widths and concentrations even if identical materials are used. In order to predict the transfer abilities of OSU scintillators, then, a computer program has been developed to arrive at absolute efficiency values in lieu of measurement.

As described earlier, scintillation is obtained in a LiF-ZnS neutron scintillator by excitation of a ZnS

phosphor following a neutron absorption interaction with lithium 6. The $\text{Li}^6(n,\alpha)\text{T}$ interaction releases a 2.05 MeV alpha particle and a 2.73 MeV tritium nucleus in opposite directions. The particles track through the scintillator screen losing energy by a succession of inelastic collisions with constituent electrons and are not appreciably deflected during collision. Although the highest concentration of ZnS is necessary to receive the largest energy proportion for efficient scintillation, the content of Li^6 needed to produce charged particles as well as transparent binder to transmit light from the opaque LiF-ZnS materials to the surface cannot be compromised. Only a fraction of the energy lost with particle interaction can be used to excite the ZnS phosphor and the Monte Carlo calculation in this program attempts to determine this fraction.

Figure 4.1 illustrates the transmission and conversion processes that occur within the LiF-ZnS scintillator where, for simplicity, Li^6 and ZnS materials are pictured as single groupings. The many factors that contribute to produce scintillation radiant energy are summarized in the figure and given in the equation below:

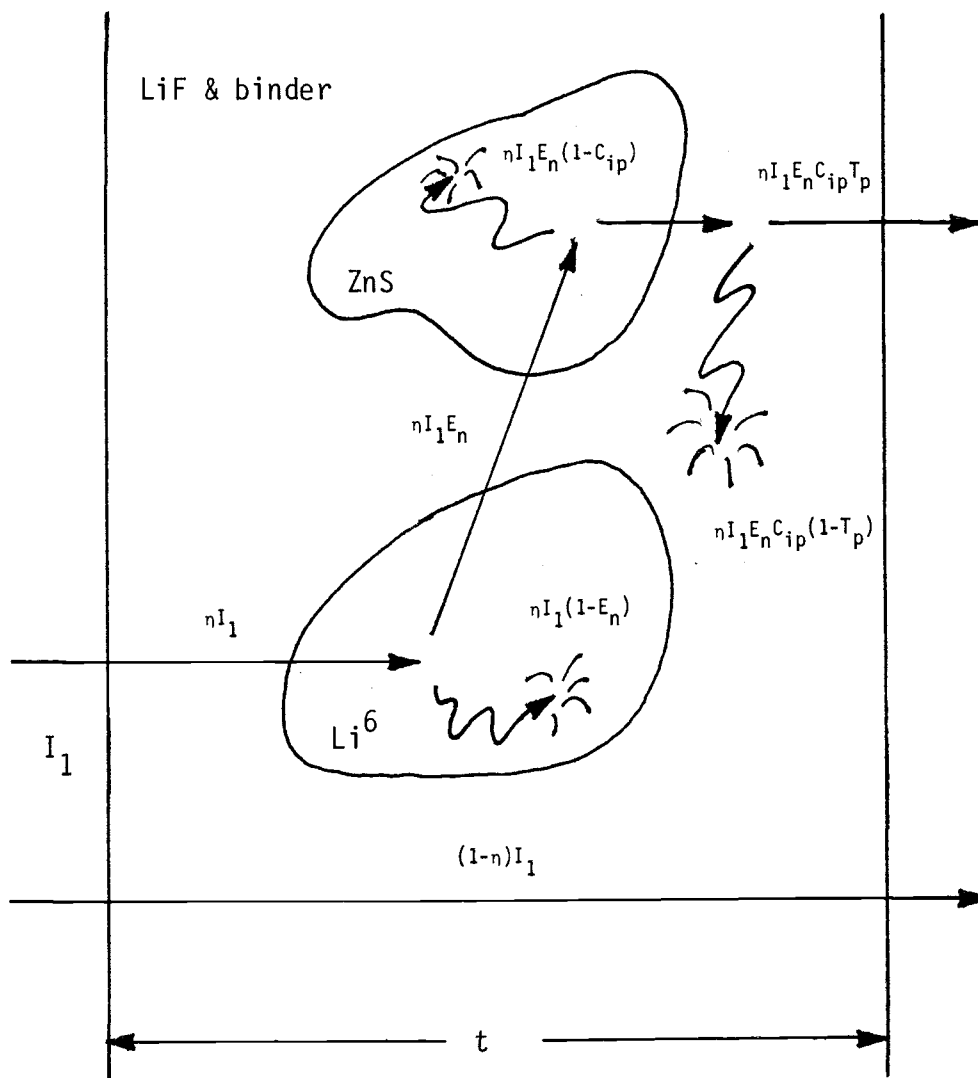


Figure 4.1: LiF-ZnS scintillator quanta transmission and conversion.

$$\begin{aligned}
 \text{Scintillator radiance} &= \text{Incident intensity} \cdot \frac{\text{neutrons absorbed}}{\text{incident neutron}} \\
 (M_e) & \quad (I_2) \quad (n) \\
 \frac{\text{neutrons absorbed by Li}^6}{\text{neutrons absorbed}} &\cdot \frac{\text{energy absorbed in ZnS}}{\text{neutrons absorbed by Li}^6} \\
 & \quad (E_n) \\
 \frac{\text{light quanta energy}}{\text{energy absorbed in ZnS}} &\cdot \frac{\text{light transmitted}}{\text{light quanta emitted}} \\
 (C_{ip}) & \quad (T_p)
 \end{aligned}$$

$$M_e/I_2 = \eta C_{ip} T_p E_n \quad 4.2$$

where

I_2 = neutron intensity incident on the scintillator
(n/cm²-s)

η = scintillator efficiency to absorb neutron flux

E_n = energy excitation of ZnS per neutron absorption interaction (MeV/n)

C_{ip} = fraction of energy absorbed in ZnS to produce radiant emission

T_p = transparency of scintillator to its own scintillations

M_e = radiance emitted from the scintillator
(Mev/cm²-s or W/cm²)

The ratio M_e/I_2 of equation 4.2 represents the transfer function of the scintillator and its value of absolute efficiency in released energy per incident neutron. The M_e/I_2 ratio, although not strictly dimensionless, will be used to calculate system gain G and determine exposure directly in its units; g_3 will represent its absolute

efficiency as the dimensionless fraction of radiant energy released from the scintillator for each neutron impinging on it.

4.4.1 ZnS Excitation Per Neutron Capture, E_n

This factor of equation 4.2 represents the energy deposition by alpha and triton particles originating from a neutron absorption in Li^6 into those particles of ZnS within their range. Due to the very large number of collisions necessary to bring a heavy charged particle to rest, alpha or triton range is determined by its initial energy within narrow limits. Also, energy loss along the particle track is not constant but follows the Bragg range curve, which may be linearly approximated over two groups--an energy loss of 69% is encountered over the first 85% of range and the remainder of 31% is dissipated over its last 15% of range. This allows a single computation of particle range and a simple method of determining the energy deposition is ZnS based on the recorded excursions through the phosphor during particle path simulation. The range of both the triton and alpha particles in ZnS, LiF, and waterglass and polyethylene binding materials have been calculated using a semiempirical formula for the ranges of heavy particles (78). Table 4.2 below summarizes energy and range

Table 4.2: Range and energy values for alpha and triton particles

	Particle	
	Triton	Alpha
Energy (Mev):	2.73	2.05
Range (microns):		
Zinc Sulphide (ZnS)	27.8	4.85
Lithium Fluoride (LiF)	26.6	4.75
Polyethylene ((CH ₂) _x)	57.8	9.86
Waterglass (Na ₂ O ₄ SiO ₂)	36.4	6.38

dependence of both particles and their ratio of energy to range.

Energy deposition in ZnS can be determined by statistical simulation of particle range and direction using a Monte Carlo numerical method. Since scintillator construction is homogeneous, the entire scintillator volume may be modeled divided into equal volume and geometry capsules containing each a phosphor grain surrounded by an appropriate volume of LiF and binder. The ZnS phosphor grains are generally spherical so each capsule may be modeled as a sphere in a box (Fig. 4.2). Although this model obeys closely the boundaries and restrictions imposed from individual particle origin in Li^6 to their encounters within the phosphor it can be further simplified since the heavy particles which track through the scintillator do not scatter and thereby remain in a single plane determined from their origin. A two dimensional capsule or cell, then, is all that is needed to simulate energy deposition provided the particles encounter an average phosphor cross section. Particle transitions between adjacent cells may be treated collectively as one cell assuming this cell has reflecting boundaries. Since cell dimensions are correctly proportioned to overall scintillator weight fractions and are symmetrical to adjacent cells, all interactions modeled to originate and complete within a

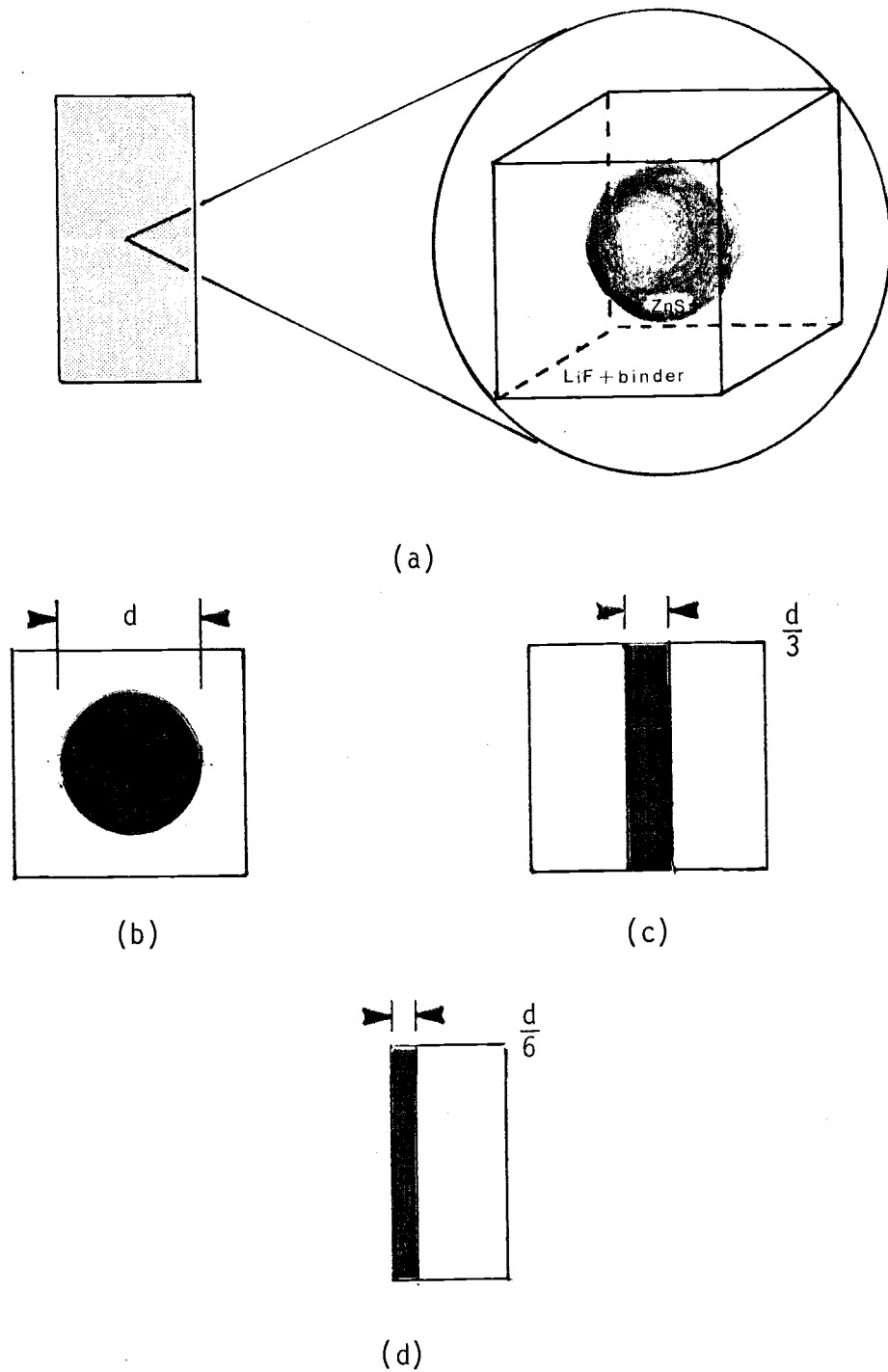


Figure 4.2: Monte Carlo scintillator model. (a) Unit cell. (b) 2D cell. (c) Slab dimensioned to average chord length. (d) Half slab.

single cell effectively represent the results of all interactions within the scintillator. Analysis of the unit cell model may be further simplified when converted to an infinite slab. If the average chord length followed by a particle through a spherical phosphor grain is equivalent to average chord length of the slab, this transformation may be made. The average chord length of a solid is

$$\bar{R} = 4V/A$$

whereas for an infinite slab

$$\bar{R}_{\text{slab}} = 2a$$

where \bar{R} is the average chord length, a is the slab width, V and A are the solid's volume and surface area respectfully. This comparison would then suggest that for equivalent average chord lengths a full slab width of one third the phosphor diameter is required. Finally, because interaction number is symmetrical about cell center and length, one half the cell width need only be considered with particles directed from angles of 0 to 180° perpendicular from the boundary.

The Monte Carlo algorithm attempts to determine total ZnS energy deposition by accumulating a number of individual path histories which originate with random position and angle in the LiF region and end when particle energy is exhausted. Following position and angle selection, the energy expended by the particle to

cross the nearest boundary is computed. Particle transitions within the unit cell model follow the guidelines below:

1. If the energy required to cross the boundary is greater than the first 69% of particle energy, particle travel will continue using range constants valid over the remaining energy from the position where the former energy group was exhausted.
2. If available energy is greater than the value to cross the boundary, the value necessary to reach the boundary is accounted and the remainder is used to calculate the travel within the material from the boundary.

The energy lost by excursions within the ZnS region is totaled for all histories then divided by their number to determine the mean fraction of energy deposited in ZnS.

Two assumptions are made by this model for E_n calculation:

1. All neutron interactions occur with Li^6 .
2. Alpha and triton path lengths are small in comparison to the physical width of the scintillator.

The first assumption may be considered well justified since less than 1% of the scintillator constituents other than Li^6 comprise the total absorption cross section of the scintillator. Scattering interactions are just as unlikely given a scintillator with any useful concentration of Li^6 . The model assumes no ions are lost from the scintillator and therefore this second assumption is not valid if these particles are

increasingly likely to escape when scintillator width becomes comparable to path length.

For hand calculations, a simple approximation for E_n which works remarkably well is given below:

$$E_n = 4.78 k V_z/V_t \quad 4.3$$

where V_z/V_t is the ratio by volume of ZnS in the scintillator, and k is an empirical factor. The volume ratio used above approximates the probability of an ion entering a zinc sulphide grain if its grain size is of the same magnitude as its track length. Normally this equation produces an E_n larger than that given by Monte Carlo but follows closely the behavior of computed values to material concentration. A reduction factor, k , appears to best offset this approximation to Monte Carlo computations.

4.4.2 Phosphor Efficiency, C_{ip}

The constant C_{ip} represents the fraction of light released by ZnS upon excitation with alpha or triton particles. Most of the phosphor ionization energy is expended as X rays, electron emission, chemical changes and chiefly heat; the remaining 20-30% is released as light. This range of C_{ip} values has been collected from the results of a number of researchers and it appears an individual measurement may vary as much as 25% due to

phosphor intrinsic resolution, optical coupling, and photocathode quantum efficiency variations (79,80). This phosphor is of the highest efficiency available and shows similar efficiencies for light and densely ionizing particles such as electrons (21%) or alpha particles (23%) (81,82). The "constant" itself may vary as a function of energy about 1 MeV (83).

4.4.3 Neutron Absorption and Light Transmission Efficiency, ηT_p

The probability of a neutron absorption in Li^6 decreases exponentially with distance from the incident face of the scintillator. Light transmission efficiency also decreases exponentially with distance from scintillation due to removal by absorption and scattering. These combined and opposing transmission probabilities from the site of interaction suggest an optimum scintillator width and composition occurs. The ηT_p factors may be determined analytically over the scintillator width. Consider over a small area of scintillator the neutron transmission path x from the input faceplate, neutron interaction and scintillation with a source plane in dx , and the remaining light transmission path to the output faceplate (Fig. 4.3). The probability density function for a neutron to cross

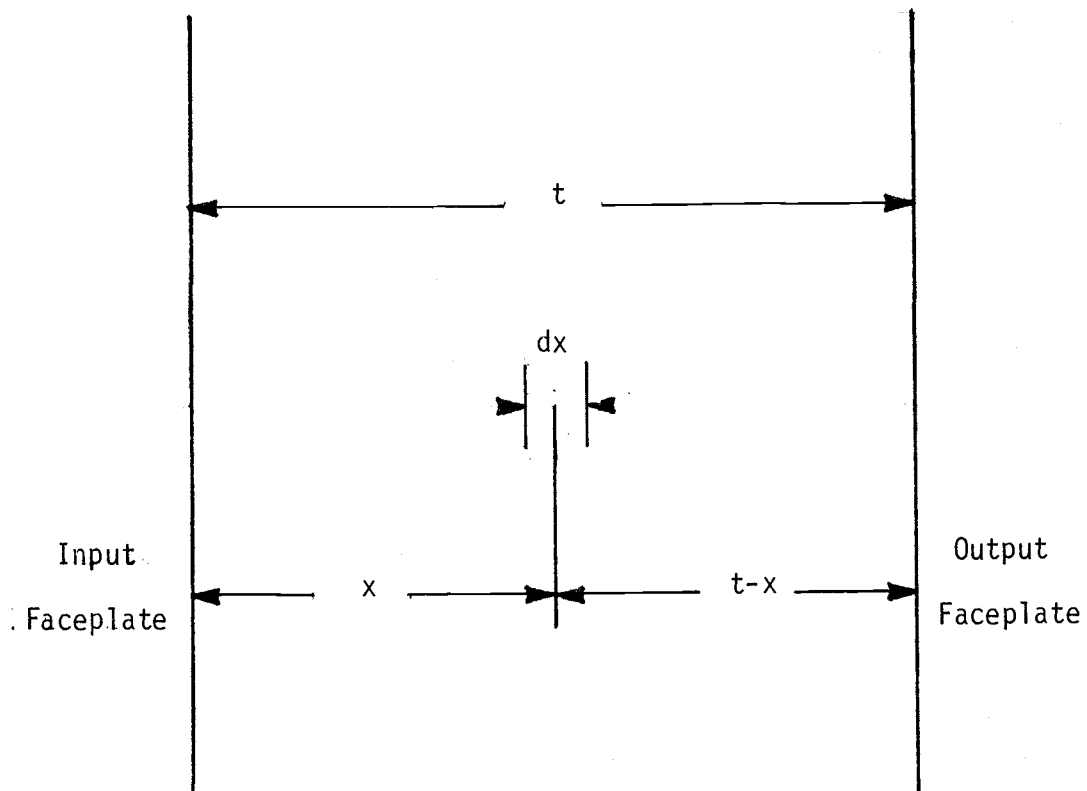


Fig. 4.3: Scintillation transmission model about differential area.

distance x until an absorption interaction within dx is given by

$$n(x)dx = \Sigma e^{-\Sigma x} dx$$

where S is the absorption macroscopic cross section of Li^6 . Transmission probability for light quanta available at the source to cross the remaining distance $t-x$ to the output faceplate is given by Lambert's law of absorption

$$T_p(t-x) = e^{-\mu(t-x)}$$

where t is the scintillator width and μ is the scintillator light attenuation coefficient. The cumulative probability density function for scintillator transmission is then the product and integral of these two probabilities over the scintillator width and is

$$\eta T_p = \frac{\Sigma e^{-\mu t} (e^{(\mu - \Sigma)t} - 1)}{\mu - \Sigma} \quad 4.4$$

The scintillator thickness for optimum transmission is then

$$t = \frac{\ln(\Sigma/\mu)}{\Sigma - \mu} \quad 4.5$$

Although equation 4.5 should be meaningful for a scintillator constructed of any concentration of ZnS to LiF, it is the best width characteristic of an optimum concentration that is desired. In practice, granular scintillators used for neutron radiography have widths below this optimum to promote spacial resolution.

Bossi has determined experimentally the light

attenuation coefficients for samples of both ZnS and LiF suspended in sodium silicate binder and these values are given below:

$$\mu_{\text{LiF}} = 61 \text{ cm}^{-1}$$

$$\mu_{\text{ZnS}} = 114 \text{ cm}^{-1} \text{ (84)}.$$

Note the mixture of both ZnS and LiF compounds will create an effective light attenuation coefficient which should be the sum of each coefficient weighted accordingly by their volume ratio. The macroscopic absorption cross section must also be weighted according to scintillator concentration of Li^6 .

4.4.4 Efficiency Predictions

The product of ZnS energy deposition, phosphor efficiency, and neutron and light transmission factors determines scintillator absolute efficiency. A program has been developed to compute this scintillator transfer function provided ZnS/LiF weight ratio, binder concentration, width, Li^6 enrichment, and ZnS particle size data from an input file. The scintillator absolute efficiency is output in units of MeV/n and the fraction of energy exciting the ZnS phosphor is also printed.

Although the primary objective of this analysis is to predict absolute efficiency values of scintillators constructed at OSU, a major portion of research has been

conducted upon efficiency of polyethylene binder LiF-ZnS scintillators and therefore programming was extended for these scintillators to first verify program operation. Unfortunately, light attenuation coefficients for LiF and ZnS materials dispersed in polyethylene were not available, and instead it was necessary to assume the program would produce a valid simulation with existing light attenuation coefficients based on sodium silicate binder. The very low attenuation coefficients of transparent plastics similar to polyethylene and their similar refractive index with sodium silicate makes this appear the opacity of LiF and ZnS dominate these measurements such that they become independent of binder type (85).

Unlike the manufacturing process used to construct scintillators with polyethylene binder, settled phosphor scintillators appear to form a constant fraction by volume of binder as the granular substances settle by weight within waterglass solution. For OSU constructed scintillators, then, a second program to simulate scintillator efficiency accepts a constant volume percent of binder instead of a given weight percent. Bossi was able to determine a binder volume percent of 40 characterized most scintillators constructed at OSU and it is this percent which is used in the analysis. Aside from the difference in data presentation in binder

concentration by volume instead of weight and use of ion ranges appropriate for waterglass, both programs are identical. Appendix B provides a listing of typical input data for either program.

The majority of either program is needed to calculate E_n by Monte Carlo and a considerable amount of time is required upon a microcomputer to complete a statistically significant solution. As mentioned earlier, an approximation for ZnS energy deposition (E_n) is available (Eq. 4.3) and if appropriate its use may obtain an absolute efficiency calculation upon a hand calculator. If terms were combined from the preceding sections in Eq. 4.2 and the E_n approximation is used, a single equation represents the absolute efficiency approximation

$$M_e/I_2 = 4.78 k V_z/V_t C_{ip} \frac{\Sigma(e^{-\Sigma t} - e^{-\mu t})}{\mu - \Sigma} \quad 4.6$$

Based on a least squares analysis of results by this approximate method to the Monte Carlo solution, a correction factor k of 0.917 for polyethylene and 0.679 for waterglass binder scintillators should be used. The resulting efficiency approximation for waterglass scintillators corresponds so well with the Monte Carlo solution it may be considered exact. Figure 4.4 provides graphical comparison between either solutions for polyethylene or waterglass scintillator models in terms of relative scintillator efficiency to ZnS/LiF weight

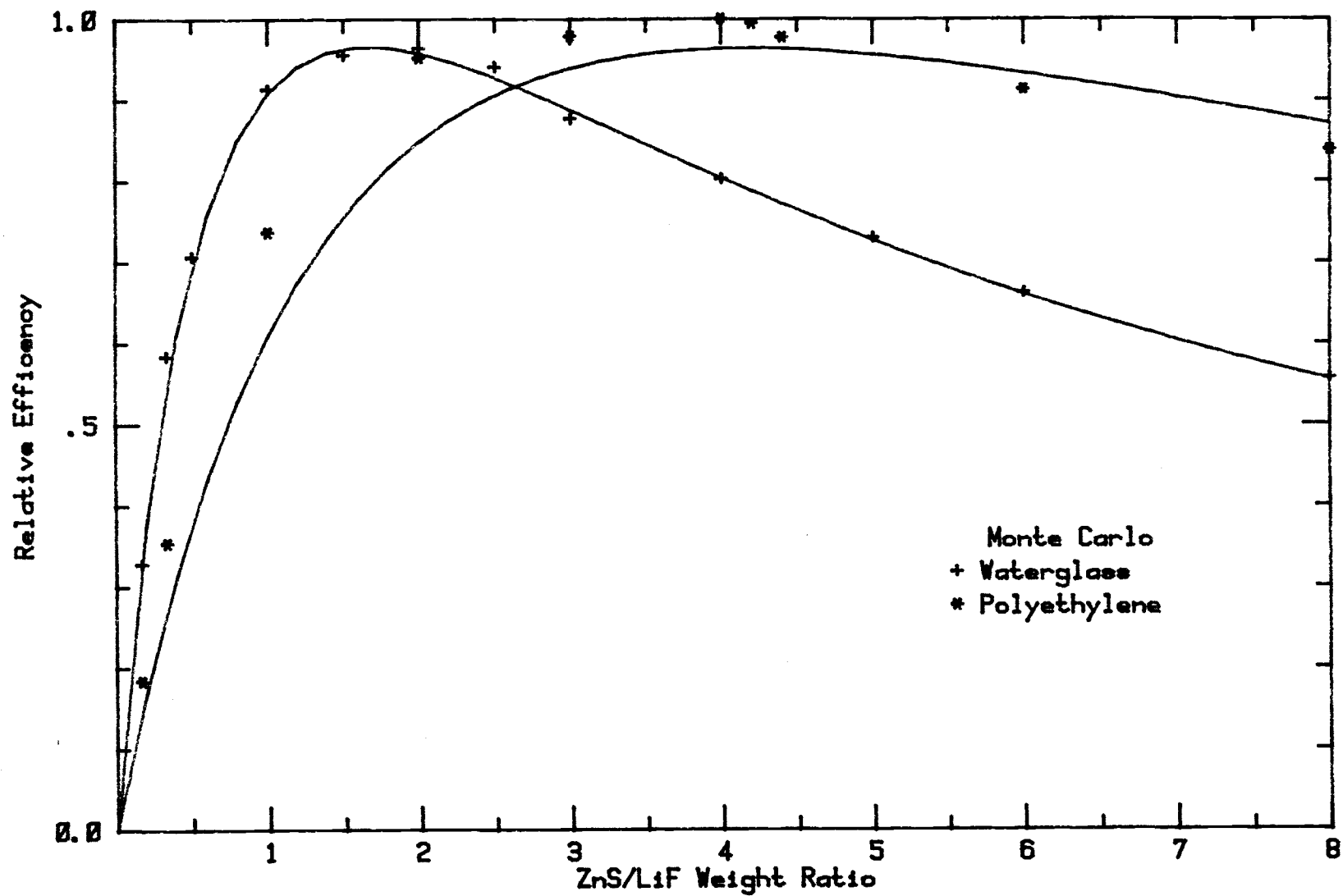


Fig. 4.4: Scintillator efficiency prediction by approximate and Monte Carlo models.

ratio.

4.4.5 Experimental Verification

Some previous research has measured absolute efficiency of LiF-ZnS scintillator specimens. Spowart has completed valuable efficiency measurements upon a number of scintillators constructed in various proportions of LiF and ZnS (86). Each scintillator under test was irradiated by a well collimated gamma filtered thermal neutron beam and its light collected by a calibrated photomultiplier and light guide. Once the absorbed neutron flux and transmission loss was known, Spowart determined the quantum efficiency for each scintillator from the measured photocathode current. A second researcher has measured absolute efficiency of the NE426 scintillator (87). Her experimental method employed a well filtered thermal neutron beam and calibrated photomultiplier as did Spowart, but also introduced several narrow passband filters before the photomultiplier to determine spectral emission of the scintillator. Spectral radiant output was determined from measured photo current given photomultiplier responsivity, gain, and the narrow passband transmittance. Total radiant output for the NE426 was then obtained by numerical integration of spectral

radiance over all wavelengths.

The scintillator efficiency program was run in an attempt to simulate each scintillator used by the researchers above and ascertain its accuracy. Additional considerations were required to arrive with a conversion factor to change Spowart's quantum efficiency units in terms of energy (i.e. photon/n to Mev/n) and enable comparison under identical units (see Appendix A). Table 4.3 lists Spowart's measurements following conversion. Technical literature from Nuclear Enterprises indicates manufacture of the NE425 and NE426 scintillators followed collaborative research with Spowart upon an optimum scintillator and therefore the results listed by Panhuise should be comparable to Spowart's 1:3:1 weight ratio scintillator, particularly if she specifies such narrow error limits. There are two reasons to believe her result is incorrect; first the NE426 spectral output curves recorded in her report and from which she used numerical integration to arrive with her value show considerable error; and, second, these curves show unusual multiple peaks for a ZnS phosphor. The error bars shown on these graphs sometimes become so large as to dominate the vertical axis and suggest considerable error has disguised the only true peak. Spectral response curves for commercial ZnS(Ag) phosphors constructed in the same chemical form as that sold for

Table 4.3: Measured absolute efficiencies for various composition LiF-ZnS scintillators (86,87).

Concentration Li:ZnS:CH ₂	t (mm)	$\frac{\text{MeV}}{n}$	$\frac{\mu W}{\text{cm}^2 \cdot \text{ng}} \times 10^{-9}$
		Spowart	
1:2:1	.73	.0336	5.38
1:2:1 (NE421)	.25	.0298	4.77
1:3:1	.22	.0310	4.96
1:6:1	.21	.0149	2.39
3:1:1	.23	.0206	3.30
6:1:1	.23	.0131	2.10
		Panhuise	
1:4:1 (NE426)	.25	.000824 <u>±.000124</u>	.132 <u>±.0198</u>

scintillator use (namely, JEDEC specification P11 phosphor) are well available, and, although performed for low energy electron excitation, never show more than a single characteristic peak. Leverentz has indicated that spectral emission of phosphors is generally unaffected by type of excitant, however, and much technical literature in both electronic and nuclear disciplines agree a single peak occurs at 450nm for this phosphor (88).

Since the absolute efficiency measurement of the NE426 scintillator by Panhuse does not appear to be correct, program verification continued using results published by Spowart only. Absolute scintillation efficiency is shown in Figure 4.5 in terms of the weight ratio of ZnS to LiF for both computed and Spowart's measured efficiencies. As shown, the model exhibits a significant difference from measurements in both an increased magnitude and a decreased descent beyond optimum concentration. Spowart suspects thermal neutron absorption calculations using the dominant Li^6 cross section alone measurably underestimates total absorption within the scintillator and has made comparisons from measurements to support this (89). If this were true, not all the neutrons stopped in the scintillator would contribute to the $\text{Li}^6(n, \alpha)\text{T}$ reaction and overall efficiency would be lower than calculated. Spowart could not account for this difference (which ranged from 12 to

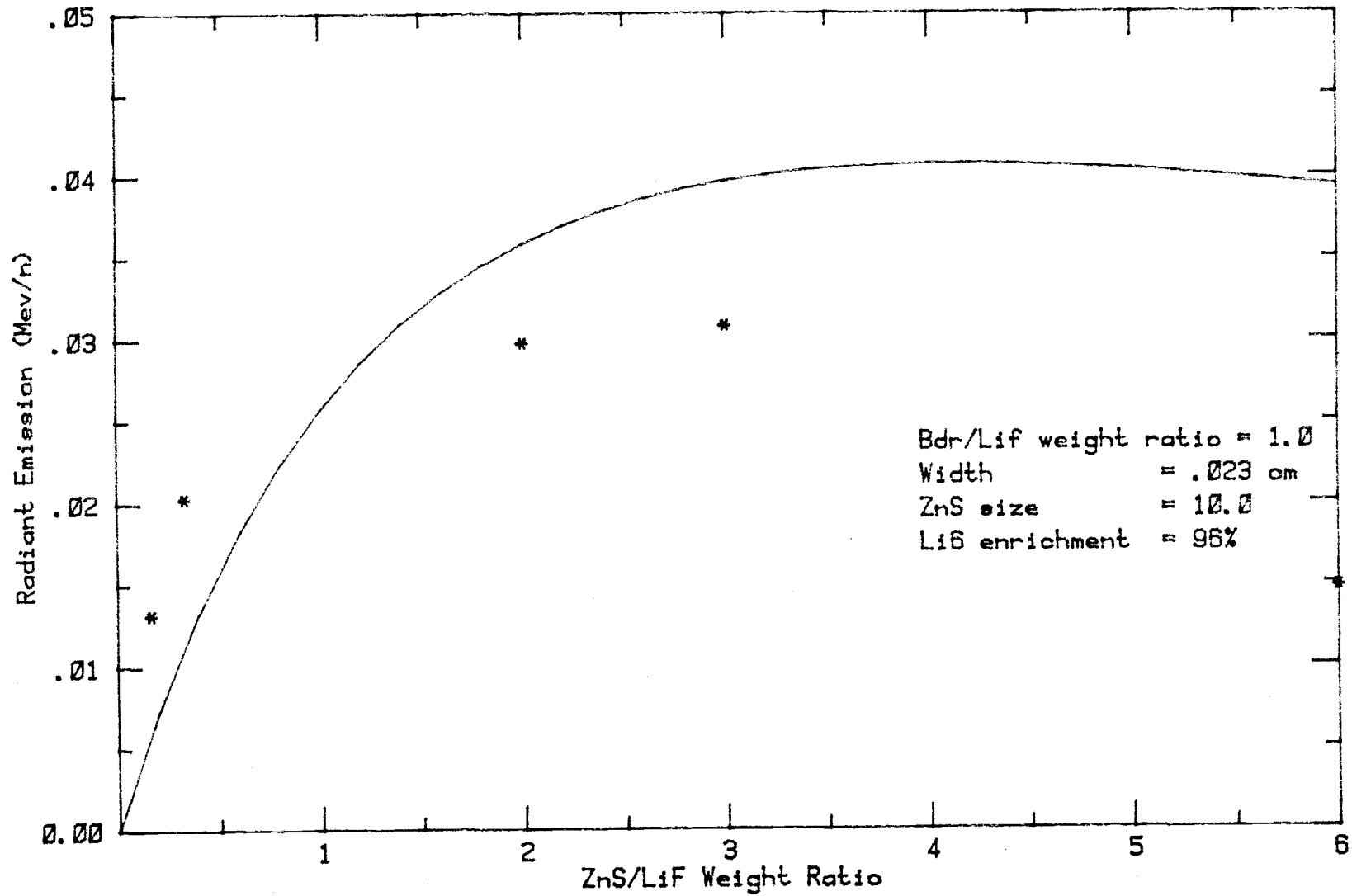


Fig. 4.5: Computed and measured radiant emission of polyethylene binder LiF-ZnS scintillators.

200%) by including calculations for parasitic interactions within the phosphor or polyethylene binder but showed even under the worst cases a difference greater than 10% should not be noticed.

Optical density measurements by Spowart show a 42% decrease in efficiency from ZnS/LiF weight ratios of 3 to 6. This descent is true of his absolute efficiency measurements (Fig. 4.5) and is attributed to increased light scattering by ZnS which occurs once sufficient content by the phosphor is present to optimize particle detection. Clearly a decrease of this magnitude does not materialize from this model and is perhaps due to an underestimate of the ZnS light attenuation coefficient since it is this value that determines the descent following the peak.

Accurate efficiency prediction of LiF-ZnS scintillators is bounded by an expected overestimate of $\text{Li}^6(n,\alpha)T$ reactions in calculations and measurements too few to make statistically significant conclusions. If this is the case, it would be justified to reduce computed efficiency to best approximate existing measurements. Figure 4.6 compares computed and measured efficiencies of scintillators studied by Spowart and scales calculations by 73.2% to agree with his measurements.

Data is available to examine performance of the

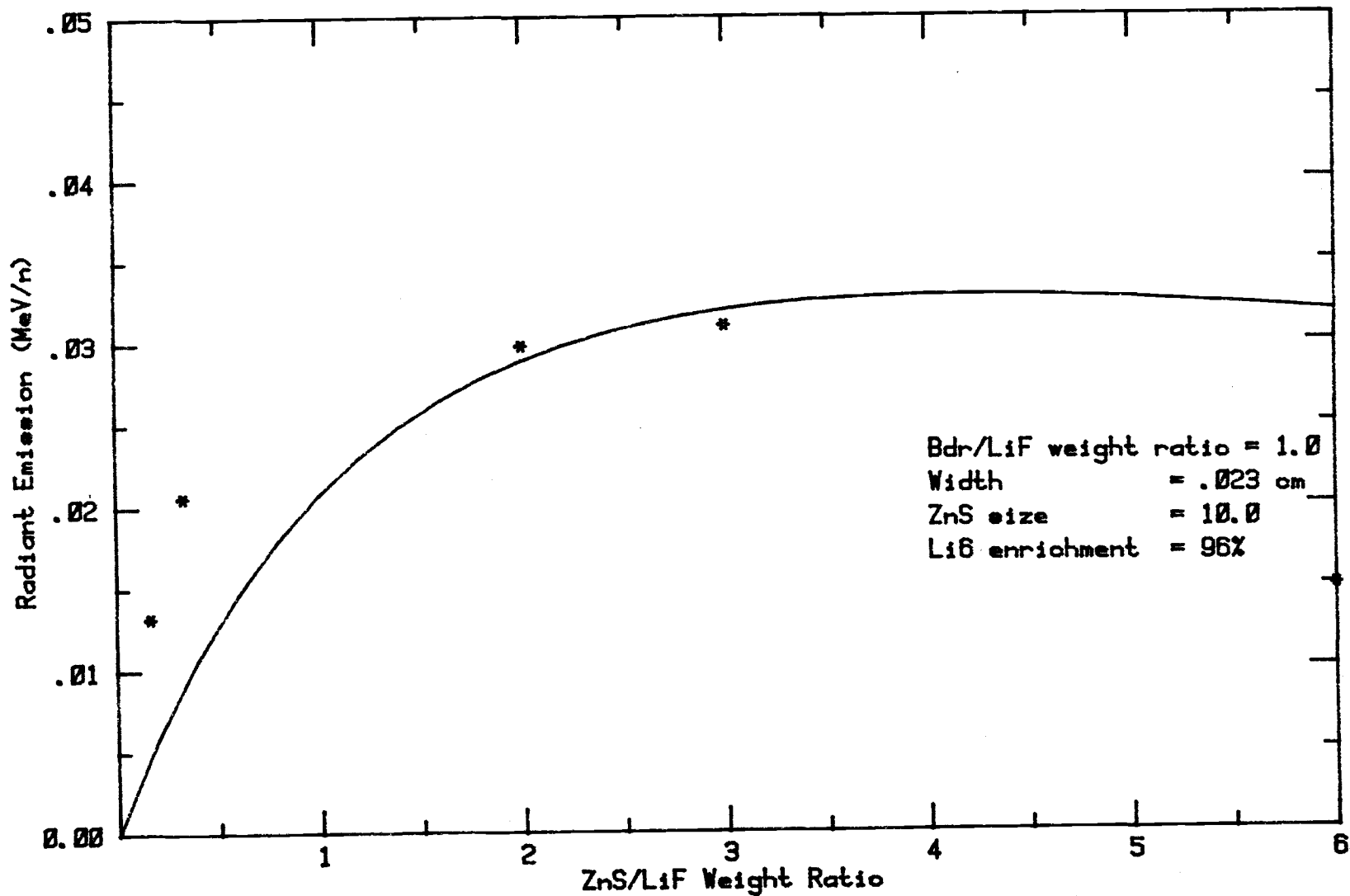


Fig. 4.6: Comparison of scaled polyethylene scintillator absolute efficiency predictions to measurements.

program with regard to scintillator width alone. Tojo and Nakajima have measured optimum efficiency in terms of width for eight varied material concentration samples of LiF-ZnS scintillators with polyethylene binder (90). Since scintillator concentration was held constant during the experiment, the shape of the efficiency-width characteristic curve is dependent only upon the transmission properties of the scintillator (i.e. neutron and photon transmission). Equations 4.4 and 4.5 of the model therefore should determine shape and peak of these curves. Comparisons in relative amplitude of efficiency by width between the model and the published data of Tojo and Nakajima has shown even less agreement than Figure 4.5 however demonstrates the 1:5:1 weight ratio of LiF, ZnS, and polyethylene promotes highest transmission of the mixtures under investigation. As an attempt to determine the LiF and ZnS light attenuation coefficients characteristic of their scintillators, each mixture attenuation coefficient was solved at the peak transmission thickness specified using equation 4.5 then regressed to the volume ratio of ZnS to LiF. The linear regression coefficients are then the individual attenuation coefficients of the materials. Although the data of Tojo and Nakajima now fit well to the model using these coefficients, their values were markedly different from those measured by Bossi and their use in the model

moved the optimum efficiency by weight of ZnS to LiF past three to seven. Clearly this model will represent both width and concentration behavior of efficiency with only moderate accuracy upon available data. Perhaps transmission is only approximated using an exponential model and instead behaves more parabolic as Tojo and Nakajima show empirically.

One final note may be mentioned regarding accuracy of the program. Spowart has shown the optimum materials concentration to be 3 to 4 parts by weight of ZnS to LiF and it has just been observed that Tojo and Nakajima found this optimum concentration to be 5 (91). As opposed to the conclusion presented by some earlier researchers who determined an optimum ratio of 2 from samples of LiF-ZnS-polyethylene scintillators, program results agree in Figures 4.4 to 4.6 the optimum occurs at 4 (92). Binder choice also appears have a significant influence upon the optimum concentration ratio since simulation of waterglass binder scintillators predict an optimum at 2 (Fig. 4.4) in agreement with Bossi's measurements (93). The flattened top of the efficiency-concentration curve that occurs in either case may help explain why some confusion exists where the optimum occurs.

So with what confidence can absolute scintillation efficiency be predicted for scintillators constructed at

OSU? Bossi has measured the relative efficiency of a number of OSU constructed scintillators by recording the density of films exposed in contact with each scintillator and has made similar measurements upon 0.18mm and 0.31mm sections of NE425 (a precursor of the NE426) (94). Comparisons with the 0.18mm NE425 and the 0.19mm OSU scintillator #57 show close agreement in efficiency. Based upon the computed and corrected absolute efficiency of a .18mm NE425 scintillator and the relative efficiency measurements by Bossi in reference to it, the absolute efficiency for each OSU scintillator measured may be determined. Figure 4.7 illustrates the correlation between Bossi's relative measurements and absolute efficiency calculations for a number of OSU scintillators constructed to various widths and concentrations and this information is repeated in Table 4.4 with radiometric units. The correlation coefficient between model and measured efficiencies exceeds 96% at a weight ratio below peak concentration however, as demonstrated earlier in Figure 4.6, accuracy of calculations become very poor following this peak.

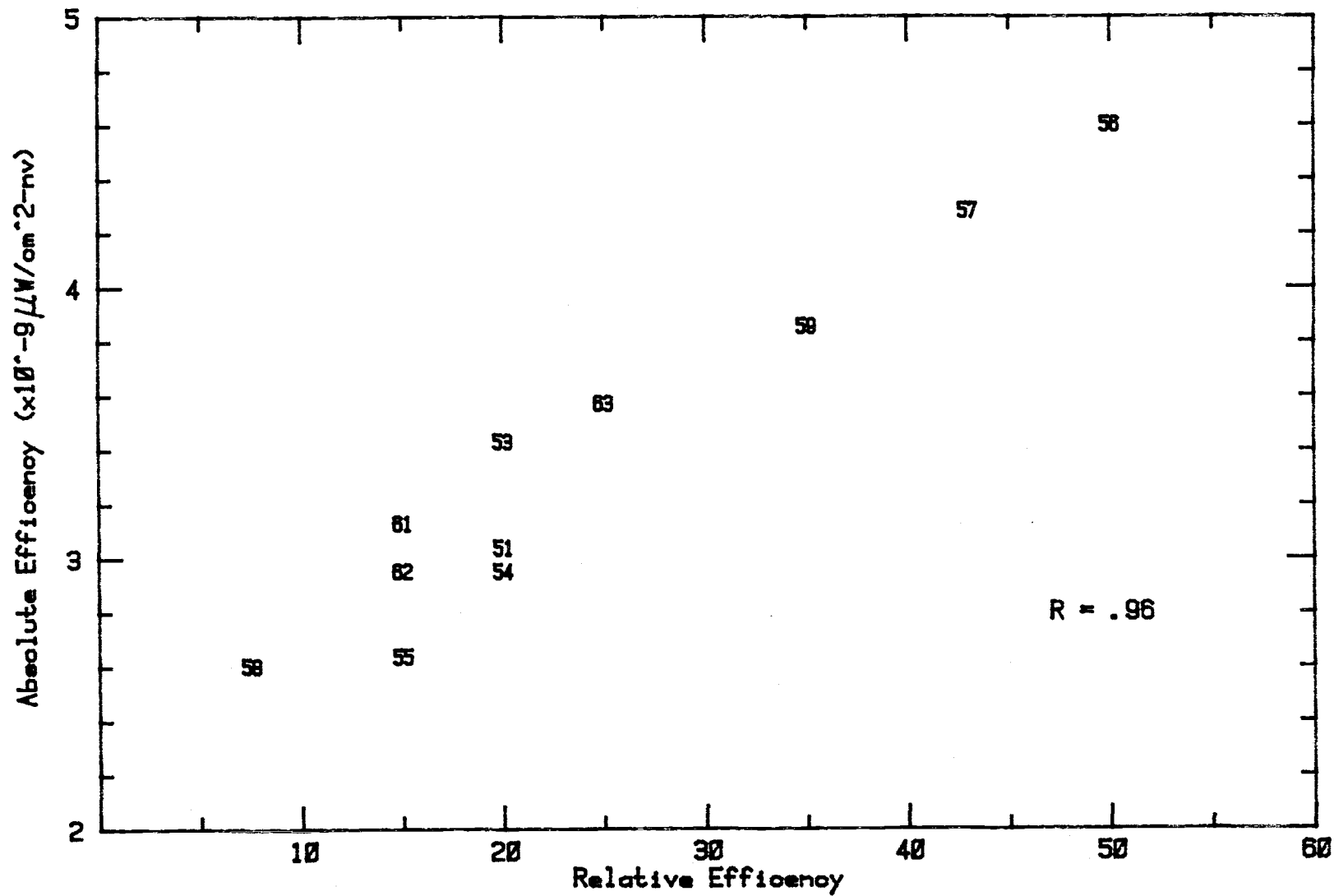


Fig. 4.7: Correlation of measured relative and calculated absolute efficiency of OSU scintillators.

Table 4.4: Absolute efficiency of OSU scintillators.

OSU#	Width mm	ZnS/LiF weight ratio	Efficiency		
			Relative	Absolute MeV/n $\mu\text{W}/\text{cm}^2\text{-nv}$ ($\times 10^{-9}$)	
55	.13	1/2	15	.0165	2.64
53	.13	1/1	20	.0214	3.43
58	.08	2/1	7.5	.0162	2.60
52	.10	2/1	20	.0190	3.04
51	.10	2/1	20	.0190	3.04
59	.15	2/1	35	.0241	3.85
57	.19	2/1	43	.0267	4.28
56	.24	2/1	50	.0287	4.60
54	.13	4/1	20	.0184	2.95
63	.13	2/1	25	.0223	3.57
61	.12	3/1	15	.0195	3.13
62	.13	4/1	15	.0184	2.95

4.5 SCINTILLATOR-INTENSIFIER COUPLING

Due to the irregular, rough shape of microcrystalline particles dispersed in granular scintillators and a low absorption to their scintillations, typically 90% of internally generated photons scatter within until escaping diffusely from the screen (95). The first advantage of granular scintillators for efficient optical coupling lies in this internal scattering. Unlike glass scintillators, the scintillator-detector interface quality is insensitive to surfaces of dissimilar refractive index since there is no mechanism similar to total internal reflection for granular scintillators and the bulk of the radiation which normally remains within the screen by total internal reflection until absorbed, is scattered out of the scintillator. At the point of excitation or a region on the scintillator face so small as to be considered a point source, the radiant intensity well approximates the cosine distribution characteristic of ideal diffusing sources known as Lambertian. An optical fiber with a numerical aperture of unity or greater will collect the entire amount of light emitted by a Lambertian source, provided Fresnel reflections at the fiber end-faces and its absorption losses are negligible (96). Since numerical apertures of 1.0 can readily be achieved in

optical fibers, the use of the comparably poor light collection ability of a lens system is to be discouraged. ITT manufacturing data claims its intensifiers use fiber optic faceplates that have a numerical aperture of unity and therefore the intensifier in use has the best available light collection efficiency and the entire radiant excitation of the scintillator is transferred to the intensifier input.

Optical coupling from the scintillator to the image intensifier must be intimate to promote as much of the internally emitted light to be collected as possible. Although transmission from the scintillator interface is not as sensitive to contact as glass scintillators, a restriction is placed upon resolution if contact is poor due to the extremely short depth of focus characteristic of high aperture fiber optics.

4.6 INTENSIFIER GAIN, g_4

The radiant gain characteristic of the image intensifier is given by

$$g_4 = \frac{g_m \alpha(3,4)}{\pi m_4^2} \quad 4.7$$

where

g_4 = intensifier radiant gain.

$\alpha(3,4)$ = spectral matching factor for scintillator-photocathode interface.

g_m = maximum radiant gain of intensifier at wavelength of peak response.

m_4 = differential magnification ratio of image tube (97).

The factor m_4 is introduced into equation 4.7 to account for the image magnification introduced during intensification. Both differential magnification and radiant gain has been measured by ITT engineers for our image tube and their most recent measurements are presented below:

$$m_4 = 0.92$$

$$g_m = 332 \text{ W/W}$$

The radiant output of the intensifier, however, is not always g_m times greater than the input irradiance; once the phosphor screen approaches saturation at a luminance of 100 foot-candela no further gain is possible

and, in fact, gain will decrease as input irradiance continues to increase past an illuminance of 0.2 fcd. Fortunately, this gain restriction does not seem to apply for very short but intense light sources and information will be provided later to verify this. Based on the rate of descent of photographic density following a pulse peak however, intensifier gain has been observed to reduce rapidly after a pulse, particularly if the subject has high transmission. The ABC feature of this intensifier does seem to limit its operation during a pulsed input, the delay and magnitude of its shutdown determined by the duration and intensity of the source. But even without a subject, the intensifier will not shutdown until following a reactor flux peak.

4.7 OPTICAL ATTENUATION, g_5

The light collection efficiency of the camera objective and internal prisms to film is given by

$$g_5 = \frac{\pi\alpha(4,5)CX\cos^4\beta}{4A^2}$$

where

C = camera flare correction factor (1.03 for a typical camera lens).

X = vignetting factor for lens barrel (approx. 1.0).

β = angle off lens axis of intensifier phosphor screen.

$\alpha(4,5)$ = transmission factor of lens to characteristic radiation of phosphor screen (98).

The above equation applies in general to any lens-source configuration however may be considerably simplified since the introduction of some variables is not expected to improve accuracy of the overall electrographic analysis. This includes the off axis lens angle, β , since for most applications the intensifier need not be tilted from horizontal. The focal plane irradiance equation of reduced complexity is

$$g_5 = \frac{\pi\alpha(4,5)}{4A^2}$$

4.8

The effective aperture of the camera optics depends not

only upon lens f-stop but upon image magnification and the natural aperture of the Hycam rotating prism by

$$A = \begin{cases} A_{\text{lens}} & A_{\text{lens}} > A_{\text{inherent}} \\ A_{\text{inherent}} & A_{\text{lens}} \leq A_{\text{inherent}} \end{cases}$$

and

$$A_{\text{lens}} = (1 + m_5)A$$

$$A_{\text{inherent}} = f/3.3$$

$$m_5 = \text{lens magnification}$$

$$A = \text{minimum lens f-stop.}$$

Although a suitable high efficiency lens may be mounted on the Hycam with an f-stop much lower than 3.3, the natural aperture of the high speed camera cannot be reduced and therefore imposes a limit upon optical image transfer. It is this restriction of the lens system which will allow no more than 2% of the light emitted by the phosphor to be collected, and represents a staggering loss not uncommon, however, to most lens transmission systems.

4.8 FILM TRANSFER FUNCTION

Photographic density is defined as

$$D = - \log(\tau/\tau_{\text{base}})$$

where τ/τ_{base} represents the fractional optical transmittance of the developed film. Density is a function of both processing time and exposure and this relationship is often represented graphically.

Manufacturers provide characteristic curves of their films but most curves are valid only for illuminants such as tungsten or daylight under specified developer and processing conditions. Such curves are useless to determine film exposure-density characteristics when a P11 phosphor is used or when the film is processed to other conditions. For an approximation, two conversion factors can scale exposure units from most existing characteristic curves for irradiation by the P11 phosphor:

$$\log H(\text{P11,panchro}) (\text{ergs/cm}^2) = \log H(\text{tungsten,panchro}) (\text{mcs}) + 1.34$$

$$\log H(\text{P11,panchro}) (\text{ergs/cm}^2) = \log H(\text{daylight,panchro}) (\text{mcs}) + .625$$

More information is given in Appendix A regarding this transformation.

Characteristic curves drawn from Kodak data sheets for both 2475 and 2484 RAR films are shown in Figure 4.8

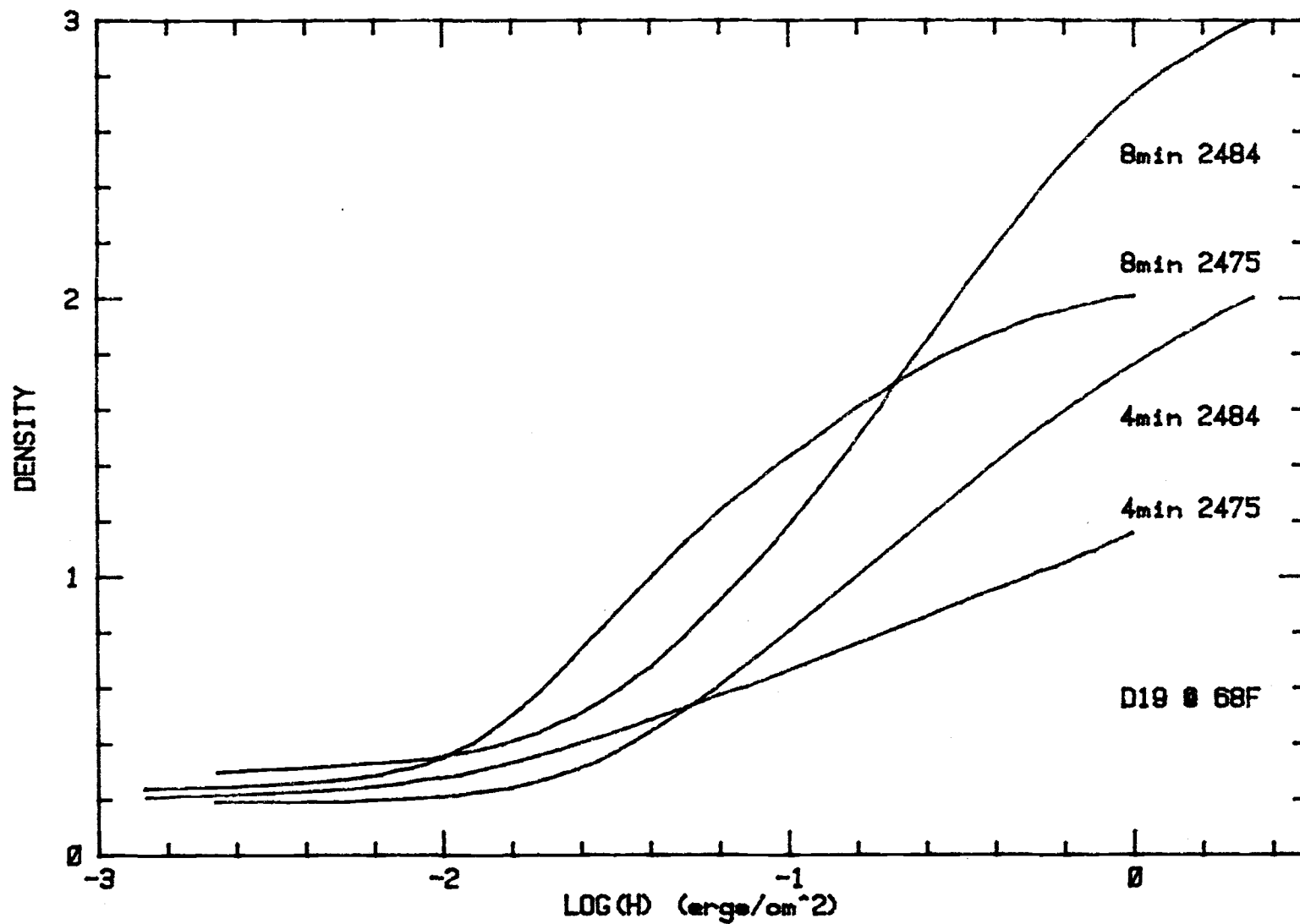


Fig. 4.8: Characteristic curves for 2484 and 2475 films for P11 source.

for processing conditions equivalent to those used for high speed neutron radiography at OSU. The 2484 film curves have been modified using the conversion above from tungsten illuminant data; the 2475 curves fortunately required no conversion.

Although less information is available regarding film sensitivity for a range of exposures, the film manufacturer also provides a single figure known as the CRT exposure index which represents the reciprocal of radiant exposure necessary by a phosphor to produce a given density above fog on a film processed to certain conditions. The CRT exposure index is normally provided for exposure by some phosphors including the P11 and is treated like an ASA figure in that it is used for film sensitivity comparisons. Listings of the CRT exposure index for Kodak films useful for high speed neutron radiography are given in Table 4.5. This figure is the least a manufacturer will provide upon phosphor sensitivity of its high speed films but an approximation is possible to obtain the exposure required to produce a net density of 1.0 or 0.1 if the index is specified for one such density

$$H(D_{\text{net}}=1.0) = 20H(D_{\text{net}}=0.1).$$

There is some risk interpreting spectrally modified characteristic curves since film gamma may not be equivalent between the phosphor to the reference light

Table 4.5: P11 CRT exposure index for five high speed films.

Film	CRT exposure index @ net density			Processing
	0.1	1.0	2.0	
2484	320 400			D19 4min @ 20C (68F) D19 1min @ 35C (95F)
2485		16,000 10,000 6,400		MX642-1 4min @ 32C (90F) MX642-1 2min @ 37C (98F) D19 12min @ 24C (75F)
2475	400	20		DK50 8min @ 20C (68F)
2496	40			D19 1min @ 35C (95F)
2498	64	8	1.6	D19 1.5min @ 35C (95F)

source. Experimental construction of characteristic curves for the P11 phosphor is preferred, but the absolute measurements of exposure required are difficult to perform. It was necessary to proceed, therefore, with the film sensitivity data available.

The density-exposure characteristic of a photographic emulsion may be defined in equation form as the product of the common log of exposure and film gamma:

$$D = \gamma \log(H(5,6))$$

where

D = photographic density

γ = film differential gain or slope of the characteristic curve for specified exposure and processing conditions $((\text{ergs/cm}^2)^{-1})$

$H(5,6)$ = film radiant exposure for focal plane irradiance and film spectral matching (ergs/cm^2) .

Exposure, in turn, is the time integral of irradiance in the focal plane but when the exposure time is short enough such that the image intensity only varies spacially during exposure this is

$$H(5,6) = E_5 t \quad 4.9$$

where

E_5 = focal plane irradiance (ergs/s-cm^2)

= $I_1 G$

t = exposure time (s).

Care must be taken that the characteristic curves used

for the film are appropriate for the light source. Figure 4.7 is applicable for P11 sources and panchromatic films however if different combinations of sources or films are used a spectral matching factor must be included in Eq. 4.9 (see Appendix A).

Equation 4.9 is a statement of the reciprocity law which is based on the premise that the response of a photographic film to exposure is determined by the total amount of light energy absorbed and is independent of the rate of absorption. The reciprocity law, however, does not hold for photographic materials when extremely long or short exposures are made and so increased developing time or exposure is necessary to compensate for lower film response. Fortunately, most black-and-white emulsions used in high speed photography show minimum reciprocity law failure and the majority of such deviation occurs for long exposure times.

Film developing probably accounts for the widest variation of any variable in the entire photographic instrumentation system unless standardized procedures of processing are adopted and followed. Developing time, temperature, and chemical activity can alter film performance dramatically and often an increase in one or all of these three variables is used to increase film response to low exposures. A "pushed" film response is normally achieved at the expense of greater background

fog and granularity however. Processing variations should be kept to a minimum by adhering to the manufacturers recommendations on replenishment and replacement of chemical solutions and developer temperature should be controlled to within 0.5°F of the value adopted as the laboratory standard to ensure uniform results (99).

4.9 SYSTEM IMAGE TRANSFER

4.9.1 Analytic

Table 4.6 summarizes the radiography system transfer function and its constituent terms. The final transfer expression deviates some from the generalized system gain equation (Eq. 3.2). First, since the spectral matching factor obviously does not apply for neutron transport this factor is unity for collimator-object-scintillator transmission. Second, the scintillator absolute efficiency, M_e/I_2 , is used instead of the dimensionless form g_3 . The product of system transfer and neutron intensity incident at the subject site represents the equivalent radiant flux available for exposure in the focal plane. Exposure and density predictions can then follow using the film transfer function.

4.9.2 Measurement

To verify the system image transfer model just discussed, data was analyzed from some high speed motion neutron radiographs. Radiographs using combinations of exposure times, lens apertures, films, processing times, and subject thicknesses were collected and the important variables of these radiography runs are summarized in

Table 4.6: System transfer function and components.

Component	Equation	Parameters
Exposure:		
1. Collimator	$I_1 = (I_0/P_0)P$	$I_0/P_0 = 145 \times 10^6$ nv/MW
2. Object	g_2	Appendix D Fe width (cm) g_2 2.35 .203 1.00 .538 0. 1.000
3. Scintillator	M_e/I_2	Table 4.4 Appendix B
4. Intensifier	$g_4 = \frac{g_m \alpha(3,4)}{\pi m_4^2}$	g_m 332 m_4 .92 $a(P11, S20)$.877 $g_4 = 109$ (W/str ⁻¹)/W
5. Optics	$g_5 = \frac{\pi \alpha(4,5)}{4A^2}$	A 3.3 minimum $a(P11, 1.5")$.729 $g_5 = .0526$
Response:		
6. Film	$D = \gamma \log(H)$	Figure 4.8

Table 4.6. In most cases, a steel slab the equivalent of 2.35cm thick was radiographed, however radiography of a 1cm steel slab and without a subject were tried.

To determine the exposure these films received required a combination of measurements and calculations. First, given the measured peak power of the reactor, the reactor power was computed for each frame interval from the peak using the computer solution of the Fuch-Nordheim equations (Appendix C). The flux at the subject site during every frame could then be calculated using equation 4.1. Next the neutron attenuation by the subject was calculated using a Monte Carlo solution (Appendix D) so the product of neutron flux, subject attenuation, scintillator efficiency, intensifier gain, and optical transfer would determine irradiation of the film. Finally, the location on the film where the peak flux occurred was identified by either measurement for the maximum density or locating its position from the event strobe flash or the mark left by the pulse peak detector circuit. Painstaking manual densitometry was performed on each frame occurring about it using a Macbeth 200 densitometer with a 1mm aperture to provide measurements of film response.

Curves have been constructed from density measurements upon each radiography run in an attempt to duplicate the manufacturer's characteristic curve upon

the film. The density-exposure information has been plotted in Figures 4.9 to 4.11 for the 2484 and 2475 films and the manufacturer's curve has been added for comparison. Each run is referenced by the OSTR pulse identification number and important information of these films are given in Table 4.7. Measured curves of each film have noise superimposed upon them due to irregularities in densitometer positioning or image density from frame to frame. Their correlation is poor but remarkable considering the number of approximations and assumptions made to this time upon system performance. Figure 4.9 compares measured and published data upon 2484 films developed for 8min of 2.35 and 1cm steel objects and Figures 4.10 and 4.11 illustrate 2484 4min and 2475 4 and 8min curves respectfully, all processed at 68⁰F in D19. The best agreement seems to occur for the latter two graphs. In Figure 4.9 the majority of measurements appear to be shifted right from the reference curve implying measured P11 sensitivity of 8min developed 2484 films may be less than that assumed. Most striking is the difference in location of radiographs for the 1cm object; about a full decade of additional exposure seems necessary to obtain densities similar to films of the 2.35cm subject. Such a deviation is beyond reasonable experimental error and has been encountered with films reviewed later.

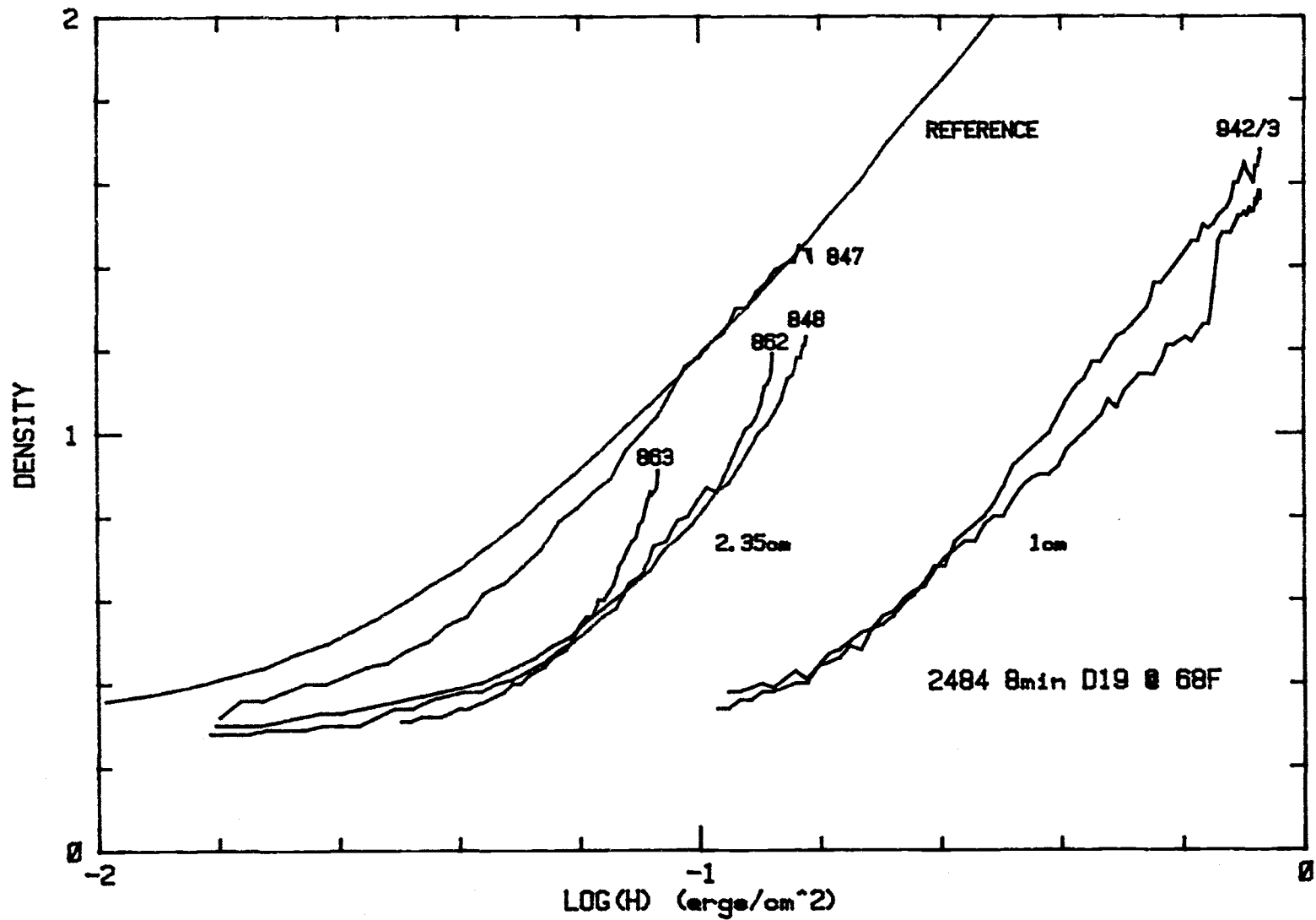


Fig. 4.9: System derived and reference P11 characteristic curves for 2484 film (8min).

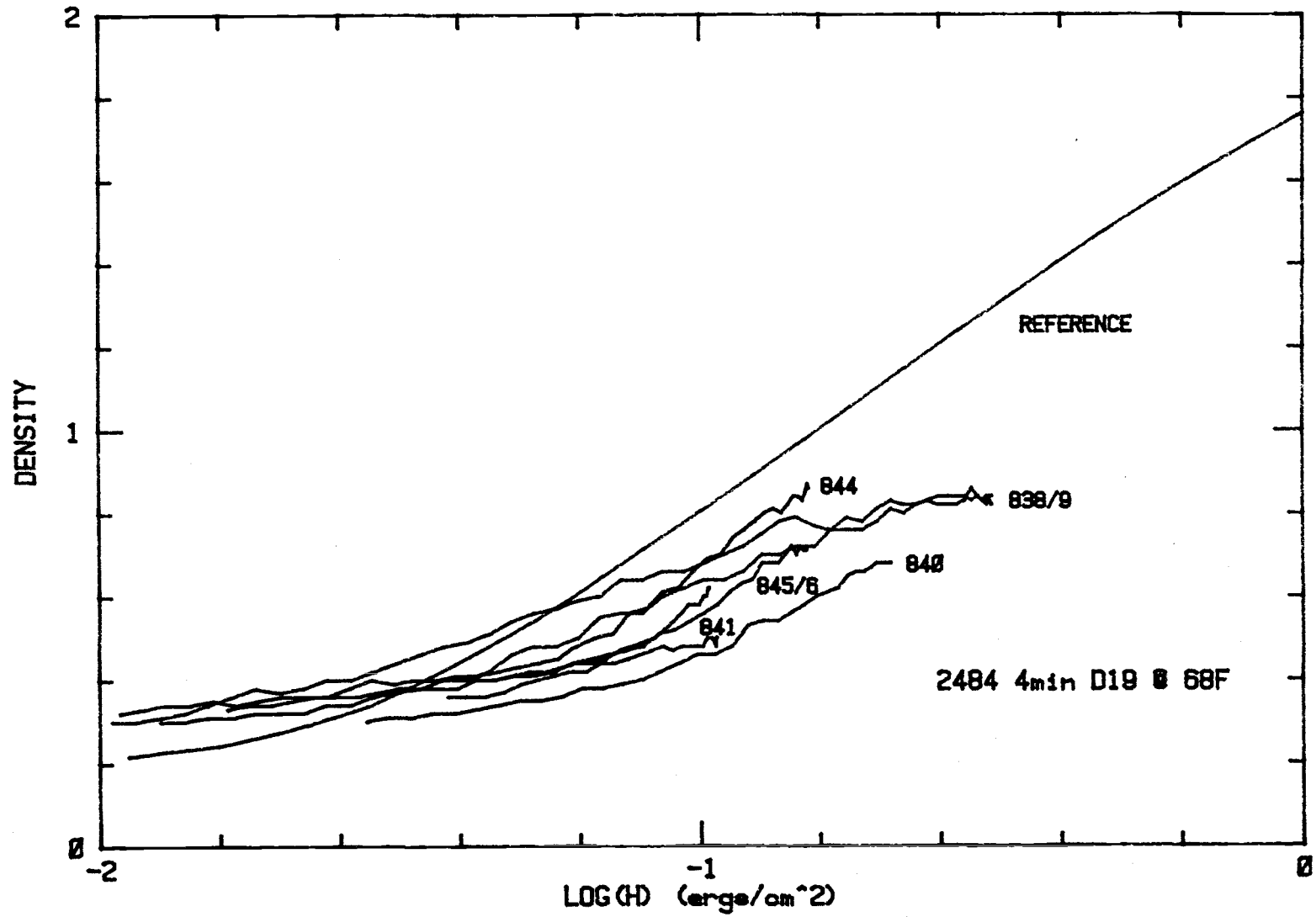


Fig. 4.10: System derived and reference P11 characteristic curves for 2484 film (4min).

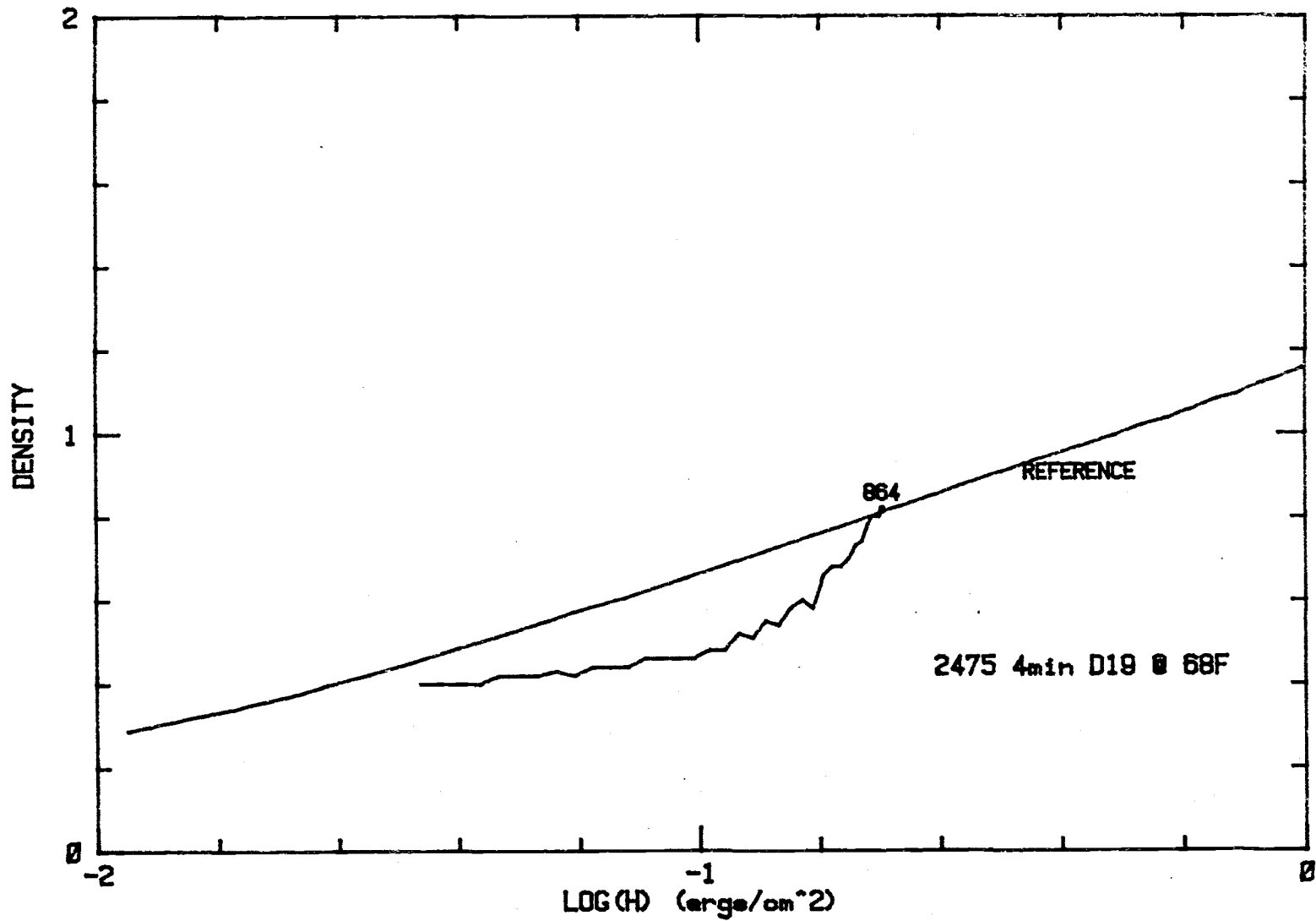


Fig. 4.11: System derived and reference P11 characteristic curves for 2475 film.

Table 4.7: Background on radiographs analyzed.

Pulse	Height (MW)	Film	Subject (cm Fe)	t ($10^{-6}s$)	A	Scintil- lator
838	3060	2484 4min	2.35	20	3.3	57
839	3060	2484 4min	2.35	20	3.3	57
840	3060	2484 4min	2.35	20	4.0	57
841	3060	2484 4min	2.35	20	5.6	57
844	3040	2484 4min	2.35	10	3.3	57
845	3020	2484 4min	2.35	10	3.3	57
846	3040	2484 4min	2.35	10	4.0	57
847	3140	2484 8min	2.35	9.8	3.3	57
848	3050	2484 8min	2.35	9.8	3.3	57
862	2900	2484 8min	2.35	9.1	3.3	57
863	2920	2484 8min	2.35	5.9	3.3	57
864	3000	2475 4min	2.35	10	3.3	57
942	2940	2484 8min	1.0	22	3.3	57
943	2940	2484 8min	1.0	22	3.3	57
1010	2880	2475 8min	0.	49	3.3	56
1012	2880	2475 8min	0.	46	3.3	NE426 (.18mm)

Blocked listings indicate runs occur on same film roll.

An alternate method for evaluating this same data for the accuracy of the system model has lead to some interesting discoveries. Instead of film sensitometric evaluation, a figure for intensifier gain as a function of input irradiance was prepared in hope these figures would indicate how the intensifier ABC behaved during a pulse. This method calculated forward from reactor power levels for the intensifier input irradiance (E_{e4}) by

$$E_{e4} = I_{19392}$$

and used a backward calculation for intensifier output radiance (L_{e4})

$$L_{e4} = H_6 / (tg_5).$$

from focal plane exposure determined by interpolation from the manufacturer's characteristic curves digitized using an HP85 computer and HP7225A plotter with pen sight and the recorded frame densities. The ratio of intensifier output radiance to its input irradiance is then its gain

$$g_4 = L_{e4} / E_{e4}.$$

Given the best data available upon film performance and neutron intensity following object attenuation Figures 4.12 to 4.14 should approximate a single transfer characteristic of the intensifier regardless of subject or film. It is quite obvious, however, few of these curves agree in position but most show a general linear trend of such a gradual slope it appears that for pulsed

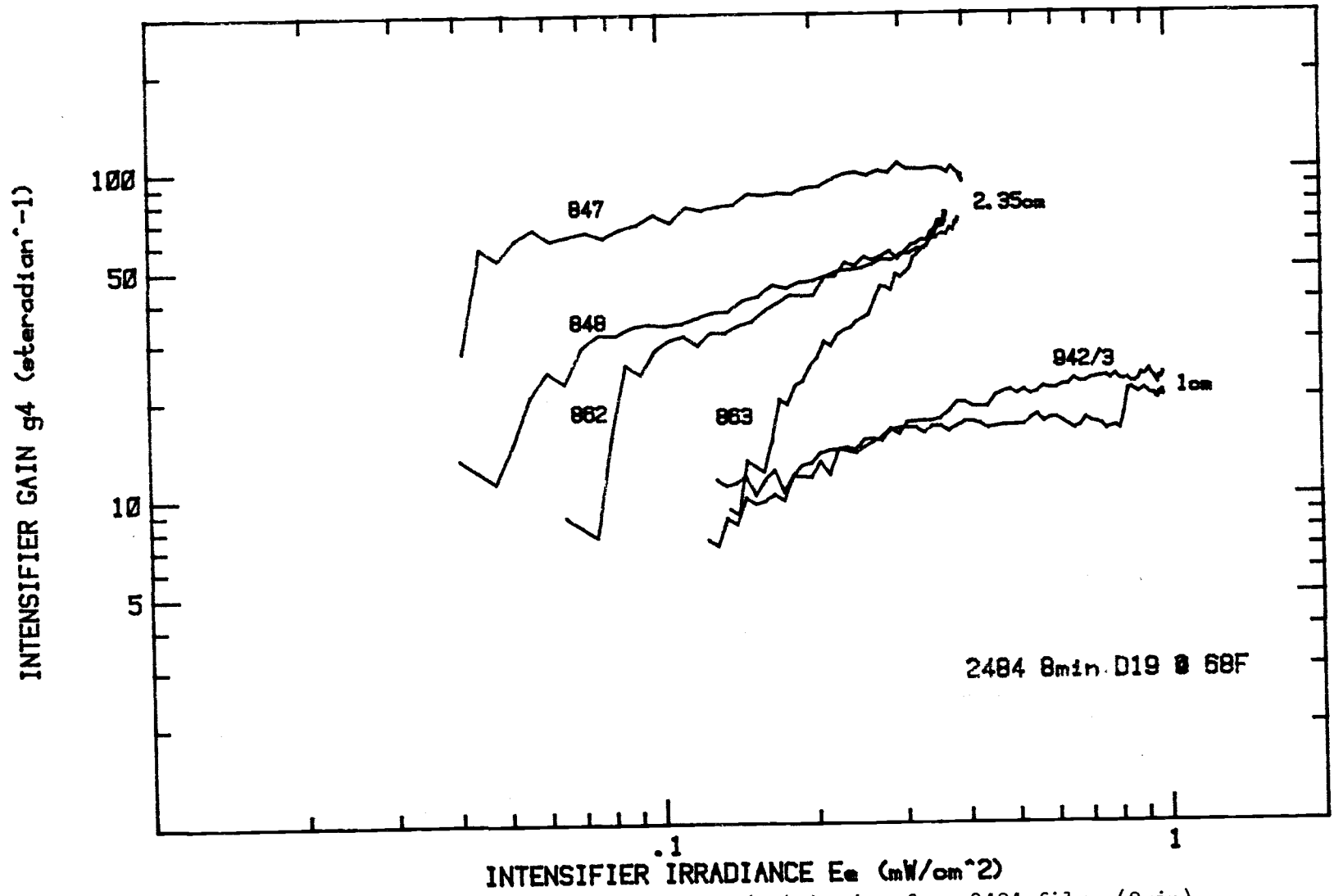


Fig. 4.12: System derived intensifier radiant gain behavior from 2484 films (8min).

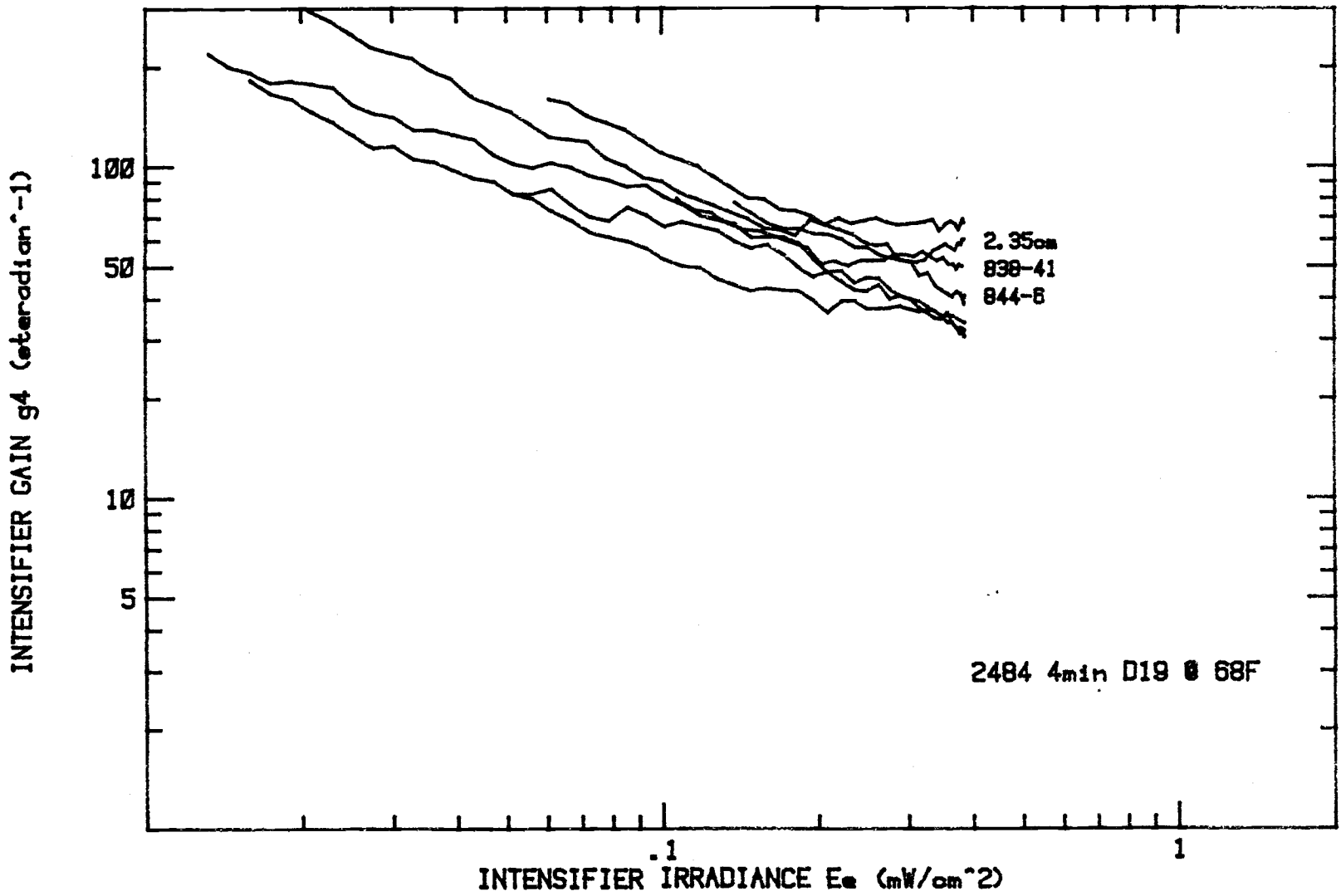


Fig. 4.13: System derived intensifier radiant gain behavior from 2484 films (4min).

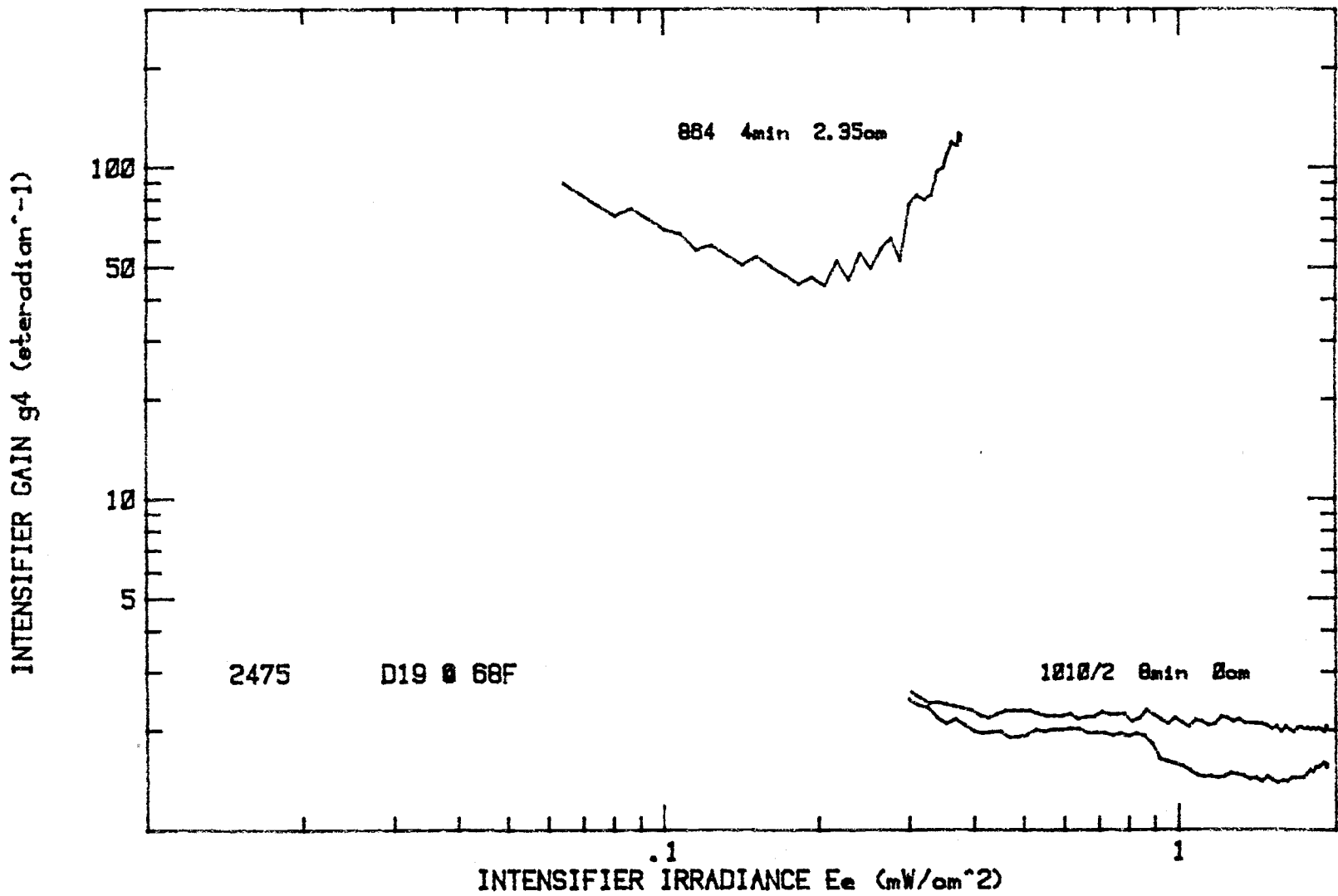


Fig. 4.14: System derived intensifier radiant gain behavior from 2475 films.

input sources of the magnitude normally encountered with the high speed neutron radiography facility the intensifier gain is independent of irradiance level. If intensifier gain g_4 remains constant during radiography at the analytic value of $109 (W/cm^2\text{-steradian})/(W/cm^2)$ only a few of the curves shown narrowly approximate this level.

Although it would appear the position and shape of individual curves in Figures 4.12 to 4.14 are random, certain variables influence their behavior. If film characteristics or neutron flux were accurately predicted for each case, their effect would be eliminated from the figures; deviation from their expected performance has introduced errors in the curves. Table 4.8 attempts to summarize the sources of error, their effect upon the curves, and their magnitude. Film processing alters the behavior of the curves to a great extent. A deviation in processing times, temperatures, or developer activity can change background fog and film gamma from the reference characteristic curves of the film. Both fog and film gamma increase with developing time and temperature and, unaccounted, can shift curves vertically and increase their slope. Use of spectrally corrected characteristics of the 2484 film from tungsten source characteristic curves provided by the manufacturer is also questionable. The gamma to which the 4min 2484 films develop appears

Table 4.8: Contributions to error in
Figs. 4.12 to 4.14.

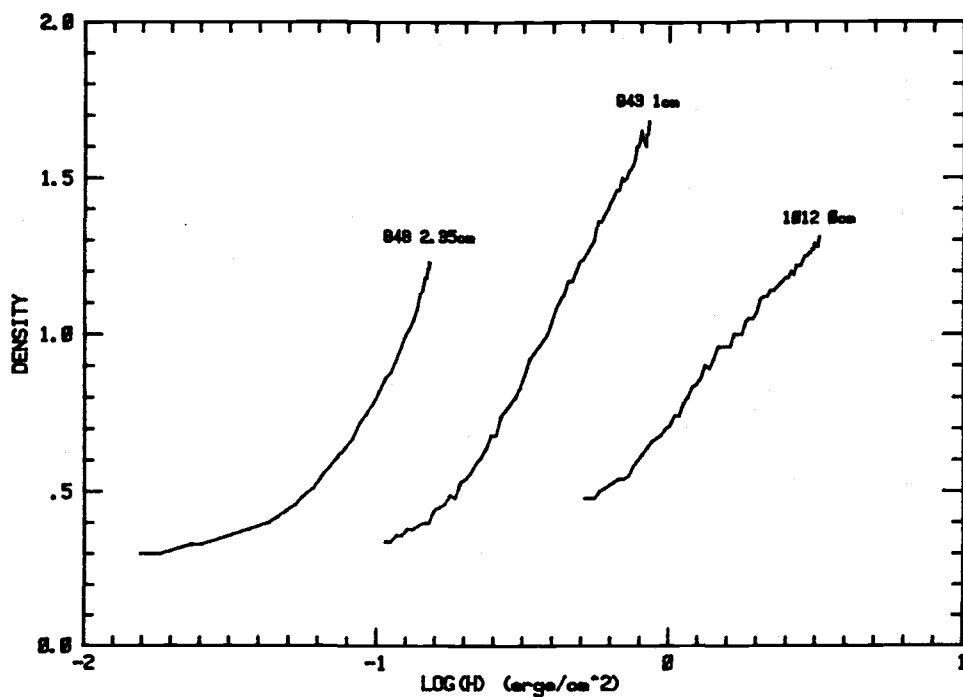
Effect	Reason
Vertical shift	Background fog due to processing/film irradiation. Densitometer position when reading films. Battery voltage (runs prior 847).
Slope	Actual film gamma different from reference.
Change of slope	Actual film characteristic curve shifted from reference. ABC circuit of intensifier (must be consistent to all curves).
Horizontal shift	Interpretation of peak flux position on film (+/- 20%). Subject attenuation different from calculations.

inaccurate for this reason due to the negative slope of their g_4 gain curves (Fig. 4.12) in comparison to the no slope behavior of the 2475 films for which the P11 source characteristic curves are known (Fig. 4.14). Eight minute developing times of the 2484 films however appear to verify a gamma equivalent to the spectral approximation. Finally, the time between completion of some of these films is as much as two years and processing techniques have improved since then; more consistent results would be expected now if the chance came to repeat the experiment.

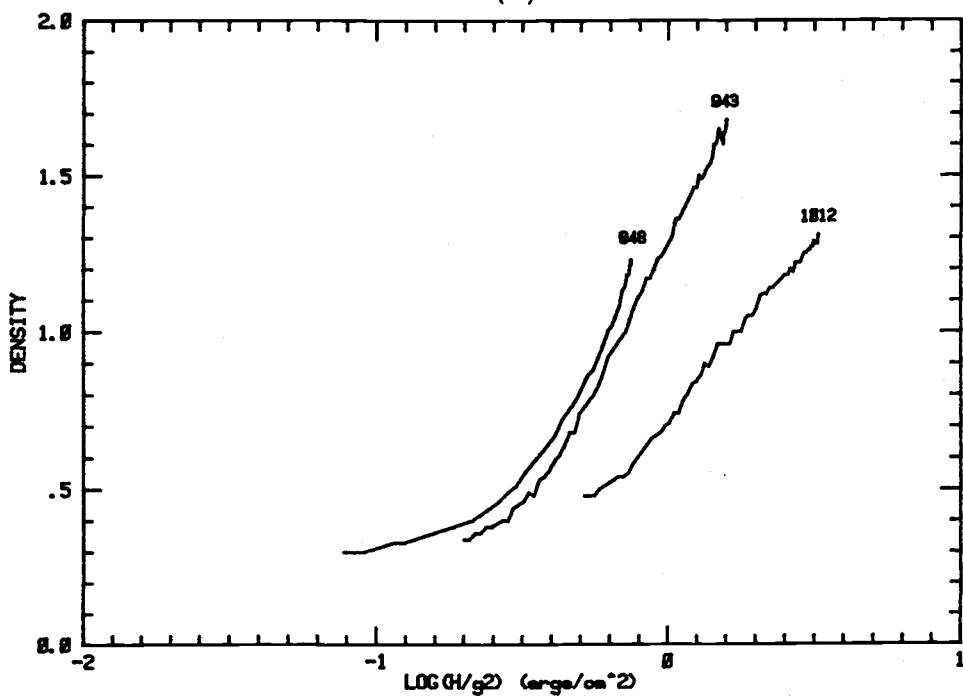
A relatively minor error may occur in each curve due to failure to locate the exact frame where the peak flux occurred. One or a combination of the methods reviewed previously were used to determine the frame of peak flux and since reactor power varies little about the peak it is estimated an error of only 20% would shift the curves left or right.

Some interesting behavior in these same figures has been observed upon not only individual curves but the relationship between groups of curves. Systematic deviations occur between radiography runs processed on the same film roll, runs on films processed for an equal time, and runs recorded on the same subject and tend to shift the position or slope of each curve group. First, most runs processed on one film roll of one subject and,

of course, processed for the same time have the least deviation in behavior between themselves regardless of lens aperture and these curves have been grouped appropriately in three figures to show this (Figs. 4.12 to 4.14). The slope relationship between films developed to varying times has already been noted but the position of each curve group with regard to subject thickness has not. One would expect the gain curve constructed from each run would coincide within some reasonable error for equal irradiance values. This is not the case and is the most obvious discrepancy which prevents a single gain curve for the intensifier to be modeled. Figure 4.15a helps demonstrate the existing relationship between film exposure and subject thickness for three films. Surprisingly, the radiographs of the 2.35, 1, and 0cm steel slab appear to have received equal exposure and the exposure correction when preparing this graph has shifted the curves of lowest thickness right. When this same information is plotted independent of object attenuation (g_2) the curves almost coincide (Fig. 4.15b). The imaging devices operate normally for each of these radiographs since exposure still varies linearly with neutron flux levels, and so, incredibly, the exposure level seems independent of subject thickness for these films. It is known, however, background fog increases with flux magnitude in the area where the reactor pulse



(a)



(b)

Fig. 4.15: Effect of object attenuation on reconstructing film performance. (a) Exposure with attenuation. (b) Exposure without attenuation.

occurs on all 16mm films and this background was not subtracted from densitometer readings. Its effect should not dominate the exposure recorded however. Additional radiography runs performed under more controlled circumstances are necessary to show a dependency exists upon subject size and exposure.

V. IMAGE RESOLUTION

5.1 INTRODUCTION

Obviously, a component good at only presenting amplitude variations is useless for interpretation since consideration in spacial information must be given as well. The degree static resolution, object velocity, and noise reduce resolution must be justified for evaluation and selection of optimum components. However a means common to each component is necessary to determine and rank ability to transmit information.

Image quality analysis in radiography systems traditionally proceeds using a technique to determine image 'unsharpness'--the transition distance between the image edge spread signal recorded from a radiographically dense knife-edge object (Fig. 5.1). Although this single figure of merit has served well in comparing systems, it is of limited use in system design since it cannot be applied in any logical sense for determining the combined effects of various components. The unsharpness technique does not always give good correlation with visual image assessment just as resolving power evaluation proves inadequate in optical systems design due to visual acuity and test object variation in contrast and geometry. Because single figure descriptions of systems and

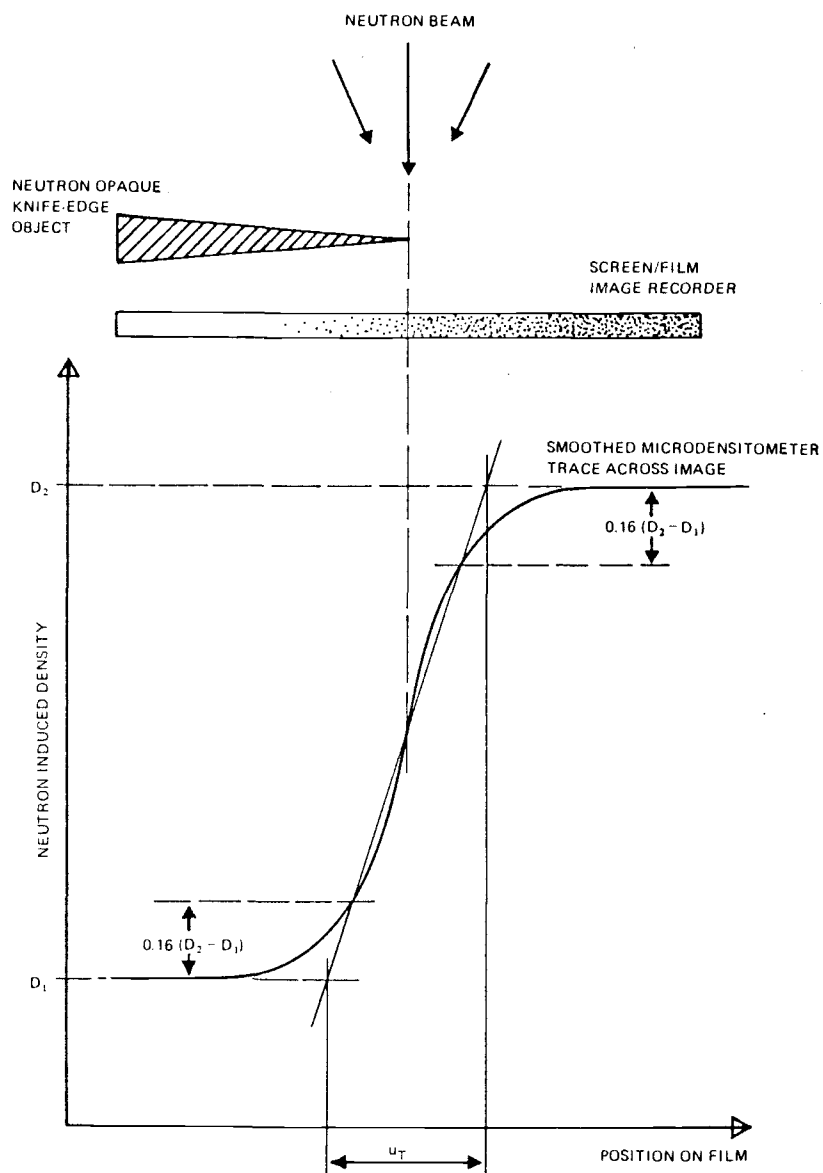


Fig. 5.1: Measurement of unsharpness from the image spread signal (100).

components resolution are attractive, it is unlikely unsharpness evaluation will be completely superseded since its measurement is so straight forward. In recent years, however, radiographers have increasingly favored a more complete method of describing resolving power using the modulation transfer function.

The choice of image quality analysis of the OSU high speed neutron radiography system by modulation transfer functions not only more adequately represents the expected resolution over a range of spacial frequencies, but is more appropriate since MTF data already exists from manufacturers of optical components and films. The image quality of collimator, subject neutron transport, and scintillator need only be determined to complete the resolution analysis.

5.2 MTF MEASUREMENT

With regard to measuring the MTF of a radiography component with neutrons, the most important item is the test object and a practical object necessarily involves certain compromises. Ideally, the MTF could be plotted directly from the image-object modulation provided by a sinusoidal test object of large frequency range. Since such an input signal is composed of one Fourier component, the measured modulation represents device response to a single spacial frequency. The difficulties of constructing such a test object for radiography has limited its use however. Instead, a method devised to calculate the MTF using a knife-edge of high attenuation material such as gadolinium foil has been most popular. The technique resembles all unsharpness measurements in so far as the signal amplitude of an edge spread image distribution is analyzed. This edge spread function, when differentiated, will give the line spread function. Equation 3.3 may then be used to determine the MTF. Numerical integration and differentiation normally must operate upon edge spread function data in the presence of significant levels of granularity and so the accuracy of the MTF obtained is limited, but fortunately the edge spread technique has been found to have as good or better precision for MTF analysis than that obtained with

sinusoidal test objects (101).

5.3 STATIC RESOLUTION

5.3.1 Collimation resolution

Since the physical dimensions of the collimator limit the magnitude of its L/D ratio, some false image shadowing occurs upon the detector. Figure 5.2 demonstrates geometric unsharpness U_g occurs on the detector theoretically in the proportion

$$U_g = d/(L/D) \quad 5.1$$

where

L = distance from the source to the object detail under evaluation (about 424cm)

D = collimator opening width

d = detail to detector distance (mm).

The L/D ratio has been determined from the subject position by unsharpness measurements and is 30 in the horizontal direction and 41 vertically. Unless there is a reason to evaluate unsharpness specifically in either of these directions, the average of the two is adequate for calculations.

The MTF for the geometric resolution is

$$T_1(\nu) = \frac{\sin(\pi\nu U_g)}{\pi\nu U_g} = \text{sinc}(\nu U_g) \quad 5.2$$

where ν is the object spacial frequency (mm^{-1}) (102).

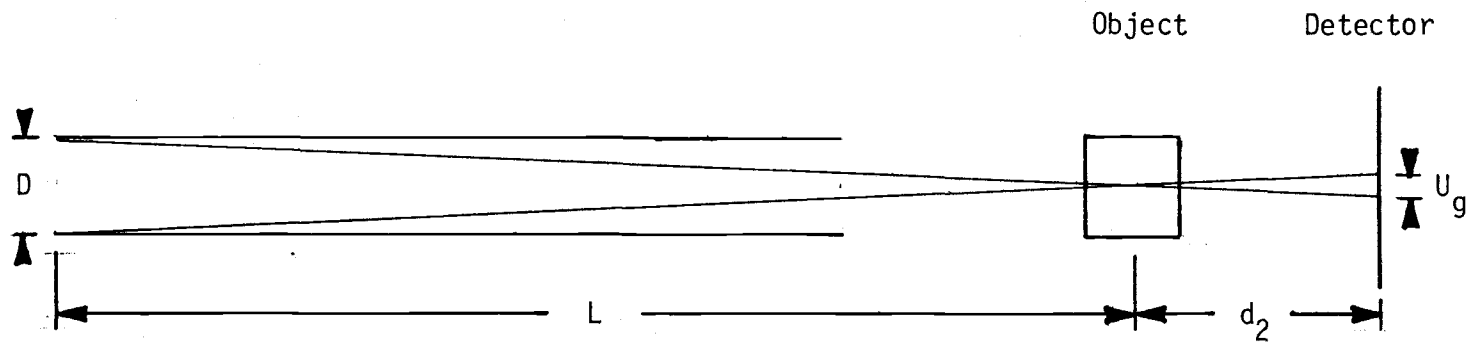


Fig. 5.2: Geometric unsharpness in collimation.

Because of scattering and other collimator deficiencies characteristic to its construction, the collimator apparent input width or effective focal spot size (EFS) is not equivalent with its physical width D (103). The EFS size can be determined by correlating Eq. 5.2 to its measured MTF then solving Eq. 5.1. The EFS size has not been obtained for the OSU facility, but obviously if the geometric MTF for the collimator were known experimentally there would be no need to use Eq. 5.2.

5.3.2 Object scattering resolution

Comparatively recently, image restoration methods in neutron radiography have shown promise and attempts to account for image spread due to neutron scatter within the subject have been made. Consider the material under evaluation as a slab of width a separated from the detection plane (e.g. scintillator) by distance b as shown in Figure 5.3. If a neutron flux impinges upon the subject at a point, neutrons may scatter within the material, emerge, cross gap b , then interact with the detection plane at distance r from the beam center. The neutron spread about the center detection point represents the degree of image spread expected. The MORSE-CG Monte Carlo code has been used to solve the

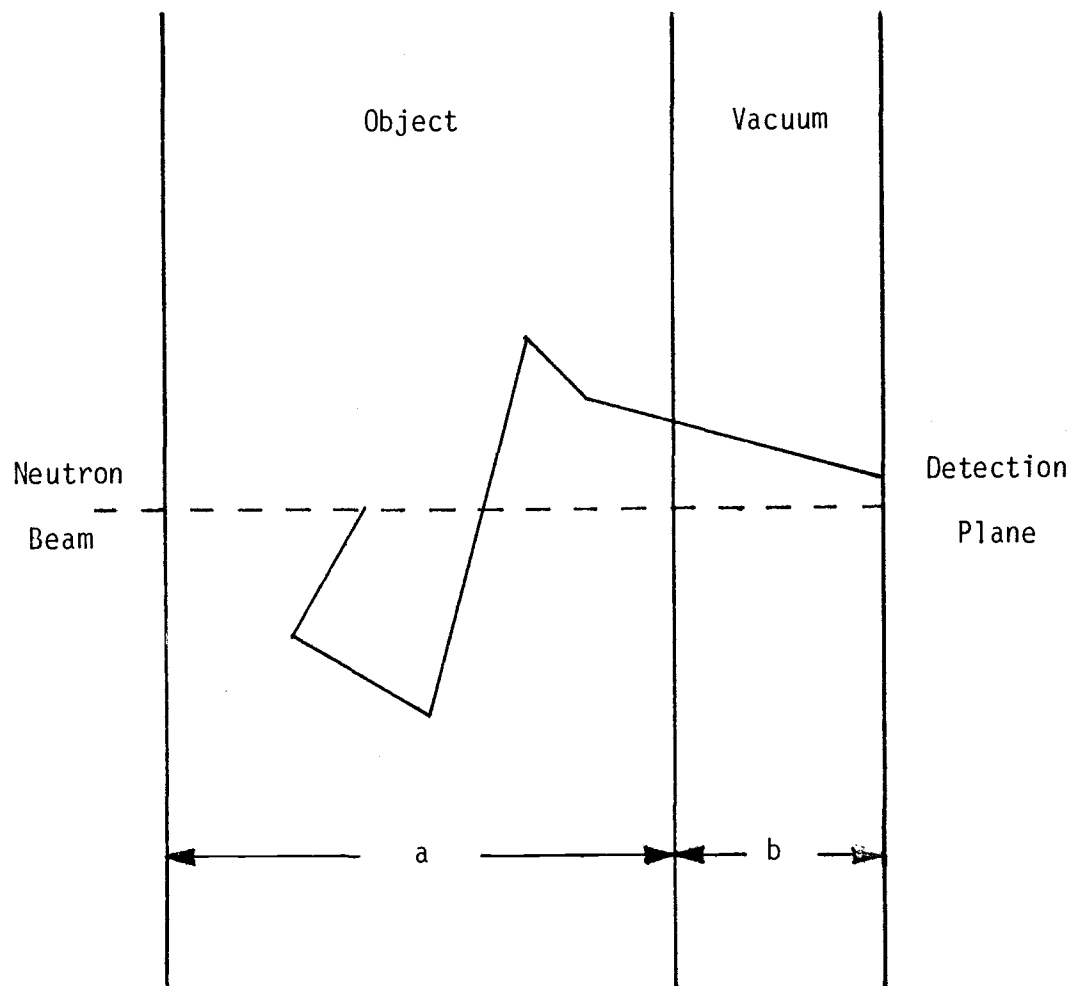


Fig. 5.3: Geometry for point spread function calculation from subject.

neutron transport problem for this geometry and estimate the point spread function for four materials--aluminum, iron, polyethylene, and zircaloy (104). From this analysis the flux spread on the detector is given by

$$\phi(r) = Ae^{-\beta r} \quad 5.3$$

where A, the representative amplitude of the scattered flux, and the governing PSF width β (mm^{-1}) are summarized in Table 5.1 for several dimensions of slab and gap distance.

Although this data could be used to reconstruct the radiographic image without image spread, the intention is to determine the expected resolution loss by scattering using the PSF data with the MTF. Since the calculation assumes the point spread function to be radially symmetric, a direct conversion to the MTF is possible. First the point spread function of the flux distribution is determined by normalization, that is

$$\int_0^{\infty} \int_0^{2\pi} P(r) r d\theta dr = 1$$

$$\text{Therefore } P(r) = \frac{\beta^2}{2\pi} e^{-\beta r}$$

The MTF of a point spread function is given as

$$T_2(v) = 2\pi \int_0^{\infty} r P(r) J_0(2\pi v r) dr \quad 5.5$$

Table 5.1: Object point spread function parameters (104).

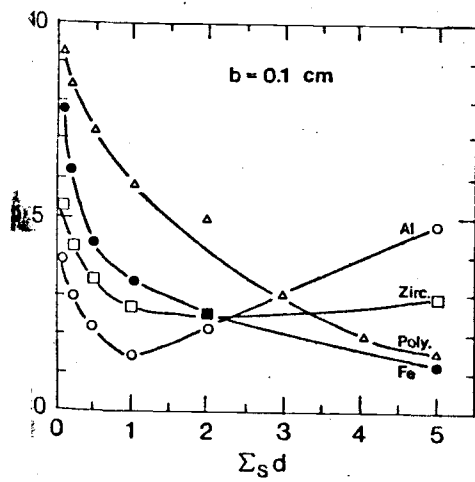
Material	$\Sigma_s d$	d	$b=0.1$ cm		$b=0.5$ cm	
			A	β	A	β
<i>Aluminum</i>	$\Sigma_s = 0.08113$	0.1	5.731×10^{-2}	3.986	9.161×10^{-3}	1.162
		0.2	4.389×10^{-2}	3.033	9.327×10^{-3}	0.903
		0.5	2.562×10^{-2}	2.222	7.360×10^{-3}	0.724
		1.0	8.629×10^{-3}	1.390	3.551×10^{-3}	0.502
		2.0	5.062×10^{-3}	2.300	1.453×10^{-3}	0.625
$\Sigma_t = 0.0938$	5.0	4.902×10^{-4}	4.777	7.298×10^{-5}	0.797	
<i>Iron</i>	$\Sigma_s = 0.9667$	0.1	0.383	7.749	2.792×10^{-2}	1.987
		0.2	0.456	6.217	4.529×10^{-2}	1.814
		0.5	0.3998	4.361	6.192×10^{-2}	1.430
		1.0	0.246	3.377	5.129×10^{-2}	1.103
		2.0	9.206×10^{-2}	2.504	1.473×10^{-2}	0.783
$\Sigma_t = 1.163$	5.0	3.229×10^{-3}	1.324	1.447×10^{-3}	0.694	
<i>Zircaloy</i>	$\Sigma_s = 0.2622$	0.1	0.162	5.369	1.865×10^{-2}	1.5
		0.2	0.157	4.214	2.399×10^{-2}	1.294
		0.5	0.141	3.530	2.629×10^{-2}	0.979
		1.0	6.619×10^{-2}	2.704	1.628×10^{-2}	0.703
		2.0	3.275×10^{-2}	2.519	8.724×10^{-3}	0.615
$\Sigma_t = 0.2702$	5.0	3.300×10^{-3}	2.829	8.903×10^{-4}	0.366	
<i>Polyethylene</i>	$\Sigma_s = 4.164$	0.1	0.720	9.201	4.036×10^{-2}	2.063
		0.2	1.148	8.449	7.456×10^{-2}	1.9998
		0.5	1.699	7.130	0.151	1.953
		1.0	1.615	5.840	0.204	1.866
		2.0	0.718	4.966	0.137	1.837
		3.0	0.447	3.050	0.134	1.304
		4.0	0.219	1.891	8.849×10^{-2}	0.854
$\Sigma_t = 4.188$	5.0	0.114	1.454	5.507×10^{-2}	1.711	

which is equal to the zero order Hankel transform (105,106). Tables of Hankel transforms exist for the PSF exponential form (Eq. 5.3) and so

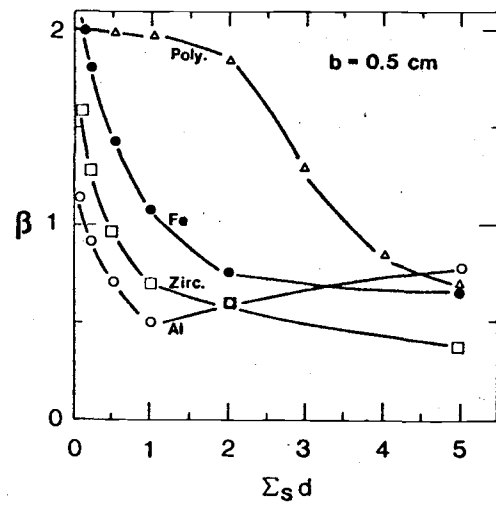
$$T_2(v) = \frac{\beta^3}{(\beta^2 + (2\pi v)^2)^{3/2}} \quad 5.5$$

This expression, then, is the MTF due to neutron scattering in the subject. It is difficult to implement on a routine basis, however, since new Monte Carlo calculations are required for each change in subject cross section and geometry. At any rate, more concern is placed upon image quality characteristics of the radiography system separate from the object; comparisons may be made upon which resolution loss is most objectionable prior subject selection.

The β term appearing in Eq. 5.3 is useful as a figure of merit for subject inherent point spread since improved object definition occurs as its magnitude increases. Although an inverse relationship should exist between β and the subject width and scattering cross section, the true behavior is not obvious due to interactions in scattering and absorption probabilities as thickness and, consequently, neutron path length increases. These interactions can introduce minima in B curves as Figure 5.4 demonstrates.



(a)



(b)

Fig. 5.4: Behavior of β with thickness of four materials.
 (a) 1mm separation distance.
 (b) 5mm separation distance (104).

5.3.3 Scintillator

Bossi has measured the MTF of one LiF-ZnS scintillator constructed at OSU, namely #51 (107). A correlation has been prepared from his graphical results and fit to the exponential form below:

$$T_3(\nu) = e^{-(\nu/\nu_0)^a} \quad 5.6$$

This equation was algebraically modified so a standard linear regression analysis routine could be employed.

The correlation parameters are:

$$\nu_0 = 1.80\text{mm}^{-1}$$

$$a = 1.82$$

$$r^2 = .985$$

where r^2 is the square of the linear correlation coefficient.

Experimental and correlation information are plotted for comparison of the OSU #51 scintillator in Figure 5.5. Modulation transfer function measurements have been performed upon other scintillators by a number of researchers (108,28).

5.3.4 Intensifier

A MTF correlation for a typical two stage electrostatic image intensifier has been prepared which

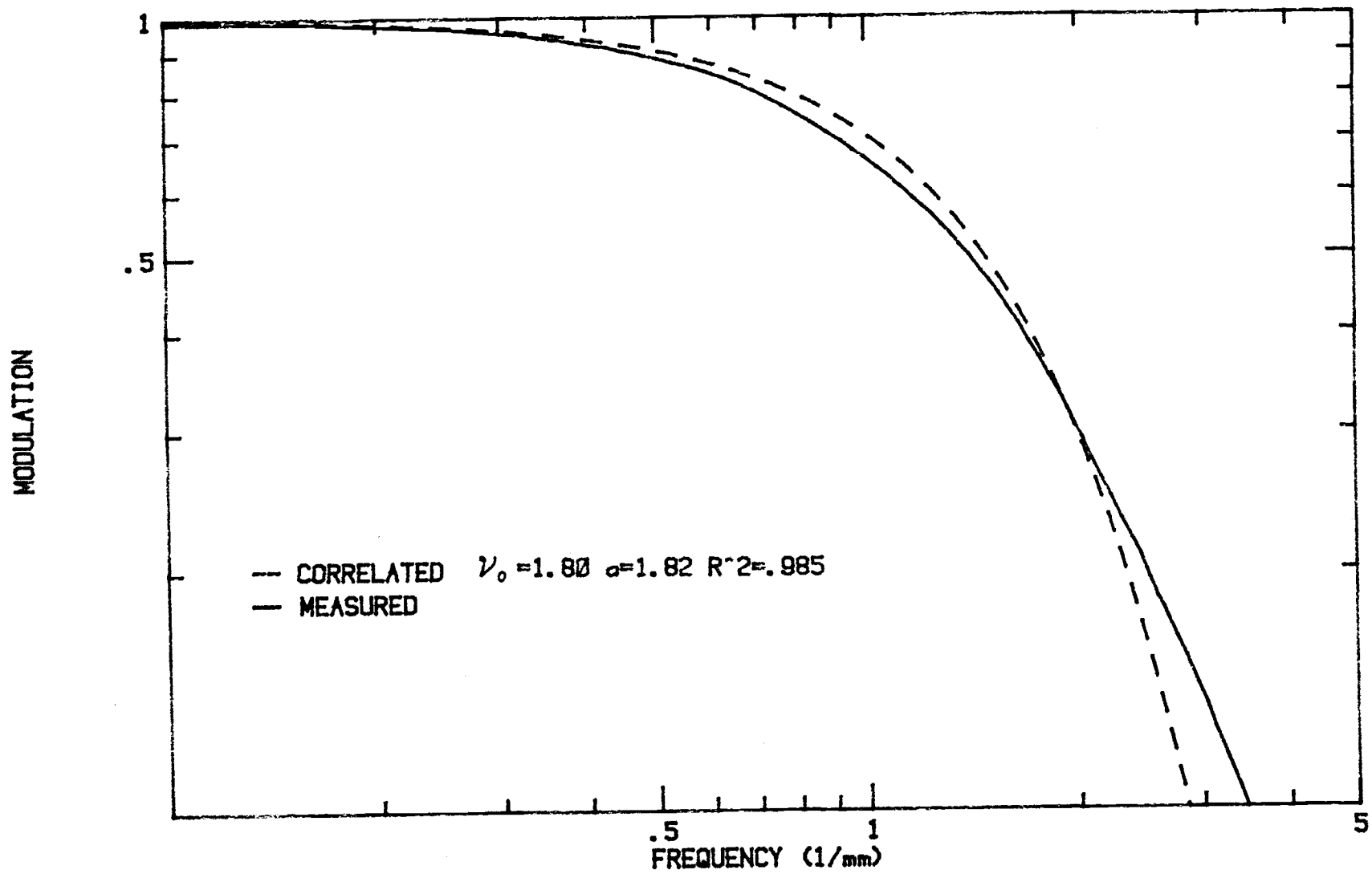


Fig. 5.5: Measured and correlated data for the OSU #51 scintillator.

closely approximates MTF data supplied by ITT:

$$T_4(\nu) = e^{-(\nu/\nu_0)^a} \quad 5.7$$

where

$$\nu_0 = 23\text{mm}^{-1}$$

$$a = 1.6 \quad (109).$$

Note a severe departure from this correlation should occur if intimate contact is not maintained between the intensifier faceplate and the scintillator due to the extremely short range of focus of high aperture fiber optics.

5.3.5 Lens

A diffraction limited lens has the following well known MTF equation:

$$T_5(\nu) = \frac{2}{\pi} \{ \cos^{-1}(\nu/\nu_L) - (\nu/\nu_L)(1 - (\nu/\nu_L)^2)^{1/2} \} \quad 5.8$$

where

$$\nu_L = \text{limiting spacial frequency for the focal plane} \\ (\text{mm}^{-1})$$

$$= 1/(A\lambda_m)$$

A = lens aperture (f/3.3 Hycam limited)

λ_m = peak wavelength of source (mm^{-1}).

This equation assumes the light source is monochromatic but the peak wavelength of the P11 phosphor is

appropriate as an approximation. Levi has tabulated the MTF response of a perfect lens with the spectral distribution of a P11 phosphor; the monochromatic approximation is comparable with his calculations (110).

It is highly important that lens focus is exact or a serious decrease in the MTF will result. This equation may only be applied about lens center since the spread function of even a good lens is symmetrical only at its optical axis (111).

5.3.6 Film

Manufacturers' data is available upon the modulation transfer characteristics of a number of films under specified processing conditions. A MTF correlation using

$$T_G(\nu) = e^{(-c_1\nu + c_2)}$$

and valid above a 5mm^{-1} spacial frequency was prepared from this data for three high speed films. The correlation parameters appear in Table 5.2. Other correlations exist for film modulation transfer functions (112).

Assuming a low signal modulation, of such a magnitude the signal excursions do not extend beyond the linear portion of the film characteristic curve, the differential gain may be approximated by the film gamma.

Table 5.2: Modulation parameters of three Kodak RAR films.

$$T(\nu) = e^{(-c_1\nu + c_2)}, \nu > 5\text{mm}^{-1}$$

Film	c_1 ($\times 10^{-3}\text{mm}$)	c_2 ($\times 10^{-3}$)	gamma	r^2	gran. ($\times 10^{-3}$)	Processing
2498	15.4	166	1.6 D	.995	34	D19 2min @ 95F
						D19 8min @ 68F
			1.6 D			D19 1.5min @ 95F
2475	41.5	167	1.00T	.997	33	DK50 8min @ 68F
			1.30P			D19 8min @ 68F
			1.95T			D19 8min @ 68F
2484	20.1	56.4	1.00T	.99	30	D19 4min @ 68F
			1.70T			D19 8min @ 68F

T = tungsten P = P11 D = daylight

Correlations performed on manufacturer's MTF curves for over 20 data points.

Since this acts on the modulation only, it is treated as a MTF constant at the region where the film characteristic slope is linear. When combined with the above equation the expression

$$T_6(v) = \gamma e^{(-c_1 v + c_2)} \quad 5.9$$

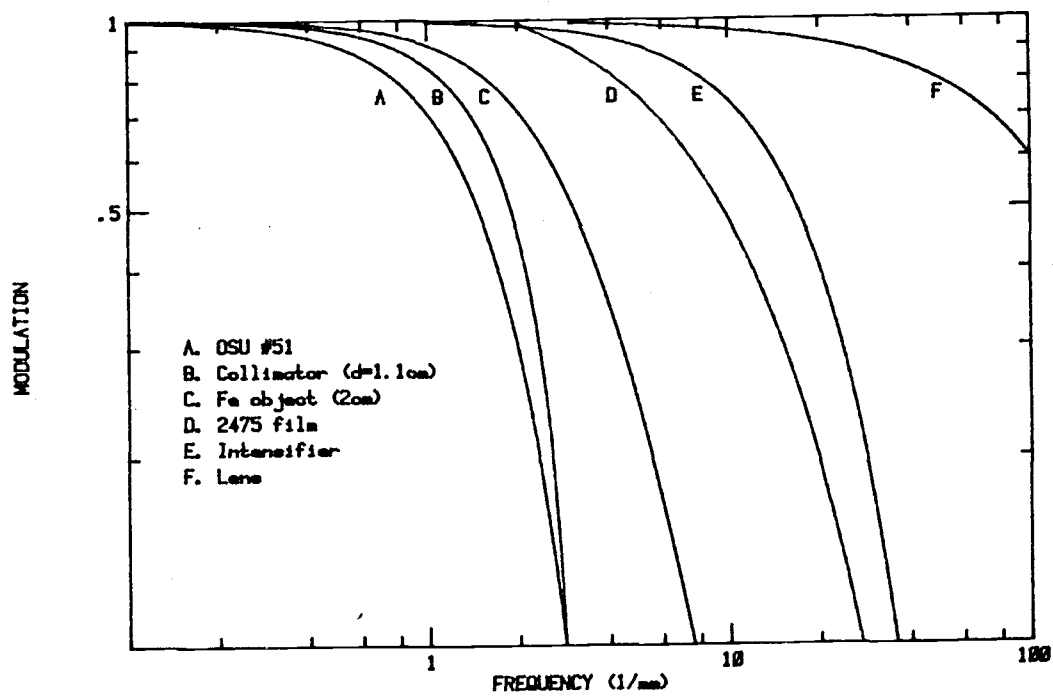
becomes the film MTF for both exposure and processing.

5.3.7 Typical system MTF

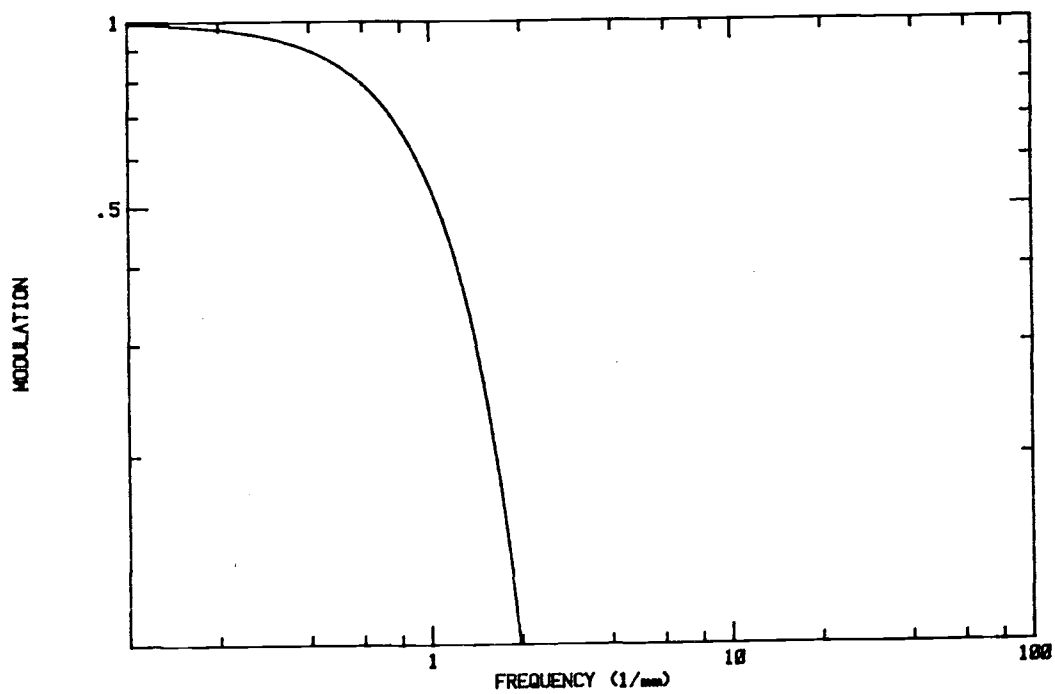
The preceding analytic expressions will now be applied to determine the expected system resolution of a typical ordinance application. For this evaluation it was assumed the image detail under consideration was centered within a 2cm iron "block" positioned 1mm from the scintillator. Other system characteristics necessary for the analysis have been given above and are summarized in Table 5.3. Figure 5.6 illustrates the component and system modulation according to the spacial frequency in object dimensions. As shown, the lens, film, and intensifier contribute negligibly to the total response whereas geometric unsharpness and scintillator resolution dominate. Accordingly, it would seem that although some choice of scintillators exist with better resolution, a high resolution replacement scintillator would only

Table 5.3: Neutron radiography system and component modulation transfer functions.

Component	m_i	g_i	v_i/v_2	$T_i(v_i)$	MBW_i (mm^{-1})
1 Collimator				$\text{sinc}(v_2 U_g)$ $U_g = d/(L/D) = .315\text{mm}$	$1/(2U_g)$
2 Object	1	2cm Fe 0.20	1	$\frac{\beta^3}{(\beta^2 + (2\pi v_2)^2)^{3/2}}$ $b = 1\text{mm} \quad \beta = 25.04\text{mm}^{-1}$	$\frac{3\beta}{32}$
3 Scintillator	1	OSU #51 4.28×10^{-9} $\mu\text{W}/\text{cm}^2\text{-nv}$	1	$e^{-(v_3/v_0)^a}$ $a = 1.82 \quad v_0 = 1.80\text{mm}^{-1}$	1.093
4 Intensifier	.846	109	1.18	$e^{-(v_4/v_0)^a}$ $a = 1.6 \quad v_0 = 23\text{mm}^{-1}$	13.37
5 Lens	.5	.0526	2.36	$\frac{2}{\pi} \{ \cos^{-1}(v_5/v_L) - (v_5/v_L)(1 - (v_5/v_L)^2)^{1/2} \}$ $v_L = \frac{1}{A\lambda_m} = 673\text{mm}$	$\frac{8(15\pi - 32)}{45\pi^2} v_L$
6 Film	1	Figure 4.7	2.36	$\gamma e^{(-c_1 v_6 + c_2)}$ 2475 D19 8min 68F $\gamma = 1.3$ $v_6 > 5\text{mm}^{-1}$ $c_1 = 41.5\mu\text{m}^{-3}$ $c_2 = 167 \times 10^{-3}$	$\gamma \left(\frac{e^{2c_2}}{2c_1} + 5 \right)$



(a)



(b)

Fig. 5.6: Static MTF for common ordinance application.
(a) Component. (b) System.

marginally improve system resolution if inherent resolution loss due to geometric unsharpness and neutron scattering could not be reduced. Since the detail-detector proximity predominantly affects resolution loss by both collimation and object self-scatter, its minimization should be the first consideration prior implementation of improved components.

Although most of the variables which determine system resolution seldom change, object dimensions, placement, and materials differ enough in any new radiography application to require separate evaluation. Some subjects may have such a favorable inherent resolution that reasonable cause exists to improve scintillator resolution until collimation itself restricts system resolution.

5.4 DYNAMIC IMAGE RESOLUTION

5.4.1 Motion MTF definition

When an image moves relative to the film during exposure or is transmitted by a device with finite response time a blur is recorded. In a linear system, this blurring may be represented by a spread function, and, hence, if it affects each point image identically, by a transfer function. Since spacial information loss due to image motion can be as equally important as static limiting resolution, a dynamic MTF contribution should be included in system resolution analysis.

Two independent forms of image motion blur occur in an electrographic system: blur due to focal plane motion between image and film and image blur which occurs due to finite response time of the electro-optical system. All photographic systems will exhibit the first type of blur if image motion has considerable magnitude during exposure and this blur is normally minimized by selecting a faster shutter time relative to image motion. When an image conversion device (e.g. scintillator or image tube) is employed in a photographic system, subject features displayed from its output can be accompanied by a trail of decaying luminescence if persistence is comparable to subject motion. Regardless of shutter time, then, this

second type of motion blur is recorded as a characteristic of the inherent response time of the device. Both forms of image blur will be treated separately for a MTF analysis but from a unified model.

Consider a single image point at x' moving over a recording medium with coordinate system x at time t . Assume that the flux distribution in the image is constant throughout exposure, but that the total image flux, $A(t)$, varies with time. The exposure an image point provides at point x during time interval dt is then

$$\delta(x - x') A(t) dt$$

Due to a finite response time of the detector system, the contribution to the total exposure at the final time t_f , is altered by a factor of $g(t_f - t)$, the impulse response of the system. The total exposure at t_f beginning from t_i is then

$$E(x, t_f) = \int_{t_i}^{t_f} \delta(x - x') A(t) g(t_f - t) dt$$

The above equation is the general expression for the point spread function due to motion. The equivalent transfer function may be determined from this by means of the Fourier transform

$$T(v) = \frac{\int_{t_i}^{t_f} A(t) g(t_f - t) e^{i2\pi v \cdot x'(t)} dt}{\int_{t_i}^{t_f} A(t) g(t_f - t) dt} \quad 5.10$$

where the denominator has been introduced for

normalization at the ν origin. This equation represents the ratio of image modulation exhibiting blur to object modulation without blur. All derivations of motion blur from this model will now be restricted to one dimensional object space.

5.4.2 Blur due to focal plane motion

In all cases of ordinance evaluation, image motion may be considered linear and the neutron source flux as constant during exposure of a single frame. The MTF for focal plane motion during an exposure time T is then

$$T(\nu) = \frac{\sin(\pi\nu\nu T)}{\pi\nu\nu T} = \text{sinc}(\nu\nu T) \quad 5.11$$

where ν and ν are the object velocity and spacial frequency, respectfully, which may be used directly for their image values in Eq. 5.11 since the cumulative magnification factor cancels when a transformation is made to the object plane.

5.4.3 System impulse response blur

Image conversion and operation by the scintillator and intensifier components require a finite time to reach equilibrium from an image signal change and therefore

exhibit response time limitations. Note although neutron transit time from the subject is significant (about 2.5 microseconds/cm) in comparison to these processes, this itself does not introduce image distortion since modulation remains constant and uniform with subject motion; the nonlinear luminescence build up and decay of photocathode and phosphor materials produces image smear.

Although distortion may be created by risetime restrictions of an image conversion device, overwhelmingly image smear is caused by phosphor persistence of the device. Measured response time of the S20 photocathode (.5ns) and ZnS excitation risetime (<10ns) are several orders of magnitude below those encountered in persistence and so are safely neglected (113,114). Persistence, or decay time, is usually measured as the time required for the luminous intensity to decrease to a value equal to either 10% or e^{-1} of its initial intensity when the source of excitation is removed. Depending on phosphor composition, two decay processes may exist; a temperature independent exponential decay of a temperature dependent hyperbolic decay. The ZnS(Ag) phosphor itself decays in a hyperbolic manner, however an exponential approximation for its decay is common practice. If phosphor risetime is negligible, the impulse response, then, obeys

$$g(t) = e^{-\lambda t}$$

for a single phosphor, where λ is the decay constant and is equivalent to the reciprocal of the phosphor's exponential time constant, τ .

The MTF accounting for linear motion and a single exponential decay phosphor has been determined from Eq. 5.10 and the square of this transform is

$$T(\nu)^2 = \frac{1 + (\sin(\pi\nu T)/\sinh(\lambda T/2))^2}{1 + (2\pi\nu/\lambda)^2} \quad 5.12$$

(115)

If phosphor decay time is much shorter than object motion during exposure, the MTF simplifies to

$$T(\nu) = \text{sinc}(\nu T)$$

which is precisely the result for focal plane image motion (Eq. 5.11). Since phosphor operation is continuous during camera shuttering, this transform as it stands does not appropriately describe image blur from the scintillator or intensifier output phosphor. If the sample period T approaches infinity, Eq. 5.12 converges to

$$T(\nu) = (1 + (2\pi\nu/\lambda)^2)^{-\frac{1}{2}}$$

which is now the phosphor motion MTF.

5.4.4 System motion resolution

The system motion MTF may now be determined as the product of each motion MTF of the scintillator, intensifier, and focal plane image, and is

$$T(\nu) = \frac{\text{sinc}(\nu T)}{(1 + (2\pi\nu/\lambda_4)^2)(1 + (2\pi\nu/\lambda_3)^2)^{\frac{1}{2}}} \quad 5.13$$

It is appropriate, however, to consider what simplifying assumptions may be made to this model since all these components do not contribute equally to the overall MTF in application.

Most phosphors have an activator impurity that controls the conversion of electron energy to light energy by activator-produced discontinuities in the phosphor and, by use of different activators or from small variations in their concentration, produce variations in phosphor brightness, color, and persistence. All P11 ZnS phosphors use silver activation however recently a second impurity, nickel, may be added to some constructions to reduce persistence. Such phosphors have decay time reductions that are striking; the original phosphor and the nickel quenched versions have decay times of 30 and .24 microseconds (e^{-1} level) respectfully (116,117). Scintillators constructed at OSU and Nuclear Enterprises use nickel quenched P11 equivalent phosphors but the version constructed with the

intensifier in use is unknown. If the intensifier phosphor persistence is 30 microseconds, contribution by the 200ns decay time scintillator may be safely neglected in the system MTF. The minimum frame time of the Hycam camera using a half-framing optical head is 2 microseconds and therefore considerable image smear would appear at such a frame rate if nickel quenched phosphors were not present in the intensifier. If such is the case, inclusion of an impulse response function accounting for phosphor decay in the intensifier is important to determine image resolution loss when imaging high velocity objects.

Figure 5.7 illustrates what device dominates system motion blur by a plot of component MTF to the product of object spacial frequency and velocity vv . Clearly if 30 microsecond time constant phosphors are used in the intensifier, intensifier persistence would dominate system resolution. If on the other hand the intensifier uses nickel quenched phosphors, phosphor persistence by both the intensifier and scintillator may be neglected in the motion MTF model. Note in this figure the focal plane image blur curve was developed using the minimum half-frame exposure time of the Hycam camera. When longer exposure times are used this curve will shift left, and, if exposure times smaller than 50 microseconds are reached, focal plane motion itself always becomes the

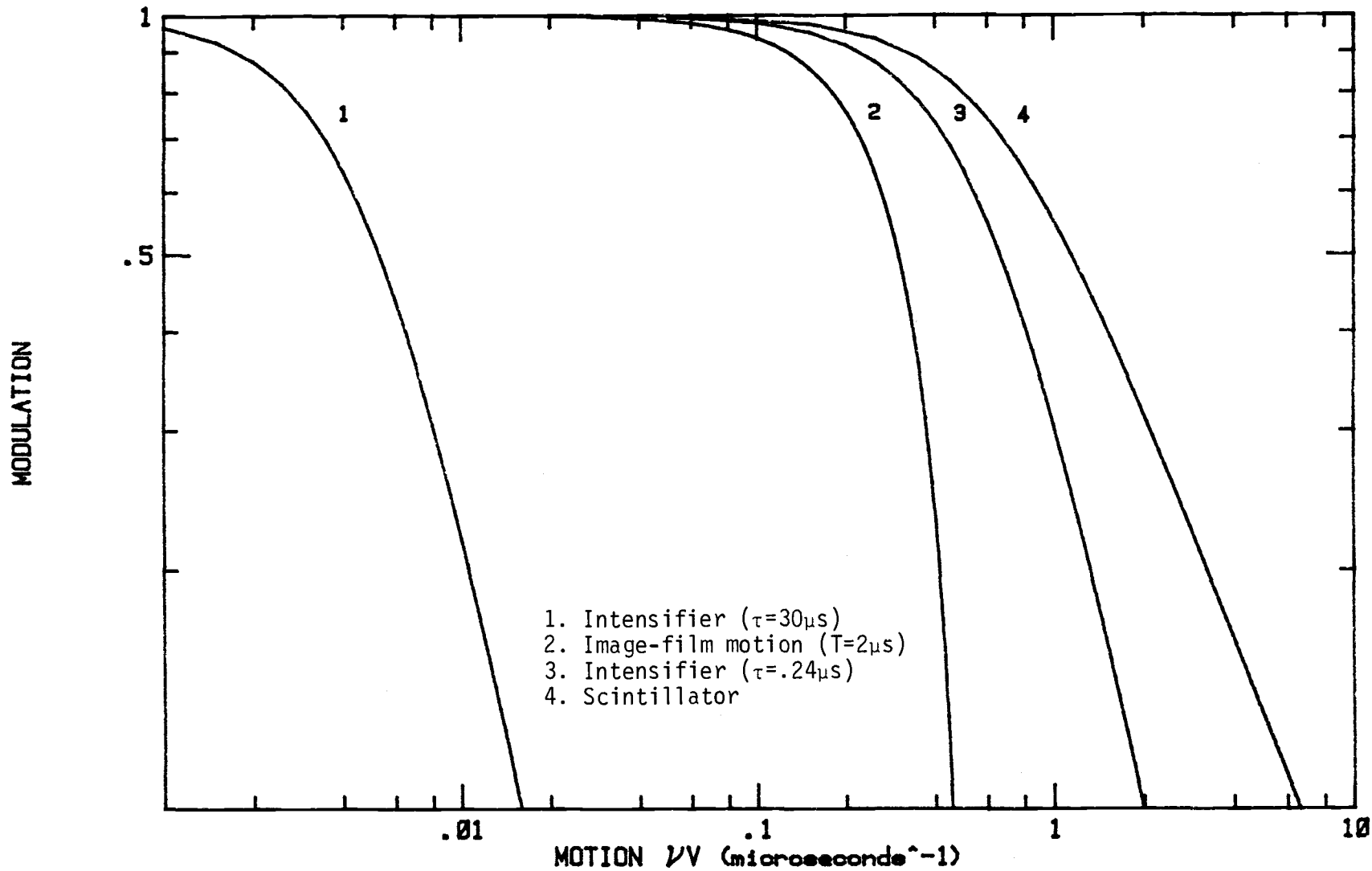
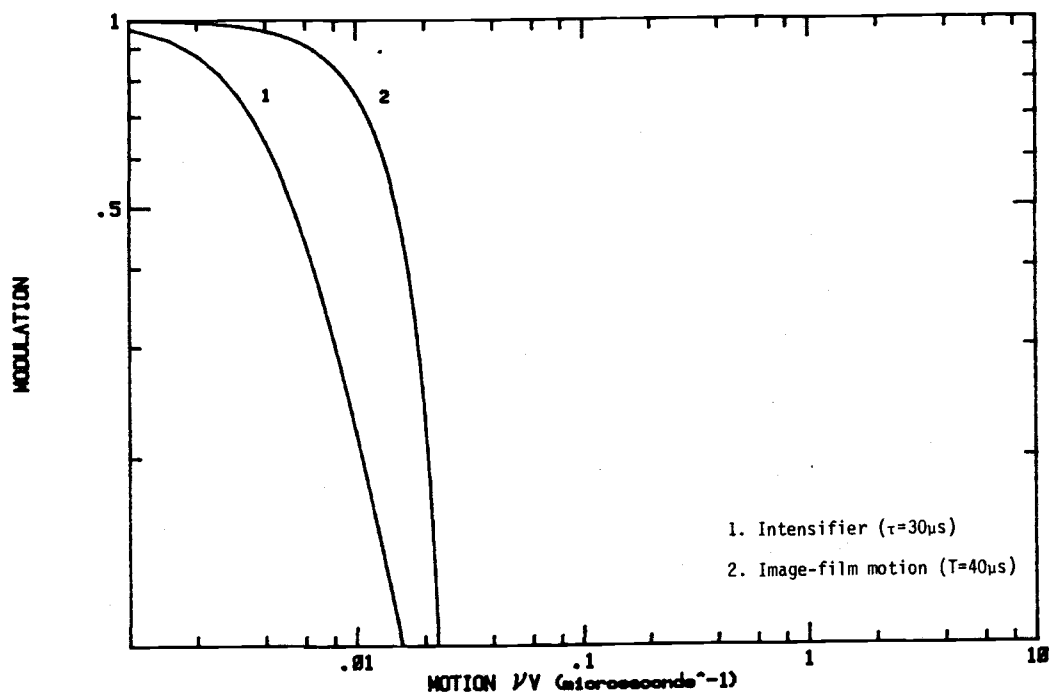


Fig. 5.7: Component motion MTF.

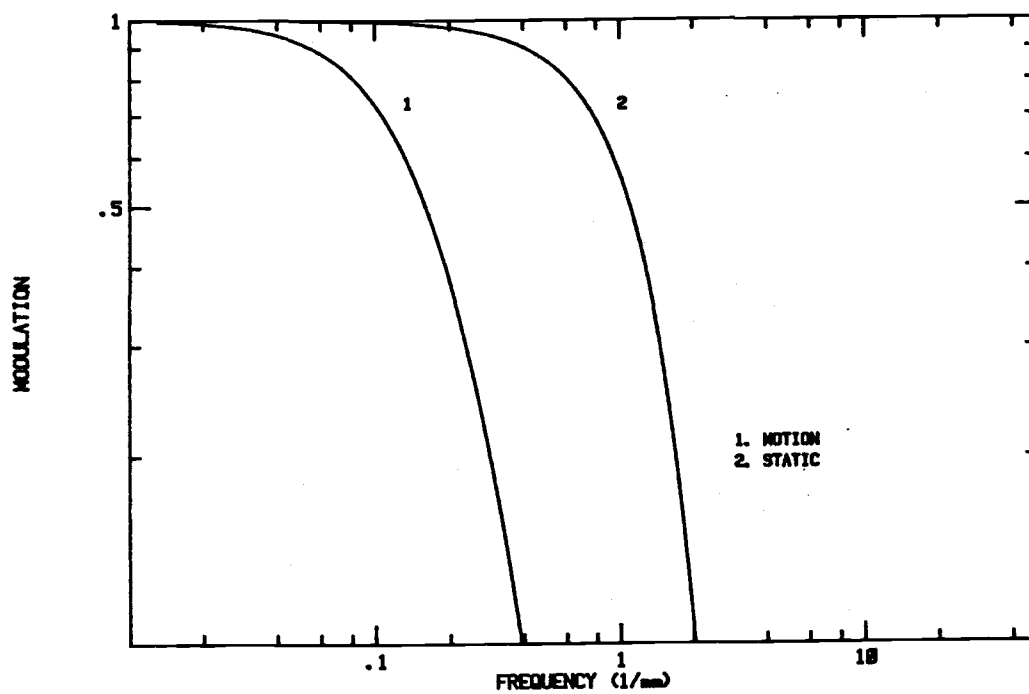
dominant factor in system motion MTF.

An attempt to verify intensifier persistence experimentally at OSU was hindered due to the lack of necessary electronic equipment, but an unusual application of high speed neutron radiography was devised to film persistence after-image using the rapid discharge of an exploding cadmium wire. Unfortunately, the results of this experiment were inconclusive.

The significance of phosphor persistence appears dubious in routine work with the high speed neutron radiography facility since the majority of radiography runs have exposure times greater or equal to 50 microseconds. The magnitude of resolution loss by motion must also be significant compared to inherent resolution limitations if the blur is to become noticeable. An experiment performed a number of years ago with this facility to demonstrate motion blur may serve as an example (118). In this experiment a cadmium spoked wheel rotating at 100 ft/s on its periphery was radiographed at a framing rate of 10,000 frames per second (fps). At this framing rate the shutter allowed a 40 microsecond exposure per frame to be recorded. Analytic predictions for focal plane, persistence, and cumulative MTF computed using the factors of Eq. 5.13 and 5.2 through 5.9 appear in Figure 5.8 and show focal plane and intensifier persistence motion blur equally contribute to a



(a)



(b)

Fig. 5.8: Limiting MTF for 100ft/s Cd bar.
 (a) Component motion MTF.
 (b) System MTF.

resolution loss below static resolution (Fig. 5.8a). A direct comparison with this figure and a measured blur MTF cannot be obtained based on the experimental data which remains, unfortunately. Instead a capability to show a visible difference exists in blur from static resolution must be sufficient. The image spread recorded on the outline of the moving spoke on adjacent frames of the original radiograph seems to support the prediction that motion blur is a magnitude greater than the static resolution of the test object in the background. A latent image appears to show when the spoke fully occupies a frame, however it would be speculation to assume this is due to phosphor persistence if it has been shown persistence and focal plane motion both contribute equally.

More detailed experimental verification should include one or both of the following methods to determine the image degradation by the linear motion MTF in the direction of motion:

1. A moving bar chart
2. A moving knife edge whose edge spread function may be used to calculate the motion MTF.

The first option is best if the MTF should be verified directly using a sine-wave modulated chart, but an approximation for the MTF could be obtained with a standard square wave bar chart. The last option is most

practical if a microdensitometer and computer are available.

5.5 OBJECT MODULATION

Object modulation is difficult to determine precisely but an approximation based upon concentration and neutron cross sections is possible. Consider within the radiographic subject a small detail composed of two different total cross sections Σ_a and Σ_b with thickness x (Fig. 5.9). If the neutron flux escaping from the object about the detail is ϕ_a and ϕ_b , the flux modulation produced is

$$M_2 = \frac{\phi_a - \phi_b}{\phi_a + \phi_b} = \frac{1 - e^{-(\Sigma_b - \Sigma_a)x}}{1 + e^{-(\Sigma_b - \Sigma_a)x}}$$

if ϕ_a is greater than ϕ_b . The highest modulation achievable would approach unity if the cross section difference, $\Sigma_a - \Sigma_b$, is large. Choice of subjects with a large cross section difference would therefore lead to the highest visibility of this detail.

System modulation is determined from the product of the object modulation and the system MTF. In this manner the modulation recorded on the film may be predicted.

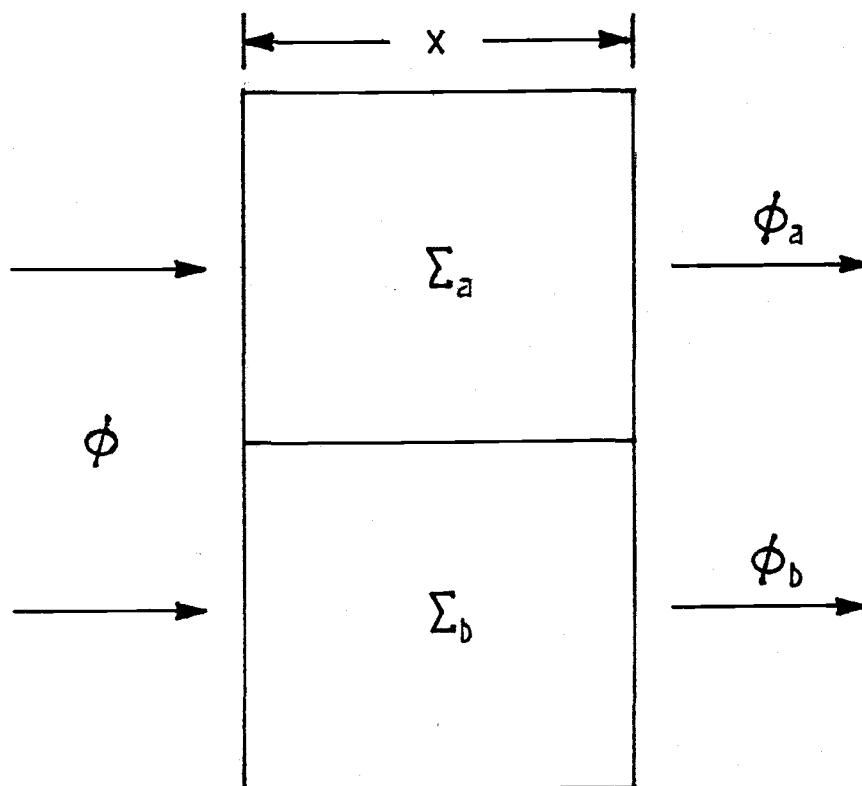


Fig. 5.9: Neutron flux modulation of a subject element.

5.6 NOISE

5.6.1. Origin and treatment

Unlike spacial resolution loss due to static or motion effects, noise obscures information and originates in some active element (e.g. intensifier, film, or video camera), is added to the signal from some external source, or is due to quantum limitations of the signal itself. Since noise travels with the signal, all system gain and resolution limitations apply to it. Using these principles and information on variance due to noise at each component, a comparison upon what magnitude the signal modulation is noise may be made. Besides film granularity, quantum limitations are the only substantial source of noise in the radiography system.

5.6.2 Quantum limitations

The combination of an electronic image amplifier and photographic film makes high speed photorecording possible by effectively extending film recording sensitivity a hundredfold. This allows individual "packets" of 10 to 20 photons each to be registered. However, the image magnitude no longer becomes of as equal concern as image rendition once an intensifier is

used since image portions are recorded randomly in time as each photon arrives. Image quality therefore suffers as fewer but more visible photon packets are recorded. Noise, and, as a consequence, resolution limitations, are imposed upon electro-optical photorecording of rapid events due to the statistical nature of incident quanta. The fundamental limit to image recognition is set by the statistical fluctuation of the incident neutron or photon flux, the exposure time allowed for the recording surface to accumulate its image, and the area it strikes to expose a single picture element. One will recognize these limitations ultimately depend upon the number of photons available to expose a given area of film. The first particle that carries any information from the subject is, however, a single neutron. Granted Poisson statistics apply to quantum image noise, the equivalent number of neutrons that contribute to film exposure on a small square resolution element of area A_e is

$$n_6 = 100G_5 I_1 t \alpha(5,6) A_e$$

where

G_5 = cumulative gain at focal plane (fraction of neutrons which contribute to focal plane irradiation)

A_e = resolution element area (mm^2)

I_1 = neutron intensity incident on subject ($\text{n/cm}^2\text{-s}$)

t = exposure time (s)

$\alpha(5,6)$ = phosphor-film spectral matching factor.

When used to calculate G_5 , the scintillator absolute efficiency, g_3 , here denotes the fraction of radiant energy released from the scintillator per neutron interaction with Li^6 and is

$$g_3 = n T_p C_{ip} E_n / 4.78 \text{MeV.}$$

where the numerator is equivalent to the tabulated absolute efficiency values (MeV/n) for OSU scintillators in Table 4.4. The reciprocal of n_6 represents the variance of focal plane quantum noise and equals the neutron specific noise, i.e.

$$R_n^{-2} = 1/n_6.$$

5.6.3 Granularity noise

When a uniformly exposed and processed photographic emulsion is scanned with an aperture large enough to cover many grains, the observed density fluctuations are found to approximate a Gaussian distribution, so that their statistics may be described by a single constant. This distribution has the following probability density:

$$P(\Delta D_0) = \left(\frac{A_s}{\pi G^2} \right)^{1/2} \exp(-A_s \Delta D_0^2 / G^2)$$

where A_s is the area of the scanning aperture, G is Selwyn's granularity constant, and $\Delta D_0 = D_0 - \bar{D}$ is the deviation of the observed density D_0 from its mean value,

\bar{D} .

By inspection, the standard deviation of the density fluctuation is

$$\sigma_{D_0} = \frac{G}{\sqrt{2A_s}} \quad 5.14$$

This deviation has been listed by Kodak as the rms granularity characteristic of a number of films processed under specified conditions to a net diffuse density of 1.0 and is obtained using a circular scanning aperture of 48 microns. Table 5.2 includes rms granularity data listed by this manufacturer. Granularity increases with development time and average density levels, however is virtually independent of scanning aperture from 4 to 50 microns.

Modulation calculations, both noise and signal, are considerably simpler to manipulate once density deviations are represented by transmittance variations on film. The transmittance change ($\Delta\tau$) corresponding to a density change (ΔD) is determined using the definition of density. Since $D = -\log(\tau/\tau_{\text{base}})$ the change in density represents

$$\begin{aligned} \Delta D = D - \bar{D} &= \log(\bar{\tau} + \Delta\tau) - \log(\bar{\tau}) \\ &= \log(1 + \Delta\tau/\bar{\tau}) \end{aligned}$$

This can be simplified by a Taylor's series approximation

so that

$$\Delta D \approx \frac{\Delta\tau}{\bar{\tau} \ln 10}, \quad \Delta\tau \ll \bar{\tau}$$

The corresponding modulation transmittance may then be defined as the deviation to mean signal transmittance

$$\Delta\tau/\bar{\tau} = \Delta D \ln 10 \quad 5.15$$

and so $\Delta\tau/\bar{\tau}$ may approximate the reciprocal absolute signal ($\bar{\tau}$) to noise ($\Delta\tau$) ratio in film transmittance due to granularity. Specifically, the noise modulation representing the standard deviation of the density fluctuations follows if ΔD approximates the standard deviation

$$\Delta\tau/\bar{\tau} = \sigma_D \ln 10 = \sigma_{D_0} \sqrt{A_s/A_e} \ln 10 \quad 5.16$$

where the proportionality to the reference rms granularity, σ_{D_0} , has been used assuming Selwyn's granularity constant does not vary over aperture size.

5.6.4 Other noise sources

Undesired radiation interactions with scintillator and intensifier materials may produce detectable

scintillations, which, when amplified together with the image signal, can increase background noise. Gamma radiation, as opposed to beta or alpha sources, is particularly likely to induce false scintillations. Fortunately, the tangential construction of the beam port #3 beam tube eliminates the majority of gamma radiation originating within the reactor and the collimator has been designed to reasonably minimize this radiation from its outlet, however prompt radiation reactions with the cadmium mask, the object under inspection, scintillator, and the intensifier itself can introduce noise. The current configuration of high speed neutron radiography instrumentation appears to produce no significant radiation noise, however no attempt has been made to measure this background on a routine basis. An awareness of instrumentation sensitivity is therefore important especially if the configuration is changed.

The number of scintillations produced by neutron as opposed to gamma interactions may be represented by a gamma rejection ratio. Typical LiF-ZnS scintillators are superior in gamma rejection ratio to other neutron scintillator materials and are 20 times better in rejection than gadolinium foil screens (102). Spowart has shown the gamma detection sensitivity of number of LiF-ZnS scintillators is 500 to 1000 times less efficient than neutron detection, this ratio increasing as LiF/ZnS

concentration increases and decreasing as gamma energy increases (120). A gamma rejection ratio this large would appear to make no contribution to gamma radiation noise.

Intensifier operation can be more sensitive to radiation noise. Detectable scintillations may occur within the intensifier's optical faceplate by either charged particles incident upon the surface such as alpha or triton particles escaping from the scintillator or by gamma ray interactions which may produce as many as 3×10^4 photons per incident gamma (121). Compton electrons may also interact with the photocathode or other materials to produce cascades of secondary electrons. The amount of increased background noise an intensifier produces will depend on the amount and energy of the radiation and on the type of materials of which the tube is constructed, and might be significant at one rad/hr.

Film condition and processing also come into play. As a photographic emulsion ages prior to its use, background fog intensity increasingly becomes a problem when the film is processed since this limits the contrast which may be achieved. Marks and wrinkles in a film develop dark in areas of physical damage as if exposed and this may obscure important details of the subject. These problems may be minimized by careful selection and handling of photosensitive materials before and during

developing.

Radiation interactions with the film itself increases background fog to a noticeable level and uniformly affects the entire film width during and moments after a reactor pulse occurs. Background fog may increase to as much as twice its static level at that time. This increased background appears to originate from secondary radiation released as neutrons interact with the film gate or other parts of the camera.

5.6.5 Resolution element area, A_e

No mention of what size the resolution area assumes has been made up to now. The element area is chosen as the smallest resolved area recorded on the film determined by the limiting resolution of the system and can be defined in terms of the equivalent pass band, N_e

$$A_e = (M/N_e)^2$$

where

$$N_e = 2NBW$$

and a transformation has been made from the object dimension using the cumulative magnification M . Table 5.3 lists component analytic and numerical values of the noise equivalent bandwidth for the system configuration under evaluation. To approximate the system NBW, Levi suggests adding the reciprocals of the squares of the

component values, i.e.

$$NBW^{-2} = \sum NBW_i^{-2} \quad (122).$$

As expected, the system noise equivalent bandwidth is predominantly determined by the scintillator and collimation, the components of lowest resolution. The system configuration has the following element area and noise equivalent bandwidth:

$$N_e = 1.68 \text{ mm}^{-1}$$

$$A_e = .0638 \text{ mm}^2.$$

5.6.6 System noise rejection

Since the film is the final component of the electro-optical system all noise contribution ends there, if noise entering the information path from the film to the observer's brain were to be neglected. The system noise contribution by quantum and granularity sources may now be combined in terms of its transmittance modulation recorded on film.

Quantum noise predominates electro-optical noise sources in this system. If other noise sources were to be accounted in the linear system (such as intensifier noise), they must be added to determine the total specific noise as in Eq. 3.9. Without additional sources, the total specific noise of the linear portion is simply

$$R_n^{-2} = R_5^{-2}.$$

By analogy to Eq. 3.3, the noise modulation recorded as transmittance variations on film is

$$(\Delta\tau/\bar{\tau})_L = \gamma/R_L$$

where γ is the differential gain characteristic of the film.

The transmittance modulation given by granularity noise (Eq. 5.16) may now be combined with the focal plane noise as

$$(\Delta\tau/\bar{\tau})_6^2 = (\Delta\tau/\bar{\tau})_g^2 + (\Delta\tau/\bar{\tau})_L^2$$

so that $(\Delta\tau/\bar{\tau})_6$ is the combined transmittance noise modulation. In practice, the granularity noise contribution is negligible in comparison to quantum noise and so has been neglected.

Transmittance image modulation is given by

$$(\Delta\tau/\bar{\tau})_{\text{image}} = T(\nu)_6 M_2$$

where M_2 is the object modulation.

Finally, when expressed as a ratio the signal-to-noise modulation on the film is

$$R = \frac{(\Delta\tau/\bar{\tau})_{\text{image}}}{(\Delta\tau/\bar{\tau})_{\text{noise}}} = \frac{T(\nu)_6 M_2 \sqrt{100 G_5^{-\alpha(5,6)} A_e I_1 T}}{\gamma}$$

To investigate noise influence upon visibility and resolution, the signal-to-noise characteristic of the

high speed neutron radiography system was plotted against object spacial frequency for unity object modulation. Such an analysis required all component magnification, transfer function, and noise contribution information discussed so far. S/N ratio curves for four neutron exposures are presented in Fig. 5.10. Interpretation of image quality given a S/N ratio is subjective, however may be categorized based on observations by numerous disciplines (Table 5.4). Most radiography is performed successfully with neutron exposures about 10^7 n/cm^2 bounded by 10^8 and 10^6 n/cm^2 and only exposures near the latter magnitude should have marginal detectability according to Table 5.4. Inspection of films with exposures near 10^6 (S/N ratios of about 2 and below) reveal exposure is the greatest limitation in image quality not noise however image details when detected do appear "patchy" at such low exposures. Image loss due to noise is not noticeable at higher exposures. As shown, resolution drops sharply at object spacial frequencies above 1 mm^{-1} for all exposures presented in Fig. 5.10 and unfortunately cannot be significantly improved with higher exposure.

It is important to realize object modulation and film gamma can change the S/N ratio for any one application and therefore the magnitude of the curves in Fig. 5.10 will vary. Unfortunately, no experiment has

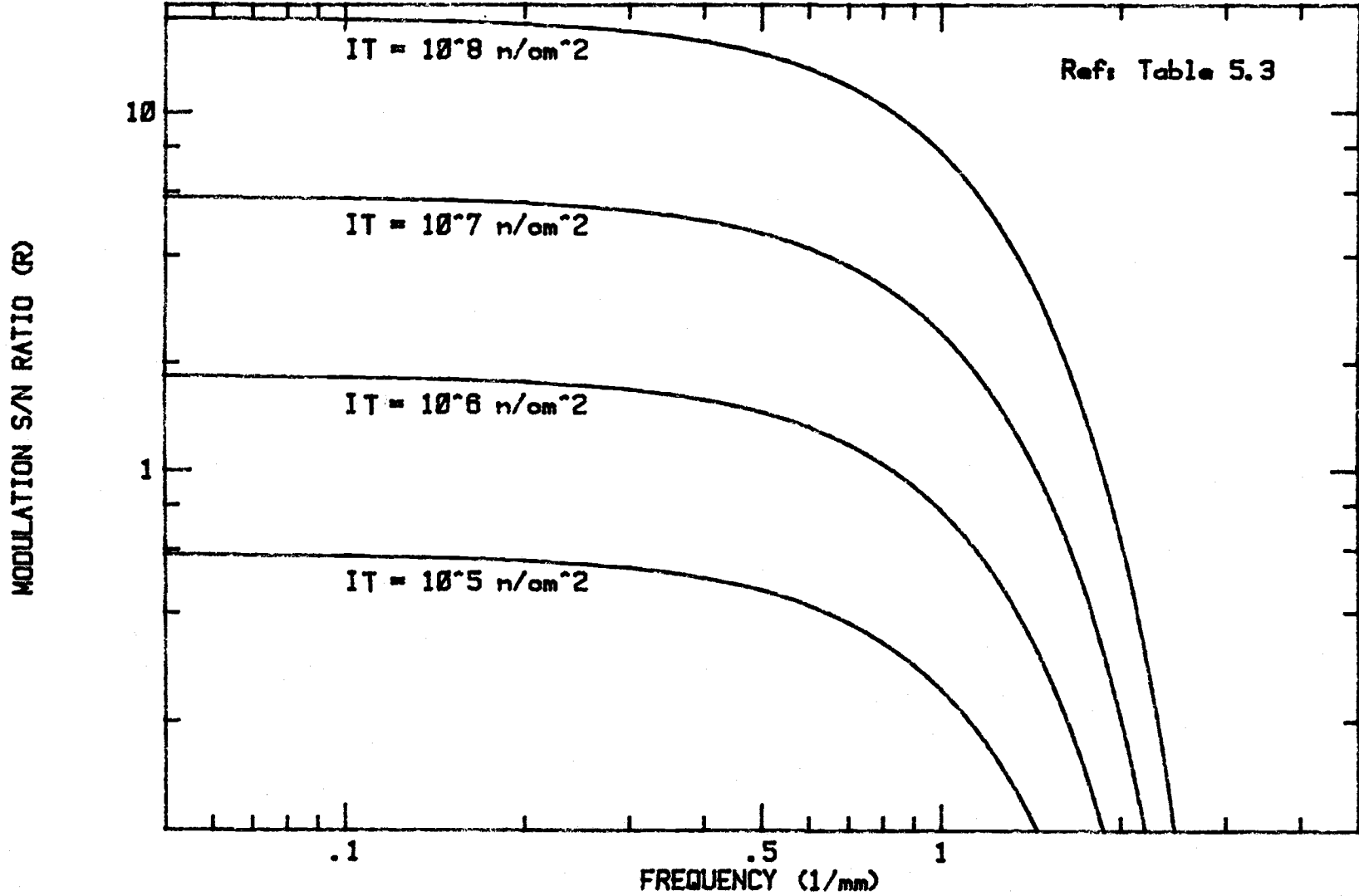


Fig. 5.10: Signal-to-noise characteristic of common ordinance application.

Table 5.4: Image quality and the S/N ratio.

Image quality	S/N
Excellent	>10 - 7
Good	7 - 5
Fair	5 - 3
Marginal	3 - 1
Unrecognizable	<1

been made upon what degree a change of either of these will affect image noise nor have enough measurements been made upon variation of noise levels with exposure, S/N ratio, and spacial frequency. If higher speed films are implemented it may be possible to observe noise limitations however. Finally, a comprehensive noise analysis is not likely to be useful; only information upon what conditions should be avoided to maintain image quality is necessary.

VI. PROPOSED ENHANCEMENTS

6.1 SUMMARY OF PRESENT LIMITATIONS

The OSU high speed motion neutron radiography facility is capable of recording neutron images of rapidly evolving phenomena. Recognition of these images, however, is often difficult at very high framing rates due to spacial resolution and exposure limitations. The magnitude of information rendered by the facility could be increased if image resolution and exposure were improved. Theory, approximations, and measurements performed at the component level were pursued and defined the system transfer function, static and motion spacial resolution, and signal-to-noise levels. This analysis demonstrated limitations of the facility and areas of improvement. The present configuration of the high speed neutron radiography facility exhibits the following limitations:

1. Object size limited to 4cm^2 .
2. A minimum exposure time of 3 microseconds when an iron object 2cm thick is recorded to best conditions (2484 film processed 8min in D19 at 68°F).
3. Static resolution of system limited predominantly by LiF-ZnS scintillator, collimation, and neutron scattering in iron, in that order.
4. Image motion blur is accountable to finite

exposure time if this interval is above 50 microseconds; at exposure times below 50 microseconds the predominant cause of blur may be intensifier persistence.

5. The minimum neutron exposure for an iron subject 2cm thick ranges about $10^5 - 10^6$ n/cm².

Improvements in system resolution and gain which can be implemented with a minimum of further research are now presented.

6.2 POSSIBLE IMPROVEMENTS

6.2.1 Scintillator

6.2.1.1 Resolution

Improvements in spacial resolution of thermal neutron scintillators requires reduction of ion path length or the distance light scatters from the phosphor to maintain a scintillation as close as possible to the origin of each neutron detected. Some combination of width reduction or alternate construction is used to increase resolution.

The first alternative to improve resolution is to reduce the width of the LiF-ZnS scintillator used. Unfortunately, only a small range of scintillator thickness for optimum image quality has been observed, bounded by scintillator inhomogeneity for very thin samples and light scattering in the thickest; Spowart claims this range is .25 to .625mm whereas OSU scintillators are constructed in an optimum range above .08mm (123,124).

The short range of the alpha particle released in scintillators using boron compounds may allow images to be recorded with higher resolution than those based on lithium. As mentioned earlier, there has not been

consensus upon whether optimum forms of lithium or boron scintillators are substantially different in resolution or efficiency. For example, research by G. Matsumoto et. al. has demonstrated their BN-ZnS scintillators have slightly improved resolution in comparison to the NE426 but lower efficiency whereas these scintillators have been observed by other researchers to perform slightly better in efficiency instead of resolution (27,28). If a similar method of examination and construction of these boron scintillators existed between researchers perhaps there would be more agreement.

Glass scintillators, due to their transparency, do not suffer from the image inhomogeneity characteristic of granular scintillators however light scattering within the scintillator reduces resolution as thickness increases. Most image quality measurements performed for limiting resolution and unsharpness of these scintillators conclude that optimum forms have image qualities between granular and gadolinium scintillators (108,125). Although thicknesses below one millimeter are difficult to manufacture, a substantial resolution improvement has been obtained by coating the unused face of the glass with matt black paint to eliminate internal reflection (125).

Gadolinium scintillators have the finest image resolution and are now being applied in some real time

neutron radiography systems (126,127). Some evidence exists that scintillators constructed of Gd_2O_3 and ZnS have better resolution than Gd_2O_2S (28).

Figure 6.1 summarizes the MTF measurements of granular, glass, and gadolinium neutron radiography scintillators performed by Bossi, Hawkesworth and Raoof, and researchers at the University of Missouri-Columbia (107,108,28). The data from the latter research group appears more favorable than conclusions reached by Bossi or Hawkesworth. It does not seem likely that the glass scintillator (NE905) tested was treated to reduce internal reflection and so its MTF shown could be improved.

6.2.1.2 Efficiency

The general requirements for an efficient scintillator were discussed in Chapter 4 and include high neutron absorption for ion producing interactions, high ion energy release and deposition in the phosphor, and high phosphor efficiency and light transmission. Since ion range increases with ion energy, high ion energy is in direct opposition to high resolution. Consequently, scintillators which produce low energy ions but from more frequent neutron interactions are favored (e.g. BN-ZnS and Gd_2O_2S). Unfortunately, this compromise in ion

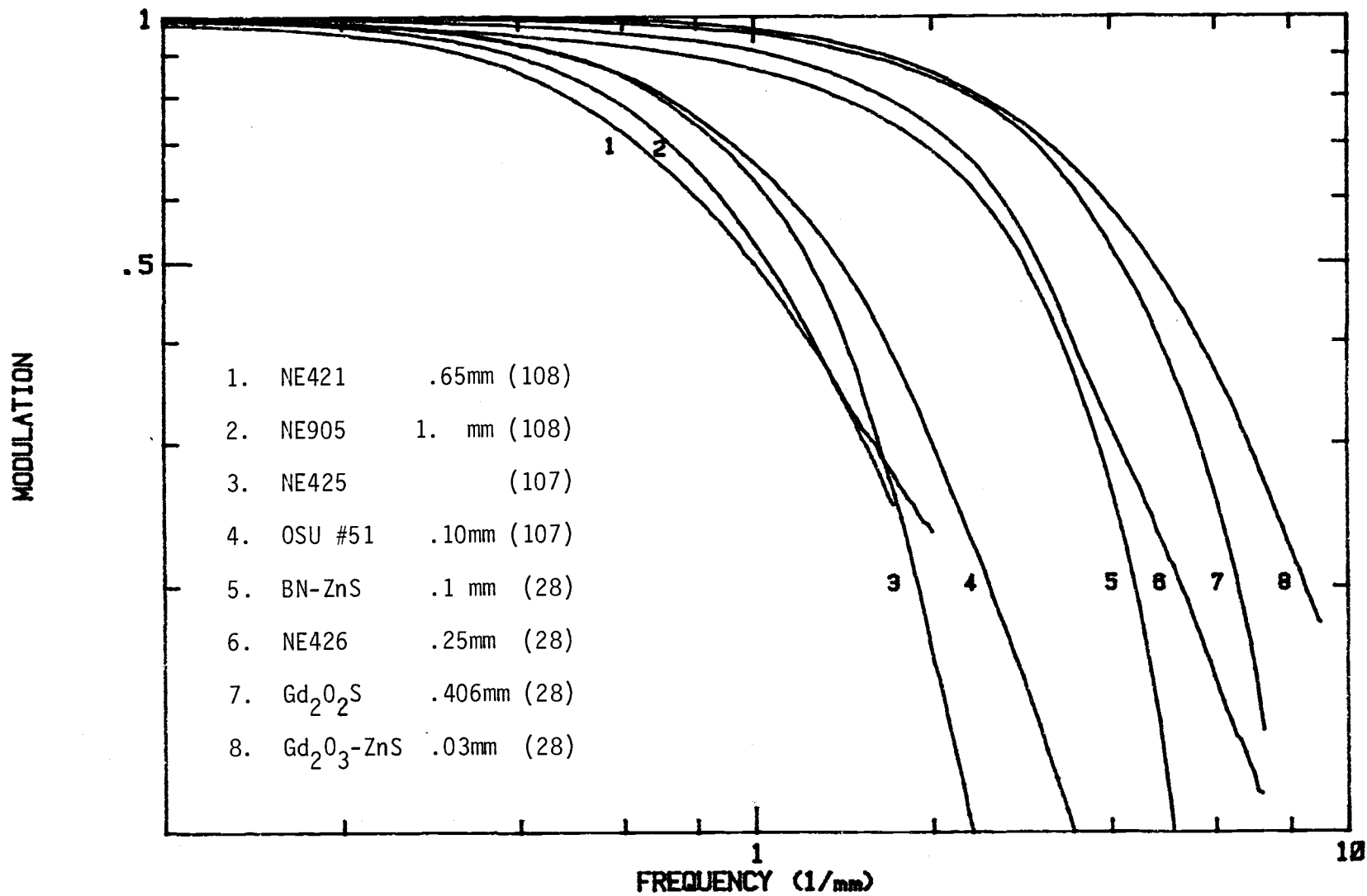


Fig. 6.1: Modulation characteristics of several scintillators.

energy and number has not improved efficiency of gadolinium or BN-ZnS above LiF-ZnS scintillators. Also, the relatively low efficiency of cerium oxide in glass scintillators reduces their potential for high efficiency. Similarly, use of ZnS, which remains the most efficient phosphor available, has an inherent disadvantage because of its poor light transmission.

Table 6.1 summarizes the absolute efficiency values for the different optimum forms of scintillators discussed. Some calculation was necessary to arrive with radiant units based on measurements performed by Spowart upon the NE905 glass (86). As shown the NE426 scintillator heads the list in efficiency followed by the NE905 glass with and without correction then the Gd_2O_2S scintillator. Some radiographic efficiency measurements (i.e. photographic density measurements following direct exposure of scintillator on film) have been performed which suggest that glass and Gd_2O_2S scintillators both have 1/10 to 1/24 the efficiency of the NE426 and similar measurements of Gd_2O_3 -ZnS indicate a radiographic efficiency 1/55 the NE426 (40,28).

6.2.1.3 Other considerations

There are other considerations which determine suitability of a scintillator for a high speed neutron.

Table 6.1: Absolute efficiency of optimum forms of LiF-ZnS, glass, and Gd₂O₂S scintillators (86,87).

Scintillator	Efficiency		
	Mev/η (x10 ⁻³)	Absolute microW/cm ² -nv (x10 ⁻⁹)	Relative
NE426	31.0	4.97	1
NE905 (1mm uncorrected for internal reflection)	6.94	1.11	1/4
NE905 (1mm corrected for internal reflection)	2.38	.382	1/10
Gd ₂ O ₂ S	.655	.105	1/50

radiography system. Phosphor persistence of glass (98ns) and nickel quenched ZnS (200ns) phosphor based scintillators is negligible in comparison to Gd_2O_2S which has a persistence as high as 400 microseconds, a persistence so high as to make recording linear object motion above 2ft/s (.6m/s) impractical since its motion blur would exceed resolution of typical LiF-ZnS scintillators at this point. In some cases the gamma sensitivity of a scintillator is also of concern. The NE905 glass is greater than 6 times more sensitive to gamma radiation than LiF-ZnS scintillators and gadolinium scintillators are not significantly better (120). Finally, due to the short wavelength emission of glass scintillators (395nm), fiber optics glasses with high ultraviolet transmission may be necessary for efficient coupling to an intensifier.

6.2.1.4 Optimum applications

Since each form of scintillator has its own advantages, choosing the best scintillator for each motion radiography application is more appropriate than seeking one for all applications. For the highest speed objects recorded under the lowest exposure conditions where a need for high resolution is not required, the LiF- or BN-ZnS scintillators serve best. If high

resolution images are required of slowly moving objects and high flux levels are available, then Gd_2O_2S scintillators should be used. These scintillators are most suitable for videography with a reactor due to the low frame rates typical of this method. Finally, glass scintillators are adequate for moderate levels of exposure or resolution.

6.2.1.5 Advanced constructions

Steps can be taken to improve resolution of glass and granular scintillators further. One interesting means of construction uses layered vapor deposition of the ZnS phosphor and Li^6 neutron detector to improve resolution (128). This procedure is capable of creating extremely thin layers without need for a binding agent and allows optimum dimensioning of layer thickness with respect to particle range. Research based on this technique demonstrated an efficiency 1/6 that of the NE426 using optimum thickness layers of 20 and 15 microns for Li^6F and ZnS respectfully. Unlike homogeneous mixtures of phosphor and detector, the thinly layered construction of this scintillator concentrates emission to a single plane thereby reducing the region light is scattered inside the scintillator. Also, resolution could be improved by constructing a glass scintillator

fiber optics bundle thereby allowing high resolution for thicker and more efficient samples. Such a technique has been successful in physics experiments (129,130). Both these unique constructions have not been reported for use in neutron radiography as yet.

6.2.2 Intensifiers

6.2.3.1 Gain

Since the time high speed neutron radiography was first implemented at OSU, second and third generation image intensifiers have become viable and are now the favored forms of image intensification. The construction differences in each generation are:

1. First generation image intensifiers employ in each stage a photoemissive surface (the photocathode) to convert incident light to photoelectrons, a high voltage source to accelerate the photoelectrons, and an output phosphor to display an amplified image.
2. Second generation image intensifiers are different from first generation image intensifiers fundamentally in the amplification process. A microchannel plate (MCP) intensifies the electron image by channel electron multiplication.
3. Third generation image intensifiers are different from the second generation primarily in their photocathode; instead of multialkali photocathodes, high sensitivity GaAs photocathodes are used.

Second and third generation intensifiers are capable of

100 times the luminous gain of their predecessor at 40% of its size. The new generation intensifiers have gains which meet or exceed that of a three stage first generation intensifier in a single stage thereby eliminating the additive effects of distortion, vignetting, and phosphor persistence of multistage tubes. Blooming and "washout" is reduced for bright portions of an image resulting in better contrast rendition in the newer generations. At peak response, third generation image intensifiers have several times the quantum efficiency of multialkali photocathodes. This high sensitivity allows large S/N ratios to be achieved in imaging. Opaque GaAs photocathodes however are only useful since the semitransparent forms have negligible response below 500nm where the entire spectral emission of glass or ZnS phosphor scintillators and the majority of emission by Gd_2O_2S resides (131). Finally, the third generation intensifier has been noted to possess improved resolution (132).

For all their advantages, however, either of the new generation intensifiers are very poor replacements for the existing intensifier since their maximum output luminance is 10 or more times less than first generation intensifiers. Hybrid intensifiers, which combine a third or second generation intensifier as input stage with that of a first generation as output, can combine high gain,

S/N ratio, and output luminance attributes of all generations together (133).

The degree of phosphor-film spectral matching and optical transmission has an affect upon system response. Photographic emulsions are most sensitive to ultraviolet light and therefore choice of intensifier phosphors which peak in the ultraviolet region are desirable. The P16 phosphor not only has a greater degree of spectral matching with films than the P11 due to its shorter wavelength of peak emission (see Table A.1) but its persistence is shorter (.1 microseconds) and is reported to offer low blooming and high resolution (134). Standard optical glasses, however, have poor transmission capabilities below 350nm and so in the outcome the P11 phosphor provides best spectral matching unless special glasses (e.g. quartz) are employed.

If object motion is to be analyzed at rates approaching the persistence of the phosphor, gated intensifiers may be used to remove phosphor excitation during periods the camera shutter is closed allowing the display time to decay. This method minimizes persistence blur between consecutive frames.

6.2.3.2 Neutron intensifiers

Neutron image intensifiers have been developed

whereby the neutron-electron conversion occurs directly within the intensifier. Most such intensifiers reported combine a neutron detector such as Gd_2O_3 or Li^6 enriched LiF with phosphor and photocathode as a single conversion screen eliminating optical coupling and the resulting resolution loss (135,136). These conversion screens have been incorporated with large input diameter first generation intensifiers which have "zoom" capability to examine details of a radiograph image under varying magnification. The scintillation-photoemission process, however, is not necessary for intensification since the ions released from neutron interaction may be used directly for amplification in a neutron image intensifier. Microchannel plates can forego the intermediate scintillation-photoemission process since each primary ionizing event can occur in a channel and therefore an image may be displayed under high resolution (137,138).

6.2.3.3 Recommendations

A hybrid intensifier or an optical connection between a third and first generation image intensifier provides the best gain, S/N ratio, and output luminance characteristics available in intensification and should be implemented for neutron radiography with a nickel

quenched P11 output phosphor (or P37 phosphor) unless precautions for high ultraviolet transmission glasses are provided. A neutron intensifier is an alternative however there appears no significant additional advantage in its use except for the choice of imaging large subjects. Selection of an intensifier with gating capability is also desirable.

6.2.4 Camera

If the camera lens system were removed somehow and replaced by an intensifier-film optical transmission system of 100% efficiency the intensifier would not be needed to boost scintillator radiance. However, because even the most efficient lens systems transfer less than 3% of the light collected from the intensifier phosphor onto film, it is not possible to design a high speed framing camera of significantly improved efficiency than the one now in use. If fiber optics were used to couple the display to the film virtually all the phosphor emission would be transferred. Unfortunately, this form of coupling cannot be used in high speed multiframe cameras without breaking optical contact for film shuttering or film motion. An image converter camera, however, offers a means of recording several frames electronically with improved intensification.

The image converter camera uses an electron tube to detect, sweep, and display the input image upon different portions of a screen for framing. Usually between 6 to 20 frames can be recorded on its screen at framing rates up to 6×10^8 fps. Besides offering an effective light gain, these cameras have other advantages:

1. The image may be recorded on Polaroid film which allows results to be examined in seconds.
2. Since the film and display are stationary persistence is no concern.
3. The camera may be triggered by the event within nanoseconds.

Perhaps the greatest disadvantage of the image converter is the relatively few number of frames which can be recorded. Otherwise image converter cameras offer opportunities to increase present exposures and framing rates several magnitudes until quantum limitations become a major restriction not phosphor persistence or film sensitivity. Increased gain also reduces the dependence upon selecting a high efficiency scintillator. In the outcome, system resolution could be increased until dominated by collimation.

6.2.5 Film

A substantial increase in sensitivity may be obtained by attempting higher speed films. As mentioned

earlier, the RAR 2485 film is over 10 times more sensitive than films now in routine use. A high speed orthochromatic film RAR 2495 designed specifically for phosphor screen recording of P11 and other phosphors should also be investigated.

6.3 RECOMMENDATIONS

Significant advances in resolution and noise reduction appear unlikely unless a high resolution and efficiency scintillator is discovered and incident neutron intensity is increased; neither are probable in the near future. Instead since the granular, glass, and Gd_2O_3 -ZnS scintillators each have their advantage, the best scintillator is that which is most appropriate for the application. These scintillators proceed in order of increasing resolution and decreasing efficiency; scintillators which begin this list are the primary consideration for applications which require the shortest exposures. Gd_2O_2S scintillators are best suited for videography using a reactor due to their high persistence.

The next consideration in gain and noise reduction regards the intensifier. A hybrid intensifier with an opaque GaAs photocathode exhibits high sensitivity, gain, resolution, and output luminance and is the most suitable

replacement for the obsolete intensifier in use. A large input diameter neutron intensifier with variable magnification is also an option. Gating capability and a short persistence P11 phosphor should be specified.

Improved system gain and reduced exposure times are viable, however, if optical transmission loss is reduced or more sensitive films are used. In the short run, higher speed films may be implemented however the next significant improvement in gain requires replacement of the rotating prism camera with an image converter. High resolution low efficiency scintillators could then be employed since exposure would no longer be limited by transmission. In the outcome, system resolution could be increased at moderate exposures until dominated by collimation.

VII. REFERENCES

1. H. Kallman. "Neutron radiography," Research, 1 (1948), 254.
2. A. R. Spowart. "Neutron radiography," Journal of Physics E, 5 (1972), 498.
3. R. L. Newacheck. "Applications and trends of industrial neutron radiography," Neutron Radiography, ed. J. P. Barton and V. D. Hardt, D. Reidel Pub. Co., 1983, 77.
4. J. P. Barton. "Introduction to the conference," Reference 3, 3.
5. W. L. Whittemore and H. Berger. "Physics of neutron radiography using selected energy neutrons," Reference 3, 26-27.
6. M. R. Hawkesworth and J. Walker. "Basic principles of thermal neutron radiography," Reference 3, 8.
7. S. O. Schriber, et. al. "A compact neutron source for research and industrial applications," IEEE Transactions on Nuclear Science, NS-30 (1983), 1668.
8. Jeffry A. Stokes, Lewis A. Parks, Charles A. Preskitt and Joseph John. "Performance of neutron radiography systems using particle accelerators," IEEE Transactions on Nuclear Science, NS-30 (1983), 1623.
9. Science Appl. Inc., La Jolla, Commercial literature, 1977.
10. R. Halmshaw. Industrial Radiology, Applied Science Publishers, 1982, 309.
11. R. J. Norton. M. Sc. Dissertation, Brunel University, 1980.
12. B. L. Blanks and R. A. Morris. "Experiments with foil-film combinations and collimators for neutron radiography," Materials Evaluation, 24 (1966), 76.
13. A. Choudry and P. K. Bandopadhyay. "Thermal neutron

- focusing by tapered rectangular collimators," Nuclear Instruments and Methods, 92 (1971), 339.
14. J. P. Barton. "Divergent beam collimator for neutron radiography," Materials Evaluation, 25 (1967), 45A.
 15. W. A. Carbiener. Nucl. Appl., 2 (1966), 468.
 16. Reference 6, 17.
 17. H. Berger. Non-destructive Testing, 20 (1962), 185.
 18. Reference 6, 18.
 19. A. R. Spowart. "Mobil unit for neutron radiography," Nuclear Engineering, London, 13 (1968), 429.
 20. H. Berger. "Neutron Radiography," Scientific American, 207 (Nov. 1962), 107.
 21. A. R. Spowart. "Optimizing neutron scintillators for neutron radiography," British Journal of Nondestructive Testing, 11 (March 1969), 2.
 22. P. G. Kootz, G. R. Keepin, and J. E. Ashley. "ZnS(Ag) phosphor mixtures for neutron scintillator counting," Review of Scientific Instruments, 26 (1955), 354.
 23. R. H. Bossi. High Speed Motion Neutron Radiography, Doctoral Dissertation, Oregon State University, 1976, 56.
 24. K. H. Sun, P. R. Malmberg, and F. A. Pecjak. "High-efficiency slow neutron scintillation counters," Nucleonics, 14 (1956), 46.
 25. Reference 23, 54.
 26. R. Stedman. "Scintillator for thermal neutrons using ^6LiF and ZnS(Ag)," Review of Scientific Instruments, 31 (1960), 156.
 27. G. Matsumoto, M. Teramura, K. Okubo, and Y. Ikeda. "A boron nitride scintillation converter for neutron radiography," Materials Evaluation, 42 (1984), 1379.
 28. J. T. Lindsay, D. M. Alger, S. R. Bull, and H. Miller. "MTF analysis of the near-real time neutron radiography facility at MURR," Reference 3, 623.

29. K. L. Swinth. "Low flux neutron imaging," British Journal of Nondestructive Testing, 16 (1974), 129.
30. J. A. Harvey and N. W. Hill. "Scintillation detectors for neutron physics research," Nuclear Instruments and Methods, 162 (1979), 511.
31. Reference 6, 16.
32. Reference 23, 51.
33. Reference 2, 502.
34. H. Berger and N. P. Lapinski. "Improved sensitivity and contrast track etch thermal neutron radiography," Transactions of the American Nuclear Society, 15 (1972), 120.
35. H. Berger. "Track-etch radiography," Nuclear Technology, 19 (1973), 191.
36. James A. Morley, "Two techniques to increase contrast of track neutron radiographs," Transactions of the American Nuclear Society, 15 (1972), 120.
37. M. Frank and L. Herforth. Kernenergie, 6 (1961), 435.
38. R. H. Herz. The Photographic Action of Ionizing Radiation, Wiley-Interscience, 1969, 165.
39. H. Tourwe. "Description and characterization of the BR1 neutron radiography facility," Reference 3, 186.
40. Reference 6, 19.
41. M. V. Davis, H. Berger, and F. Patricelli. "Real-time neutron radiography at the Georgia Tech Research Reactor," Transactions of the American Nuclear Society, 41 (1982), 241.
42. Lawrence E. Bryant, Jr. "Real time radiography using X-rays and neutrons," Los Alamos Mini Review, LALP-83-45 (Oct. 1983).
43. Kenneth Kalata. "A computer controlled television detector for light, X-rays and particles," IEEE Transactions on Nuclear Science, NS-28 (1981), 852.

44. G. Charpak, G. Melchart, G. Peterson and F. Sauli. "The multistep chamber as a high accuracy localization device for beta chromatography and slow neutron imaging," IEEE Transactions on Nuclear Science, NS-28 (1981), 849.
45. Joseph E. Hall and James D. Austrey. "Real-time image enhancement using 3x3 pixel neighborhood operator functions," Optical Engineering, 19 (1980), 421.
46. John P. Choisser. "Detecting photoelectron images with semiconductor arrays for multichannel photon counting," Optical Engineering, 16 (1977), 262.
47. Selig N. Kaplan, Bruce A. Director, Victor Perez-Medez, and Kenneth H. Valentine, "Digital neutron radiography using plane converters with multiwire proportional chambers," Reference 3, 961.
48. J. L. Wiza. "Microchannel plate detectors," Nuclear Instruments and Methods, 162 (1979), 587.
49. S. K. Wang. High Speed Motion Neutron Radiography of Two-Phase Flow, Masters Thesis, Oregon State University, 1980.
50. Reference 23, 131-4.
51. Reference 23, 122-131.
52. C. T. Oien. Feasibility of Neutron Radiographing Reactor Fuel Assemblies, Masters Thesis, Oregon State University, 1980.
53. Dennis A. Tollefson. Application of High Speed Motion Neutron Radiography Techniques to Liquid Streams Injected into a Pressurized Steel Chamber, Masters Thesis, Oregon State University, 1981.
54. A. H. Robinson, J. P. Barton. "High-speed motion neutron radiography," Transactions of the American Nuclear Society, 15 (1972), 140.
55. R. H. Bossi, A. H. Robinson, and J. B. Barton. "High-speed motion neutron radiography," Nuclear Technology, 59 (1982), 363.
56. Mossoud T. Simnad, Fabian C. Fousee, and Gordon B. West. "Fuel elements for pulsed TRIGA research reactors," Nuclear Technology, 28 (1976), 40.

57. V. K. Russel and D. L. Duncan. "An analytical model for nonadiabatic reactor excursions," Transactions of the American Nuclear Society, 43 (1982), 714.
58. A. H. Robinson and G. L. Upham. "Applications of time-sharing computer to reactor problems and simulation of TRIGA reactor pulses," Simulation, 11 (1968), 203.
59. Safety Analysis Report of the Oregon State TRIGA Research Reactor, Oregon State University, August 1968, 4-104.
60. Reference 53, 65.
61. Reference 23, 43.
62. Amendment #4 to the Safety Analysis Report for the Oregon State TRIGA Reactor (OSTR), April 3, 1975 (Rev. September 11, 1975), 28.
63. Safety Analysis Report for the Torrey Pines TRIGA Mark III Reactor, GA-9064, January 5, 1970, 3-26, 8-12.
64. Reference 56, 47.
65. D. L. Hetrick. Dynamics of Nuclear Reactors, University of Chicago Press, 1971, 169.
66. Reference 62, 19.
67. Richard S. Stone, H. P. Sleeper Jr., Ralph H. Stahl, and Gordon West. "Transient behavior of TRIGA, a zirconium-hydride, water-moderated reactor," Nuclear Science and Instrumentation, 6 (1959), 258.
68. Terry Anderson. Radiation Center, Oregon State University, private communication.
69. Reference 62, 13.
70. Reference 23, 39.
71. Reference 23, 55-60.
72. Reference 23, 65.
73. Lucien M. Biberman. "Specifications for electronic image forming devices," Photoelectronic Imaging

- Devices, Vol. 1, Lucien M. Biberman and Sol Nudelman, ed., Plenum Press, 1971, 245.
74. Leo Levi. Applied Optics, Vol. 2, John Wiley and Sons, 1980, 704-14.
75. Rudolf Kingslake. Optical System Design, Academic Press, 1983, 18.
76. Frank Scott and Denis Frauehofer. "The modulation transfer function and methods of measurement," Reference 73, 291.
77. R. P. Jenks, K. Greek, and A. H. Robinson. Neutron Radiography Report: Beam Characteristics for BP #3, Radiation Center, Oregon State University, July 21, 1983, unpublished.
78. Gerhart Friedlander, Joseph W. Kennedy, and Julian Malcom Miller. Nuclear and Radiochemistry, 2ed., John Wiley and Sons, 1964, 95.
79. Humbolt W. Leverenz. An Introduction to Luminescence of Solids, John Wiley and Sons, 1950, 320.
80. Reactor Physics Constants ANL-5800, 2ed., United States Atomic Energy Commission, July 1963, 688.
81. G. F. J. Garlick. "Cathodo- and radioluminescence," Luminescence of Inorganic Solids, Paul Goldberg, ed., Academic Press, 1966, 699.
82. Arthur H. Snell, ed. Nuclear Instruments and their uses, Vol. 1, John Wiley and Sons, 1962, 105.
83. Reference 79, 317.
84. Reference 23, 77-8.
85. Jack A. Bamberg. "Scintillation detector optimization using GUERAP-3," Radiation Scattering in Optical Systems, Proceedings of the Society of Photo-Optical Instrumentation Engineers (SPIE), Gary H. Hunt, ed., Sept. 30 - Oct. 1, 1980, 90.
86. A. R. Spowart. "Measurement of the absolute scintillation efficiency of granular and glass neutron scintillators," Nuclear Instruments and Methods, 75 (1969), 35.
87. Vicki Ellen Panhuse. An Investigation of an Imaging

- System for Portable Real Time Neutron Radiography, PhD dissertation, University of Missouri-Columbia, 1979, 136.
88. Reference 79, 210.
 89. A. R. Spowart. "Resolution improvements in neutron radiography with phosphor detectors," The Journal of Photographic Science, 19 (1971), 9.
 90. T. Tojo and T. Nakajima. "Preparation of thermal neutron scintillators based on a mixture of ZnS(Ag), ^6LiF and polyethylene," Nuclear Instruments and Methods, 53 (1967), 163.
 91. A. R. Spowart. "Optimizing neutron scintillators for neutron radiography," British Journal of Nondestructive Testing, 11 (March 1969), 7.
 92. R. Stedman, "Scintillation counters for thermal neutrons using ^6LiF and ZnS(Ag)," CRRP-931, Atomic Energy of Canada Limited, Chalk River Project, May 1960.
 93. Reference 23, 75.
 94. Reference 23, 60.
 95. Reference 89, 5.
 96. W. B. Allen. Fiber Optics Theory and Practice, Plenum Press, 1973, 11.
 97. Reference Data for Radio Engineers, H. K. Sams Co., 1975, 17-38.
 98. Allan Stimson. Photometry and Radiometry for Engineers, Wiley-Interscience, 1974, 406.
 99. William G. Hyzer. Photographic Instrumentation Science and Engineering, U.S. Government Printing Office, 1965, 4-25.
 100. M. R. Hawkesworth. "Neutron radiography: equipment and methods," Atomic Energy Review, 15 (1977), 196.
 101. Reference 23, 91.
 102. Reference 10, 312.

103. R. H. Bossi, J. L. Cason and C. N. Jackson, Jr., "The modulation transfer function and effective focal spot as related to neutron radiography," Materials Evaluation, May 1972, 103.
104. Y. Segal, A. Gutman, A. Fishman and A. Notea, "Point spread functions due to neutron scattering in thermal neutron radiography of aluminum, iron, zircaloy and polyethelene (sic) objects," Nuclear Instruments and Methods, 197 (1982), 557.
105. Reference 74, 742.
106. Ronald N. Bracewell, The Fourier Transform and its Applications, 2 ed., McGraw Hill Book Company, 1978, 249.
107. Reference 23, 101.
108. M. R. Hawkesworth and M. A. Raoof, "Some measurements of the resolving power of intensifying screens used for radiography with beams of thermal neutrons," Journal of Physics E, 3 (1970), 853.
109. Reference 74, 576.
110. L. Levi. "Detector response and perfect-lens-MTF in polychromatic light," Applied Optics, 7 (1969), 607.
111. Harold V. Soule. Electro-Optical Photography at Low Illumination Levels, John Wiley and Sons Inc., 1968, 329.
112. C. B. Johnson. "MTF parameters for all photographic films listed in Kodak pamphlet P-49," Applied Optics, 15 (1976), 1130.
113. Reference 111, 266.
114. J. F. Mullaney, F. Reines, and H. G. Weiss. "Excitation time of silver activated zinc sulphide on electron bombardment," Physics Review, 74 (1948), 491-2.
115. L. Levi. "Motion blurring with decaying detector response," Applied Optics, 10 (1971), 39.
116. Reference 110, 154.
117. Joseph A. Davis. "Recent advances in cathode-ray

- tube display devices," Recent Advances in Display Media, NASA, SP-159 (1968) 32-3.
118. A. H. Robinson, J. P. Barton. "High speed neutron radiography," Transactions of the American Nuclear Society, 15 (1972), 140.
119. Reference 76, 710.
120. A. R. Spowart. "Measurement of gamma sensitivity of granular and glass neutron scintillators and films," Nuclear Instruments and Methods, 82 (1970), 1.
121. Reference 111, 285.
122. Reference 74, 750.
123. Reference 10, 297.
124. Reference 89, 10.
125. Reference 89, 3.
126. Vicki E. Panhuise, Stanley R. Bull and James A. Seydel. "Scintillation converter screen investigation for real time neutron radiography," ANS Transactions, American Nuclear Society, 35 (1980), 172.
127. M. V. Davis, H. Berger and F. Patricelli. "Real time radiography at the Georgia Tech Research Reactor," ANS Transactions, American Nuclear Society, 41 (1982), 241.
128. F. Mantler-Niederstatter, F. Bensch, and F. Grass. "An extremely thin scintillation detector for thermal neutrons," Nuclear Instruments and Methods, 142 (1977), 463.
129. R. Ruchti et. al. "Scintillating glass, fiber optic plate detectors for active target and tracking applications in high energy physics experiments," IEEE Transactions on Nuclear Science, NS-31 (1984), 69.
130. R. Ruchti. "A scintillating glass, fiber-optic plate imaging system for active target and tracking applications in high energy physics experiments," IEEE Transactions on Nuclear Science, NS-30 (1983), 40.

131. Carl M. Thomas. "Photocathodes," Image Intensifiers: Technology, Performance, Requirements and Applications, Avin D. Schnitzler and Myron W. Klein. ed., SPIE Proceedings, SPIE, 1974, 71.
132. J. R. Howorth et. al. "Exploring the limits of performance of third generation image intensifiers," Vacuum, 30 (1980), 551.
133. Illes P. Csorba. Image Tubes, Howard W. Sams, 1985, 40.
134. William G. Hyzer. Engineering and Scientific High Speed Photography, Macmillian Co., 1962, 382.
135. H. Berger. "Characteristics of a thermal neutron television imaging system," Materials Evaluation, 24 (1966), 475.
136. M. Verat, H. Rougeot, and B. Driard. "Neutron image intensifier tubes," Reference 3, 601.
137. R. A. Schrack. "A microchannel plate neutron detector," Nuclear Instruments and Methods in Physics Research (Sec. A), 222 (1984), 499.
138. B. J. Kaiser, W. R. Sloan, J. L. Fuller. "Pinhole imaging of high-energy neutrons, gamma rays, and charged particles using microchannel plates," ANS Transactions, American Nuclear Society, 45 (1983), 226.

IX. APPENDICES

A. SPECTRAL MATCHING FACTORS

A.1 Source-detector spectral matching

Overall transmission between radiant source and detector configurations is dependent upon not only the magnitude of source emission and detector sensitivity but the spectral response of the devices themselves. To simplify source-detector transmission analysis, a dimensionless spectral matching factor may be used to represent the fraction of source spectrum recorded within the envelope of the detector spectrum. The overall source-detector radiant transfer function may then be represented by

$$s_i/s_o = g_0 \frac{\int_0^\infty e_\lambda \omega_\lambda d\lambda}{\int_0^\infty \omega_\lambda d\lambda}$$

$$= g_0 \alpha(i,o)$$

where

- g_0 = maximum spectral gain of detector
- e_λ = normalized spectral response of detector at wavelength λ
- ω_λ = normalized spectral emission of source at wavelength λ
- $\alpha(i,o)$ = spectral matching factor for given source i and detector o .

Spectral matching factors must be calculated

individually for each source-transmission-detector combination--usually by means of numerical integration techniques. The spectral matching factor is bounded between a value of unity for perfect detector response within the source bandwidth and zero when no detector response occurs. Table A.1 provides a short listing of such factors provided from the references.

A few entries on Table A.1 include spectral matching factors of blue sensitive, orthochromatic and panchromatic films and lens transmission through an equivalent of 1/2" dense flint glass. Two sources were available on phosphor-film spectral matching factors and each are normalized to a peak wavelength of 400nm however the outcome of each author's value is different. Visual spectral matching factors are also included for the light adapted (photopic) eye.

A.2 Lens transmission

Since lenses are not standardized to any particular thickness of glass for the sake of equivalent transmission capability, the tabulated transmission factor for 1/2" dense flint glass would not be of much universal use if it were not observed that lens thickness degrades transmission with the power of the multiple in thickness. Stated in equation form

Table A.1: Spectral Matching Factors (1-3).

Phosphor	Photocathodes				Eye	E - p
	S1	S11	S20	S25	photopic	$\lambda/1200$
P4	0.349	601	699	746	402	437
P5	0.410	892	895	933	329	
P11	0.207	917	879	908	201	392
P16	0.827	880	902	972	003	326
P20	0.393	428	583	639	707	476
P24	0.277	700	727	768	540	437
P31	0.276	698	722	868	626	437
NaI	0.534	889	900	933	046	348

	Films			Lens Trans.
	Blue-sens.	Ortho.	Panchro.	1/2" D Flint
P5	0.68	.87		.85
P11	0.50, .429	.87, .243	.688	.90
P16	0.95, 1.341	.93, .941	.969	.70

$$\alpha(\omega_\lambda, \text{lens } x'') = \alpha(\omega_\lambda, \text{lens } \frac{1}{2}'')^{2x}$$

This equation may be used to calculate lens transmission losses with lenses thicker than 1/2".

For the Nikon f/1.2 lens with an equivalent glass thickness of 1.5" in use with the Hycam, the fraction of transmission by a P11 source is

$$\alpha(\text{P11, lens } 1\frac{1}{2}'') = 0.729$$

A.3 Photometric to radiometric conversion

Units of optical radiation may be photometric (light capable of producing direct visual response, 280-770nm) and radiometric (optical radiation, 1nm-1mm) quantities however only radiometric units are meaningful for use with detectors other than the eye. Often conversions are necessary for luminous flux expressed in lumens to radiant flux in watts for a specific spectral distribution ω_λ and may be accomplished given the luminous efficacy, K , the ratio of luminous to radiant flux ϕ_v/ϕ_e . Given the luminous flux of the spectral distribution ω_λ , its equivalent radiometric flux in watts

is

$$\phi_e = \frac{\phi_v}{680 \text{lumen/W } \alpha(\omega_\lambda, \text{eye})}$$

where

ϕ_v = luminous flux (lumen).

ϕ_e = radiant flux (W).

A.4 Alternate source response predictions

In certain detector applications, such as television cameras or photographic films, the response of the detector is known in photometric units for a calibration source and the output of the detector is to be predicted for an alternate source. In the case of photographic film, spectral matching factors may be used to determine the magnitude of exposure correction necessary to produce equivalent film densities between calibration and alternate sources. For radiant exposure units, the relationship between both types of sources is

$$H(\text{cal}) = \frac{\alpha(\text{cal}, \text{film})}{\alpha(\omega_\lambda, \text{film})} H(\omega_\lambda)$$

If the calibration exposure is presented in photometric units this becomes

$$H(\text{cal})(\text{mcs}) = 0.68 \alpha(\text{cal}, \text{eye}) \frac{\alpha(\text{cal}, \text{film})}{\alpha(\omega_\lambda, \text{film})} H(\omega_\lambda)(\text{ergs}/\text{cm}^2)$$

where a conversion has been made between the most common photographic exposure units for luminous exposure (the meter-candle-second or lumen-s/m²) and radiant exposure (ergs/cm²). For a P11 phosphor source exposure conversion to daylight or tungsten luminous exposure

$$\log H(\text{cal})(\text{mcs}) = \log H(\omega_\lambda)(\text{ergs}/\text{cm}^2) + \log .68 \frac{\alpha(\text{cal}, \text{film})}{\alpha(\omega_\lambda, \text{film})}$$

where one step further was followed to convert to the logarithm of exposure. If daylight or tungsten calibration sources are specified, their luminous exposure required to produce an equivalent panchromatic film response for a P11 radiant exposure is

$$\log H(\text{tungsten}, \text{panchro})(\text{mcs}) = \log H(\text{P11}, \text{panchro})(\text{ergs}/\text{cm}^2) - 1.342$$

$$\log H(\text{daylight}, \text{panchro})(\text{mcs}) = \log H(\text{P11}, \text{panchro})(\text{ergs}/\text{cm}^2) - .625$$

where the spectral matching factors for the calibration sources applied over a 300 to 1200nm interval are

$$\begin{aligned} \alpha(\text{tungsten}, \text{panchro}) &= .259 \\ \alpha(\text{tungsten}, \text{eye}) &= .1777 \\ \alpha(\text{daylight}, \text{panchro}) &= .648 \\ \alpha(\text{daylight}, \text{eye}) &= .3702 \end{aligned} \quad (3).$$

A.5 Radiometric to quantum conversions

Since the energy of each photon released by a monochromatic source is hc/λ , then the photon flow rate corresponding to their energy of emission from source spectral distribution ω_λ is

$$\begin{aligned}\phi_v/\phi_e &= \frac{\int_0^\infty \lambda/hc \omega_\lambda d\lambda}{\int_0^\infty \omega_\lambda d\lambda} \\ &= \frac{\alpha(\lambda, \omega_\lambda)}{hc}\end{aligned}$$

where

h = Planck's constant (4.136×10^{-21} Mev-s).

c = speed of light (2.997×10^{17} nm/s).

ϕ_v = quantum flux (photons/s).

ϕ_e = radiant flux (W).

$\alpha(\lambda, \omega_\lambda)$ = average wavelength weighted over source spectral distribution (nm).

This relationship enables source emission energy-to-photon conversion. The factor $\alpha(\lambda, \omega_\lambda)$ is not treated like a spectral matching factor although it shares its symbol. Table A.1 has tabulated values of scaled by 1200nm for a number of phosphors whose emission is confined to the 300-1200nm spectral range. As an

example, the radiometric-to-photon flow rate of the P11 phosphor is

$$\begin{aligned}\phi_v/\phi_e &= \frac{1200\alpha(\lambda/1200, P11)}{hc} \\ &= 2.37 \times 10^{18} \frac{\text{photons/s}}{\text{W}}\end{aligned}$$

REFERENCES

1. Leo Beiser. "A unified approach to photographic recording from the cathode-ray tube," Photographic Science and Engineering, 7 (1963), 196.
2. Edward H. Eberhardt. "Source-detector spectral matching factors," Applied Optics, 7 (1968), 2037.
3. Leo Levi. Applied Optics, Vol. 2, John Wiley & Sons, 1980, 1083.

B. LiF-ZnS SCINTILLATOR EFFICIENCY PROGRAM

B.1 Description

These programs attempt to calculate the absolute efficiency of LiF-ZnS scintillators with polyethylene or waterglass binders.

B.2 Theory

A Monte Carlo solution for excitation of the ZnS phosphor (E_n) and a neutron and light transmission equation (Eq. 4.4) are combined in this program to determine the ratio of light energy emitted from the scintillator to the number of thermal neutrons which impinge upon it (Eq. 4.2). As a result of this work, it was confirmed an approximation for E_n (Eq. 4.3) may be used instead of the Monte Carlo solution for waterglass binder scintillators with a great reduction in computer time.

The majority of either program calculates E_n by the Monte Carlo method for a slab whose two regions are dimensioned according to the volumetric concentrations of ZnS and LiF and binder within the scintillator. The inner slab boundary (A) represents half the average chord length and the outer boundary (B) is proportioned

according to the ratio of the total volume of all materials in the scintillator to the volume of ZnS, i.e. $B = A(V_t/V_z)$. The only physical dimension which needs to be specified, therefore, is the phosphor diameter. Alpha and triton path simulation originate in the LiF region between boundaries A and B and track through the slab losing their energy in the fraction determined by a two value approximation of the Bragg curve (69% of particle initial energy is lost over its first 85% of range and 31% of its initial energy is lost over the remaining range). The range in each region is determined by its material concentration. Particles are also assumed to reflect from the outer boundaries. The energy deposited in the ZnS region is recorded over the lifetime of each particle which ends when all its energy has been lost.

B.3 Use

Figures B.1 and B.2 provide listings for the programs which solve for polyethylene and waterglass binder scintillators. The programs are identical aside from treating either a constant volume or weight ratio of binder to LiF, the range-energy constants for the binder, and the binder density. Both programs receive input from a file instead of interactively. Efficiency values are printed to the designated output device once each batch

is completed and their average and standard deviation is printed upon program completion. Tables B.2 and B.3 are sample output listings for either program. The fraction of energy which excites the phosphor is included in the output. Table B.1 defines the symbol designations for both programs.

B.4 Accuracy

Accuracy of the results deteriorates when scintillators with low concentrations of LiF are simulated and therefore a greater number of iterations are required for the result to converge. The interbatch standard deviation is printed as an aid to estimate the accuracy.

Table B.1: SCNT symbols.

Symbol	Meaning
A	Inner boundary of slab (microns).
B	Outer boundary of slab (microns).
BDR	Volume ratio of binder to total volume.
CIP	Phosphor efficiency.
D	Li ⁶ enrichment of LiF.
E	Efficiency 1. Absolute (MeV/n). 2. Energy fraction deposited in ZnS.
EB	Required particle-boundary energy (MeV).
EF	Particle energy (MeV) 1,1. Triton, 69% energy. 1,2. Triton, 31% energy. 2,1. Alpha, 69% energy. 2,2. Alpha, 31% energy.
ENZS	Energy deposited in ZnS (MeV).
ET	Efficiency 1. Absolute. 2. Energy fraction absorbed in ZnS.
IHIST	Number of histories/batch.
NB	Number of batches.
RB	Binder particle range (microns). 1. Triton. 2. Alpha.
RHOB	Density of binder (g/cm ³).
RHOL	Density of LiF (g/cm ³).
RHOZ	Density of ZnS (g/cm ³).

Table B.1: SCNT symbols (continued).

Symbol	Meaning
RL	LiF particle range (microns). 1. Triton. 2. Alpha.
RM	Weighted LiF & binder particle range (microns) 1. Triton. 2. Alpha.
RZ	ZnS particle range (microns) 1. Triton. 2. Alpha.
SIGL6	Weighted cross section of Li ⁶ .
SIZE	ZnS diameter (microns).
T	Scintillator thickness (cm).
TRANSFR	Transmission fraction.
U	Direction cosine.
U0	Direction cosine at particle origin.
UL	LiF light attenuation coefficient (cm ⁻¹).
US	Weighted system light attenuation coefficient (cm ⁻¹).
UZ	ZnS light attenuation coefficient (cm ⁻¹).
VBL	Volume ratio of binder to LiF.
VZL	Volume ratio of ZnS to LiF.
W	% range value.
WBL	Weight ratio of binder to LiF.
WZL	Weight ratio of ZnS to LiF.
X	Position in slab (microns).

Table B.1: SCNT symbols (continued).

Symbol	Meaning
X0	Position in slab at particle origin.
XCL6	Macroscopic cross section of Li^6 .

```

$USES APPLESTUFF
PROGRAM SCNT
C THIS PROGRAM CALCULATES THE RADIANT ENERGY OUTPUT FROM A LIF-ZNS
C (POLYETHYLENE BINDER) SCINTILLATOR (MEV/NEUTRON)
C WZL=WEIGHT RATIO OF ZNS/LIF      T=THICKNESS (CM)
C WBL=WEIGHT RATIO OF BINDER/LIF  D=LI6 ENRICHMENT
C SIZE=DIAMETER OF ZNS GRAINS (MICRONS)
EXTERNAL RAND
COMMON IX
DIMENSION ET(2),C(2),RB(2),RL(2),RZ(2),R(2,2),EP(2,2,2),EF(2,2),
1W(2),RM(2)
CHARACTER FNAME*15
EQUIVALENCE (A,C(2)),(B,C(1))
DATA UL,UZ,RHOL,RHOZ,XCL6,CIP/61.,114.,2.635,4.102,60.2,.23/
DATA RHOB/.93/,RZ/27.8,4.85/,RL/26.6,4.75/,RB/57.8,9.86/
DATA EF/1.88,1.41,.846,.636/,W/.85,.15/,R/4*0./
C READ DATA
REWIND(7)
OPEN(7,FILE='#4:INPUT.TEXT',STATUS='OLD')
50 READ(7,30,END=40)WZL,WBL,T,D,SIZE
30 FORMAT(5F12.8,2I4)
C MISC PARAMETER CALCULATIONS
VZL=WZL*RHOL/RHOZ
VBL=WBL*RHOL/RHOB
A=SIZE/6
VW=(1+VZL+VBL)
B=A*VW/VZL
SIGL6=XCL6*D/VW
US=(UL+VZL*UZ)/VW
TRNSFR=CIP*SIGL6*EXP(-US*T)*(EXP((US-SIGL6)*T)-1)/(US-SIGL6)
DO 20 I=1,2
RM(I)=(RL(I)+VBL*RB(I))/VW
DO 20 L=1,2
EP(1,L,I)=EF(I,L)/(W(L)*RM(I))
20 EP(2,L,I)=EF(I,L)/(W(L)*RZ(I))
READ(7,'(3I3)')IHIST,NB,IX
WRITE(*,30)WZL,T,D,O.,SIZE,IHIST,NB
READ(7,'(A15)')FNAME
OPEN(6,FILE=FNAME,STATUS='NEW')
WRITE(6,70)WZL,WBL,T,D,SIZE,IHIST
70 FORMAT('ZNS/LIF WEIGHT RATIO=',F9.6/'BINDER/LIF WGT RATIO=',F9.6/
1'WIDTH=',16X,F7.6,' CM'/'LI6 ENRICHMENT=',6X,F8.6/'ZNS PARTICLE SI
2ZE= ',F6.2,' MICRONS'//I3,' HISTORIES EACH'//5X,'RADIANT EMISSIO
3N ZNS ABS FRAC'/10X,'MEV/N'//)
DO 14 J=1,NB
ENZS=0
C START MONTE CARLO INTERACTION SIMULATION: POSITION & RECOIL ANGLE IN LI
DO 10 M=1,IHIST
XO=(B-A)*RAND()+A
11 UO=2*RAND()-1
IF(UO.EQ.0)GOTO 11
C TRITON (I=1) & ALPHA (I=2) EXCURSIONS
U=UO
DO 10 I=1,2
X=XO
E=EF(I,1)
L=1
K=1
C LIF: REMOVE TRAVEL & REFLECT PARTICLE
1 IF(U) 3,4,4

```

Fig. B.1: Polyethylene binder scintillator program.

```

2 U=-U
3 K=2
4 EB=(C(K)-X)/U*EP(1,L,I)
  IF(E.LE.EB)GOTO 7
  E=E-EB
  X=C(K)
  IF(K-2) 2,6,2
C ZNS: RECORD ENERGY DEPOSITION & REFLECT
5 K=1
  U=-U
6 TF=(2-K)*A
  EB=(TF-X)*EP(2,L,I)/U
  ENZS=ENZS+AMIN1(EB,E)
  IF(E.LE.EB)GOTO 8
  E=E-EB
  X=TF*A
  IF(K-1) 5,4,5
C DETERMINE NEW POSITION & SET FOR SECOND ENERGY GROUP (L=2)
7 N=1
  GOTO 9
8 N=2
9 IF(L.EQ.2)GOTO 10
  L=2
  X=X+E/EP(N,1,I)*U
  E=EF(1,2)
  IF(X-A) 6,6,1
10 U=-UO
C DETERMINE ENERGY DEPOSITED & RADIANT EMISSION
  ET(1)=TRNSFR*ENZS/IHIST
  ET(2)=ENZS/(4.78*IHIST)
  DO 13 IY=1,2
  DO 13 IZ=1,2
13 R(IY,IZ)=R(IY,IZ)+ET(IY)**IZ
14 WRITE(6, '(I3,6X,F7.5,10X,F7.5)')J,(ET(IN),IN=1,2)
C SUMMARIZE RESULTS
  DO 15 I=1,2
  R(I,1)=R(I,1)/NB
15 R(I,2)=SQRT((R(I,2)-NB*R(I,1)**2)/(NB-1))
  WRITE(6, '(/'AVE',6X,F7.5,10X,F7.5)')R(I,1),I=1,2)
  WRITE(6, '(/'STD-DEV',2X,F7.5,10X,F7.5)')R(I,2),I=1,2)
  CLOSE(6)
  DO 60 I=1,2
  DO 60 L=1,2
60 R(I,L)=0.
  GOTO 50
40 CLOSE(7)
  END
  FUNCTION RAND()
C GENERATES RANDOM NUMBERS (0-1)
  COMMON IX
  DO 10 I=1,IX
10 RAND=RANDOM()
  RAND=RAND/32768.
  IX=1
  RETURN
  END

```

Fig. B.1: Polyethylene binder scintillator program (continued).

```

$USES APPLESTUFF
PROGRAM SCNT
C THIS PROGRAM CALCULATES THE RADIANT ENERGY OUTPUT FROM A LIF-ZNS
C (WATERGLASS BINDER) SCINTILLATOR WITH SETTLED PHOSPHOR (MEV/NEUTRON)
C WZL=WEIGHT RATIO OF ZNS/LIF T=SCINTILLATOR THICKNESS (CM)
C D=LI6 ENRICHMENT SIZE=DIAMETER OF ZNS GRAINS (MICRONS)
C BDR=VOLUME RATIO OF BINDER/LIF
EXTERNAL RAND
COMMON IX
DIMENSION ET(2),C(2),RB(2),RL(2),RZ(2),R(2,2),EP(2,2,2),EF(2,2),
1W(2),RM(2)
CHARACTER FNAME*15
EQUIVALENCE (A,C(2)),(B,C(1))
DATA UL,UZ,RHOL,RHOZ,XCL6,CIP/61.,114.,2.635,4.102,60.2,.23/
DATA RHOB/.93/,RZ/27.8,4.85/,RL/26.6,4.75/,RB/36.4,6.38/
DATA EF/1.88,1.41,.846,.636/,W/.85,.15/,R/4*0./
C READ DATA
REWIND(7)
OPEN(7,FILE='#4:INPUT.TEXT',STATUS='OLD')
50 READ(7,30,END=40)WZL,BDR,T,D,SIZE
30 FORMAT(5F12.8,2I4)
C MISC PARAMETER CALCULATIONS
VZL=WZL*RHOL/RHOZ
VBL=BDR*(VZL+1)/(1-BDR)
A=SIZE/6
VW=(1+VZL+VBL)
B=A*VW/VZL
SIGL6=XCL6*D/VW
US=(UL+VZL*UZ)/VW
TRNSFR=CIP*SIGL6*EXP(-US*T)*(EXP((US-SIGL6)*T)-1)/(US-SIGL6)
DO 20 I=1,2
RM(I)=(RL(I)+VBL*RB(I))/VW
DO 20 L=1,2
EP(1,L,I)=EF(I,L)/(W(L)*RM(I))
20 EP(2,L,I)=EF(I,L)/(W(L)*RZ(I))
READ(7,'(3I3)')IHIST,NB,IX
WRITE(*,30)WZL,T,D,O.,SIZE,IHIST,NB
READ(7,'(A15)')FNAME
OPEN(6,FILE=FNAME,STATUS='NEW')
WRITE(6,70)WZL,BDR,T,D,SIZE,IHIST
70 FORMAT('ZNS/LIF WEIGHT RATIO=',F9.6/'BINDER VOLUME RATIO= ',F9.6/
1'WIDTH=',16X,F7.6,' CM/'LI6 ENRICHMENT=',6X,F8.6/'ZNS PARTICLE SI
2ZE= ',F6.2,' MICRONS'//I3,' HISTORIES EACH'//5X,'RADIANT EMISSIO
3N ZNS ABS FRAC'/10X,'MEV/N'//)
DO 14 J=1,NB
ENZS=0
C START MONTE CARLO INTERACTION SIMULATION: POSITION & RECOIL ANGLE IN LI
DO 10 M=1,IHIST
XO=(B-A)*RAND()+A
11 UO=2*RAND()-1
IF(UO.EQ.0)GOTO 11
C TRITON (I=1) & ALPHA (I=2) EXCURSIONS
U=UO
DO 10 I=1,2
X=XO
E=EF(I,1)
L=1
K=1
C LIF: REMOVE TRAVEL & REFLECT PARTICLE
1 IF(U) 3,4,4

```

Fig. B.2: Waterglass binder scintillator program.

```

2 U=-U
3 K=2
4 EB=(C(K)-X)/U*EP(1,L,I)
  IF(E.LE.EB)GOTO 7
  E=E-EB
  X=C(K)
  IF(K-2) 2,6,2
C ZNS: RECORD ENERGY DEPOSITION & REFLECT
5 K=1
  U=-U
6 TF=(2-K)*A
  EB=(TF-X)*EP(2,L,I)/U
  ENZS=ENZS+AMINI(EB,E)
  IF(E.LE.EB)GOTO 8
  E=E-EB
  X=TF*A
  IF(K-1) 5,4,5
C DETERMINE NEW POSITION & SET FOR SECOND ENERGY GROUP (L=2)
7 N=1
  GOTO 9
8 N=2
9 IF(L.EQ.2)GOTO 10
  L=2
  X=X+E/EP(N,1,I)*U
  E=EF(I,2)
  IF(X-A) 6,6,1
10 U=-UO
C DETERMINE ENERGY DEPOSITED & RADIANT EMISSION
  ET(1)=TRNSFR*ENZS/IHIST
  ET(2)=ENZS/(4.78*IHIST)
  DO 13 IY=1,2
  DO 13 IZ=1,2
13 R(IY,IZ)=R(IY,IZ)+ET(IY)**IZ
14 WRITE(6, '(I3,6X,F7.5,10X,F7.5)')J,(ET(IN),IN=1,2)
C SUMMARIZE RESULTS
  DO 15 I=1,2
  R(I,1)=R(I,1)/NB
15 R(I,2)=SQRT((R(I,2)-NB*R(I,1)**2)/(NB-1))
  WRITE(6, '(/'AVE'',6X,F7.5,10X,F7.5)')(R(I,1),I=1,2)
  WRITE(6, '( 'STD-DEV'',2X,F7.5,10X,F7.5)')(R(I,2),I=1,2)
  CLOSE(6)
  DO 60 I=1,2
  DO 60 L=1,2
60 R(I,L)=0.
  GOTO 50
40 CLOSE(7)
  END
  FUNCTION RAND()
C GENERATES RANDOM NUMBERS (0-1)
  COMMON IX
  DO 10 I=1,IX
10 RAND=RANDOM()
  RAND=RAND/32768.
  IX=1
  RETURN
  END

```

Fig. B.2: Waterglass binder scintillator program (continued).

ZNS/LIF WEIGHT RATIO= 2.000000
 BINDER VOLUME RATIO= .400000
 WIDTH= .023000 CM
 LI6 ENRICHMENT= .960000
 ZNS PARTICLE SIZE= 10.00 MICRONS

100 HISTORIES EACH

	RADIANT EMISSION MEV/N	ZNS ABS FRAC
1	.03830	.21495
2	.04439	.24916
3	.03639	.20422
4	.04007	.22488
5	.04294	.24100
6	.03979	.22332
7	.04093	.22971
8	.03683	.20671
9	.04067	.22828
10	.03838	.21539
11	.03850	.21605
12	.04243	.23815
13	.04180	.23460
14	.03791	.21277
15	.03862	.21676
16	.04049	.22726
17	.04268	.23952
18	.04367	.24512
19	.03948	.22159
20	.04082	.22911
21	.03754	.21069
22	.03896	.21865
23	.04339	.24351
24	.04404	.24718
25	.04221	.23688
26	.03927	.22039
27	.04163	.23366
28	.03717	.20861
29	.04509	.25307
30	.04135	.23205
AVE	.04052	.22744
STD-DEV	.00241	.01351

Table B.2: Sample output listing of CH₂ binder scintillator program.

ZNS/LIF WEIGHT RATIO= 3.000000
 BINDER/LIF WGT RATIO= 1.000000
 WIDTH= .022000 CM
 LI6 ENRICHMENT= .960000
 ZNS PARTICLE SIZE= 10.00 MICRONS

100 HISTORIES EACH

	RADIANT EMISSION MEV/N	ZNS ABS FRAC
1	.04566	.34850
2	.03772	.28790
3	.04118	.31435
4	.04212	.32147
5	.04120	.31445
6	.04215	.32171
7	.04106	.31339
8	.04096	.31267
9	.04181	.31909
10	.03784	.28882
11	.04248	.32424
12	.04356	.33245
13	.03992	.30466
14	.03830	.29237
15	.03949	.30139
16	.04211	.32145
17	.04152	.31688
18	.04099	.31284
19	.03930	.29995
20	.03828	.29217
21	.04212	.32150
22	.04311	.32905
23	.04256	.32488
24	.04051	.30920
25	.04029	.30756
26	.04026	.30729
27	.03917	.29896
28	.04138	.31584
29	.04273	.32612
30	.04362	.33295
AVE	.04111	.31380
STD-DEV	.00185	.01413

Table B.3: Sample output listing of waterglass scintillator program.

C. COMPUTER SIMULATION OF OSTR PULSES

C.1 Description

This program solves the Fuch-Nordheim equations by a fourth order Runge-Kutta method and tabulates OSTR core thermal power and peak fuel temperature as a function of time during a pulse. The table also includes the ratio of power to peak power identified by the time following the thermal peak. A heading of thermal and kinetic parameters characteristic to the OSTR used in the program is printed with analytic solutions for peak power, peak fuel temperature occurring at the power peak, and peak fuel temperature following the pulse.

C.2 Theory

The Fuch-Nordheim equations are a pair of nonlinear coupled first order differential equations incorporating the models of variable heat capacity and prompt negative temperature coefficient of reactivity characteristic of OSTR FLIP fuel. The equations assume the fuel is adiabatic and the contribution of delayed neutrons is negligible, and is valid if the pulse is largely determined by prompt thermal and kinetic effects. The equations used have been given earlier as Eq. 2.6 to 2.8

and 2.14. Also, the pulse peak fuel temperature (T_f) is determined from the root of Eq. 2.15.

Average fuel temperatures must be used in the model. For comparisons to core peak fuel temperature given by OSTR instrumentation, all temperatures output from the program are adjusted using a peak to average correction factor to predict the temperature of the instrumented fuel rod.

C.3 Use

A FORTRAN program listing developed for use with an Apple II microcomputer is given in Fig. C.1 and a sample output is displayed in Table C.2.

C.4 Accuracy

Figures 2.5 to 2.9 represent behavior of computed and measured data characteristic of an OSTR pulse and demonstrate the best agreement in OSTR predictions obtained so far. Due to the limited precision of the Apple II microcomputer (6 decimal digits) on which this program was run, a smooth curve was not always obtained from computations. Round-off error may also explain the slight deviation of the power trace shown in Fig. 2.5 from the symmetrical Gaussian shape normally measured.

Some investigation, particularly with peak fuel temperature predictions, showed a reduction in erratic curve behavior could be obtained using a microcomputer with twice the precision. There is some question whether enhanced machine precision is necessary due to inherent deviation of OSTR pulse measurements.

Table C.1: PULSE symbols.

Symbol	Meaning
A (a_1)	Rate of change of prompt negative temperature coefficient with temperature ($MWs/^\circ C^2$).
A0 (α_0)	Prompt negative temperature coefficient evaluated at initial fuel temperature T_{ss} ($MWs/^\circ C$).
B (a_0)	Prompt negative temperature coefficient valid when fuel temperature is $0^\circ C$ ($MWs/^\circ C$).
CO (C_0)	Fuel heat capacity at initial fuel temperature T_{ss} ($MWs/^\circ C$).
CF	Peak to average fuel temperature ratio.
DX	Incremental search temperature increment (C).
EPS	Convergence factor for half interval search of T_{sf} .
GAMA (γ)	Rate of change of heat capacity with temperature ($MWs/^\circ C$).
H	Solution time increment (s).
IPSZ	Number of iterations per tabulated output.
P	Thermal core power (MW).
PO	Initial critical core thermal power (MW).
PDOT (\dot{P})	Rate of change of power with time (MW/s).
PL (l)	Prompt neutron lifetime (s).
PM (P_{max})	Analytic solution for peak pulse power (MW).
RHO (ρ)	Prompt reactivity insertion in dollars.
ROW	Prompt reactivity insertion ($ROW = RHO * .0071$).
T	Average core fuel temperature (C).

Table C.1: PULSE symbols (continued).

Symbol	Meaning
TD (T_{Δ})	Fuel temperature above steady state temperature T_{SS} averaged over core.
TDF ($T_{\Delta f}$)	Final fuel temperature above initial fuel temperature (C).
TDOT (\dot{T})	Rate of change of fuel temperature with time (C/s).
TSS (T_{SS})	Initial fuel temperature (C).
X (t)	Time into pulse (s).
XT	Terminal time for solution (s).
XM	Time when pulse peak occurs (s).
ZM	Peak power calculated by Runge-Kutta method (MW).
ZP	Table listings are printed above this power level (MW).

```

PROGRAM PULSE
C DETERMINES POWER AND TEMP BEHAVIOR OF TRIGA PULSE BY FUCHS-NORDHEIM
C EQUATIONS
  CHARACTER FNAME*6
  REAL K1,K2,K3,K4
  DATA T,ZM,X,EPS,DX,RL,RM,ZP /23.,2*0.,1E-3,10.,50.,900.,10./
C TRIGA DATA FOR FUCHS-NORDHEIM MODEL
C CO & GAMA FOR 85 FLIP ELEMENTS. PO=100 W. CF=PEAK-AVERAGE TEMP RATIO
C ZP=POWER LEVEL ABOVE WHICH RESULTS ARE PRINTED.
C EPS,DX,RL,RM=CONVERGENCE FACTOR, INCREMENT, AND RANGE VALUES FOR HALF
C INTERVAL ROOT SEARCH.
C ALPHA=B+A*T.
  DATA A,B,PL,GAMA,PO,CO/.15E-6,.267E-4,.295E-4,.14E-3,1E-4,.06673/
  DATA CF /1.17/
C FUNCTION DEFINITIONS
  FNT(TD)=3*A*GAMA*TD**3+4*(GAMA*AO+A*CO)*TD**2-6*(GAMA*RHO-AO*CO)
  1*TD-12*RHO*CO
  PDOT(X,T,P)=(RHO-(B+A*T)*(T-TSS))/PL*P
  TDOT(X,T,P)=(P-PO)/(CO+GAMA*(T-TSS))
  TSS=T
  P=PO
  WRITE(*,('ENTER PROMPT REACTIVITY ($)'))
  READ(*,('F6.3'))ROW
  RHO=ROW*.0071
  AO=A*TSS+B
C INCREMENTAL SEARCH FOR TF AT PULSE TAIL
  XR=RL
  5 XL=XR
  XR=XL+DX
  ER=FNT(XR)*FNT(XL)
  IF(ER)15,20,10
  10 IF(XR.LT.RM)GOTO 5
  WRITE(*,('NO TFINAL BETWEEN',F6.2,' TO ',F6.2,' C'))RL,RM
  STOP
C SOLUTION BY HALF INTERVAL METHOD FOR T FINAL
  15 TDF=(XL+XR)/2
  ER=FNT(TDF)*FNT(XL)
  IF(ER.EQ.0)GOTO 20
  IF(ER.LT.0) XR=TDF
  XL=TDF
  IF(ABS((XR-XL)/XR).GT.EPS)GOTO 15
C DETERMINE PMAX AND T @ PEAK ANALYTICALLY
  20 TD=(-AO+SQRT(AO**2+4*A*RHO))/(2*A)
  PM=(-AO*GAMA*TD**3+(3*GAMA*RHO-2*AO*CO)*TD**2+8*RHO*CO*TD)/(12*PL)
  WRITE(*,('OUTPUT DEVICE?'))
  READ(*,('A6'))FNAME
  WRITE(*,('ENTER TERMINAL T, H, & PRINT SIZE'))
  READ(*,27)XT,H,IPSZ
  OPEN(7,FILE=FNAME,STATUS='NEW')
  WRITE(*,27)XT,H,IPSZ
  27 FORMAT(2F12.6,I3)
  WRITE(7,29)ROW,PL,CO,GAMA,A,B,PM,CF*TD+TSS,CF*TDF+TSS,X,T,P
  29 FORMAT('RHO= ',F6.4,' PL= ',E10.4,' CO= ',E11.4,' GAMA= ',E11.4/
  1'A= ',E11.4,' B= ',E11.4,' PEAK POWER=',F10.2,' MW',5X,' T @ PEA
  2K= ',F7.2,' C',5X,' T FINAL=',F7.2,' C'//10X,' TIME',11X,' T',10X,' P(M
  3W)',7X,' P/PMAX',3X,' TIME ABOVE PMAX'/8X,F8.6,5X,F7.2,5X,F9.4)
C PERFORMS RUNGE-KUTTA
  H=H/IPSZ
  30 DO 33 I=1,IPSZ
  K1=H*PDOT(X,T,P)
  Q1=H*TDOT(X,T,P)
  K2=H*PDOT(X+H/2,T+Q1/2,P+K1/2)
  Q2=H*TDOT(X+H/2,T+Q1/2,P+K1/2)
  K3=H*PDOT(X+H/2,T+Q2/2,P+K2/2)
  Q3=H*TDOT(X+H/2,T+Q2/2,P+K2/2)
  K4=H*PDOT(X+H,T+Q3,P+K3)
  Q4=H*TDOT(X+H,T+Q3,P+K3)
  P=P+(K1+2*(K2+K3)+K4)/6
  T=T+(Q1+2*(Q2+Q3)+Q4)/6
  33 X=X+H
  IF(P.LT.ZM)GOTO 34
  ZM=P
  XM=X
  34 IF(P.GT.ZP)WRITE(7,35)X,CF*(T-TSS)+TSS,P,P/ZM,X-XM
  35 FORMAT(8X,F8.6,5X,F7.2,4X,F10.4,2(5X,F8.6))
  IF(X.LT.XT)GOTO 30
  CLOSE(7)
  STOP
  END

```

Fig. C.1: TRIGA pulse simulation program PULSE.

RHO= \$1.5200
 PL= .2950E-04
 CO= .6673E-01
 GAMA= .1400E-03
 A= .1500E-06
 B= .2670E-04

PEAK POWER= 2999.11 MW T @ PEAK= 240.55 C T FINAL= 394.47 C

TIME	T	P(MW)	P/PMAX	TIME ABOVE PMAX
.000000	23.00	.0001	1.000000	.000000
.031600	23.50	10.4716	1.000000	.000000
.032000	23.58	12.1194	1.000000	.000000
.032400	23.67	14.0261	1.000000	.000000
.032800	23.78	16.2322	1.000000	.000000
.033200	23.90	18.7845	1.000000	.000000
.033600	24.04	21.7372	1.000000	.000000
.034000	24.21	25.1527	1.000000	.000000
.034400	24.40	29.1029	1.000000	.000000
.034800	24.61	33.6712	1.000000	.000000
.035200	24.87	38.9533	1.000000	.000000
.035600	25.16	45.0596	1.000000	.000000
.036000	25.50	52.1173	1.000000	.000000
.036400	25.89	60.2726	1.000000	.000000
.036800	26.34	69.6935	1.000000	.000000
.037200	26.87	80.5729	1.000000	.000000
.037600	27.47	93.1317	1.000000	.000000
.038000	28.17	107.6230	1.000000	.000000
.038400	28.97	124.3340	1.000000	.000000
.038800	29.90	143.5950	1.000000	.000000
.039200	30.97	165.7790	1.000000	.000000
.039600	32.20	191.3080	1.000000	.000000
.040000	33.61	220.6590	1.000000	.000000
.040400	35.24	254.3640	1.000000	.000000
.040800	37.12	293.0210	1.000000	.000000
.041200	39.26	337.2870	1.000000	.000000
.041600	41.73	387.8850	1.000000	.000000
.042000	44.54	445.5970	1.000000	.000000
.042400	47.76	511.2580	1.000000	.000000
.042800	51.43	585.7410	1.000000	.000000
.043200	55.60	669.9360	1.000000	.000000
.043600	60.32	764.7140	1.000000	.000000
.044000	65.67	870.8800	1.000000	.000000
.044400	71.69	989.1030	1.000000	.000000
.044800	78.45	1119.8300	1.000000	.000000
.045200	86.00	1263.1800	1.000000	.000000
.045600	94.38	1418.8000	1.000000	.000000
.046000	103.65	1585.7100	1.000000	.000000

Table C.2: Sample output listing of PULSE.

.046400	113.82	1762.1200	1.000000	.000000
.046800	124.90	1945.3000	1.000000	.000000
.047200	136.88	2131.4100	1.000000	.000000
.047600	149.71	2315.4700	1.000000	.000000
.048000	163.32	2491.3600	1.000000	.000000
.048400	177.59	2652.0900	1.000000	.000000
.048800	192.39	2790.1500	1.000000	.000000
.049200	207.55	2898.0900	1.000000	.000000
.049600	222.87	2969.2600	1.000000	.000000
.050000	238.14	2998.5400	1.000000	.000000
.050400	253.15	2983.0800	.994844	.000400
.050800	267.69	2922.7000	.974707	.000800
.051200	281.58	2820.0200	.940463	.001200
.051600	294.67	2680.2100	.893838	.001600
.052000	306.83	2510.4100	.837210	.002000
.052400	317.98	2318.9000	.773342	.002400
.052800	328.09	2114.2700	.705099	.002800
.053200	337.16	1904.6400	.635189	.003200
.053600	345.20	1697.0900	.565973	.003600
.054000	352.26	1497.3300	.499352	.004000
.054400	358.43	1309.5400	.436726	.004400
.054800	363.76	1136.4900	.379014	.004800
.055200	368.35	979.6770	.326718	.005200
.055600	372.27	839.5810	.279996	.005600
.056000	375.62	715.9080	.238752	.006000
.056400	378.45	607.8300	.202709	.006400
.056800	380.85	514.1800	.171477	.006800
.057200	382.86	433.6080	.144606	.007200
.057600	384.56	364.7020	.121627	.007600
.058000	385.98	306.0680	.102072	.008000
.058400	387.17	256.3830	.085503	.008400
.058800	388.17	214.4290	.071511	.008800
.059200	389.00	179.1050	.059731	.009200
.059600	389.69	149.4380	.049837	.009600
.060000	390.27	124.5700	.041544	.010000
.060400	390.75	103.7620	.034604	.010400
.060800	391.15	86.3751	.028806	.010800
.061200	391.49	71.8635	.023966	.011200
.061600	391.76	59.7637	.019931	.011600
.062000	391.99	49.6830	.016569	.012000
.062400	392.19	41.2901	.013770	.012400
.062800	392.34	34.3063	.011441	.012800
.063200	392.48	28.4978	.009504	.013200
.063600	392.59	23.6686	.007893	.013600
.064000	392.68	19.6549	.006555	.014000
.064400	392.75	16.3199	.005443	.014400
.064800	392.82	13.5494	.004519	.014800
.065200	392.87	11.2483	.003751	.015200

Table C.2: Sample output listing of PULSE (continued).

D. NEUTRON ATTENUATION PROGRAM

D.1 Description

This program uses a Monte Carlo method to determine the fraction of neutrons which escape unattenuated behind a slab placed in a monodirectional beam of neutrons.

D.2 Theory

Two variables determine position randomly for the Monte Carlo simulation: path length and direction. The path length a neutron will travel from location x_0 before its interaction is assigned the probability distribution

$$P(x-x_0) = e^{-\Sigma(x-x_0)}$$

and therefore the distance the neutron reaches position x is

$$x - x_0 = -\ln(R)/\Sigma_t$$

where R is a random number from 0 to 1. This definition is used to calculate both position and path length for scattered neutrons and the position to which a neutron will travel from the slab face before its first interaction (i.e. x when $x_0 = 0$). Next, neutrons are assumed to scatter both randomly and isotropically according to

$$\mu = -1 + 2R$$

where μ is the direction cosine. Calculation of the direction a neutron scatters is unnecessary if prior to the first interaction it escapes the slab (i.e. x is greater than the slab width).

Neutron histories end whenever the particle scatters out of the slab's bombarded face or is absorbed. The type of interaction is determined randomly; if a random number is less than the ratio of absorption to total cross section an absorption occurs and the history is terminated. Otherwise a particle history is scored when a neutron escapes behind the slab either uncollided or following one or more collisions. The escape probabilities for both uncollided and total scores are determined after summation of these scores and division by the total number of histories simulated.

D.3 Use

The user enters the absorption and scattering cross section for the homogeneous slab material via a DATA statement prior execution otherwise important information such as slab width, batch number, the number of histories desired per batch, and a random seed is entered interactively. Since the cross sections for iron have been important to this research, these figures appear in the program listing (Fig. D.1). After each batch is

completed the uncollided and total batch escape probabilities as well as their running means are printed to a user declared output file. Although only the total escape probability is used, the uncollided escape probability is printed to compare to its analytic solution

$$P_{f0} = e^{-\Sigma a}$$

and determine convergence of either result.

D.4 Accuracy

Interbatch standard deviation is calculated and printed with the final results to help determine their statistical accuracy. It should be noted increased computation time is required for increased cross sections and slab width.

Table D.1: MNTTE symbols

Symbol	Meaning
A	Full width of slab (cm).
ESP	Escape probability 1. uncollided 2. collided (one or more scatterings).
MU	Direction cosine.
NB	Number of batches.
NH	Number of histories/batch.
P	Number of neutrons escaping behind slab 1. uncollided 2. collided.
PL	Path length (cm).
PMEAN	Average escape probability.
SIGA	Macroscopic absorption cross section (cm^{-1}).
SIGS	Macroscopic scattering cross section (cm^{-1}).
SIGT	Macroscopic total cross section (cm^{-1}).
X	Position in slab from bombarded face (cm).

```

$USES APPLESTUFF
PROGRAM MNTE
C CALCULATES ESCAPE PROBABILITY FOR HOMOGENOUS SLAB
REAL MU,SP(2),SPS(2),ESP(2)
INTEGER P(2)
CHARACTER FNAME*7,FMT(2)*30
EXTERNAL RAND
COMMON IX
DATA FMT(1)/('/'/'FIRST FLIGHT ESC PROB=' '$)'/
DATA FMT(2)/('/'/'ESCAPE PROBABILITY=' '$,3X$)'/
DATA SP,SPS,SIGA,SIGS/4*0.,0.197,0.9667/
WRITE(*,('ENTER FILE NAME'))
READ(*,('A7')) FNAME
OPEN(8,FILE=FNAME,STATUS='NEW')
WRITE(*,('ENTER A'))
READ(*,('F10.6')) A
WRITE(8,B) A,SIGA,SIGS
8 FORMAT('FULL WIDTH (CM)=' ,F10.6/'MACRO ABS X-SECTION=' ,F10.6/
1'MACRO SCAT X-SECTION=' ,F10.6/'BATCH',6X,'PFO',9X,'PF',6X,'PFO M
2EAN',5X,'PF MEAN'/)
WRITE(*,('ENTER NUMBER OF HISTORIES, BATCHES, AND SEED'))
READ(*,('3I3')) NH,NB,IX
C BEGIN CALCULATIONS
SIGT=SIGA+SIGS
DO 45 K=1,NB
DO 22 I=1,2
22 P(I)=0
DO 40 L=1,NH
I=1
C DETERMINE POSITION IN SLAB
X=-ALOG(RAND())/SIGT
IF(X.GE.A)GOTO 39
I=2
C DETERMINE PATH LENGTH AND DIRECTION COSINE
25 MU=-1+2*RAND()
PL=-ALOG(RAND())/SIGT
C TEST FOR DIRECTION OF NEUTRON
IF(MU) 34,35,31
C TEST IF NEUTRON PASSES BOUNDARY
34 IF(PL+X/MU) 35,35,40
31 IF(PL.GE.(A-X)/MU)GOTO 39
C NEUTRON ABSORBED IF RAND.LT.SIGA/SIGT
35 IF(RAND().LT.SIGA/SIGT)GOTO 40
C CALCULATE NEW POSITION TO SCATTER FROM
X=X+PL*MU
GOTO 25
C COUNT NEUTRONS ESCAPING
39 P(I)=P(I)+1
40 CONTINUE
P(2)=P(2)+P(1)
DO 42 I=1,2
ESP(I)=REAL(P(I))/NH
SP(I)=SP(I)+P(I)
42 SPS(I)=SPS(I)+ESP(I)**2
KT=K
45 WRITE(8,47) K,(ESP(I),I=1,2),(SP(I)/(NH*K),I=1,2)
47 FORMAT(I3,1X,4(E12.6,1X))
C DISPLAY FINAL ESCAPED MEAN, S DEVIATE, AND PROBABILITY
DO 49 I=1,2
PMEAN=SP(I)/(NH*NB)
S=SQRT((SPS(I)-PMEAN**2*KT)/(KT-1))
WRITE(8,FMT(1))
49 WRITE(8,50)PMEAN,S
50 FORMAT(F10.4,3X,'STD DEVIATION=' ,F10.4)
CLOSE(8)
STOP
END
C CALCULATES RANDOM NUMBER
FUNCTION RAND()
COMMON IX
DO 10 I=1,IX
10 RAND=RANDOM()
RAND=RAND/32768.
IX=1
RETURN
END

```

Fig. D.1: Object attenuation program MNTE.

FULL WIDTH (CM)= 1.000000
 MACRO ABS X-SECTION= .197000
 MACRO SCAT X-SECTION= .966700

BATCH	PFO	PF	PFO MEAN	PF MEAN
1	.265000E+00	.490000E+00	.265000E+00	.490000E+00
2	.285000E+00	.485000E+00	.275000E+00	.487500E+00
3	.340000E+00	.530000E+00	.296667E+00	.501667E+00
4	.290000E+00	.505000E+00	.295000E+00	.502500E+00
5	.335000E+00	.515000E+00	.303000E+00	.505000E+00
6	.275000E+00	.480000E+00	.298333E+00	.500833E+00
7	.320000E+00	.545000E+00	.301429E+00	.507143E+00
8	.325000E+00	.615000E+00	.304375E+00	.520625E+00
9	.280000E+00	.510000E+00	.301667E+00	.519444E+00
10	.320000E+00	.520000E+00	.303500E+00	.519500E+00
11	.320000E+00	.545000E+00	.305000E+00	.521818E+00
12	.325000E+00	.605000E+00	.306667E+00	.528750E+00
13	.290000E+00	.535000E+00	.305385E+00	.529231E+00
14	.290000E+00	.550000E+00	.304286E+00	.530714E+00
15	.270000E+00	.470000E+00	.302000E+00	.526667E+00
16	.325000E+00	.535000E+00	.303437E+00	.527188E+00
17	.315000E+00	.545000E+00	.304118E+00	.528235E+00
18	.330000E+00	.495000E+00	.305556E+00	.526389E+00
19	.320000E+00	.575000E+00	.306316E+00	.528947E+00
20	.285000E+00	.515000E+00	.305250E+00	.528250E+00
21	.260000E+00	.490000E+00	.303095E+00	.526429E+00
22	.335000E+00	.530000E+00	.304545E+00	.526591E+00
23	.350000E+00	.565000E+00	.306522E+00	.528261E+00
24	.295000E+00	.510000E+00	.306042E+00	.527500E+00
25	.275000E+00	.500000E+00	.304800E+00	.526400E+00
26	.290000E+00	.520000E+00	.304231E+00	.526154E+00
27	.225000E+00	.520000E+00	.301296E+00	.525926E+00
28	.355000E+00	.570000E+00	.303214E+00	.527500E+00
29	.310000E+00	.565000E+00	.303448E+00	.528793E+00
30	.340000E+00	.550000E+00	.304667E+00	.529500E+00

FIRST FLIGHT ESC PROB= .3047 STD DEVIATION= .0306
 ESCAPE PROBABILITY= .5295 STD DEVIATION= .0353

200 histories per batch

Table D.2: Sample output listing of MNTE.